

GL-TR-89-0194

QUANTIFICATION OF EXPLOSION SOURCE CHARACTERISTICS  
FROM NEAR SOURCE, REGIONAL AND TELESEISMIC DISTANCES

Brian Stump  
Sharon Reamer  
Douglas Anderson  
Kenneth Olsen  
Robert Reinke

Southern Methodist University  
Department of Geological Sciences  
Dallas, TX 75275

Date of Report: 89 July 31

Final Report:  
Period Covered: 87 Feb. 23 to 89 July 31

approved for public release; distribution unlimited.

GEOPHYSICS LABORATORY  
AIR FORCE SYSTEMS COMMAND  
UNITED STATES AIR FORCE  
HANSCOM AIR FORCE BASE, MASSACHUSETTS 01731-5000

DTIC  
ELECTE  
DEC 13 1989  
S E D


89 12 18 130

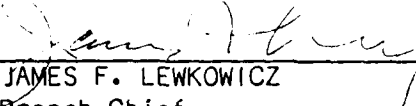
SPONSORED BY  
Defense Advanced Research Projects Agency  
Nuclear Monitoring Research Office  
ARPA ORDER NO. 5299

MONITORED BY  
Geophysics Laboratory  
Contract No. F19628-87-K-0021

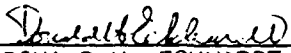
The views and conclusions contained in this document are those of the authors and should not be interpreted as representing the official policies, either expressed or implied, of the Defense Advanced Research Projects Agency or the U.S. Government.

This technical report has been reviewed and is approved for publication.

  
JAMES F. LEWKOWICZ  
Contract Manager  
Solid Earth Geophysics Branch  
Earth Sciences Division

  
JAMES F. LEWKOWICZ  
Branch Chief  
Solid Earth Geophysics Branch  
Earth Sciences Division

FOR THE COMMANDER

  
DONALD H. ECKHARDT, Director  
Earth Sciences Division

This report has been reviewed by the ESD Public Affairs Office (PA) and is releasable to the National Technical Information Service (NTIS).

Qualified requestors may obtain additional copies from the Defense Technical Information Center. All others should apply to the National Technical Information Service.

If your address has changed, or if you wish to be removed from the mailing list, or if the addressee is no longer employed by your organization, please notify AFGL/DAA, Hanscom AFB, MA 01731-5000. This will assist us in maintaining a current mailing list.

Do not return copies of this report unless contractual obligations or notices on a specific document requires that it be returned.

SECURITY CLASSIFICATION OF THIS PAGE

## REPORT DOCUMENTATION PAGE

1a. REPORT SECURITY CLASSIFICATION Unclassified			1b. RESTRICTIVE MARKINGS		
2a. SECURITY CLASSIFICATION AUTHORITY			3. DISTRIBUTION/AVAILABILITY OF REPORT Approved for public release; distribution unlimited		
2b. DECLASSIFICATION/DOWNGRADING SCHEDULE					
4. PERFORMING ORGANIZATION REPORT NUMBER(S) SMU G-6			5. MONITORING ORGANIZATION REPORT NUMBER(S) GL-TR-89-0194		
6a. NAME OF PERFORMING ORGANIZATION Southern Methodist Univ. Dept. of Geological Sci.		6b. OFFICE SYMBOL (if applicable)	7a. NAME OF MONITORING ORGANIZATION Geophysics Laboratory		
6c. ADDRESS (City, State, and ZIP Code) Southern Methodist University Dept. of Geological Sciences Dallas, TX 75275			7b. ADDRESS (City, State, and ZIP Code) Hanscom Air Force Base Massachusetts 01731-5000		
8a. NAME OF FUNDING/SPONSORING ORGANIZATION DARPA/NMRO		8b. OFFICE SYMBOL (if applicable)	9. PROCUREMENT INSTRUMENT IDENTIFICATION NUMBER #F19628-87-K-0021		
8c. ADDRESS (City, State, and ZIP Code) 1400 Wilson Blvd. Arlington, VA 22209			10. SOURCE OF FUNDING NUMBERS		
			PROGRAM ELEMENT NO. 61101E	PROJECT NO. 7A10	TASK NO. DA
					WORK UNIT ACCESSION NO. CS
11. TITLE (Include Security Classification) Quantification of Explosion Source Characteristics From Near Source, Regional and Teleseismic Distances					
12. PERSONAL AUTHOR(S) Brian Stump, Sharon Reamer, Douglas Anderson, Kenneth Olsen, Robert Reinke					
13a. TYPE OF REPORT Final Report		13b. TIME COVERED FROM 87 Feb. 23 TO 89 Jul 31		14. DATE OF REPORT (Year, Month, Day) 89 July 31	
				15. PAGE COUNT 188	
16. SUPPLEMENTARY NOTATION					
17. COSATI CODES			18. SUBJECT TERMS (Continue on reverse if necessary and identify by block number)		
FIELD	GROUP	SUB-GROUP	Chemical explosions, mining blasts, seismic source, quarry		
19. ABSTRACT (Continue on reverse if necessary and identify by block number) Work over the contract period is summarized in four papers: (1) Source Parameter Estimation for Large, Bermed, Surface Chemical Explosions; (2) Seismic Wave Generation by Mine Blasts; (3) Pomona Quarry Seismic Experiment, Near-Source Data; and (4) MISTY ECHO, The Seismic Source Physics Experiment. The first paper attempts to quantify source differences between large surface chemical explosions ranging in yields from 0.075 to 1.65 kilotons. Scaling relations for the long period part of the source spectrum as well as for the source corner frequency are developed. The second paper documents millisecond delay blasting practices in the mining industry and illustrates the effects of these practices on near-source seismic observations. The effects of scatter in design blasting times is illustrated. Source spatial and temporal finiteness are easily identified in the observations and modeled.					
20. DISTRIBUTION/AVAILABILITY OF ABSTRACT <input type="checkbox"/> UNCLASSIFIED/UNLIMITED <input type="checkbox"/> SAME AS RPT. <input type="checkbox"/> DTIC USERS			21. ABSTRACT SECURITY CLASSIFICATION Unclassified		
22a. NAME OF RESPONSIBLE INDIVIDUAL James Lewkowicz			22b. TELEPHONE (Include Area Code) 617) 377-3222		22c. OFFICE SYMBOL AFGL/LWH

19. A set of experiments designed to begin the comparison between single and production mining explosions are described in the third paper. The multiple explosion production shot was documented with high speed photography so that the design and actual firing times of the individual explosions could be compared. Significant variations between design and actual explosion times were found.

The final paper is a preliminary data report describing the first of a series of free field and free surface seismic experiments designed to document the effects of the free surface on seismic radiation from underground nuclear explosions. The particular experiment, MISTY ECHO, was detonated in Rainier Mesa at the Nevada Test Site. Eight, three component free-field gauges were emplaced in the 193-886m range while twelve, three component accelerometers were fielded at the free surface (0.68-1.99 km).

Accession For	
NTIS GRA&I	<input checked="" type="checkbox"/>
DTIC TAB	<input type="checkbox"/>
Unannounced	<input type="checkbox"/>
Justification	
By	
Distribution/	
Availability Codes	
Dist	Avail and/or Special
A-1	

## CONTENTS

	<u>PAGE</u>
SOURCE PARAMETER ESTIMATION FOR LARGE, BERMED, ..... SURFACE CHEMICAL EXPLOSIONS	3
Introduction .....	4
Description of Experiment and Velocity Structure .....	10
Waveform Characteristics and Seismic Phases .....	15
Amplitude Decay With Range .....	20
Source Parameter Estimation .....	24
Source Parameter Scaling .....	26
Long Period Amplitude Scaling .....	30
Corner Frequency Scaling .....	32
High Frequency Spectral Decay .....	33
Regional Corner Frequency Estimates .....	33
Discussion .....	40
References .....	42
SEISMIC WAVE GENERATION BY MINE BLASTS .....	47
Introduction .....	49
Principles of Millisecond Blasting .....	50
Seismic Source Representation .....	55
Temporal Source Effects .....	59
Spatial Source Effects .....	63
Initiator Accuracy .....	66
Efforts to Control Vibration Using Delays .....	68
Conclusions .....	73
References .....	75
POMONA QUARRY SEISMIC EXPERIMENT: NEAR SOURCE DATA .....	79
Introduction .....	81
Description of Experiment .....	81
Description of Explosive Events .....	84
Data .....	86
Preliminary Data Analysis .....	119
Noise Estimates .....	119
Time Series Comparisons .....	119
Range Effects .....	137
Conclusions .....	139
MISTY ECHO. THE SEISMIC SOURCE PHYSICS EXPERIMENT .....	143
Introduction .....	145

## Contents (Cont.)

Objectives .....	145
Justification .....	145
Experiment Description .....	146
In-Tunnel Instrumentation .....	146
Mesa-Top Surface Array .....	146
Results .....	147
Free-Field Data .....	148
Free-Surface Data .....	148
Conclusions .....	149

## INTRODUCTION

Work over the contract period is summarized in four papers: (1) Source Parameter Estimation for Large, Bermed, Surface Chemical Explosions; (2) Seismic Wave Generation by Mine Blasts; (3) Pomona Quarry Seismic Experiment, Near-Source Data; and (4) MISTY ECHO, The Seismic Source Physics Experiment.

The first paper attempts to quantify source differences between large surface chemical explosions ranging in yields from 0.075 to 1.65 kilotons. Scaling relations for the long period part of the source spectrum as well as for the source corner frequency are developed.

The second paper documents millisecond delay blasting practices in the mining industry and illustrates the effects of these practices on near-source seismic observations. The effects of scatter in design blasting times is illustrated. Source spatial and temporal finiteness are easily identified in the observations and modeled.

A set of experiments designed to begin the comparison between single and production mining explosions are described in the third paper. The multiple explosion production shot was documented with high speed photography so that the design and actual firing times of the individual explosions could be compared. Significant variations between design and actual explosion times were found.

The final paper is a preliminary data report describing the first of a series of free field and free surface seismic experiments designed to document the effects of the free surface on seismic radiation from underground nuclear explosions. The particular experiment, MISTY ECHO, was detonated in Rainier Mesa at the Nevada Test Site. Eight, three component free-field gages were emplaced in the 193-886m range while twelve, three component accelerometers were fielded at the free surface (0.68-1.99 km).

**SOURCE PARAMETER ESTIMATION  
FOR LARGE, BERMED, SURFACE CHEMICAL EXPLOSIONS**

**Sharon K. Reamer  
Brian W. Stump**

**Department of Geological Sciences  
Southern Methodist University  
Dallas, Texas 75275**



## ABSTRACT

Near-source velocity waveforms (0.2-2.0 km range) were acquired from a series of bermed surface charges detonated in alluvium at a test site near Yuma, Arizona. The large areal extent of the explosion test beds affords the unique opportunity to study finite spatial effects of surface explosions. Separation of P and Rayleigh waves using particle motions shows development of complex waveforms with increasing range as a result of surface wave phases which change from fundamental mode Rayleigh waves at an intermediate range to a combination of higher mode and fundamental mode Rayleigh waves at the farthest range. Peak velocity decay rates are 20% higher than would be predicted for a simple geometrical spreading model, with values which compare favorably to other chemical explosion studies in alluvium. Consistent seismic source parameters are obtained using the spectral ratio technique. Source corner frequency is proportional to source geometry and long period amplitude levels scale directly with yield. Additionally, the two orders of magnitude change in yield between the smallest and largest charge (from 0.075 to 1.65 kilotons) provides a basis for a linear relative moment-yield scaling relation of large yield chemical explosions in alluvium. Relative moments are obtained with the smallest source serving as an empirical Green's function to the largest source. Spectral ratio corner frequency estimates compare favorably with regional P wave corner frequencies and validate the use of the spectral ratio technique for near-source seismic data.

## INTRODUCTION

The objective of this study is to isolate and examine scaling of seismic source parameters from large surface chemical explosions. Separation of

propagation and attenuation effects from source parameters can be accomplished using seismic modeling techniques or with a more empirically-based approach such as spectral ratios. The latter method obviates the necessity for a detailed knowledge of the path effects, although not without some limitations. Spectral ratios were used successfully for regional earthquake data by Chael (1987) to scale the spectra of several closely spaced events. The parametric spectral model described by Chael (1987) is characterized by a long period, constant amplitude level, corner frequency and high frequency spectral decay. The physical basis for interpretation of seismic source spectra and associated parameters depends on the type of seismic events under consideration, differing for earthquakes and explosions. Source spectral shape and parameterization can be generalized to a functional form (Serenio et al, 1987) given by:

$$S(f) = S_0 \cdot s(f),$$

where:  $S_0$  = constant long period level  
 $s(f)$  = functional spectral form  
 $S(f)$  = spectral values  
 $f$  = frequency.

Additionally, long period level can be related to scalar seismic moment ( $M_0$ ) in a simplified way for both earthquakes and explosions by:

$$S_0 = k \cdot M_0,$$

where the constant,  $k$ , depends on both the source model and a geometrical spreading term. For compressional waves generated from earthquakes, the constant  $k$  is specified by (Stevens and Day, 1985):

$$k = \frac{P}{4\pi(\rho_r \rho_s \alpha_r \alpha_s^5)^{1/2} R},$$

where: P = P wave radiation pattern

$\rho$  = density

$\alpha$  = compressional velocity, and

R = geometrical spreading term

the subscripts r and s denote the receiver and source material properties, respectively. When considering earthquake seismic spectra, long period level provides a measure of the area of slip across the fault surface for kinematic earthquake models (Aki and Richards, 1980). Scalar moment estimates from earthquake data are used to establish empirical relations between seismic moment and body and surface wave magnitudes (Kanamori and Anderson, 1975).

For compressional waves from explosions, the proportionality constant takes the form of (Stevens and Day, 1985),

$$k = \frac{1}{4\pi(\rho_r \rho_s \alpha_r \alpha_s^5)^{1/2} R},$$

differing only from the earthquake constant in the absence of a radiation pattern term. Long period amplitude levels for explosions provide a measure of the compressive strength of the explosions (Mueller and Murphy, 1971; U.S. OTA Report, 1988). Seismic moment versus yield empirical relations for nuclear explosions are used as a basis for yield scaling laws. Body and surface wave magnitudes when plotted against yield provide different sets of scaling relations for nuclear explosions. By combining moment-yield and magnitude-yield scaling relations, the

inherent random uncertainties in each of the methods can be reduced (U.S. OTA Report, 1988).

Corner frequency ( $f_c$ ) is a source parameter associated with a 'characteristic time' for earthquakes and explosions (Savage, 1972; Mueller and Murphy, 1971). Characteristic times associated with earthquakes represent total rupture time along the fault, which is inversely proportional to source dimensionality by the rupture velocity. Thus, corner frequency is given by (Savage, 1972),

$$f_c = \frac{v_r}{L},$$

where:  $v_r$  = rupture velocity

$L$  = fault length or radius.

For large earthquakes, corner frequency may underestimate actual source dimensionality but is still a finite spatial effect of the fault, related to a coherence length rather than an actual fault length (Aki, 1967).

Characteristic times of explosions are related to expansion of a pressure pulse in a spherical cavity. Mueller and Murphy (1971) derive the corner frequency parameter for explosions as,

$$f_c = \frac{c}{2\pi r_{el}},$$

where:  $c$  = compressional wave velocity

$r_{el}$  = elastic radius

If the elastic radius scales with cube root of explosive yield ( $Y$ ), then corner frequency also scales inversely with the cube root of yield. However, the Mueller-Murphy source model includes the effects of source depth and scales as,

$$f_c = \frac{c}{Y^{0.19}},$$

for nuclear explosions at contained depths of  $122Y^{1/3}$ .

Scaling of surface chemical explosions is explored by Murphy (1981) using the analytical spectral response of airblast loading at the free surface. This representation, independent of site characteristics, predicts that long period level of surface explosions scales directly with yield (Y). Corner frequency scaling, free of depth effects, is given by,

$$f_c \approx \frac{1}{Y^{1/3}}.$$

The opportunity to study large, single-burst chemical explosions in a controlled seismic experiment occurs infrequently. Seismic data was collected from a set of high yield, surface charges detonated at a test site in Alberta, Canada with reported yields ranging from 0.25 tons to 0.1 kilotons (kt) (Jones et al, 1963). The Canadian study focused on surface wave propagation and seismic phase analysis as a function of range. Gupta and Hartenberger (1981) examined seismic phases and range-dependent yield scaling of small surface explosives (5-200 lbs.) in both alluvial and granitic environments at local distances from 0.5 to 3 km. Flynn and Stump (1988) utilized near-source seismic data from a series of shallow explosions (1.8 to 11.5 m depths) of 254 lbs. in alluvium at ranges from 17 to 228 m to assess the effects of changing source depth on wave propagation and quantify seismic energy partitioning with range and depth. Additionally, Grant (1988) examined wave propagation, seismic source parameters, and scaling

using near-source data (10-60 m ranges) from a controlled experiment also with near-surface charges (5 lb. charges at 1 to 3 m depth) in alluvium.

The unique aspects of this experiment motivate the source parameter estimation and analysis as follows: (1) since the explosion test beds cover a relatively large surface area, source dimensionality should be observable in the seismic spectrum, similar to earthquake spatial finiteness effects; (2) the explosions are detonated at the surface, offering the opportunity to test long period level scaling with yield; and (3) several different yields were detonated at the same test bed, allowing development of an empirical relationship between seismic moment and explosive yield for large yield chemical explosions in dry alluvium. Additionally, range-dependent wave propagation from the high-yield chemical explosions in this study can be compared to the Canadian surface explosion events and also provide a link to the smaller yield, near-source chemical explosion studies in alluvial environments. However, unlike most surface charges, the explosives were covered with a dirt berm to reduce airblast effects. This may account for some differences in source parameters and propagation effects from this study and other surface chemical explosion studies.

## **DESCRIPTION OF EXPERIMENT AND VELOCITY STRUCTURE**

Near-source seismic data was collected from a series of high-yield, chemical explosions at a test site near Yuma, Arizona by the Air Force Weapons Laboratory. Yields of the four explosions considered in this study were 0.075, 0.15, 1.00 and 1.65 kilotons (kt). Data were acquired from two-component accelerometers deployed in a single azimuth at geometrically progressive distances for each of the four shots. The test beds consisted of planar sheets of Iremite 60 explosives extruded in a partitioned, circular

form and covered with a soil overburden to reduce air blast effects (Bell et al, 1988), thus the loading to the ground was limited to the bermed area. The firing mechanism was designed to produce near-simultaneous detonation of explosives across the test bed. Relative radii of the sources (Figure 1a) scale as 1:1 between the 1.65 and 1.0 kt shots; 1:2 between the 0.15 and 0.075 kt shots, and 1:3 between the 1.65 and 0.075 kt shots. Relative station locations (Figure 1b) coincide between the 1.65 and 1.00 kt sources and between the 0.15 and 0.075 kt sources. Three ranges for each source size are considered in this study (Table 1); propagation path differences due to non-coincidence of stations at a given range are assumed to be minimal when compared to path effects between ranges. Vertical and radial accelerograms originally digitized at  $1 \times 10^4$  samples per second (sps) are filtered recursively with a passband between 0.5 and 125 Hz and resampled at  $1 \times 10^3$  sps. The low frequency cutoff at 0.5 Hz was chosen to minimize the effects of background noise which are emphasized during integration from acceleration to velocity. After resampling, the accelerograms are integrated, tapered and padded to a common time window for each range.

The plane-layered overburden at the test site, primarily composed of clayey sands underlain by consolidated clays, corresponds to a relatively high Poisson's ratio of  $0.33 \pm 0.015$  (Jackson, 1984a,b). Body wave velocity and density estimates are taken from material property studies conducted adjacent to the test site (Jackson, 1984a,b) (Figure 2). Both P and S wave velocities follow a linear trend for the first 0.25 km with the deeper layers exhibiting an exponential increase in velocity with depth. The water table level ( $\sim 0.12$  km) marks a transition from consolidated, unsaturated clay to saturated clay layers. Deeper layers are sequenced as sandstones followed by conglomerates, and underlain by an igneous basement.

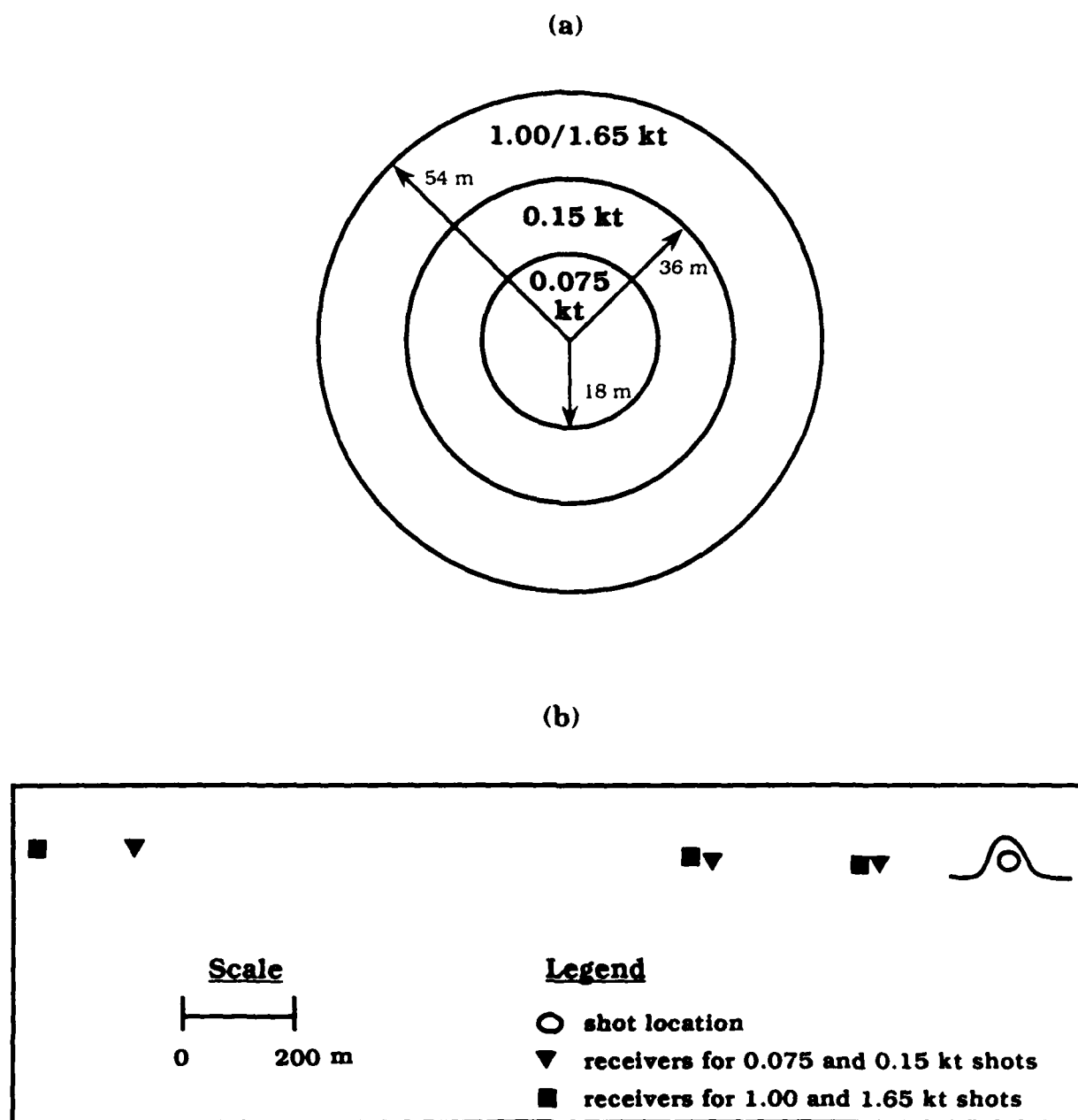


**Figure 1.** Experimental configuration for the chemical explosions detonated near Yuma, Arizona: (a) Source radii for the four bermed surface charges are shown diagrammatically, and (b) the relative station and shot locations are depicted.



**Table 1. Seismic Station Ranges**

Yield (kt)	Ranges (km)		
0.075	0.24	0.56	1.7
0.15	0.24	0.56	1.7
1.00	0.28	0.58	2.0
1.65	0.28	0.58	2.0

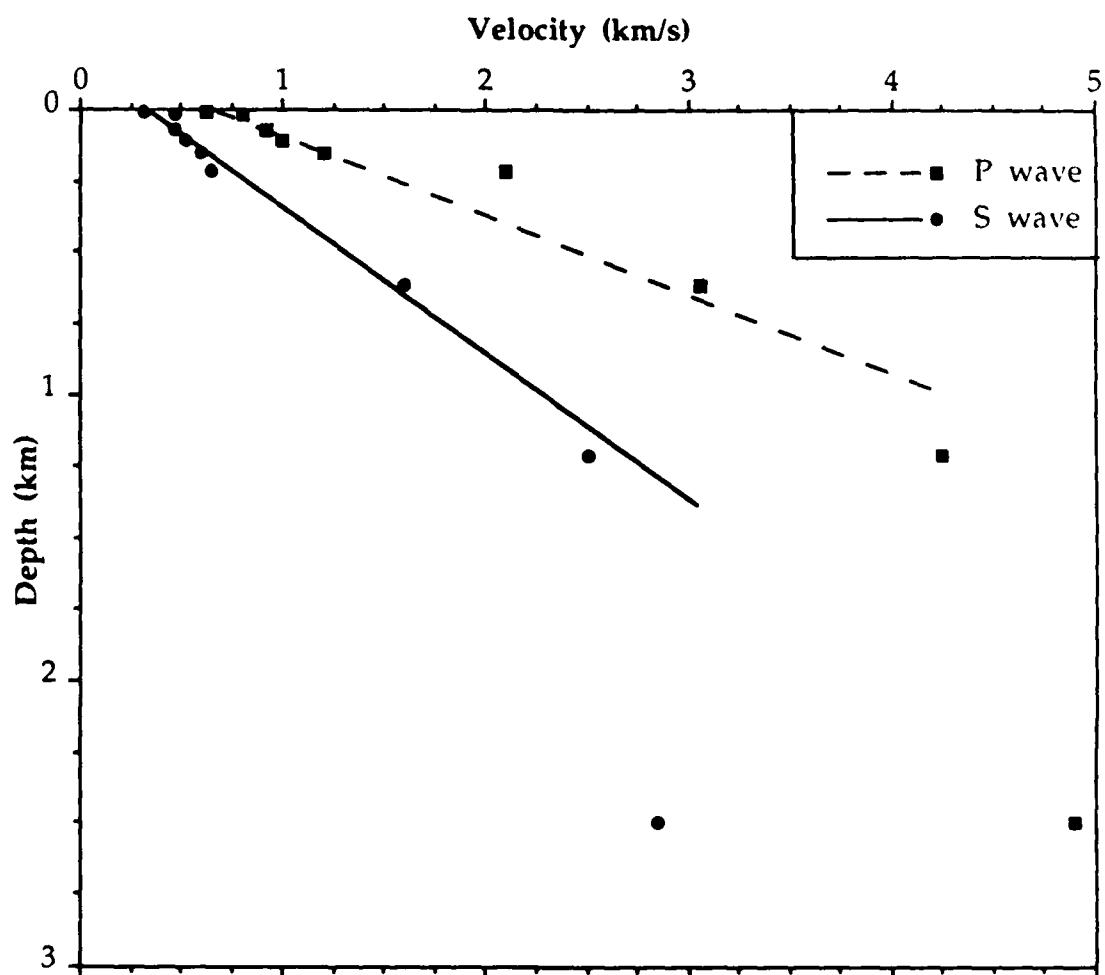


**Figure 2.** The velocity with depth functions shown here are derived from geologic studies adjacent to the test site. The velocity gradient behaves linearly down to 1 km. From 1 to 3 km the velocity-depth function is best described by an exponential velocity gradient.

## WAVEFORM CHARACTERISTICS AND SEISMIC PHASES

To facilitate comparison of wave propagation from sources in this study to other chemical explosion studies, seismic phases are identified using particle motion diagrams. Radial velocity waveforms show increasing complexity as a function of range from the source as observed in the times series plots (Figure 3) with decreased period and amplitude of the first arrival with increasing range. Waveshape complexity and amplitude attenuation will be further quantified in the following discussions. Peak radial amplitudes at the closest range increase by a factor of three from the smallest to largest source size and by a factor of four at the farthest distance. Radial and vertical velocity waveforms are comprised of P waves and SV-Rayleigh waves. SV wave arrivals are masked by the Rayleigh wave arrivals at local distances due to the closeness in arrival times (Flynn and Stump, 1988; Grant, 1988). For the three ranges considered in this study, P and SV-Rayleigh waves show clearer separation with increasing range. Figure 4 illustrates the vertical and radial time series for the 1.0 kt source for all three ranges and includes the time slices used in the particle motion studies. Time windows used to separate the P and Rayleigh waves for the 1.0 and 1.65 kt sources are identical. For the 0.075 and 0.15 kt sources, the actual length and location in time of the windows varied. For all four sources, however, the same number of windows are used at each range, and the particle motions identify the same phases as shown in Figure 5.

At 0.28 km, separation of P and Rayleigh waves is not clear in the first few cycles of the waveform (Figure 5a). The motion shifts back and forth from prograde to retrograde, and the shape is not very rectilinear. The second time window represents an elliptical prograde phase. At

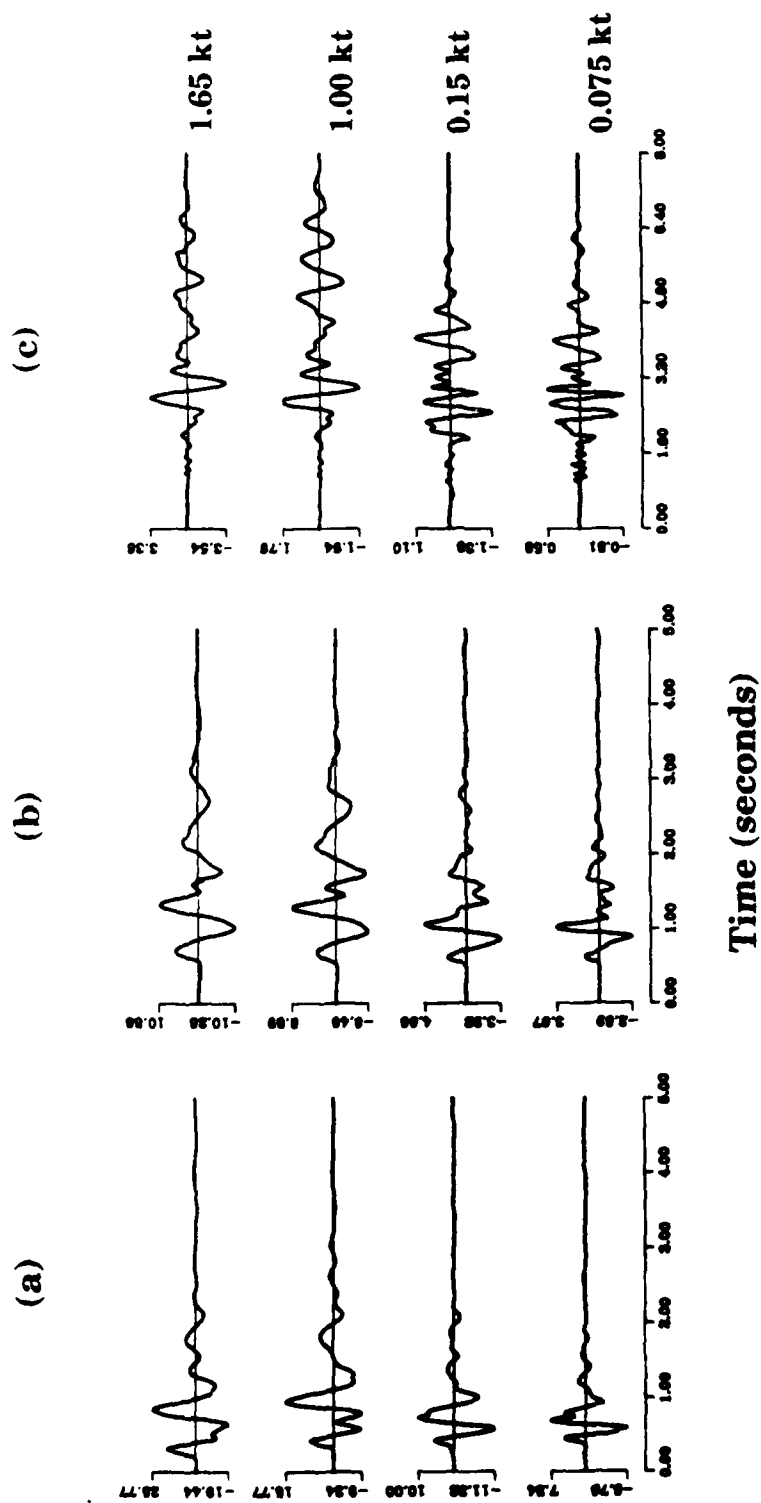
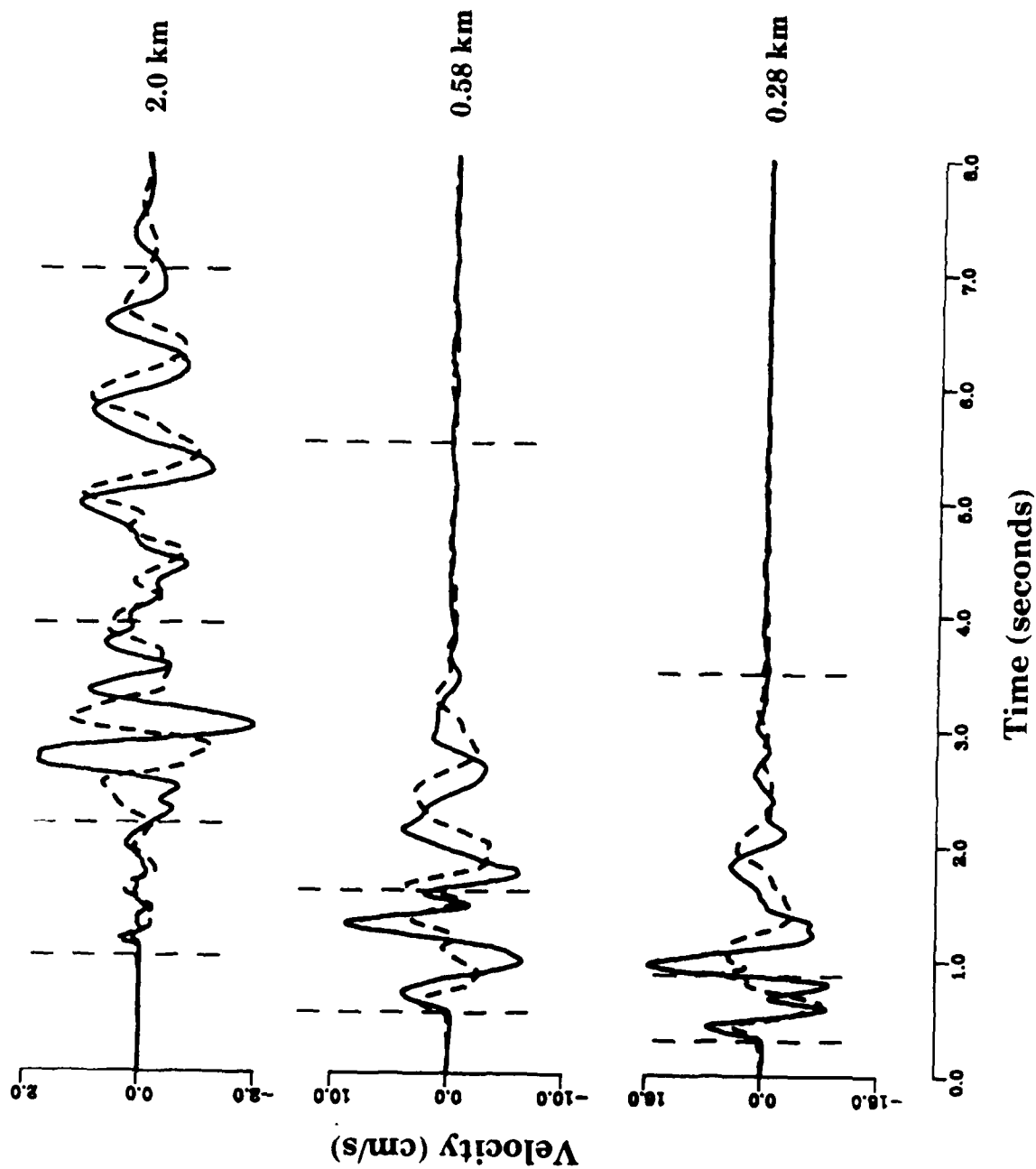
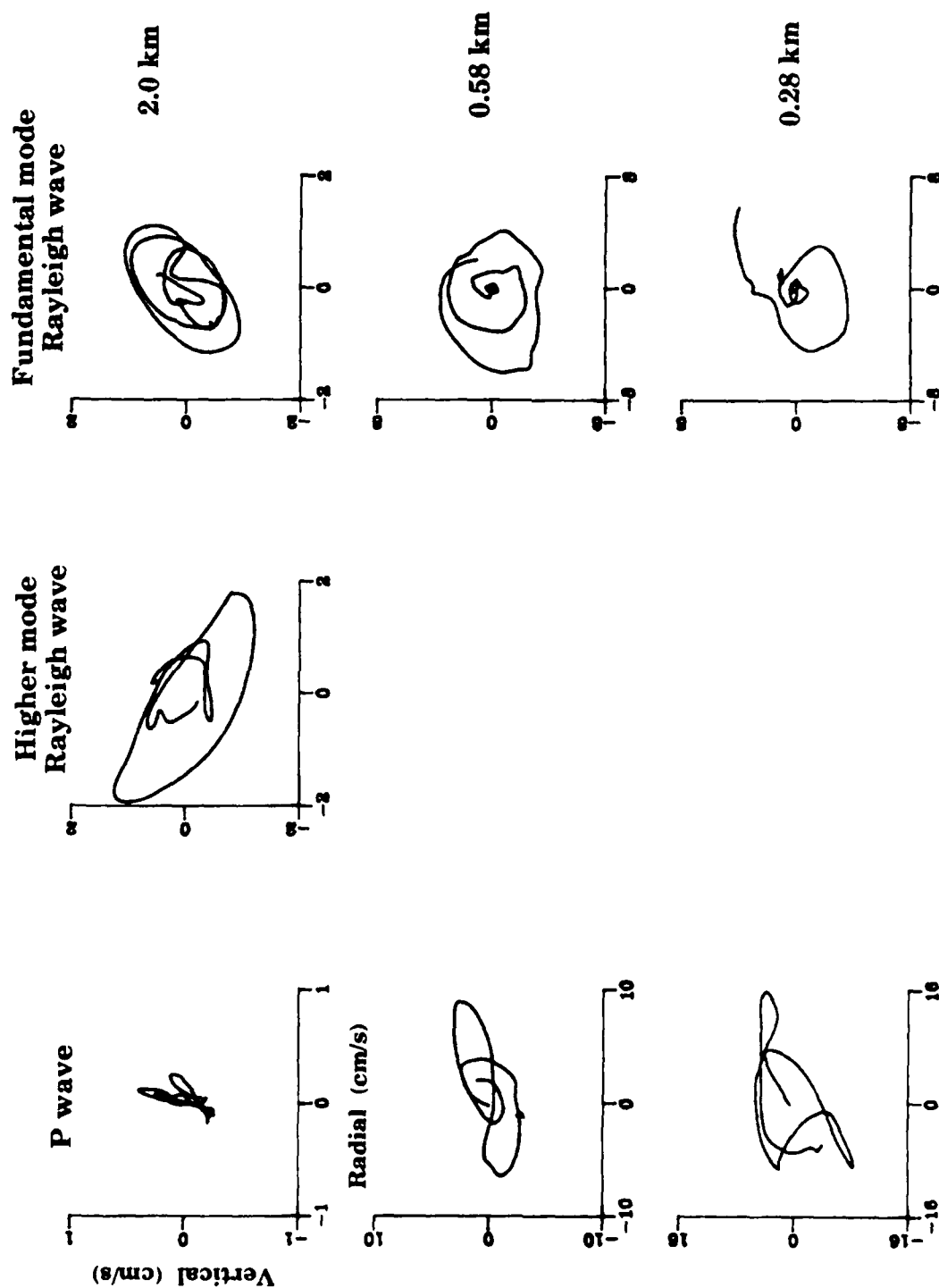


Figure 3. Radial time series for all three ranges and all four explosions. Vertical axis is velocity in cm/s: (a) 0.24/0.28 km, (b) 0.56/0.58 km, (c) 1.7/2.0 km



**Figure 4.** Vertical (dashed line) and radial (solid line) time series for the 1.0 kt shot are plotted for all three ranges. The dashed vertical lines indicate the time windows used for the particle motion diagrams (Figure 5).



**Figure 5.** Particle motion diagrams for all three ranges for the 1.0 kt source. At the farthest range, the direction of motion on the higher mode surface waves is prograde elliptical. Direction of motion for the fundamental mode Rayleigh wave is retrograde elliptical.

0.58 km (Figure 4b and 5b), the Rayleigh waves are clearly identified by retrograde, elliptical particle motion and exhibit weak reverse dispersion. The P wave particle motion shape is essentially rectilinear but slightly open, and orbit of motion reverses near the end of the time window although the shape remains rectilinear. The transition from rectilinear to elliptical motion occurs on the same cycle for all four sources at the 0.56/0.58 km range; however, for the 1.65 and 1.00 kt explosions, the air blast arrival (although not visible in Figure 4) coincides with onset of the Rayleigh waves. The coincidence of this arrival with the air blast may indicate some air-coupled Rayleigh waves as described by Jones et al (1963) and Gupta and Hartenberger (1981) or may be a result of the slow, near-surface shear velocities (Figure 2).

At the 2.0 km range, three time windows are easily identified from the particle motions (Figure 5c). The first phase is rectilinear motion; note the decreased amplitude and increased complexity of the P waves as compared to the rectilinear motion at the middle range (Figure 5b). The increase in the vertical component motions relative to the radial is reflective of waves turned by the shallow geological structure. The second phase is prograde, while the third phase is retrograde elliptical. For the two larger sources, arrival of the air blast occurs well back in the retrograde Rayleigh wave train. Arrival of the air blast also does not coincide with onset of the retrograde elliptical phase for the 0.15 and 0.075 kt sources. The air blast wave, visible on other surface explosion studies (Gupta and Hartenberger, 1981; Jones et al, 1963) is muted or absent on the records from this study due to berming of the explosives. The second time window particle motions correspond to normally dispersed, higher mode Rayleigh waves which were observed by Gupta and Hartenberger (1981) as long period precursors

to the air blast with prograde elliptical motion. This type of particle motion is also noted by Jones et al (1963) as a dispersed Rayleigh wave which precedes the air blast arrival and exhibiting both prograde and retrograde elliptical motion. At the farthest range, the prograde higher modes are then followed by inversely dispersed, fundamental mode Rayleigh waves with retrograde particle motions. This development of two distinct surface wave packages exhibiting the same change in orbital direction and dispersion characteristics with increased range was, also observed by Reinke (1978) for surface wave propagation in the unconsolidated graben fill of the Tularosa Basin.

### AMPLITUDE DECAY WITH RANGE

Body and surface wave peak velocity decay with range depends on both geometrical spreading and local propagation effects. Amplitude decay due to geometrical spreading is frequency independent, due only to the radial distance from the source. Since body and surface waves travel as spherical and cylindrical waves, respectively, amplitudes decay as  $1/r$  and  $1/r^{1/2}$ , where  $r$  is the radial distance from the source and loss of energy due to layering effects. This simple, range-dependent decay factor will increase as propagation through layered structures becomes more complex. Local propagation effects cause additional attenuation and absorption in the form of anelasticity and scattering of seismic energy due to local inhomogeneities. Total amplitude decay may be expressed as a combination of geometrical spreading and anelastic attenuation as,

$$A = \frac{e^{-\alpha r}}{r^n}$$

where:  $A$  = attenuation as a function of frequency



$\alpha$  = attenuation constant

$r$  = radial distance from source

$n$  = geometrical spreading exponent

The attenuation constant,  $\alpha$ , is related to rock anelasticity by,

$$\alpha = \frac{\pi f}{Qv}$$

where:  $f$  = frequency

$Q$  = coefficient of internal friction

$v$  = wave velocity.

Local propagation affects near-source data by increasing the  $1/r$  and  $1/r^{1/2}$  attenuation factors and causing scatter in the peak amplitude values from a linear decay rate.

Vertical and radial velocity peak amplitudes are chosen based on maximum zero-to-peak amplitude values for the time windows corresponding to the P and Rayleigh waves. For the 0.15 and 0.075 kt sources, some peak amplitudes at ranges from 0.08 to 0.14 km are also included in the P wave amplitude data. Scaled ranges ( $m/kt^{1/3}$ ) are used to compensate for source size differences. The P waves decay linearly with scaled range at the rate of -1.8 and -1.4 for radial and vertical components, respectively (Figure 6a). Correlation coefficients for the best line fits are 0.92 and 0.93, respectively with a factor of four maximum scatter. For the Rayleigh waves, decay exponents are -1.0 and -0.75 for the radial and vertical components, respectively (Figure 6b). Correlation coefficients of 0.86 and 0.87 indicate a higher degree of overall scatter among Rayleigh wave peak velocities but a maximum scatter of only a factor of two. These decay rates represent large attenuation rates which are a combination of

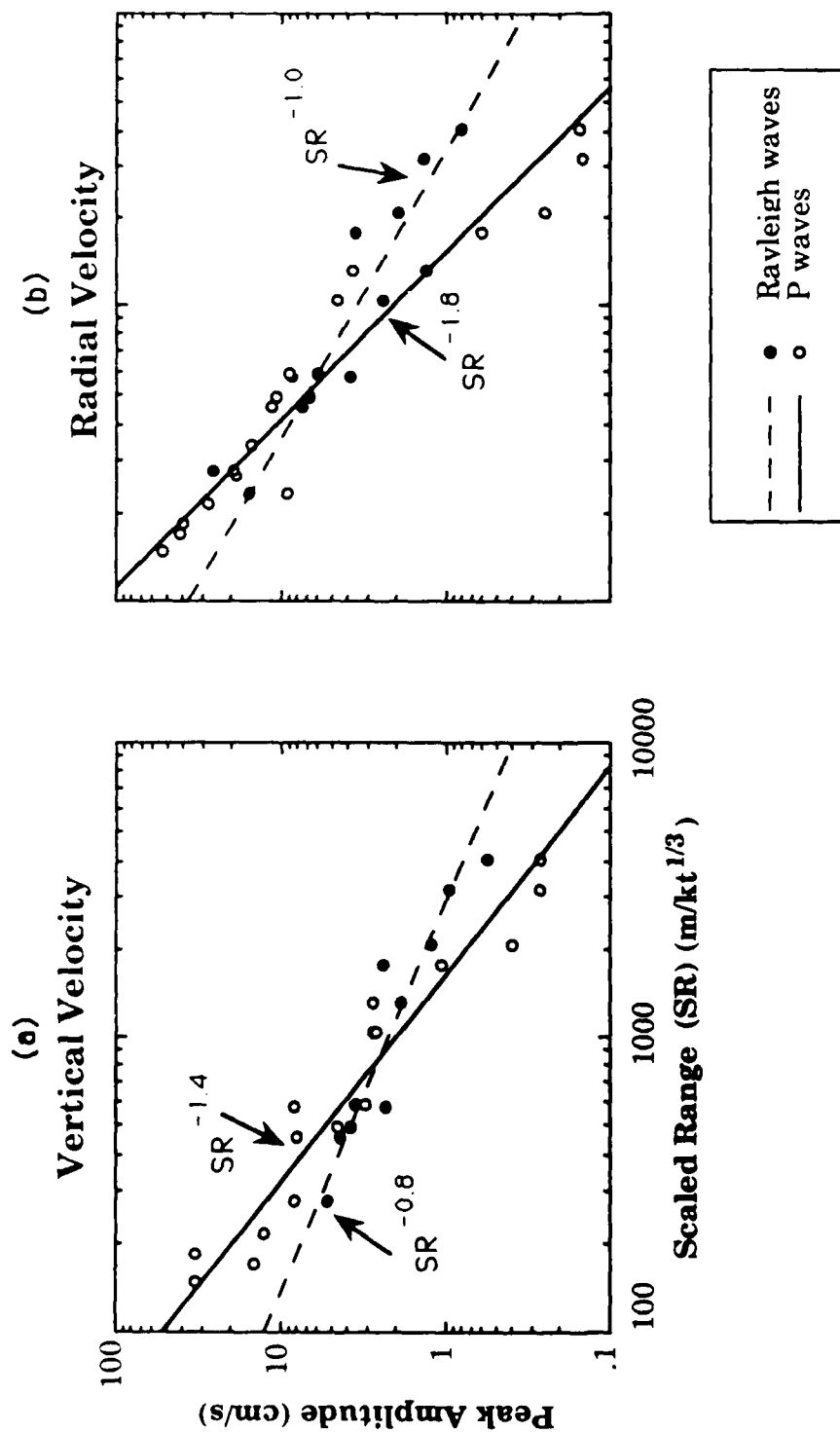


**Figure 6.** Log of peak velocity amplitude versus log of scaled range is plotted for both (a) vertical and (b) radial motions for all sources sizes. P wave and Rayleigh wave peak amplitudes are picked based on particle motions (Figure 5). Also included are some peak amplitudes from 0.08-0.14 km (included in P wave amplitudes) from the 0.075 and 0.15 kt records.

increased geometrical spreading due to near-surface layering and local propagation path anomalies.

P wave spatial decay constants of -1.6 for radial and -1.3 for vertical components obtained from chemical explosions at depth in alluvium at comparable distances to the ranges considered in this study (Flynn and Stump, 1988) compare favorably to those obtained for these sources indicating that local propagation effects in alluvial overburden are similar, regardless of source size. In support of this idea, average peak velocity decays rates for body waves from small buried charges at depth in dry alluvium obtained by Grant (1988) of -1.6 and -1.8, respectively, for the radial and vertical components also correlate well with values in this study. The higher decay rates for the radial component may be due to the much shorter distances sampled by Grant (1988), reflecting more wave propagation within the low velocity surface layers. However, the decay rates still fall within the range of scatter in the linear fits to these data. Average SV-Rayleigh decay rates reported by Flynn and Stump (1988) of -1.0 and -0.9 also compare favorably to exponents for surface waves in this study. The vertical decay constant is somewhat higher but also falls within the range of scatter for these data. Decay rates of surface waves obtained by Gupta and Hartenberger (1981) of -1.33 and -1.15 for radial and vertical components, respectively, from surface charges in beach sand overburden are also higher than the rates in this study and probably reflect a dissimilarity in the geologic media between the two test sites.

## SOURCE PARAMETER ESTIMATION

Two approaches to consider for isolating seismic source parameters are based on the assumption of a simplified convolutional seismic model (Robinson, 1963),

$$U = P \otimes S$$

where,  $U$  = ground displacement or velocity

$S$  = contribution of seismic source

$P$  = contribution of propagation and attenuation

As noted by Chael (1987), instrument response and ambient background noise contribute to the seismic signal and should also be included in this model. A source time history or frequency response may be obtained using seismic modeling techniques with sufficient *a priori* knowledge of the effects of propagation and attenuation. Alternatively, when local propagation effects are not well constrained, an empirically based method such as the spectral ratio technique may be used. The spectral ratio method also assumes the validity of the convolutional seismic model; however, by applying a Fourier transform, the time domain convolution becomes multiplication in frequency. Relative source spectra are obtained by taking ratios of two individual spectra at a given range.

As pointed out earlier in the time series analyses, high attenuation rates and increasing waveform complexity with increasing range confirm the assessment that local propagation effects strongly influence these near-source waveforms. Since these effects are not well-constrained in the present study, the use of spectral ratios seems an appropriate method for separating source parameters from local propagation effects. For this study, propagation and attenuation effects (as well as instrument effects

and ambient noise levels) are assumed to be similar even though respective ranges do not exactly coincide for all ratios.

The convention is adopted here where the smaller source serves as an empirical Green's function for the larger source (Mueller, 1985). A general assumption is that the source types between the ratioed sources is similar. The use of an estimated source as the empirical Green's function has the advantage of stability with respect to source non-stationarity, and specific assumptions about propagation effects, noise or instrumentation are unnecessary (Clayton and Wiggins, 1976; Mueller, 1985). Complex spectral division results in a quotient spectrum (Mueller, 1985), here regarded as the end product or spectral ratio to be used in source parameter estimation. The complex spectral division is given by (Clayton and Wiggins, 1976),

$$\frac{U_2}{U_1} = \frac{(X_R \cdot X_R + X_I \cdot X_I)^{1/2}}{(Y_R \cdot Y_R + Y_I \cdot Y_I)^{1/2}}$$

where:  $\frac{U_2}{U_1}$  = quotient spectrum (spectral ratio)

X = numerator spectral components

Y = denominator spectral components

and the subscripts R and I denote the real and imaginary components.

Previous studies note that where the denominator spectral values become small, instability results as the noise level becomes increased (Clayton and Wiggins, 1976). A "waterlevel" value of 0.001 per cent of the maximum denominator spectral value is applied here to prevent the noise level from dominating the spectrum. The smaller the waterlevel, the more unrestricted deconvolution becomes; therefore, use of a smaller waterlevel parameter reduces biasing the spectrum at low frequencies (Mueller, 1985;

Clayton and Wiggins, 1976). The spectral ratios are band-limited from 0.5 to 10 Hz to reject frequencies where noise enhancement becomes problematic. Additionally, quotient spectra are smoothed with a five-point, symmetrical, weighted average window at each frequency. Our approach differs in that full waveform spectral estimates are utilized instead of only the body wave phases used by Clayton and Wiggins (1976). The bandwidth of the source spectra are enhanced in this manner since the surface waves contribute more to the low frequency portion of the spectrum with P waves enriching the high frequencies (Figure 7).

### **SOURCE PARAMETER SCALING**

Spectral ratio estimates are decomposed into relative source parameters following the model of Chael (1987) but with the divisor/dividend convention reversed (Figure 8). Parameters are estimated by fitting the model to each individual ratio and include a long period level, upper corner frequency corresponding to the numerator (larger) source, lower corner frequency corresponding to the denominator (smaller) source, and a high frequency spectral decay in the frequency band between corners. The spectral ratios for the radial component records are characterized by consistent shape as a function of range for each ratio (Figure 9). When viewed in this manner, the "envelope" of a given spectral ratio type, which includes the ratios at all three ranges, provides a good visual average of the source parameter estimates. Similar consistent results are obtained for the vertical component records.

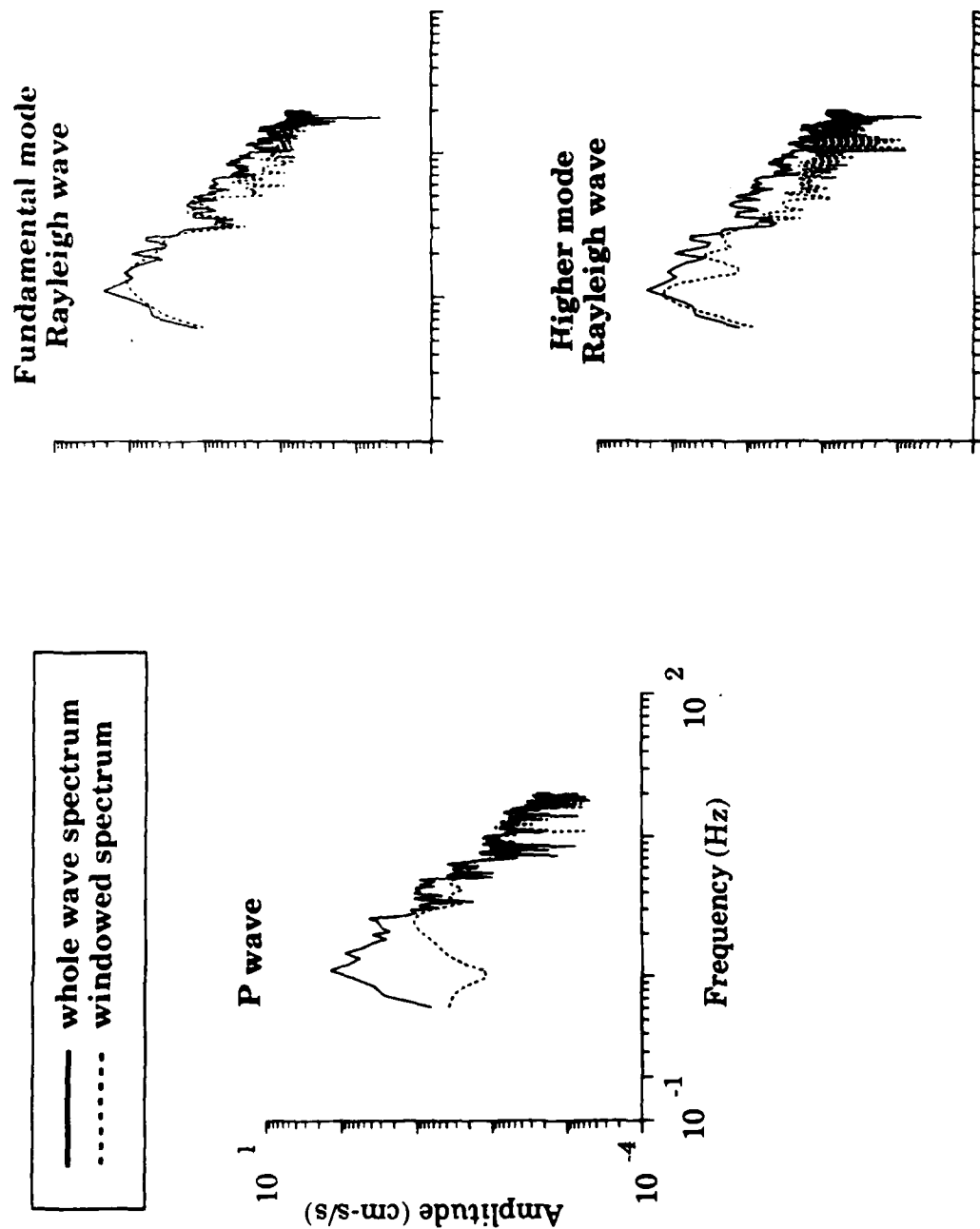


**Figure 7.** Windowed velocity spectra are plotted against the spectrum of the whole seismic record. The windows are picked based on the particle motion results of Figure 5. The P wave contributes to the spectrum between 5 and 15 Hz while the Rayleigh waves contribute more to the spectrum between 0.5 and 5 Hz.

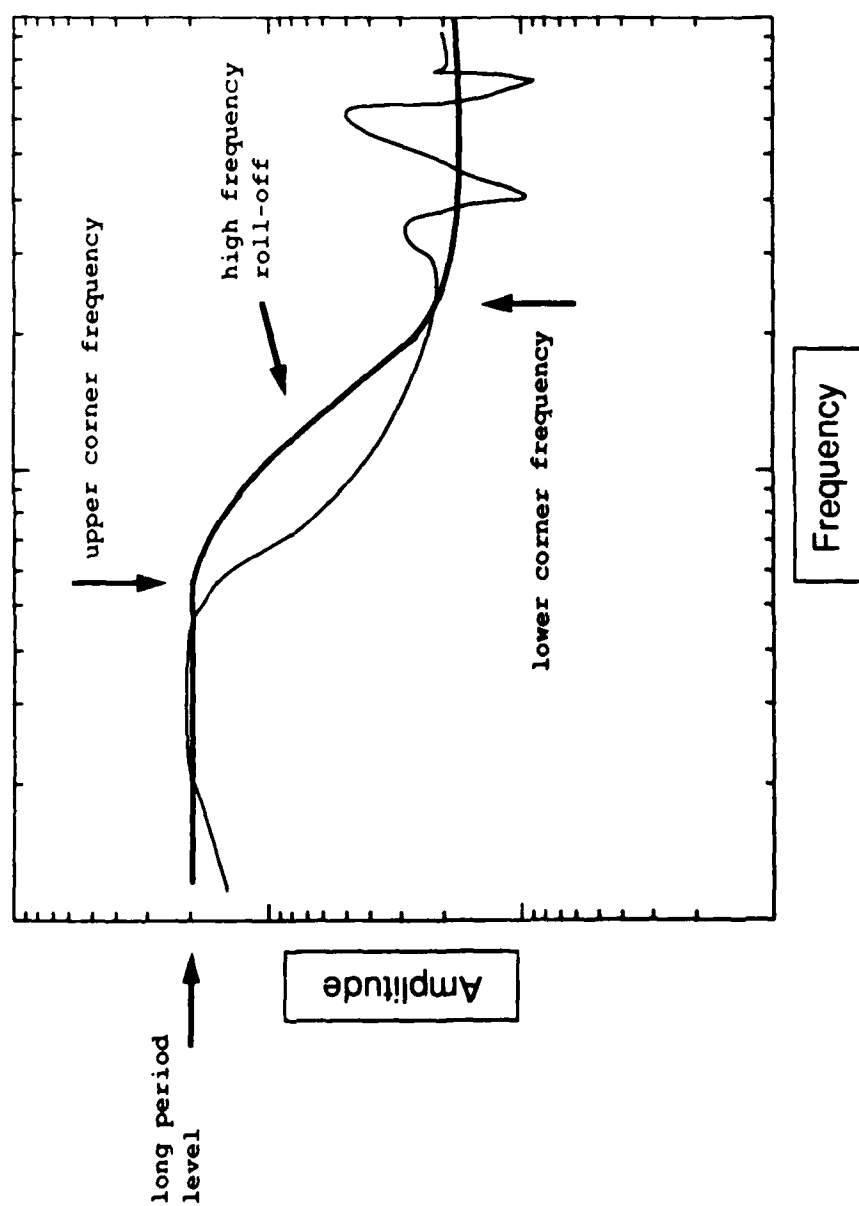


**Figure 8.** This schematic depiction of the assumed spectral ratio model includes the source parameters to be estimated from the observed spectral ratios: long period amplitude level, upper corner frequency corresponding to the numerator source, high frequency spectral decay, and lower corner frequency corresponding to the denominator source.



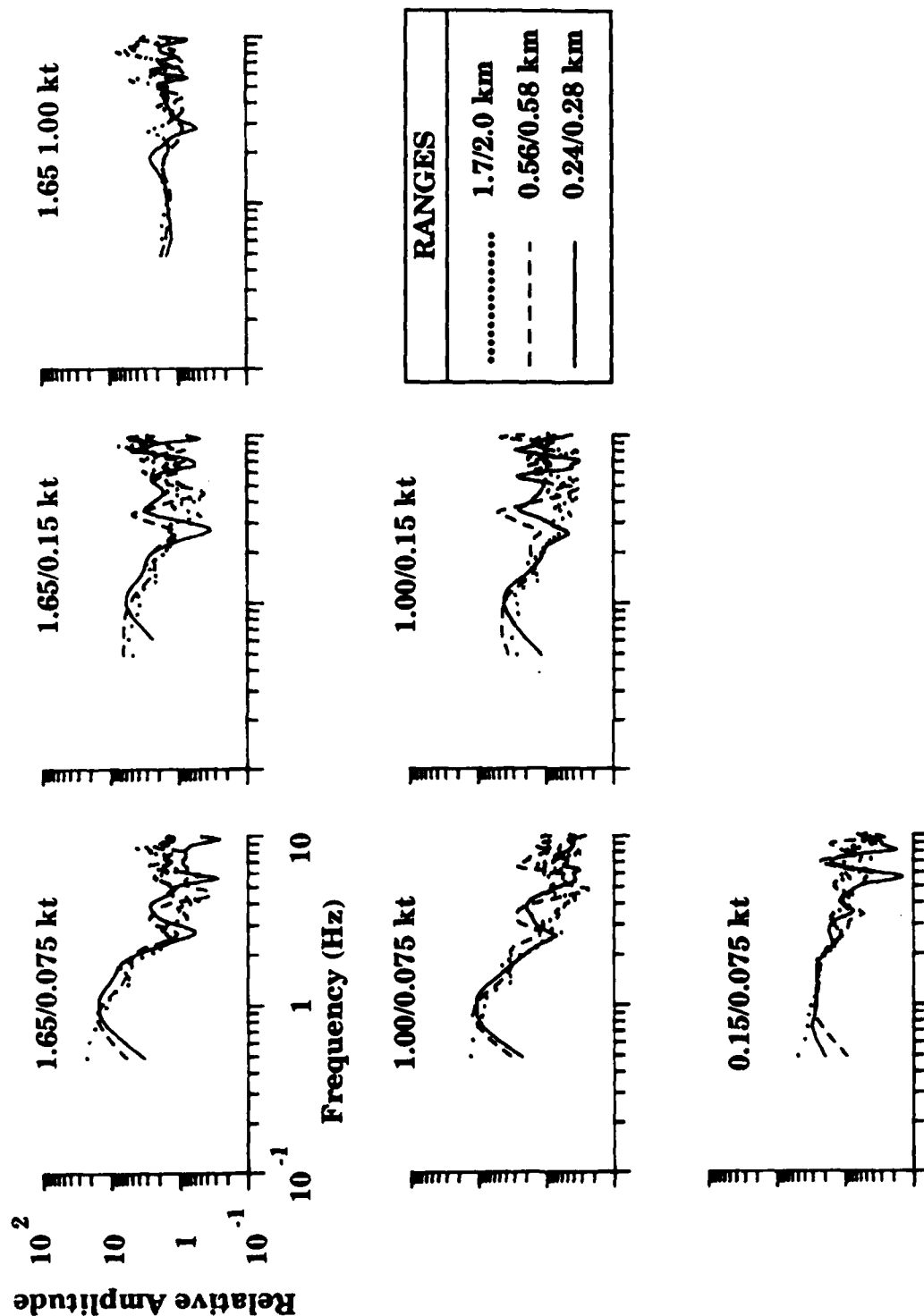


**Figure 9.** Spectral ratios estimated from radial velocity spectral amplitudes show good consistency as a function of range. The three ranges are superimposed on each spectral ratio plot. Numerator and denominator sources for each plot are indicated at the top.

### Long Period Amplitude Scaling

Explosion yield scaling is expressed in terms of a ratio of two explosive yields raised to an exponent,

$$\left(\frac{Y_1}{Y_2}\right)^n$$

The exponent describes the yield scaling relationship and has been shown to be frequency dependent for contained nuclear explosions (Mueller and Murphy, 1971). For surface explosions calculated using analytical surface wave calculations, long period amplitude ratios scale directly with yield (Murphy, 1981). This yield scaling relationship is supported in this study by the relative long period amplitude levels estimated from the spectral ratios (Figure 9) and summarized in Table 2. Relative amplitude levels are averaged for each ratio type for all ranges in the study and the average values and standard deviations are given along with the yield exponent calculated for the average values. This corresponds to six relative amplitude values for each ratio type as listed in the table; except that ratios with the 1.65 kt source have only five estimates, since no radial component is available at the 0.28 km range. The correlations are surprisingly good considering how few data points contribute to the statistics. Although some variation is observed in this scaling parameter, when taken together the yield exponent values average to  $1.01 \pm 0.23$ .

These results support the validity of the spectral ratio method. Long period level, proportional to the scalar seismic moment, here provides the relative scalar seismic moment. Plotting relative moment versus yield provides an empirical moment-yield relation for surface chemical

Table 2. Long Period Level Scaling with Yield

Yield Ratio	Yield Scaling		Yield Exponent
1.65/0.075	23.0	$\pm 2.6$	1.01
1.00/0.075	14.0	$\pm 2.8$	1.02
0.15/0.075	2.7	$\pm 0.2$	1.45
1.65/0.15	7.6	$\pm 1.1$	0.85
1.00/0.15	4.5	$\pm 1.1$	0.79
1.65/1.00	1.6	$\pm 0.1$	0.96

explosions in alluvium observed at close distances (Figure 10). This linear relationship, shown here for the 1.65/0.075 ratios is given by:

$$M_{Y0} = 0.3 + 13.8Y$$

where:  $M_{Y0}$  = relative scalar seismic moment, equal to,  

$$\frac{M_{\alpha(1.65)}}{M_{\alpha(0.075)}}$$

and  $Y$  = yield

with a correlation coefficient of 0.999. Standard deviations of the relative moments used in the empirical relationship were listed in Table 2 and are plotted as error bars in Figure 10.

### Corner Frequency Scaling

Upper and lower corner frequencies are estimated by fitting a model such as that in Figure 8 to all spectral ratios. Examination of the spectral ratio plots (Figure 9) reveals some of the important features of the corner frequency scaling of these sources. The 1.65/1.00 kt ratios exhibit no discernible corners. There are some small oscillations in the ratios that we attribute to spectral scalloping. This contrasts markedly to the other spectral ratios which exhibit corners in accordance with our spectral ratio model. A plot of corner frequency versus range (Figure 11) demonstrates quantitatively the consistency with range that was viewed qualitatively in Figure 9, and a proportionality that can best be explained by examining the relative source geometries for these explosions.

The 1.65 and 1.00 kt corner frequencies plot together reflecting the 1:1 correspondence of their source radii. Similarly, 0.15 kt corner frequencies average slightly less than twice the value of the larger source corners in

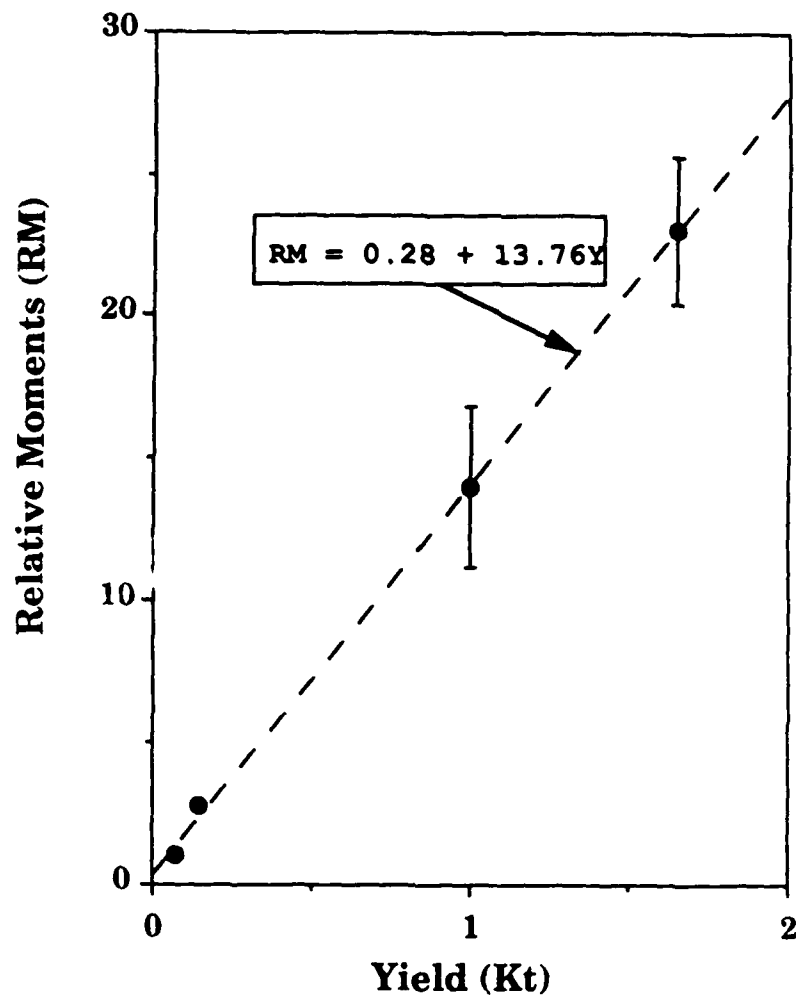


**Figure 10.** Relative moment versus yield results in the linear fit shown in the inner box on the graph with a correlation value of 0.999. Error bars correspond to the standard deviation values listed in Table 2.

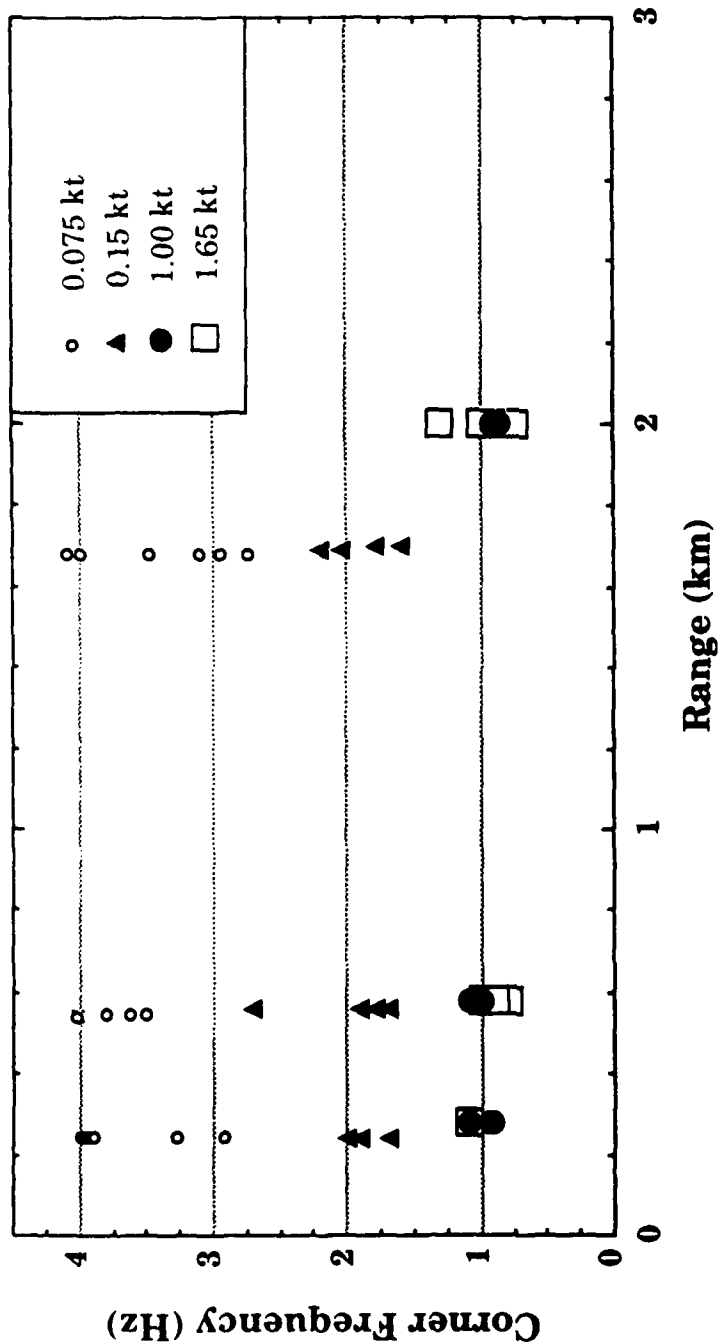


**Figure 11.** Corner frequencies plotted versus range for all spectral ratios scale with relative source geometry. Both upper and lower corner frequencies have been included. The 0.075 kt corner frequencies exhibit the largest scatter since they are estimated from the high frequency end of the spectral ratio where noise becomes enhanced.

accordance with a 1.5:1 ratio of source radii. The 0.075 kt corner frequencies exhibit considerable scatter, scaling between 2.7 and 4.1 Hz. The large amount of variability in the 0.075 corner frequencies is attributable to the fact that the lower (denominator) corners are harder to estimate consistently due to higher variability in the spectral ratio estimates with increasing frequency.

Corner frequencies of surface explosions from analytical surface wave calculations (Murphy, 1981) scale with the cube root of yield. Table 3 shows a comparison of corner frequencies from cube root yield scaling (column 3) with average corner frequencies estimated from the spectral ratios (column 2). The spectral ratio average corner frequencies are obtained by taking an average of all the corner frequencies estimated from the spectral ratios for each source and taking ratios of the averages. Although the cube root yield scaled values are close to the source geometry radius ratios (column 4), the spectral ratio corner frequencies scale slightly more consistently with the source radii than the cube root yield values for all but the 1.65/0.075 and 1.00/0.075 corners. These corners may be biased high due to the large variability in 0.075 corner estimation as mentioned earlier. Although the cube root scaling model could account for the corner frequencies estimated in this study, we feel that the proportionality to source geometry exhibited by these sources is more consistently demonstrated by these results. Additionally, berming of the explosives may account for some differences in corner frequency scaling observed in this study and corner frequency scaling due to air blast loading at the surface.

**Table 3. Corner Frequency Scaling with Yield**

<b>Yield Ratio</b>	<b>Spectral Ratio Average Corner</b>	<b>Cube Root Yield Scaling</b>	<b>Source Radius Ratio</b>
1.65/0.075	3.7	2.8	3.0
1.00/0.075	3.7	2.4	3.0
0.15/0.075	1.9	1.3	2.0
1.65/0.15	2.0	2.2	2.0
1.00/0.15	2.0	1.9	2.0
1.65/1.00	1.0	1.2	1.0



### **High Frequency Spectral Decay**

High frequency roll-off estimates are inconsistent for these data with values ranging from  $f^{-2}$  to  $f^{-4}$ . The effects of attenuation and local propagation although similar, are not exact for all spectral ratio estimates and may lead to variation in the spectral ratio estimates which obscure consistent values for this parameter.

### **Regional Corner Frequency Estimates**

To judge the efficacy of local seismic studies in characterizing chemical explosion sources, it is desirable to compare estimates of source parameters from local data to regional corner frequency estimates. Empirical relationships established in this way provide a measure for future scaling relationships where local data may be unavailable. Corner frequencies of regional P wave spectra from the Scarlet network (Figure 12) are estimated for the 1.0 kt source. As seen from the comparison of corner frequency versus range (Figure 13), regional corner frequencies compare favorably to local spectral ratio estimates. Local P wave spectra are calculated from the time windows established for the particle motion diagrams. Corner frequencies of local P wave spectra for the 1.0 kt source are biased high and show less consistency with range when compared to the spectral ratio estimates. The same holds true for all source parameters estimated from velocity spectra, even when the full waveforms are used in the spectral estimates. We assert that this bias is due to local propagation and attenuation effects and base our conclusion by contrast with the consistency of the spectral ratio source parameter estimates.

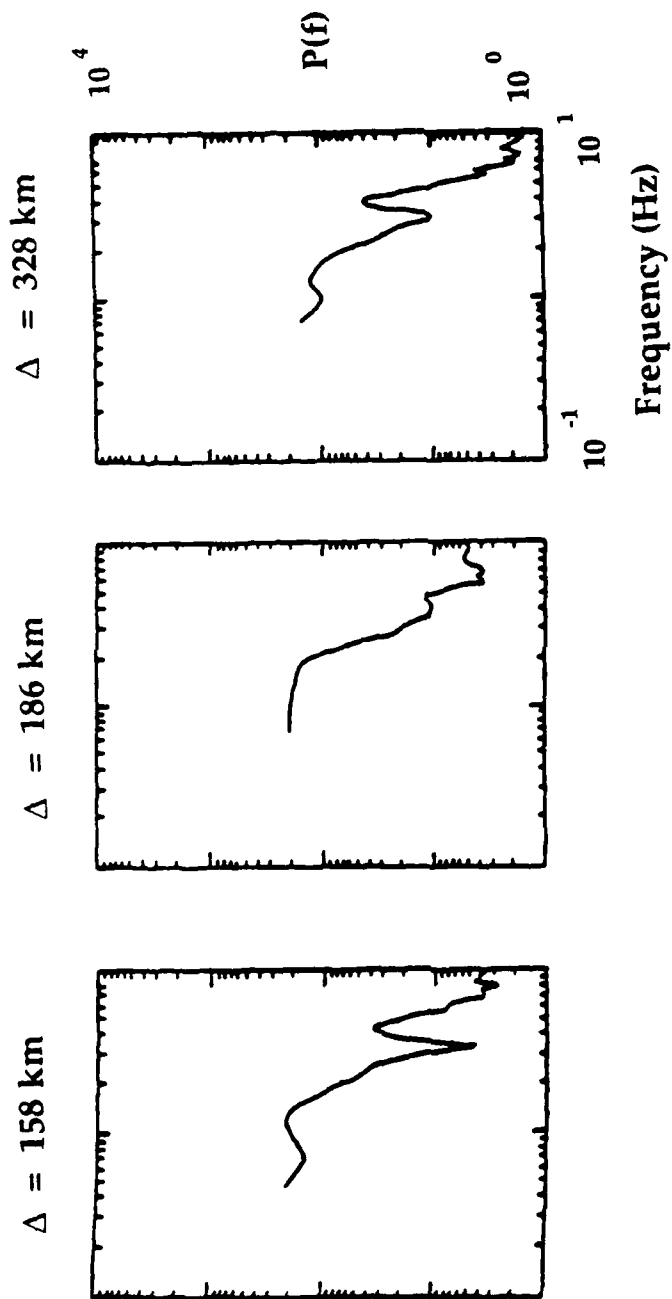


**Figure 12.** P wave spectra from the 1.0 kt source are estimated from records taken from the Scarlet regional seismic network (courtesy of Jack Murphy) shown here at three different ranges.

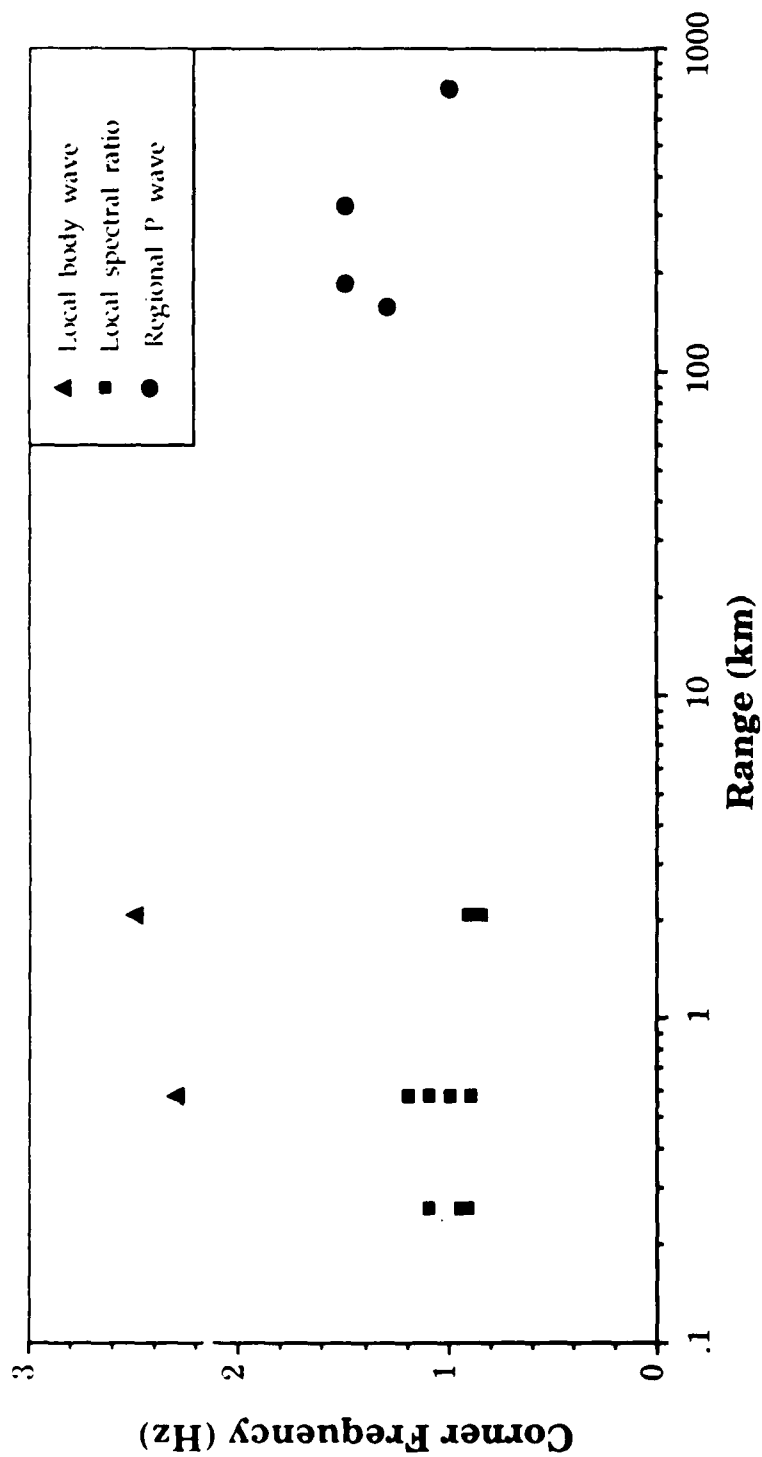


**Figure 13.** Regional P wave corner frequencies compare well with local spectral ratio corner frequencies for the 1.0 kt source. Local body wave corner frequencies are biased high due to local propagation path effects. P wave windows are based on the particle motion diagrams (Figure 5).

## DISCUSSION

For the large chemical explosion sources examined in this study, development of surface waves with range illustrates the increasing complexity of waveforms with range. High spatial decay rates are not accounted for by simple geometrical spreading models and are comparable to decay rates from other surface chemical explosion studies in alluvium, even though source size differences represent several orders of magnitude. However, better constraint of local propagation effects cannot fully compensate for waveform complexity and attenuation as a function of range for these explosions. This necessitates the use of empirical methods for estimation of seismic source parameters, such as the spectral ratio technique. In the absence of well defined structural data, the spectral ratio method proves to be a good approach for estimating corner frequencies and long period amplitude levels. Consistent estimates are obtained in this manner which show little variability with range. The estimated source parameters clearly show that average relative amplitudes scale directly with yield in support of earlier work by Murphy (1981) and specific ratios may be used to construct empirical moment-yield relations as presented here. More calibration studies of this type are necessary to develop and reduce the statistical uncertainties in empirical moment-yield scaling relations for chemical explosions. Additional studies will also serve to better characterize these sources and may serve as a basis for comparison to nuclear explosion moment-yield relations. Proportionality of corner frequency to source dimensionality is demonstrated, indicating that spatial finiteness from these large surface explosions controls spectral scaling instead of cube root of yield scaling. This places restrictions on the types of seismic source models that may be used to simulate wave propagation from

large chemical explosions. The efficacy of using the near-source seismograms to characterize these sources is validated by a favorable comparison of spectral ratio corner frequencies to those estimated from P wave spectra at regional distances. This further enhances the usefulness of additional calibration studies of local seismic data to characterize chemical explosion seismic data.

## REFERENCES

- Aki, K., 1967, Scaling law of seismic spectrum, **J. Geophys. Res.**, **72**, 1217-1231.
- Bell, K. G., J. S. Jarpe, H. J. Aguilar, 1988, HEST and BLEST developments for the ASH/ISST test program, **NMERI final report**, AFWL, Kirtland AFB, New Mexico, 79 pp.
- Chael, E.P., 1987, Spectral scaling of earthquakes in the Miramichi region of New Brunswick, **Bull. Seism. Soc. Am.**, **77**, 347-365.
- Clayton, R. W. and R. A. Wiggins, 1976, Source shape estimation and deconvolution of teleseismic body waves, **Geophys. J. Royal ast. Soc.**, **47**, 151-177.
- Flynn, E. C., and B. W. Stump, 1988, Effects of source depth on near-source seismograms, **J. Geophys. Res.**, **93**, 4820-4834.
- Grant, L. T., 1988, Experimental determination of seismic source characteristics for small chemical explosions, **Ms. thesis**, Southern Methodist Univ., Dallas, Texas, 247 pgs.
- Gupta, I. N. and R. A. Hartenberger, 1981, Seismic phases and scaling associated with small high-explosive surface shots, **Bull. Seism. Soc. Am.**, **71**, 1731-1741.
- Jackson, A. E., Jr., 1984, Preliminary material property estimates for ISST ground shock calculations, Report prepared for Ballistic Missile Office (ENSN).
- Jackson, A. E., Jr., 1984, Revised geologic profile and seismic velocity estimates for ISST ground shock calculations, Report prepared for Ballistic Missile Office (ENSN).

- Jones, G. H. S., G. T. Maureau, S. A. Cyganik, 1963, Air blast coupling to prograde and retrograde surface waves, **J. Geophys. Res.**, **68**, 4979-4987.
- Kanamori, H. and D. L. Anderson, 1975, Theoretical basis of some empirical relations in seismology, **Bull. Seism. Soc. Am.**, **65**, 1073-1095.
- Mueller, C. S., 1985, Source pulse enhancement by deconvolution of an empirical Green's function, **Geophys. Res. Letters**, **12**, 33-36.
- Mueller, R. A. and J. R. Murphy, 1971, Seismic characteristics of underground nuclear detonations, Part I., seismic spectrum scaling, **Bull. Seism. Soc. Am.**, **61**, 1675-1692.
- Murphy, J. R., 1981, Near-field Rayleigh waves from surface explosions, **Bull. Seism. Soc. Am.**, **71**, 223-248.
- Reinke, R. E., 1978, Surface wave propagation in the Tularosa and Jornada del Muerto basins, south central New Mexico, **Ph.D. dissertation**, Southern Methodist Univ., Dallas, Texas, 148 pp.
- Robinson, E. A., 1967, Predictive decomposition of time series with application to seismic exploration, **Geophysics**, **32**, 418-484.
- Rulev, B. G., 1965, The energy in a Rayleigh surface wave from explosions in different kinds of rock, **Izv., Earth Physics Series**, No. 4, 23-37.
- Savage, J. C., 1972, Relation of corner frequency to fault dimensions, **J. Geophys. Res.**, **77**, 3788-3795.
- Sereno, T. J., S. R. Bratt, T. C. Bache, 1987, Regional wave attenuation and seismic moment from the inversion of NORESS spectra, **AFGL-TR-87-0237**, Hanscom AFB, Ma., 105 pp, ADA187399.

Stevens, J. L., and S. M. Day, 1985, The physical basis of  $m_b:M_s$  and variable frequency magnitude methods for earthquake/explosions discrimination, **J. Geophys. Res.**, **90**, 3009-3020.

U.S. Congress, Office of Technology Assessment, 1988, Seismic verification of nuclear testing treaties, **OTA-ISC-361**, Washington, DC.



## ACKNOWLEDGEMENTS

The authors gratefully acknowledge Robert E. Reinke for the data acquisition on this project and to Jack Murphy for use of the seismic data from the Scarlet network.

# SEISMIC WAVE GENERATION BY MINE BLASTS

*Douglas A. Anderson  
Vibra-Tech Engineers, Inc  
Hazelton, PA 18201*

*Brian W. Stump  
Department of Geological Sciences  
Southern Methodist University  
Dallas, TX 75275*

## ABSTRACT

The principles of millisecond delay blasting are presented as they apply to problems of seismic wave generation. The utilization of both electric and non-electric blasting systems are discussed. Mining blasts are typically sources which are extended in time and space. The implications of this temporal and spatial source finiteness are explored with respect to near-source data where the observations are within 2-20 source dimensions. Both time and frequency domain realizations of these effects are given. Peak time domain amplitudes are generally controlled by the single source while the duration of ground motion is controlled by source duration at near ranges. Source finiteness is expressed in near source ground motions as an increase in seismogram amplitude with time for sources moving towards the receiver and as decaying amplitudes for the case where the sources move away from the receiver. These geometric effects lead to spectra which exhibit some constructive and destructive interference although it is difficult to identify regularly spaced peaks and troughs. Strong near-source transverse motions are observed from these extended sources. Frequency domain methods for reducing ground motion from mining blasts are discussed. Specific frequency bands of energy can be minimized with proper blast design. Scatter in design and actual detonator times in the explosive array lead to observed spectra which have reduced amplitude and irregularly spaced spectral scalloping. These effects are replicated with synthetic seismograms.

## INTRODUCTION

Recently there has been renewed seismological interest in mine blasts with respect to verification of a Reduced Threshold Test Ban Treaty (RTBT). The size of the largest mining blasts become comparable to the smallest nuclear explosions especially when decoupling scenarios are considered (Seismic Verification of Nuclear Testing Treaties, Office of Technology Assessment Report, 1988). Application of a RTBT would require the discrimination of these mining blasts from small nuclear explosions as well as from earthquakes. The basis for any discrimination effort is that mine blasts should give predictably different seismic signatures, since the source location is known *a priori*, and the source is comprised of ripple-fired cylindrical explosive charges.

Millisecond-delay blasting (as ripple-firing is known in the blasting industry) first came into general practice in the late 1940's and 1950's. This approach to blast design has the multiple benefits of improving rock breakage, minimizing excess throw of material (*flyrock*), and reducing ground vibration to neighboring structures. With all of these benefits, even unsophisticated operators now use millisecond blasting techniques (Chiappetta, 1987). The authors are not aware of *any* blasting operations in the US which do not use delayed blasting. It is also the common practice in Europe and S. America.

Pollack (1963) showed that delay time between individual explosions and the number of delays could influence the spectra observed from ripple-fired blasts. He summarized his results thus:

*Fourier theory shows a relationship to exist between the spectrum of a signal  $F(t)$  and the spectrum observed from a summation of  $F(t)$  repeated a given number of times with a fixed delay time between each repetition. This relationship has been observed on seismograms of a series of controlled ripple-fired quarry blasts. This analysis suggests that the delay time between shots was about 22.5 milliseconds instead of the nominal value of 17 milliseconds announced at the time of the experiment.*

In addition to the early work of Pollack, Frantti (1963) investigated the energy in the radiated wavefield from quarry explosions while Willis (1963) described spectral effects of ripple-fired explosions. A comprehensive study was done on the seismic effects of small chemical explosions by Kisslinger et al (1963). They investigated source functions and synthesis of motion by phase equalization; radiation patterns from ripple-fired shots; horizontally polarized shear waves; and the effect of source depth and shot point medium on the seismic signal. They found that linear superposition of time-delayed single-charge shots could accurately predict the waveforms at all azimuths.

Greenhalgh (1980) extended the work of Pollack and showed that near-regional seismograms (100-200 km) are more sensitive to long delays with a few intervals (such as those between rows) than to many short delays (between holes).

Stump and Reinke (1988) experimentally investigated superposition of small chemical explosions detonated in alluvium. They found that superposition of two simultaneously detonated charges held for charges spaced as close as to result in overlapping craters from the individual explosions. In order to make the superposition comparisons, deterministic wave propagation effects were first separated from stochastic effects. Within the plane perpendicular to the two charges direct superposition was validated. Accelerograms in the plane of the charges exhibited constructive and destructive interference and were modeled as resulting from the phase difference between the two charges.

Spectral scalloping results from the phase shifts introduced by the timing differences in the individual explosions. A number of recent studies have indicated that this effect can be observed at regional distances (Smith and Grose, 1988; Baumgardt and Ziegler, 1988; and Hedlin et al, 1989) although one can not uniquely separate propagation path effects such as multipathing from source effects unless direct measurements of the source such as those reported in this paper are made in conjunction with the regional observations. Other investigators show that spectral scalloping from mine blasts may not always be observed (Suteau-Henson and Bache, 1988). There are three major reasons for these discrepancies:

- \*The actual firing times of the individual explosions may deviate significantly from the nominal times as noted by Pollack.

- \*Blast designs may be quite complex, involving several different delay sequences. Each sequence then superimposes a different scallop pattern.

- \*The spatial dimensions of the source array introduce additional phase delays which increase the complexity of near-source spectra.

These three issues will be addressed as they apply to near-source observations in this paper as well as a review of common blasting practice, terminology, and deviations from ideal practice. The results of these effects will be demonstrated with both observational and synthetic ground motion data.

### **Principles of Millisecond Blasting**

Certain common procedures are used in millisecond-delay blasting. Although individual shots may vary from the basic pattern we will describe, in general most operations follow these procedures. The explosives used are

based upon an ammonium-nitrate/fuel-oil formulation (ANFO). Ammonium nitrate pellets (or *prills*) are combined with 6% fuel oil to produce a cheap, safe, efficient blasting agent. If there is water in the boreholes, the ANFO is used in the form of a water-gel or an emulsion. ANFO is not cap-sensitive, so a booster of about 1 or 2 pounds is used.

Shots are generally fired with an array of vertical boreholes although angled boreholes are common in Europe. The source array is often rectangular, or "curvi-rectangular", where one side follows the curvature of a vertical free-face. The holes along the free-face, or in the longest array if there is no free-face, constitute a row. There may be one row (common in Europe) or many rows. Several geometric patterns, as viewed from the bench top, are common: square, staggered, and echelon (Figure 1).

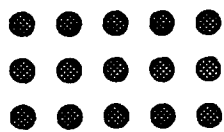
Each hole charged with explosives may have multiple explosive columns which are detonated with a delay between them. Crushed stone or drill cuttings (*stemmings*) are used to separate the explosive columns. Such holes are termed *decked* holes. There is sometimes confusion in terminology about the number of decks. Some operators call the number of explosive columns the decks; others call the number of stemming layers the decks. To avoid confusion, we will only refer to the number of charges per hole. With these source geometries there are three different delays possible in a shot reflecting the three dimensional aspect of the source:

1. Delay between charges in a hole
2. Delay between holes in a row
3. Delay between rows

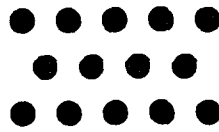
Currently there are two detonation systems used: electric and non-electric. The significant differences for the purposes of this discussion are the flexibility of the firing times and the pre-selected delay times.

The electric detonation systems employ two basic elements: Electric initiators (*blasting caps*) and a blasting machine. The electric initiators have built-in pyrotechnic delays, most of which are multiples of 25 ms. Each type of initiator produced by a manufacturer has several delay periods. For example, period 1 may be 25 ms, 2 would be 50 ms, 3 would be 75 ms, etc. These initiators are wired in series, and fired by the blasting machine which typically fires them with a voltage of about 400 V DC. Commonly each row of a shot is fired on one circuit, and delays between rows are accomplished through delays in the blasting machine. These delays may be restricted to certain pre-set values (commonly 8, 17, 34, 59, 68, 100, 125) or may be varied in 1 ms increments from 5 to 999 ms. A typical diagram for an electrically initiated shot is shown in Figure 2.

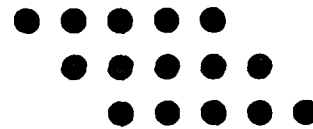
## BLAST GEOMETRY



SQUARE

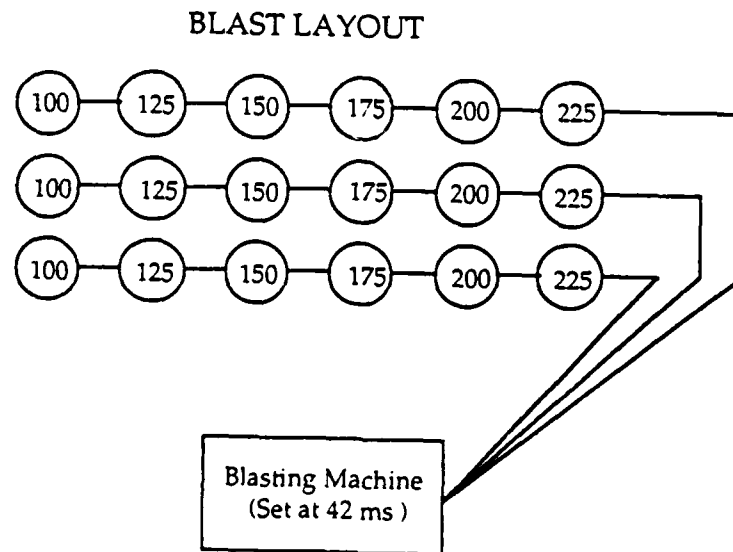


STAGGERED



ESCHELON

FIGURE 1: Three typical blast arrays as viewed from the bench top.



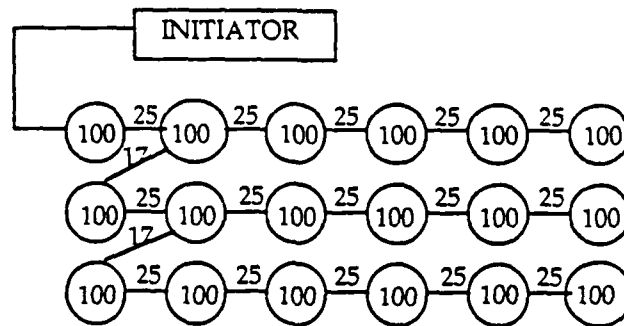
ACTUAL FIRING TIMES

100	125	150	175	200	225
142	167	192	217	242	267
184	209	234	259	284	309

FIGURE 2: Typical blast design utilizing electric initiators and a blasting machine. The blasting machine supplies the between row delays while the electric initiators provide the delay between explosions in a row.



### BLAST LAYOUT



### ACTUAL FIRING TIMES

100	125	150	175	200	225
142	167	192	217	242	267
184	209	234	259	284	309

FIGURE 3: A blast design with a non-electric initiation system utilizing downhole blasting caps.

Because blasting cap connections are on the surface, which eventually moves as the rock is fragmented, the first cap to fire generally has a period of 100 ms or greater, depending on the delays between circuits. In the figure, all holes would be initiated before the first cap fires since the maximum between-row delay (84 ms) is less than the 100 ms period.

Non-electric systems communicate the firing impulse through a tube which is either filled with an explosive gas mixture or lined with a small amount of explosive. The delays are accomplished through the propagation time of the detonation of the explosive in the tube. The detonation sequence is started by a conventional blasting cap fired by a blasting machine. The surface delays are accompanied by downhole delays to protect against connections being severed by rock movement. The blasting caps are therefore triggered and sleep for typically a couple of hundred milliseconds before they fire. This process allows initiators to be activated well before the rock begins to move around them. Typical firing times in non-electric systems are 8, 17, 25, 34, and 42 ms. Multiples may be linked together, and hybrid systems may be constructed. A typical diagram for a non-electrically initiated shot is given in Figure 3.

Recently electronic detonators have become available (Hinzen et al, 1987). These initiators offer improved accuracy and flexibility in blast design at nearly an order of magnitude increase in cost. The accuracy of the blasting caps and their effect on the wavefield will be discussed later.

Decked columns may use different period initiators for the charges, separate circuits, or different lengths of non-electric tubing. Complex detonation sequences may result although three rules are usually observed:

1. The amount of explosive *per charge* is kept constant in a shot.
2. The number of charges per hole and number of holes per row are kept constant.
3. The delay between charges in each column and the delay between holes and delay between holes and rows is kept a constant.

Figure 4 is one of a set of quarry explosions from which ground motion records were recovered for this study. In this case there is only one charge per column (338 lbs) with the delay between charges in a row of 25 ms and a delay between rows of 42 ms.

## SEISMIC SOURCE REPRESENTATION

Based upon the practices of the mining industry there are six important numbers used in characterizing the source function:

# SHOT 3

ms delay time		1-9'-1
(84) (109) (134) (159) (184) (209) (234) (259) (284) (309) (334) (359) (384) (409) (434) (459) (484) (509) (534) (559) (584) (609) (634) (659) (684)		
(42) (67) (92) (117) (142) (167) (192) (217) (242) (267) (292) (317) (342) (367) (392) (417) (442) (467) (492) (517) (542) (567) (617) (642)		
(0) (25) (50) (75) (100) (125) (150) (175) (200) (225) (250) (275) (300) (325) (350) (375) (400) (425) (450) (475) (500) (525) (550) (575)		

TOTAL LBS: 24350

MAX HOLES/DELAY: 2

MAX LBS/DELAY: 696

HOLE DEPTH: 58'-60'

STEMMING: 4'-8.5'

QUARRY  
FACE

FIGURE 4: A non-electric blast design from an actual detonation, Shot 3. Each hole contains 338 lbs of explosive with the between hole delay of 25 ms and the between row delay of 42 ms.

# ACCELEROMETERS

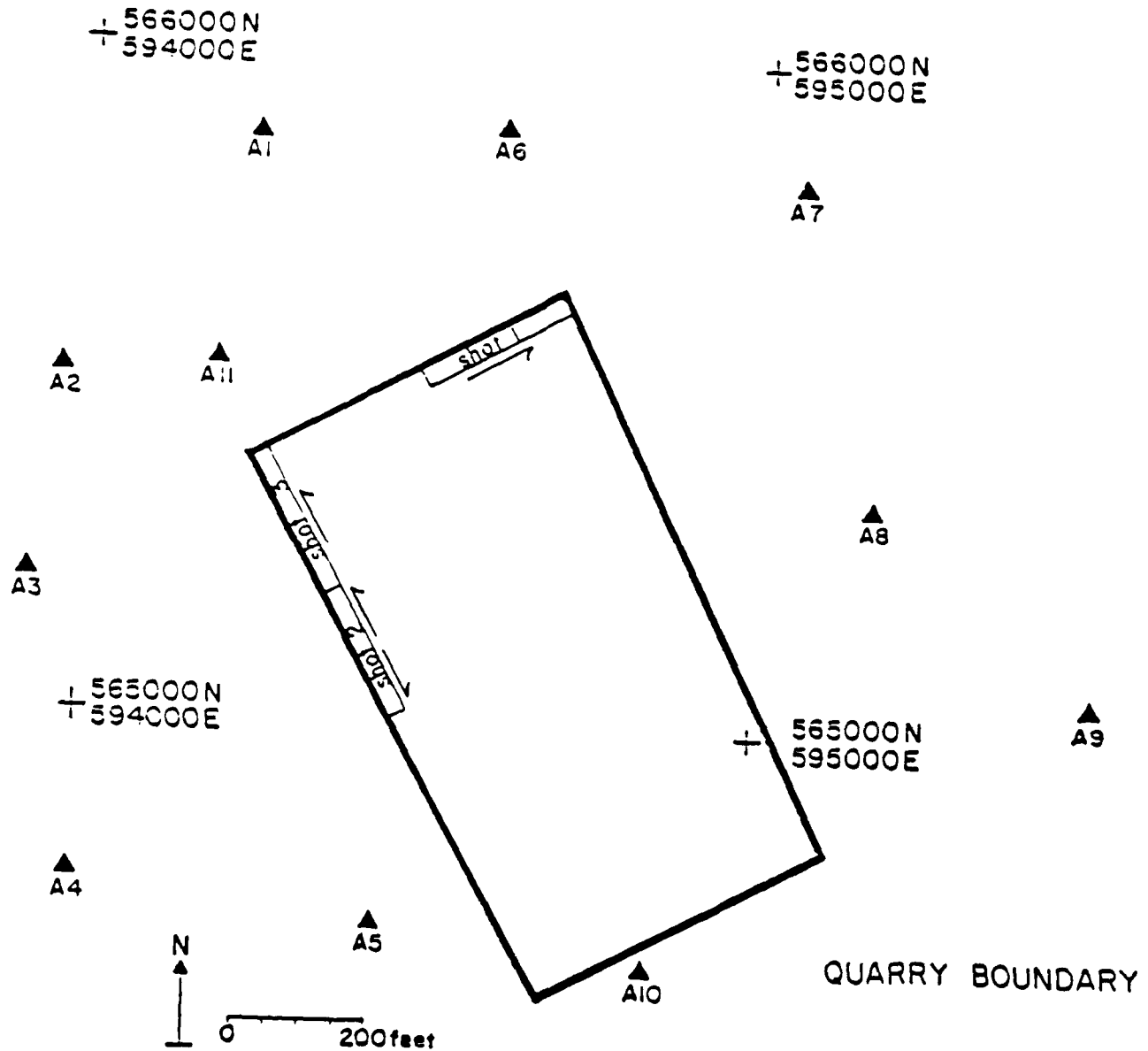


FIGURE 5: Instrumentation array for the quarry shots described in Figures 4 and 6. Each solid triangle represents a three component accelerometer that was digitally recorded.

1. Number of charges per hole ( $n_c$ ): 1 in Fig 4.
2. Delay between charges in a hole ( $d_c$ ): 0 in Fig 4.
3. Number of holes in a row ( $n_h$ ): 24 in Fig 4.
4. Delay time between holes in a row ( $d_h$ ): 25 ms in Fig 4.
5. Number of rows ( $n_r$ ): 3 in Fig 4.
6. Delay time between rows ( $d_r$ ): 42 ms in Fig 4.

With this information a set of synthetic seismograms can be created either through some numerical technique which accounts for the possible nonlinear interaction of the individual explosions or by superposition of results from single explosions. Superposition has been shown to practically characterize observed seismograms over a fairly broad frequency band (Anderson et al, 1985; Hinzen et al, 1987; Stump and Reinke, 1988).

When linear superposition is appropriate, the following representation is utilized in modeling the observed waveforms from these mining blasts:

$$U(x,t) = \sum_{r=1}^{n_r} \sum_{h=1}^{n_h} G(x,t;x'_{rh},t_{rh}) \otimes S(x'_{rh},t_{rh}) \quad (1)$$

Where  $U(x,t)$  are the observed or computed ground motion,  $G$  are the Green's functions or propagation path effects for the media, and  $S$  is the source time history. Since each of the sources has a different location in time ( $t_{rh}$ ) and space ( $x_{rh}$ ), in general a different Green's function must be computed for the spatial location of each explosion. In this manner the phase shifts associated with the different source to receiver propagation path effects can be taken into account. For source to receiver distances long compared to the dimension of the source array and wavelengths long compared to this dimension the variation in  $G$  for the different source locations,  $x_{rh}$  will be negligible.

$$U(x,t) = G(x,t;x',0) \otimes \sum_{r=1}^{n_r} \sum_{h=1}^{n_h} S(x',t_{rh}) \quad (2)$$

Quantification of the spatial and temporal effects of the source amounts to characterizing the importance of  $t_{rh}$  and  $x_{rh}$  in the ground motion,  $U$ . This comparison can be done synthetically where analytical solutions for  $G$  are made. Alternatively one can take an experimental approach to the solution where single burst waveforms are captured experimentally and used to model the complete array of explosions. Given the single and multiple burst waveforms, one can explore deconvolution as a method of determining relative importance and timing of individual charges. This approach works best in the region where the Green's functions change little with the variation in source locations (equation 2).

## TEMPORAL SOURCE EFFECTS

As equation 1 illustrates, the observed wavefield from quarry blasts will be dependent upon the propagation path effects or Green's function,  $G(x,t; x_{rh}, t_{rh})$ , the source time effects,  $t_{rh}$ , and the source spatial finiteness,  $x_{rh}$ . We first investigate the importance of the temporal finiteness of the source as illustrated in Figures 2, 3, and 4.

The temporal finiteness of quarry explosions leads to near source wavefields whose length is controlled by the duration of blasting. A number of near source observations were made of a set of three quarry explosions in Massachusetts (Figure 5).

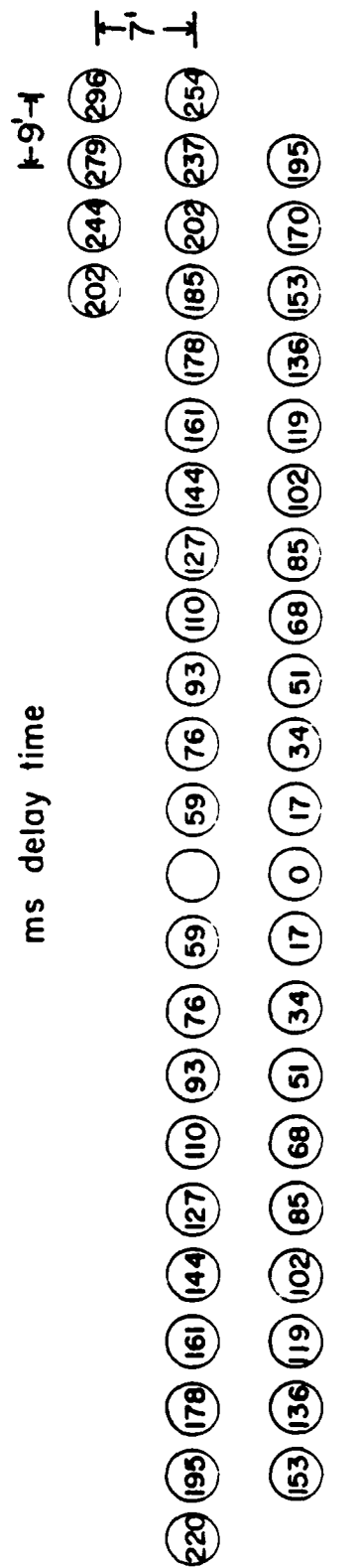
Three component force-balance accelerometers were used to digitally recover data from the locations indicated in the figure. The data were sampled at 200 samples per second. This array was designed to characterize the azimuthal variations in the wavefield as well as recover data from a variety of explosive arrays. We will discuss results from analysis of two of these explosions. The nominal firing times for Shot 3 are given in Figure 4. In this case there are some 72 shots with a time duration of 684 ms and a total charge weight of 24,350 lbs. The echelon array begins in the lower left corner and propagates to the upper right in 684 ms.

Shot 2 is described in Figure 6. This source involves 47 individual explosions, a total source duration of 296 ms, and a total charge weight of 15670 lbs. The individual explosions begin in the center of the array and propagate bilaterally. The ratio of source durations between Shot 3 and Shot 2 is 2.3. One set of representative vertical waveforms from these two shots is given in Figure 7. These accelerograms are from Station 5 which is slightly closer to Shot 2. The ratio of the time durations of the two observations is 2.2.

Comparison of the source array and the observed seismograms reveals that these near source waveforms are reflective of the source time history. This conclusion can be further supported through a set of synthetic seismograms. Simple elastic half-space Green's functions (Johnson, 1974) were developed based upon refraction surveys from the experimental site. Near surface velocities of 5-6 km/s were determined below a 2-4 m weathered layer. A simple isotropic single source function was then superposed based upon the spatial and temporal locations of the source array (Figures 4 and 5). The synthetics for Station 5 are given in Figure 8.

Comparing Figures 7 and 8 indicate that qualitatively these models have replicated several of the characteristics of the observations. The ringing nature of the seismograms resulting from the multiple energy depositions is modeled. General characteristics such as the inability to identify individual

# SHOT 2



TOTAL LBS: 15670

MAX HOLES/DELAY: 2

MAX LBS/DELAY: 664.68

HOLE DEPTH: 58'-60'

STEMMING: 4'-8.5'

FIGURE 6: Shot 2 blast design. The sources begin in the center of the array and then move bilaterally.

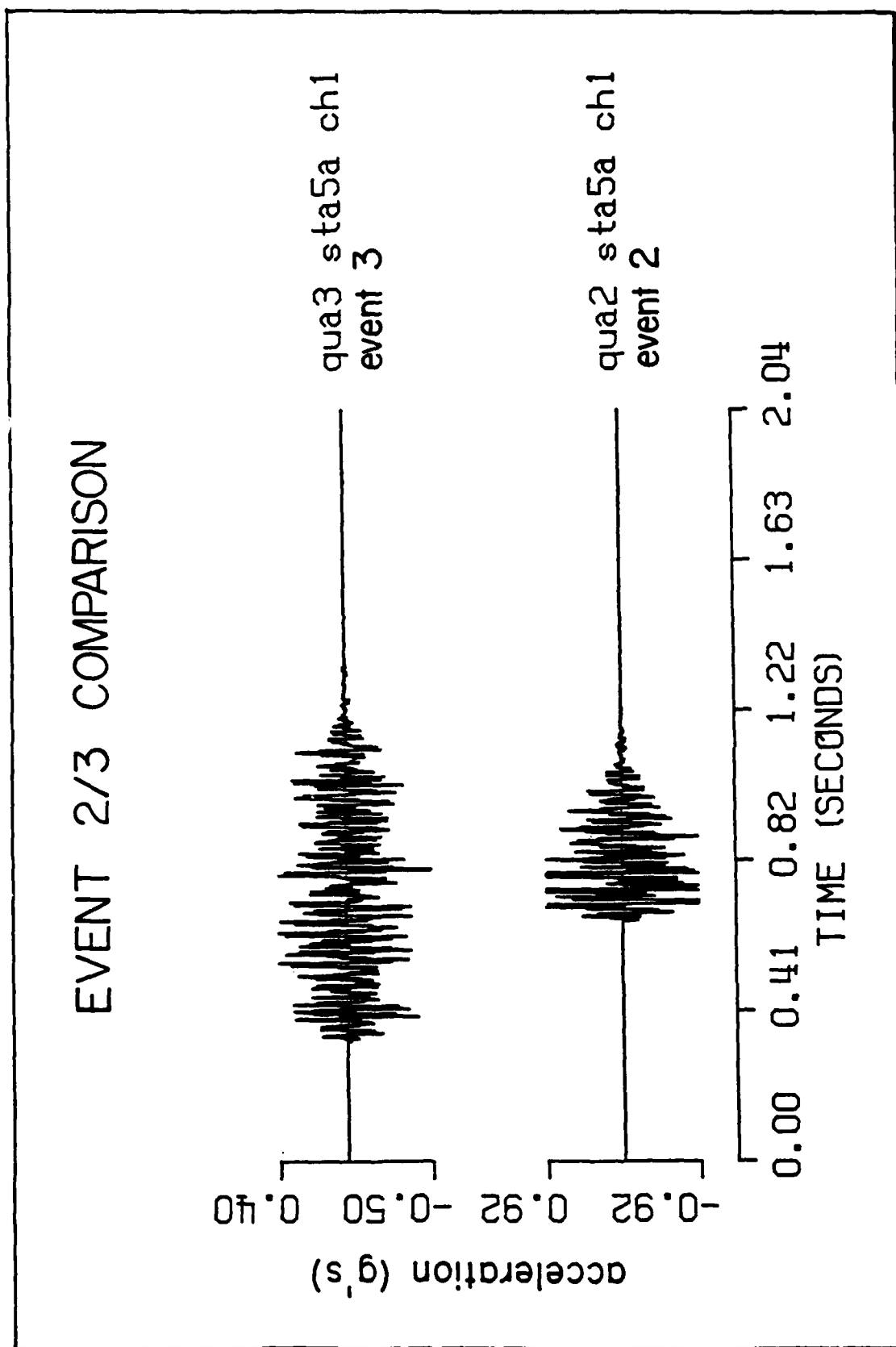


FIGURE 7: Vertical accelerations from Shot 3 (Figure 4) and Shot 2 (Figure 5) at Station 5 (Figure 5).



## EVENT 2/3 SYNTHETIC COMPARISON

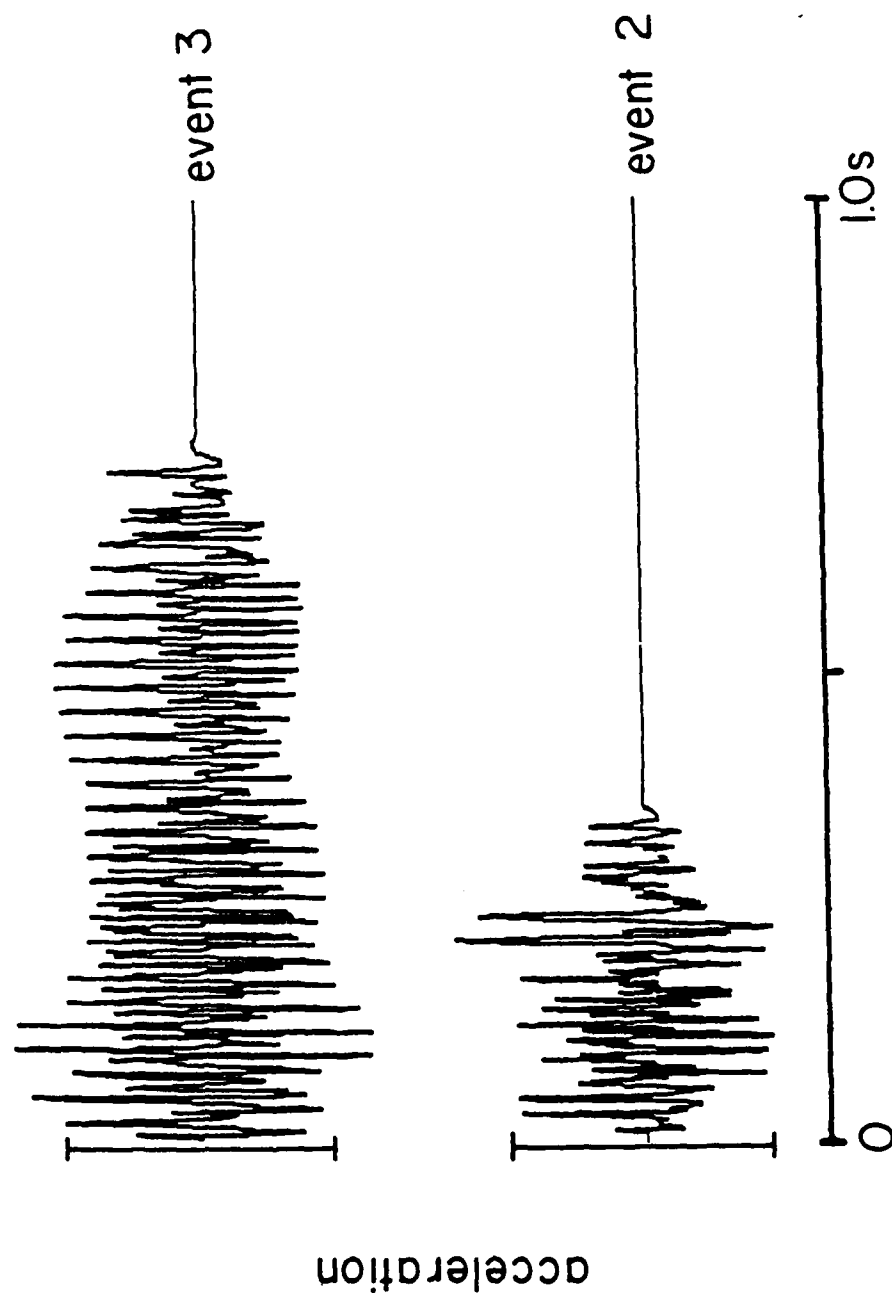


FIGURE 8: Synthetic vertical accelerations for Station 5, Shots 2 & 3. The synthetics are for simple half-space Green's functions, nominal shot times, and Mueller-Murphy single explosion time function.

phases within the seismogram are also modeled. In the case of the synthetics the peak time domain amplitudes are controlled by the peak amplitude of the single explosion synthetic. The propagation path effects are quite simple resulting in seismogram duration dominated by source duration. The ratio of the synthetic accelerogram duration for the two sources is 2.1 matching the observations (2.2) and the ratio of source durations (2.3). These near source observations and synthetics reflect the source temporal character.

### SPATIAL SOURCE EFFECTS

In the near source region the spatial locations of the individual explosions may be important in modeling the observations. Different Green's functions must be utilized for each of the sources in an explosive array such as that in Figure 4. Such spatial effects can lead to significant azimuthal variation in the radiated wavefield. Smith (1988) and Hedlin et al (1989) have tried to constrain these effects with regional data. In both of these exercises there is a lack of experimental control of the source. We shall investigate these effects in the near source data where additional source constraints are available and attempt to model them.

Waveforms from Shot 3 (Figure 4) are used in this part of the study. Representing the azimuthal effects of the source, accelerograms from Station 2 and 5 are reproduced in Figure 9. Station 2 is at the far end of the source array so that the individual explosions of Shot 3 begin far from the station with the latter explosions moving closer to the receiver. This geometrical effect is shown in the accelerogram with small initial amplitudes that increase to a peak amplitude late in the waveform. The accelerogram recorded at Station 5 is the same duration as that for Station 2 but it exhibits quite a different time domain character. In this case the largest amplitudes are early in the record with a general decay in amplitude with time. The individual explosions move farther from the receiver as time progresses.

These effects were replicated synthetically. Each explosion utilized a separate Green's function to account for the change in propagation path effects. In Figure 10 the synthetics for Stations 5 and 2 have the same duration, controlled by the source temporal character. The synthetic for Station 5 (away) peaks early in the waveform and slowly decays to zero. The synthetic for Station 2 builds from early time to a peak very near the end of the waveform. Both the synthetic duration and its general character match the observations from this experiment and show the effects of source finiteness. The finer structure in the observations such as specific peaks and nulls are not modeled and may reflect the fact that actual shot times of the individual explosions vary from the design times and that coupling may vary between individual explosions.

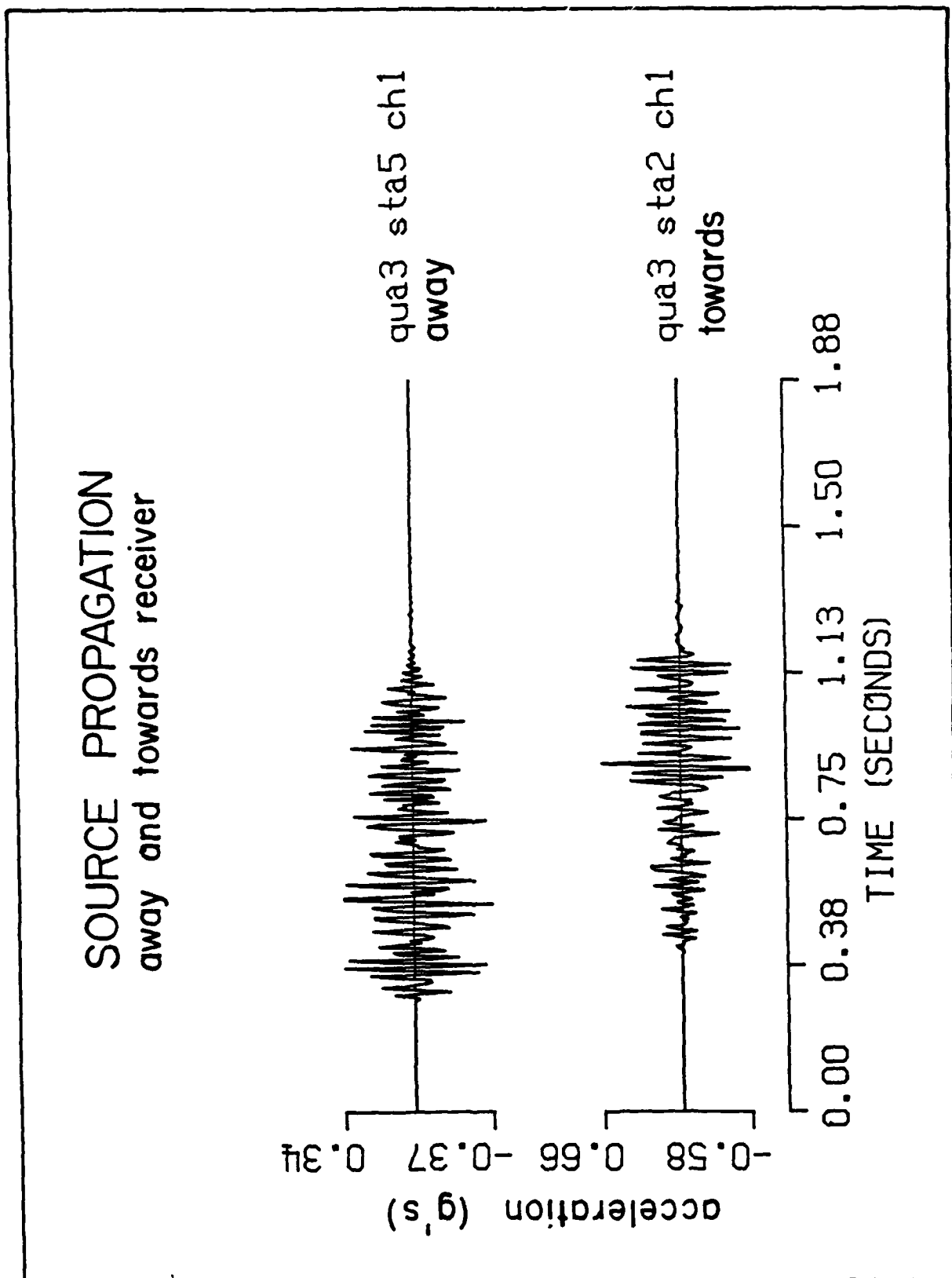


FIGURE 9: Vertical accelerations from Shot 3 observed at Stations 5 & 2. The sources are moving away from Station 5 with time while they are moving towards Station 2.

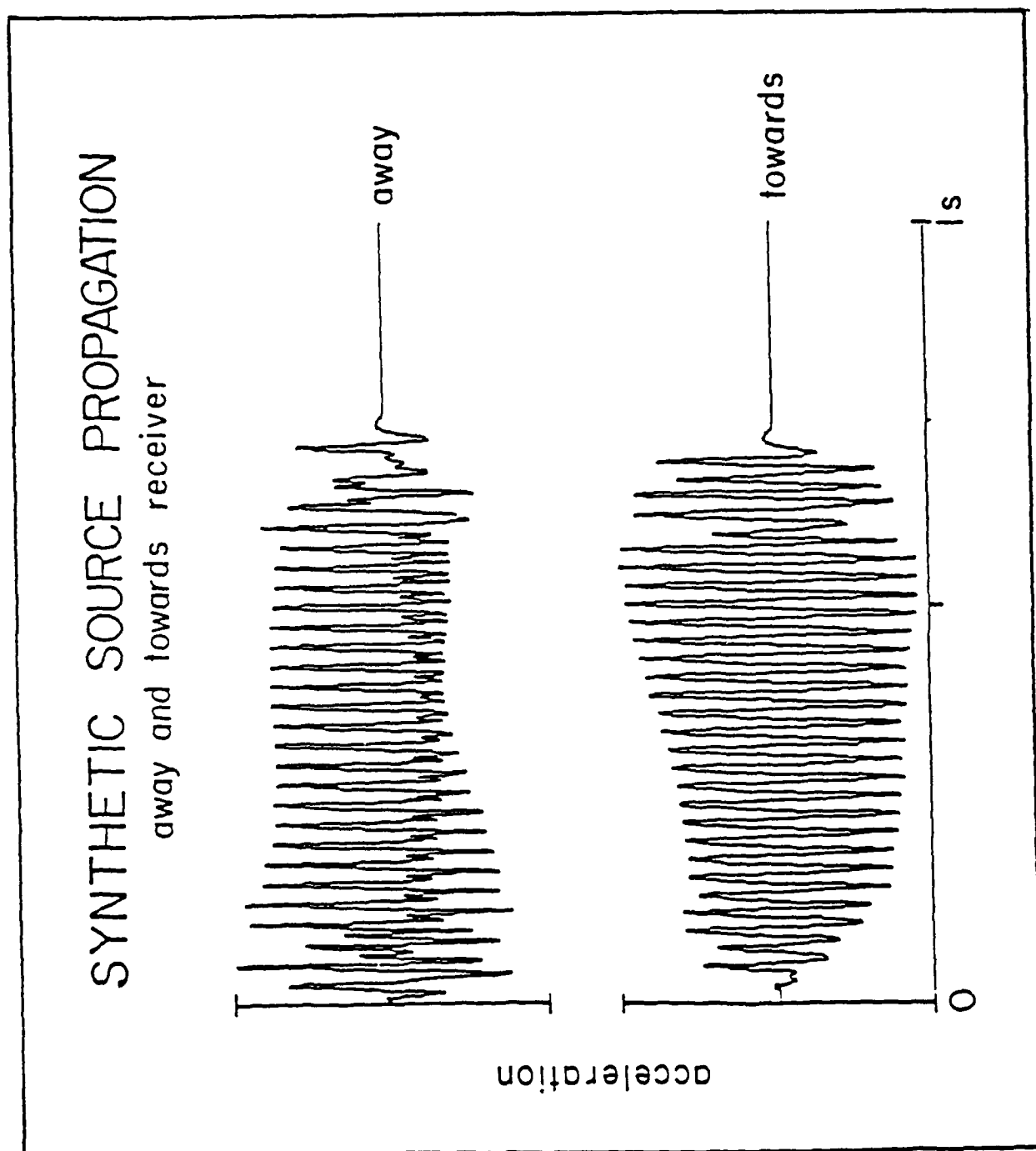


FIGURE 10: Synthetic seismograms similar to those in Figure 8 but for Stations 5 (away) and 2 (toward) of Shot 3 (Figure 9).

Spectral comparisons can be made between the observational data from Shot 3 and the synthetics. One such comparison is given in Figure 11 for Station 5a which was sampled at 600 samples/sec. In this example acceleration spectra are given for both the vertical observations and synthetics. The single shot synthetic includes a Mueller-Murphy (1971) isotropic source time history convolved with an elastic half-space Green's function. The source corner frequency for the chemical explosion in granite is near 40 Hz. The single burst synthetic is very smooth with the 70 Hz spectral scalloping a result of the delay time between the P and Rayleigh arrivals. When the finite source synthetic is created by superposing a set of such single source accelerograms this corner frequency moves very little. The spectrum exhibits great variability with frequency. Constructive and destructive interference patterns are clearly observed although due to the spatial effects of the source array much of the regularly spaced interference is masked. A relative comparison with the observed spectra indicates that source multiplicity has done a good job of replicating the general scatter observed in the spectra from Shot 3. The peaks observed in the spectra near 50 and 160 Hz are modeled in the synthetics. The source corner frequency in the observation matches the model. Above 200 Hz, the comparison between the synthetic and the observation degrades.

## INITIATOR ACCURACY

The superposition method is dependent upon accurate firing times of pyrotechnic delay initiators. Winzer (1978) showed that commercially available initiators had substantial scatter, and that it was detrimental to blasting performance. For economic reasons, a certain amount of scatter in this type of initiator must be accepted. The actual delay time is affected by the packing and shape of powder particles, and the size and geometry of the pellet in the delay train. Firing times have been found to have a Gaussian distribution about the mean firing time, which may be different from the nominal. Typical blasting caps used in the U S have a standard deviation of the mean firing time of 5 ms (Anderson and Reil).

In order to test the effect of cap time variance on radiated wavefield equation 1 can be used to create a set of synthetics where the actual shot times are replaced with those drawn from a Gaussian distribution with a specified variance.

Following the approach of Reil et al (1985) the mean firing times were assumed to be the nominal delay times for the source. A single row of eight sources each delayed by 25 ms was simulated. The resulting spectrum is

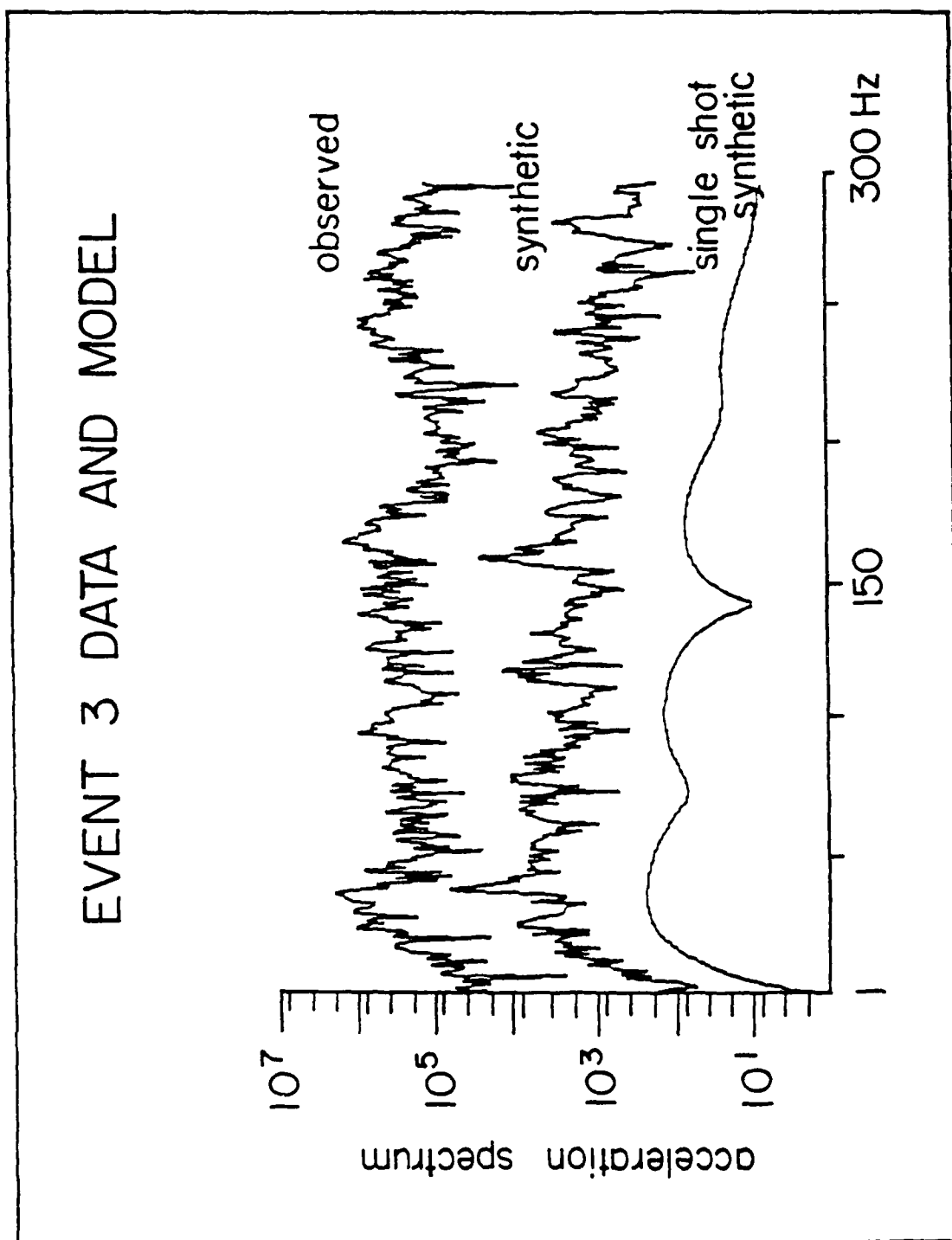


FIGURE 11: Single explosion synthetic, Shot 3 synthetic, and Shot 3 - Station 5 observed vertical acceleration spectra. The spectra have been offset so spectral shape comparisons could be made.

given in Figure 12a. The primary interference peak at 40 Hz resulting from the source delays with the secondary peaks at 7.5, 12.5, 17.5, 22.5, 27.5, 32.5 and 47.5 are easily observed.

A second set of synthetics were developed with the shot times chosen from a Gaussian distribution with a standard deviation of 5 ms. The resulting source times were 23, 55, 79, 92, 127, 142, 179, and 202 ms. The spectrum from this more realistic 'detonation' is given in Figure 12b. The peak in the spectrum at 40 Hz is 40% of the value without scatter in shot times. Secondary peaks near 17, 27, and 33 Hz are enhanced to levels comparable to that at 40 Hz. The scatter in shot times has greatly reduced the primary peak while spreading the energy to surrounding frequencies. The more realistic spectrum exhibits spectral scalloping but not at evenly spaced frequencies. Small variations in individual shot times lead to complex high frequency spectra from the explosions.

As indicated in the shot designs of Figures 2 and 3, the usual practice in charge design is to introduce both a between hole and between row delay. In the case of the observational data described in Figure 4 the between hole delay was 25 ms and the between row delay was 42 ms. A set of synthetic spectra were developed for eight holes in a row and three rows with this same delay pattern. Nominal shot times were used in developing the synthetics and spectrum given in Figure 13. A complex spectral scalloping pattern is found with the peak at 40 Hz from the 25 ms and at 23.8 Hz from the 42 ms delay missing.

These simple examples illustrate the types of complexity that can be introduced in observed spectra from quarry explosions. The details of the spectra are highly dependent on the practices at a particular mining operation as well as the quality of blasting.

### EFFORTS TO CONTROL VIBRATION USING DELAYS

One of the uses for ripple-firing is to reduce the effect of annoying and potentially damaging ground motion from blasting on neighboring structures. As the time domain synthetics in Figure 8 and data in Figure 7 indicate, the peak amplitude in a properly designed array is controlled by the single burst waveform. By spreading the shots in time a larger volume of rock may be excavated while keeping ground motion to a minimum. This approach leads to constructive and destructive interference phenomena in the frequency domain as illustrated in Figure 11.

Many mines and quarries are in close proximity to communities. This is partially due to the growth of the communities and partially to the need to reduce transportation costs of the quarry products from the mine. As a result,

### 25 ms BETWEEN 8 HOLES - 1 ROW

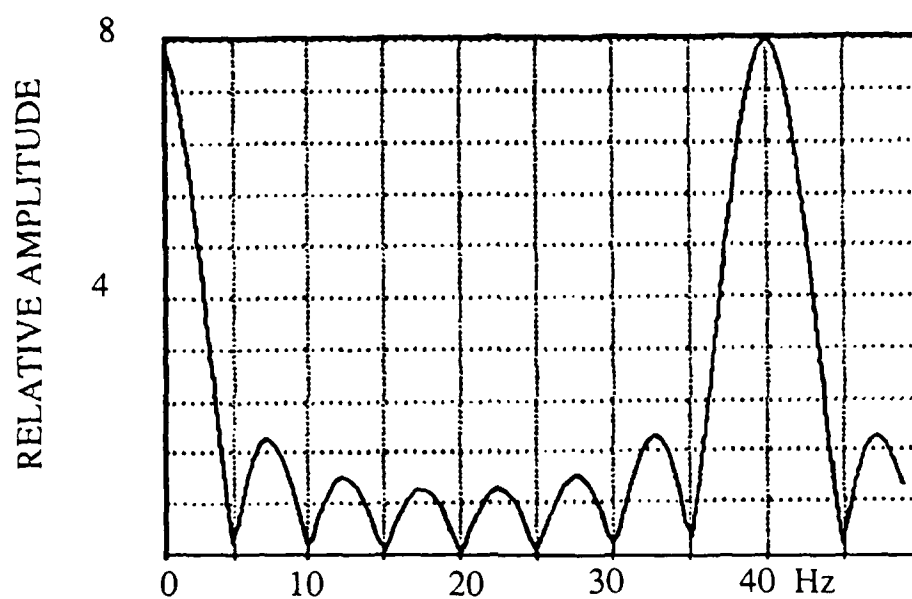


FIGURE 12a: Synthetic spectrum for eight explosions in a row each delayed by 25 ms from the previous explosion.



**25 ms BETWEEN 8 HOLES - 1 ROW**  
**SCATTER IN TIMES:**  
**23, 55, 79, 92, 127, 142, 179, 202**

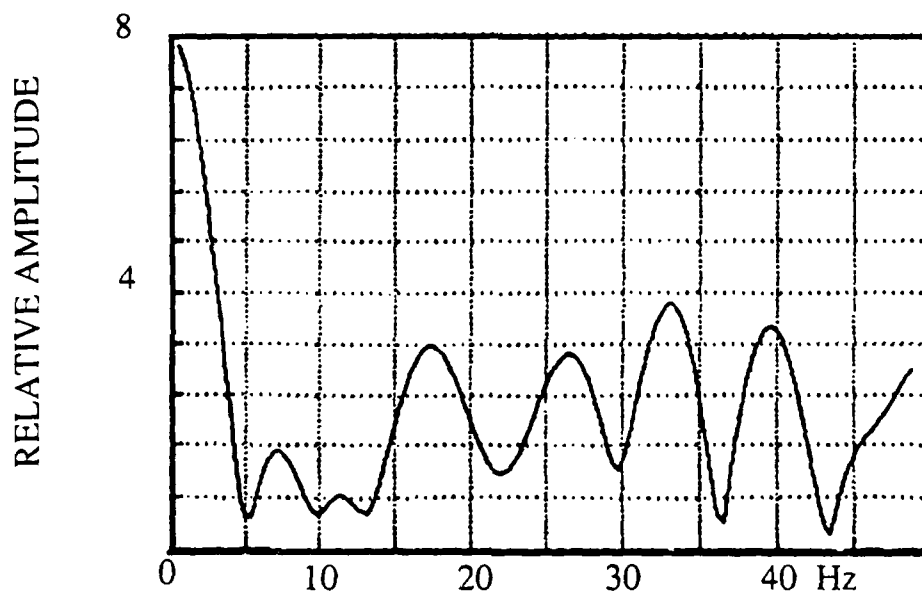


FIGURE 12b: Same as Figure 12a but with a standard deviation of 5 ms introduced into the shot times.

**25 ms BETWEEN 8 HOLES**

**42 ms BETWEEN 3 ROWS**

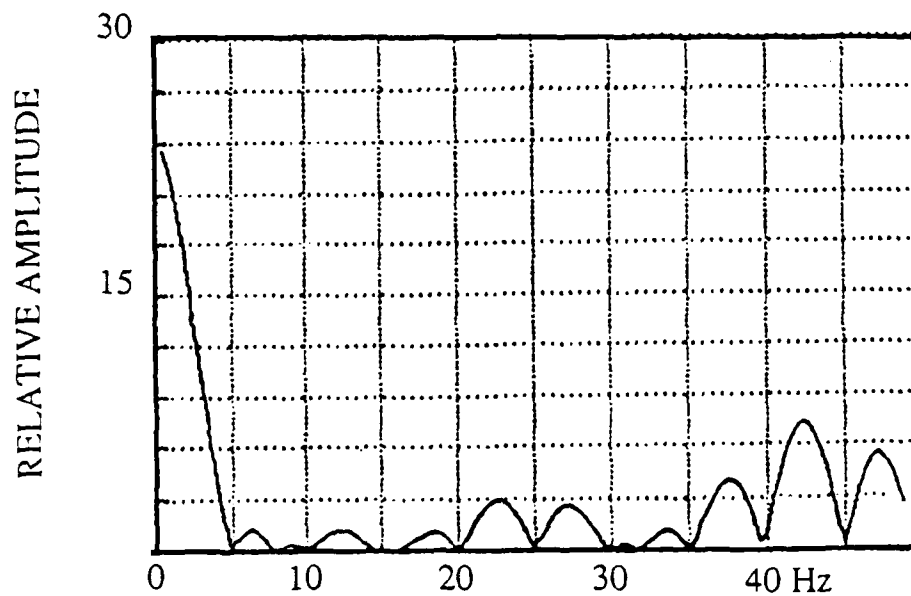


FIGURE 13: Synthetic spectrum for three rows of eight explosions. Like the production blast in Figure 4, the between hole delay is 25 ms and the between row delay is 42 ms.

there is often conflict due to the environmental effects of the mines upon the communities. Typical residential structures (one and two story) resonate in the frequency range from 3 to 18 Hz (Medearis, 1977). In addition, overburden geology often generates vibration with frequencies in this range, so the waves from blasting are amplified both by geology and the structure. These effects lead to motions which, while rarely damaging, give an impression to a resident that the house is being shaken so much that it is being damaged.

There have been many attempts over the years to find a successful means of minimizing ground vibration from blasting while keeping the process economically viable. Thoenen and Windes (1942) showed that, in principle, delay times could be chosen to cancel vibration waves from a test production shot. Fish (1951) demonstrated similar results. Thoene and Windes though concluded that delay shooting was not practical because of problems in identifying geological amplification effects and accurately constraining blasting cap times.

The conventional approach to controlling ground vibration from blasting was based upon research conducted by the Bureau of Mines in the 1960's. Duvall et al (1963) investigated the effect of delay time on ground vibration. They showed that, for single-row shots at the location they tested, a shot with a delay of 9 ms between holes generated substantially lower peak velocities than one detonated instantaneously. They also tested shots with 17 and 34 ms delays which generated lower vibration than the shot with 9 ms delays, but the difference was not as striking as that between instantaneous detonation and the 9 ms delay.

Since early damage criteria were based on peak velocity (independent of frequency) and these early tests indicated substantial reduction in velocities with a 9 ms delay, ground vibration criteria were based upon the amount of explosives detonated within an 8 ms period. The amount of explosive detonated within an 8 ms period is called the *charge per delay*. If multiple holes are detonated within an 8 ms window, the vibration is characterized as if the charges were detonated simultaneously. If individual holes are separated by more than 8 ms, then the vibration from each charge is assumed totally independent with no superposition.

Andrews (1981) showed that at sites where a single frequency of vibration dominated, that shot delay times could be chosen at half the vibration period and the vibration was reduced. Extension of the method to multiple frequencies was difficult. Anderson et al (1983) introduced a semi-empirical technique for vibration reduction where a single charge blast was recorded and designated as the *signature*. This signature was then time-lagged and superposed to replicate the complete mining blast. This approach is similar to an empirical Green's function solution utilizing equation 2 which assumes

that propagation path differences for the sources is negligible. The experimental Green's function is:

$$U_s(x,t) = G(x,t; x_s,0) \otimes S(x_s,t_s) \quad (3)$$

The superposed seismogram which replicates the temporal finiteness of the source becomes:

$$U_T(x,t) = U_s(x,t) \otimes \sum_{r=1}^{n_r} \sum_{h=1}^{n_h} \sum_{c=1}^{n_c} \delta(t-t_{rhc}) \quad (4)$$

In this case the final waveform,  $U_T$ , is dependent upon the number of charges per column,  $n_c$ , the number of holes per row,  $n_h$ , and the number of rows,  $n_r$ , in the charge array. This approach also assumes that the time function and coupling efficiency of each charge is equal. If coupling varies between charges as suggested by Hinzen (1988) then the equation becomes:

$$U_T(x,t) = U_s(x,t) \otimes \sum_{r=1}^{n_r} \sum_{h=1}^{n_h} \sum_{c=1}^{n_c} W_{rhc} \delta(t-t_{rhc}) \quad (5)$$

Testing and validation of this procedure utilizing equation 4 was reported by Anderson et al (1985) and Reil et al (1985). A seismogram from a planned shot with a given number of rows, holes, and charges can be generated. In order to explore the delay times that best reduce ground motion a search of possible delay times from 0 to 200 ms at 4 ms increments is made. Spectral plots of this suite of seismograms are displayed in frequency-delay space in order to identify the optimum shot design. One of these "vibra-maps" is given in Figure 14. The darker the pattern the higher the amplitude in a particular frequency band. Shot design is completed by choosing a delay that minimizes energy in the 3-18 Hz band. Delays between 48 and 64 ms are the best for the example. The method provides a quantitative method for minimizing ground motions within a predetermined frequency band. Crenwelge and Peterson (1986) and Hinzen (1987) have reported success with this procedure.

## CONCLUSIONS

The principles of millisecond delay blasting as utilized by the blasting community have been presented. The three dimensional nature of these explosive sources is reflected by the general representation of the sources in terms of the number of charges per hole ( $n_c$ ), the number of holes per row ( $n_r$ ), and the number of rows in the explosive array ( $n_h$ ). Three common rules normally followed in practice were demonstrated with actual source arrays from a set of experiments in a granite quarry in Massachusetts; (1) The

## VIBRA-MAP

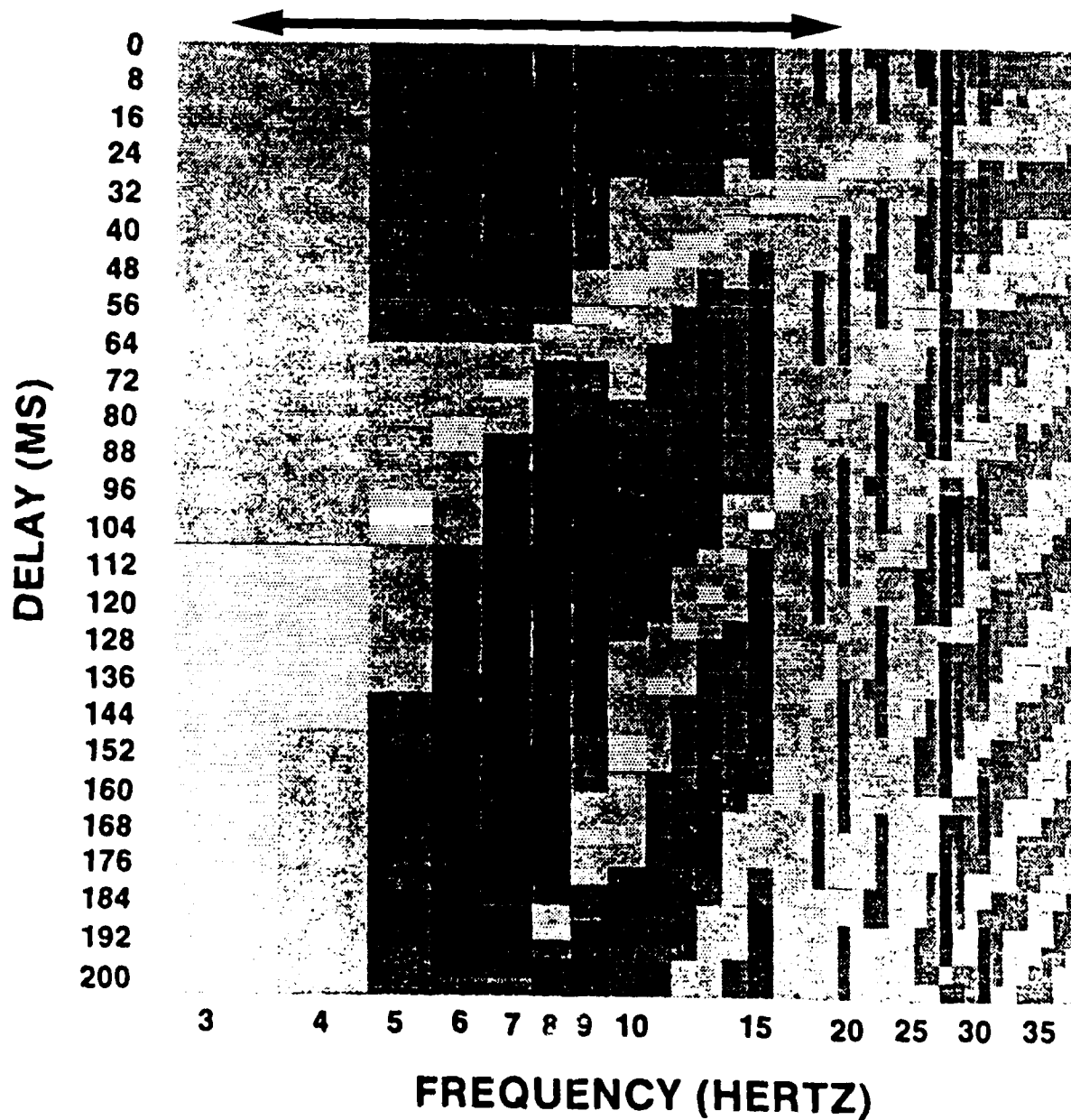


FIGURE 14: A single explosion experimental waveform is superposed to simulate a row of explosions with delays between 0 and 200 ms. The resulting spectra are plotted with the darker patterns representative of increased energy in a particular frequency band. The frequency band of 3-18 Hz is marked with an arrow.

amount of explosive per charge is kept constant in a shot; (2) The number of charges per hole and number of holes per row are kept constant; and (3) The delay between charges in each column and the delay between holes and delay between holes and rows is kept constant. Both electric and nonelectric detonating systems are used leading to a wide range of possible source configurations. Three dimensional source arrays can lead to complex and variable interference effects in the frequency domain. Scatter in the most commonly used blasting caps can be as much as 5 ms or more. This scatter leads to significant time and frequency domain effects in the 10-50 Hz band. Variation in these shot times can destroy some frequency domain interference effects that might be expected from design shot times and create others. High precision caps are currently available although their costs currently precludes them from practical use. Spatial and temporal source effects are demonstrated with observational and synthetic data. Near source accelerogram duration in a granite quarry is shown to be controlled by the multiple source duration while the peak amplitude is controlled by the coupling of a single source. Spatial source effects are observed and modeled as increasing or decreasing amplitudes in the seismogram with time depending on whether the sources are moving towards or away from the receiver. In the frequency domain these spatial effects result in observed and modeled spectra which do not include well developed peaks and troughs but complicated variation which could be characterized as high variance when compared to the single burst results. For some observations simple time domain superposition based upon a single burst experimental Green's function is successful in identifying detonation patterns that minimize ground motion in prescribed frequency bands. Mining explosions are utilized for many different tasks from rock fragmentation for construction purposes to mineral recovery. Each task has its own special problems and thus unique spatial and temporal character. These different applications can lead to great variability in observed motions in the near source regime and possibly in the regional regime.

## REFERENCES

- Anderson, D. A., A. P. Ritter, S. R. Winzer, and J. W. Reil (1985). A method for site-specific prediction and control of ground vibration from blasting, **Proceedings of the First Mini-Symposium on Explosives and Blasting Research**, San Diego, CA, 28-43.
- Anderson, D. A., S. R. Winzer, and A. P. Ritter (1983). Synthetic delay versus frequency plots for predicting ground vibration from blasting, **Proceedings of the Third International Symposium on Computer Aided Seismic Analysis and Discrimination**, Washington, DC, 70-74.
- Andrews, A. B. (1981). Design criteria for sequential blasting, **Proceedings of the Seventh Conference on Explosives and Blasting Techniques**, Phoenix, AZ, 173-192.
- Bajpayee, T. S., R. J. Mainiero, and J. E. Hay (1985). Overlap probability for short-period delay detonators used in underground coal mining, U. S. Bureau of Mines RI 8888, 21 pp.
- Baumgardt, D. R. and K. A. Ziegler, 1988. Spectral evidence for source multiplicity in explosions: application to regional discrimination of earthquakes and explosions, **Bull. Seism. Soc. Am.** 78, 1773-1795.
- Chiappetta, R. F. and D. G. Borg (1987). **Explosives and Rock Blasting**, Atlas Powder Company, Dallas, Texas, 662 pp.
- Crenwelge, O. E. , Jr., and T. A. Peterson (1986). Overburden blasting vibrations: analysis, prediction, and control, **Proceedings of the Twelfth Conference on Explosives and Blasting Technique**, Atlanta, GA, 269-283.
- Devine, J. F., R. H. Beck, A. V. C. Meyer, and W. I. Duvall (1966). Effect of charge weight on vibration levels from quarry blasting, U. S. Bureau of Mines RI 6774, 37pp.
- Duvall, W. I., and C. F. Johnson, A. V. C. Meyer, and J. F. Devine (1963), Vibrations from instantaneous and millisecond-delayed quarry blasts, U. S. Bureau of Mines RI 6151, 34 pp.
- Fish, B. G. (1951). Seismic vibrations from blasting, **Mine and Quarry Engineering**, 17, 189.

Frantti, G. E. (1963). Spectral energy density for quarry explosions, **Bull. Seism. Soc. Am.**, **53**, 989-996.

Greenhalgh, S. (1980), Effect of delay shooting on the nature of P-wave seismograms, **Bull. Seism. Soc. Am.**, **70**, 2037-2050.

Hedlin, M. A. H., J. B. Minster, and J. A. Orcutt, 1989. The time-frequency characteristics of quarry blasts and calibration explosions recorded in Kazakhstan, U. S. S. R., preprint.

Hinzen, K.-G., R. Ludeling, F. Heinemeyer, P. Roh, and U. Steiner (1987), A new approach to predict and reduce blast vibration by modeling of seismograms and using a new electronic initiation system, **Proceedings of the Thirteenth Conference on Explosives and Blasting Technique**, Miami, Fl.

Johnson, L. R. (1974). Green's functions for Lamb's problem, **Geophys. J. Roy. astr. Soc.** **37**, 99-131.

Kisslinger, C., E. J. Mateker, Jr., and T. V. McEvilly (1963). Seismic waves generated by chemical explosions, Final Report to Air Force Cambridge Research Laboratories, Contract AF 19(604)-7402.

Medearis, K. (1977). The development of rational damage criteria for low-rise structures subjected to blasting vibrations, in **Proceedings of the Eighteenth U. S. Symposium on Rock Mechanics**, Golden, CO, 1-16.

Mueller, R. A. and J. R. Murphy (1971). Seismic characteristics of underground nuclear detonations. Part I. seismic scaling law of underground nuclear detonations, **Bull. Seism. Soc. Am.** **61**, 1675-1692.

Pollack, H. N. (1963), Effect of delay time and number of delays on the spectra of ripple-fired shots, **Earthquake Notes**, **34**, 1-12.

Reil, J. W., D. A. Anderson, A. P. Ritter, D. A. Clark, S. R. Winzer, and A. J. Petro (1985). Geologic Factors affecting vibration from surface mine blasting, (Contract H0222009) Bureau of Mines OFR 33-86; NTIS PB86-175858, 191 pp.

**Seismic Verification of Nuclear Testing Treaties**, Congress of the United States, Office of Technology Assessment, U. S. Government Printing Office, Washington, D. C., May 1988.

Smith, A. T. and R. D. Grose, 1989. High-frequency seismic observation and models of chemical explosions: implications for discrimination of ripple-fired mining blasts, submitted for publication in **Bull. Seism. Soc. Am.**



Stump, B. W. and R. E. Reinke (1988). Experimental confirmation of superposition from small-scale explosions, **Bull. Seism. Soc. Am.** 78, 1059-1073.

Suteau-Henson, Anne and Thomas C. Bache, 1988. Spectral characteristics of regional phases recorded at NORESS, **Bull. Seism. Soc. Am.** 78, 708-725.

Thoenen, J. R., and S. L. Windes (1942). Seismic effects of quarry blasting, U. S. Bureau of Mines Bulletin 442, 83 pp.

Willis, D. E. (1963). A note on the effect of ripple firing on the spectra of quarry shots, **Bull. Seism. Soc. Am.** 53, 79-85.

Winzer, S. R. (1978). The firing times of ms delay blasting caps and their effect on blasting performance, Report to the National Science Foundation, Contract DAR-77-05171.

**POMONA QUARRY SEISMIC EXPERIMENT:**

**NEAR-SOURCE DATA**

**December 1-3, 1987**

**Greensboro, North Carolina**

**Sharon K. Reamer and Brian W. Stump**

**Southern Methodist University**

**Dallas, Texas 75275**

**Robert E. Reinke and John A. Leverette**

**AFWL/NTEC**

**Kirtland AFB, NM 87117-6008**

## INTRODUCTION

Near-source seismic records from a series of quarry blasts were recorded at the Pomona Quarry near Greensboro, North Carolina. The program was a cooperative one with the Atlas Blasting Company and instrumented by the Air Force Weapons Laboratory. The purpose of the experiment was to obtain near-source (30-225 m) seismological measurements of cylindrical explosive sources. Both single shots detonated on the floor of the quarry (floor shots) and a multi-explosion production shot on the quarry bench (bench shot) were recorded. Waveforms from the single shot explosions will be used to quantify the cylindrical source mechanism. Once an adequate single shot source characterization has been made, the multiple event shot will be built from the single source results to test linear superposition. This method will be the first step in a quantitative study of the spatial and temporal finite effects of multiple shot arrays. The results of this study will be used to supplement modeling of New England near-source quarry blast seismic data (Stump et al, 1988). The purpose of this preliminary report is to document the experiment.

## DESCRIPTION OF EXPERIMENT

The Pomona quarry is composed of a biotite granite matrix interspersed with gabbritic dike inclusions which trend north-northeast. A total of five explosive events were recorded: four single shots and one multiple-delay shot. The layout of stations and shot locations is given in Figure 1. Station distances and explosive charges for all five shots, which ranged from 30-226 m, are summarized in Table 1. The data were collected using three-component, force-balanced accelerometers and a recording system with 12-bit dynamic range. Both linear and azimuthal arrays were employed in the experiment (Figure 1).

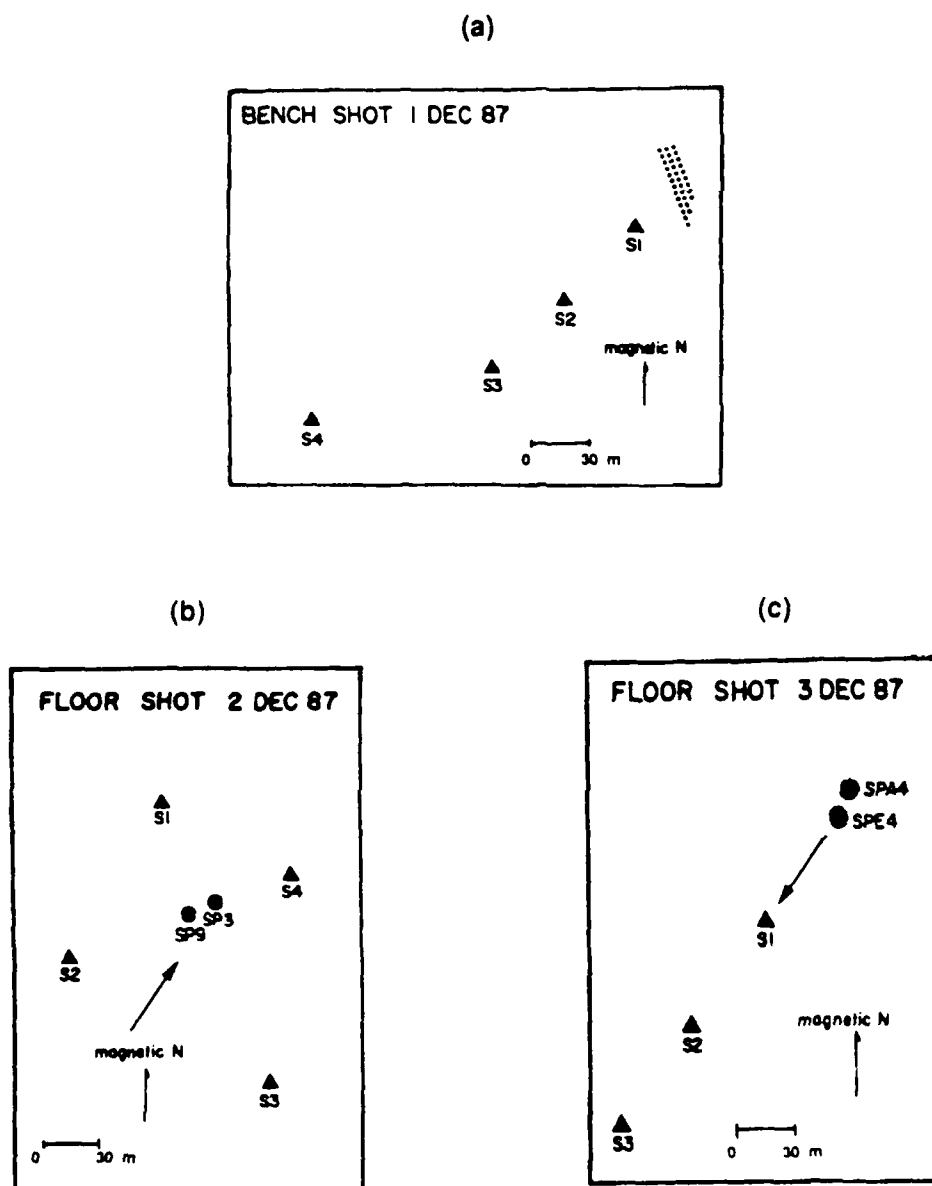


**Figure 1.** Pomona Quarry station (triangles) and shot (circles) locations: (a) the multiple-hole shot on the quarry bench, (b) the two single floor shots (SP3 and SP9), and (c) the two single floor shots (SPA4 and SPE4). The arrow on the two floor shots indicates the direction of the radial component, toward the center of the two shots on December 2 and away from the center on December 3.

Table 1. Pomona Quarry explosions and station ranges

	BENCH 12/1/87	SP3 12/2/87	SP9 12/2/87	SPA4 12/3/87	SPE4 12/3/87
CHARGE WEIGHT (LBS) →	8425	27	34	30	47
STATIONS	RANGES (m)				
S1	28	60	60	76	61
S2	78	84	68	137	122
S3	130	100	100	198	183
S4	226	58	58		

## DESCRIPTION OF EXPLOSIVE EVENTS

The four single shots consist of two shots (SP3 and SPA4) of 27 lbs. and 30 lbs., respectively, of ammonium nitrate fuel oil (ANFO) explosive and two shots (SP9 and SPE4) of 34 lbs. and 47 lbs., respectively of emulsion type explosive. Depth of the holes ranged from 4-5 m with hole diameters of 13-14 cm. The purpose of the single-shot experiments is two-fold: (1) to characterize the cylindrical, single-shot sources and (2) to quantify coupling differences between the two explosive types. The linear array for the bench shot was recorded at four stations ranging southwest from the shot and spaced at comparable distances to the linear array for the two single shots SPA4 and SPE4. The single shots SPA4 and SPE4 were recorded at three stations. The two single shots SP3 and SP9 were recorded by an azimuthal array of four stations. The use of both linear and azimuthal arrays for the single shots will allow for more complete separation of source and propagation path effects.

The bench shot consisted of 33 individual charges of 255 lbs. each of ANFO with a total explosive charge of 8425 lbs. (4.2 tons). Shot geometry was a rectangular grid of three rows of charges with between hole spacing of 4 m and a burden spacing of 3.3 m (Figure 2). Depth of the holes ranged from 15-16 m including 6 m of stemming for the front row charges and 4 m of stemming for the back two rows. The firing sequence was a unidirectional, staggered row pattern as indicated by the design delay times (Figure 2). Design firing times included between-hole delays of 25 ms while between-row delays (closest delay times between rows) were 8 ms. One of the unique aspects of this experiment, actual firing times were recorded by high speed photography (1000 frames per second). The addition of the actual firing times allows a better characterization of the finite temporal effects of the multiple shot event. The actual shot times are indicated in Figure 2. Total source duration

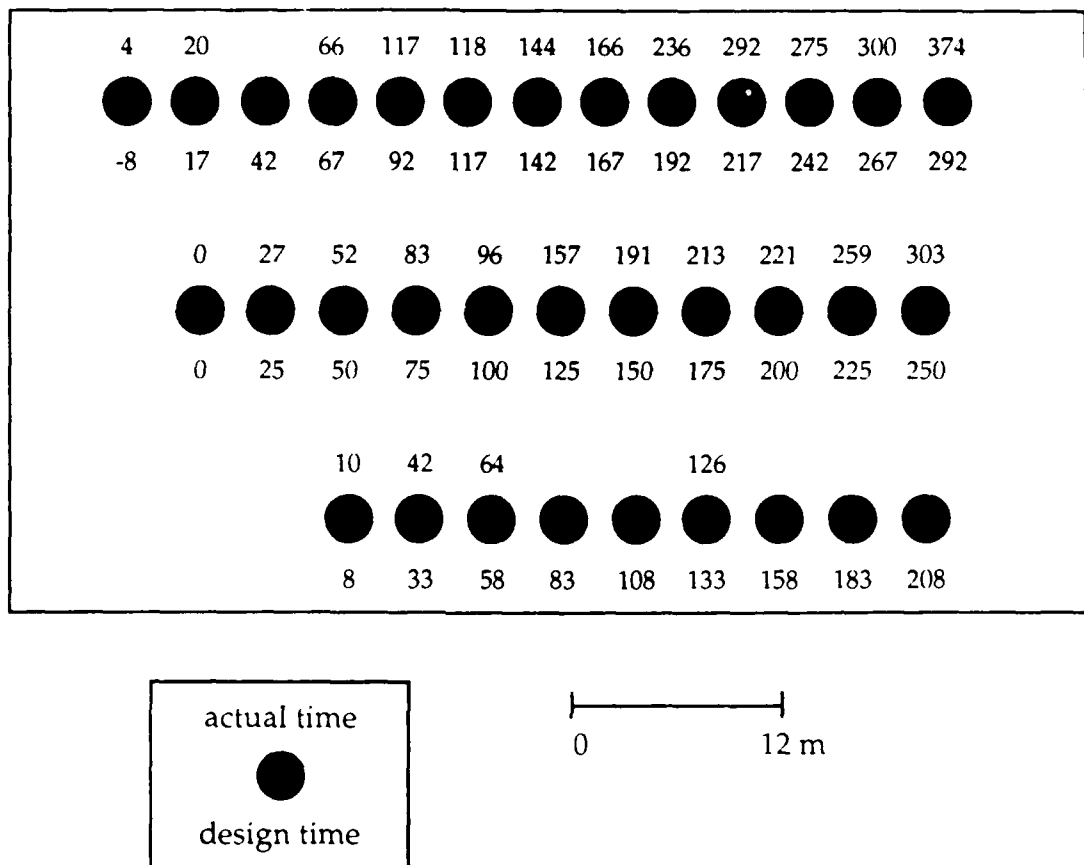


**Figure 2.** Shot geometry is presented including design and actual shot times for the multiple quarry shot (bench shot). Upper numbers beside each shothole represent actual times; lower numbers represent design times in milliseconds. The horizontal scale shows the between-hole spacing. Burden spacing is not to scale.

design time was 292 ms versus an actual total source duration of 374 ms. A plot of actual versus design firing times (Figure 3) illustrates the high variance associated with blasting cap firing times which were as high as 20% of the individual delay times. Additionally, not all of the times were ascertainable because of blast debris obscuring the high-speed film so that some of the design times have not been mapped to actual times.

## DATA

Acceleration and velocity waveforms have been included in this report. A one-second time window is displayed for both the acceleration and velocity waveforms. All but two stations were recorded on three channels at 200 samples per second (sps). Two stations (S1 and S4) for SP9 were recorded on a single (vertical) channel at 600 sps.

For the acceleration time series (Figures 4-19), the vertical amplitude scale is in gals; the velocity records (Figures 20-34) have been converted to cm/s. Channel 1 is vertical; channel 2 is transverse; and channel 3 is the radial component of motion for the single shot data. Channel 1 is vertical for the multiple shot data. Velocity records are obtained by integrating the acceleration records using the trapezoid rule, removing a ramp in velocity, and applying a small smoothing window to both ends of the seismic record. In order to minimize the effects of long period noise, which are emphasized during the integration process, a high pass, two-pole recursive filter with a corner at 3 Hz is applied to all records. The natural corner of the accelerometers is between 70-110 Hz, and a five-pole antialias filter with a corner at 70 Hz is applied to the 200 sps data when recorded. The shots and stations are identified in accordance with the naming in Table 1.



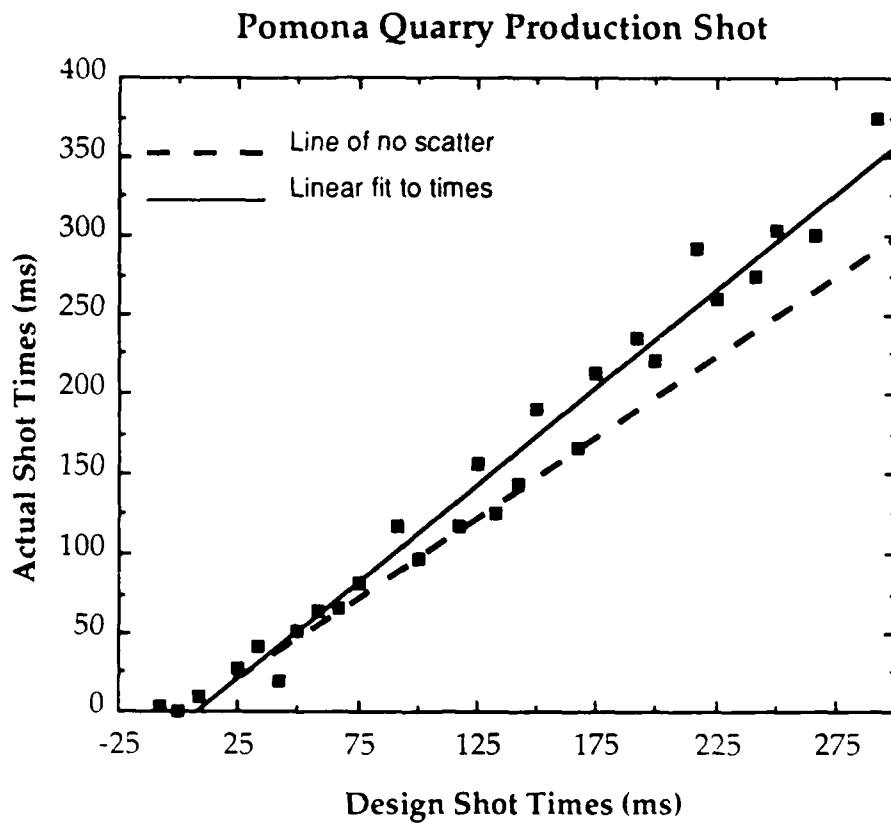


**Figure 3.** Comparison of actual and design shot times for the production shot (bench shot) on December 1, 1987. The solid line represents a linear fit to the data and illustrates the scatter of the actual times. The dashed line represents where the points would lie if design and actual shot times were exactly the same.

Figure 4. Bench shot station 1  
Acceleration (gals)

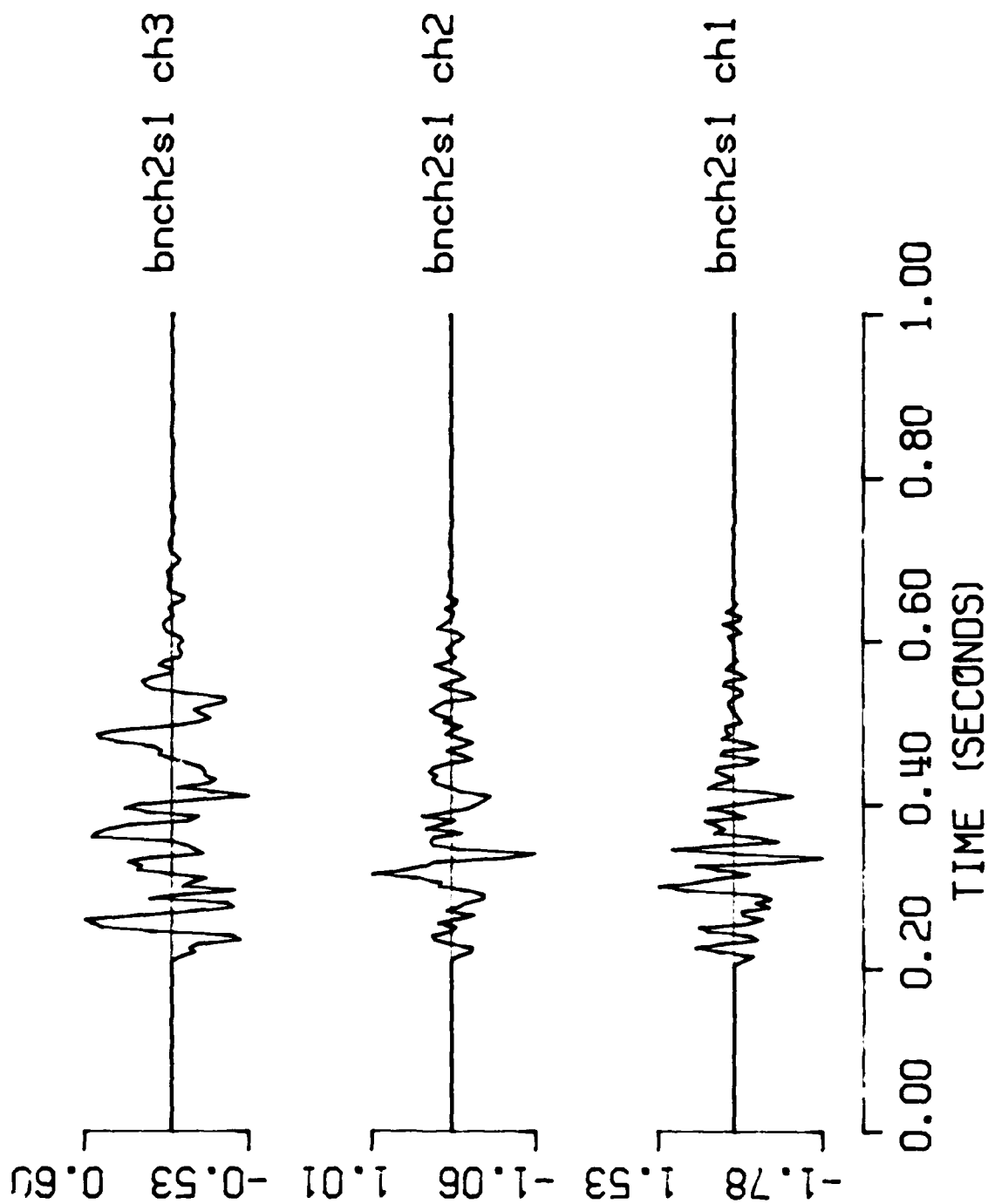


Figure 5. Bench shot station 3  
Acceleration (gals)

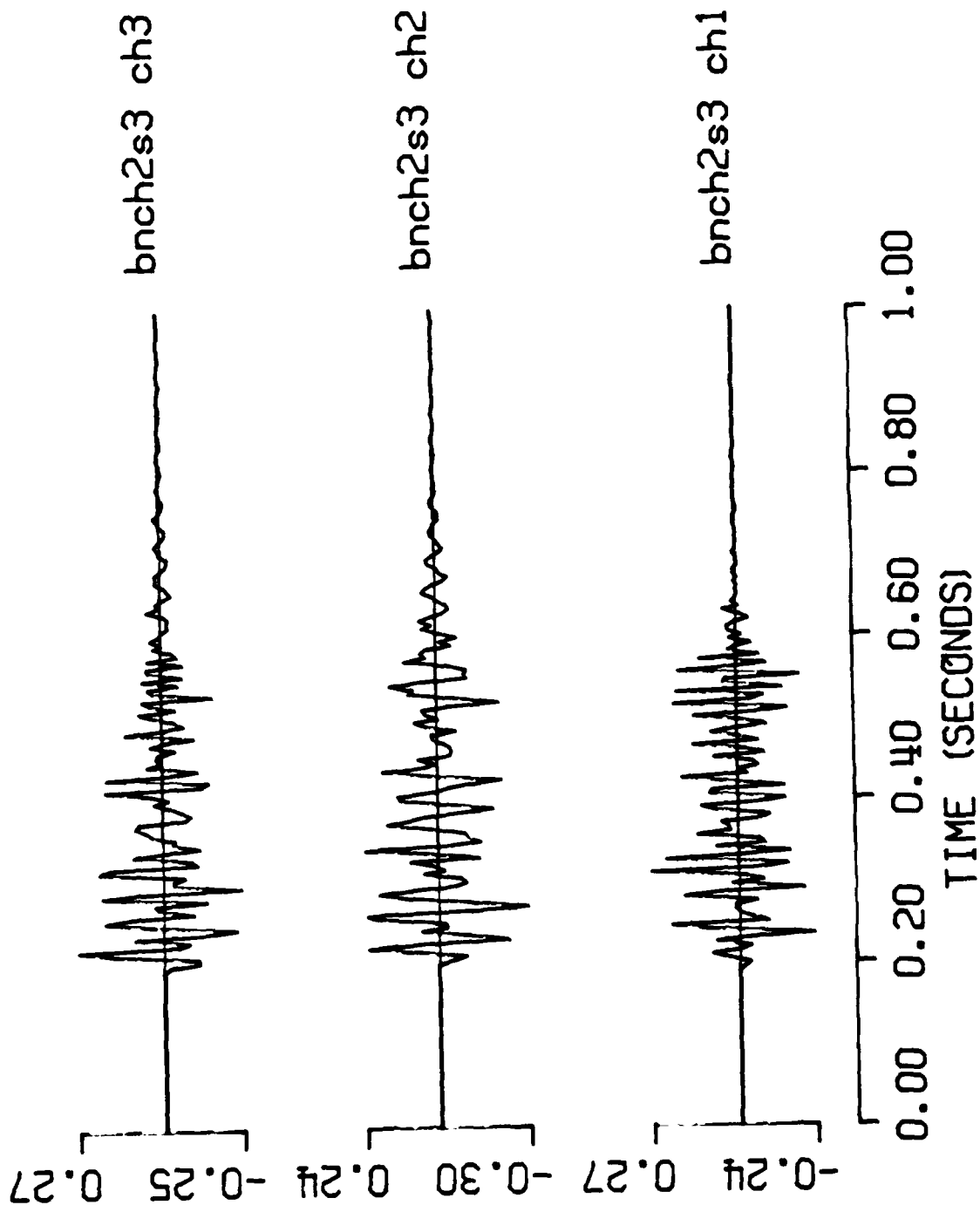


Figure 6. Bench shot station 4  
Acceleration (gals)

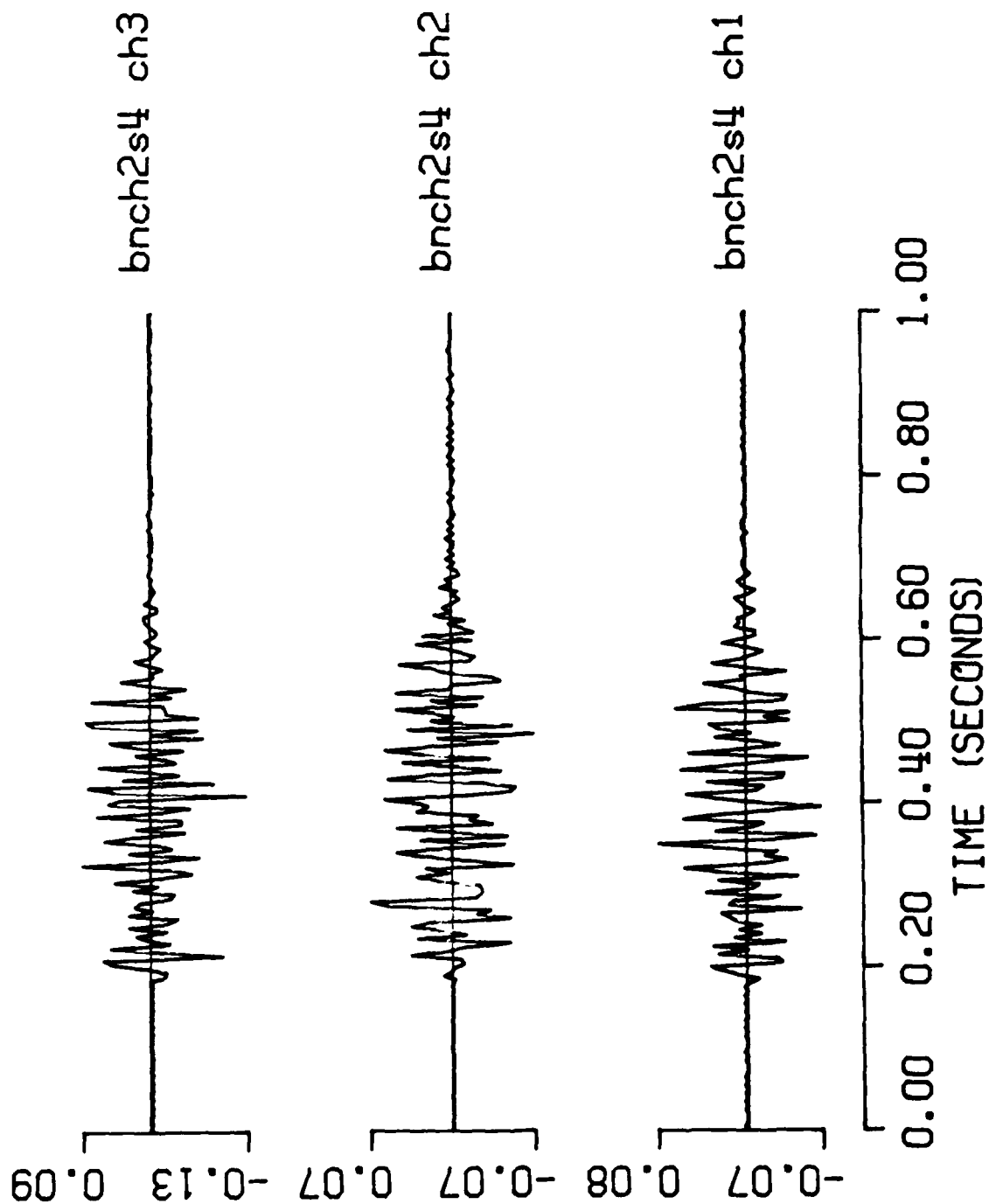


Figure 7. Floor Shot SP3 station 1  
Acceleration (gals)

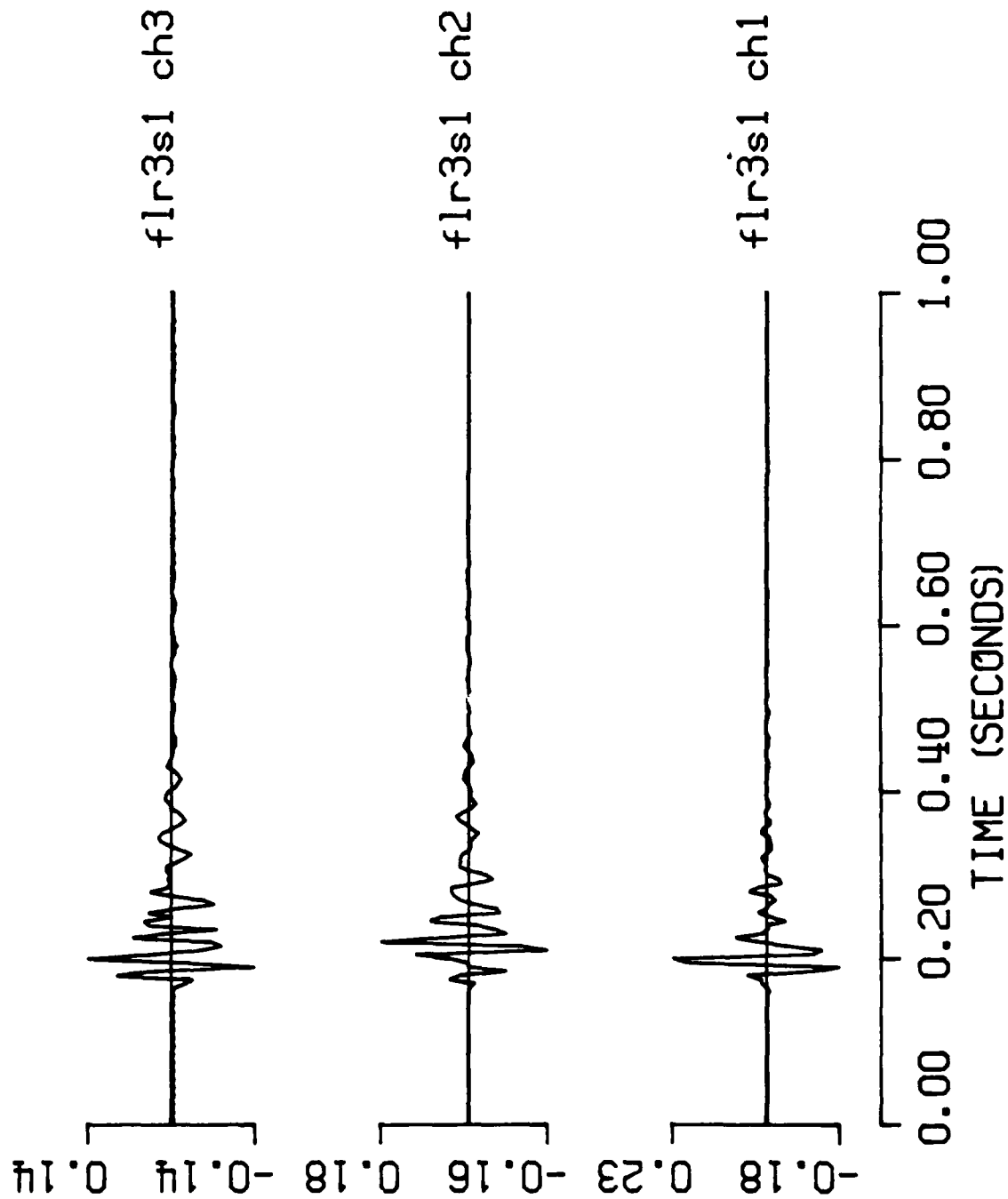


Figure 8. Floor Shot SP3 station 3  
Acceleration (gals)

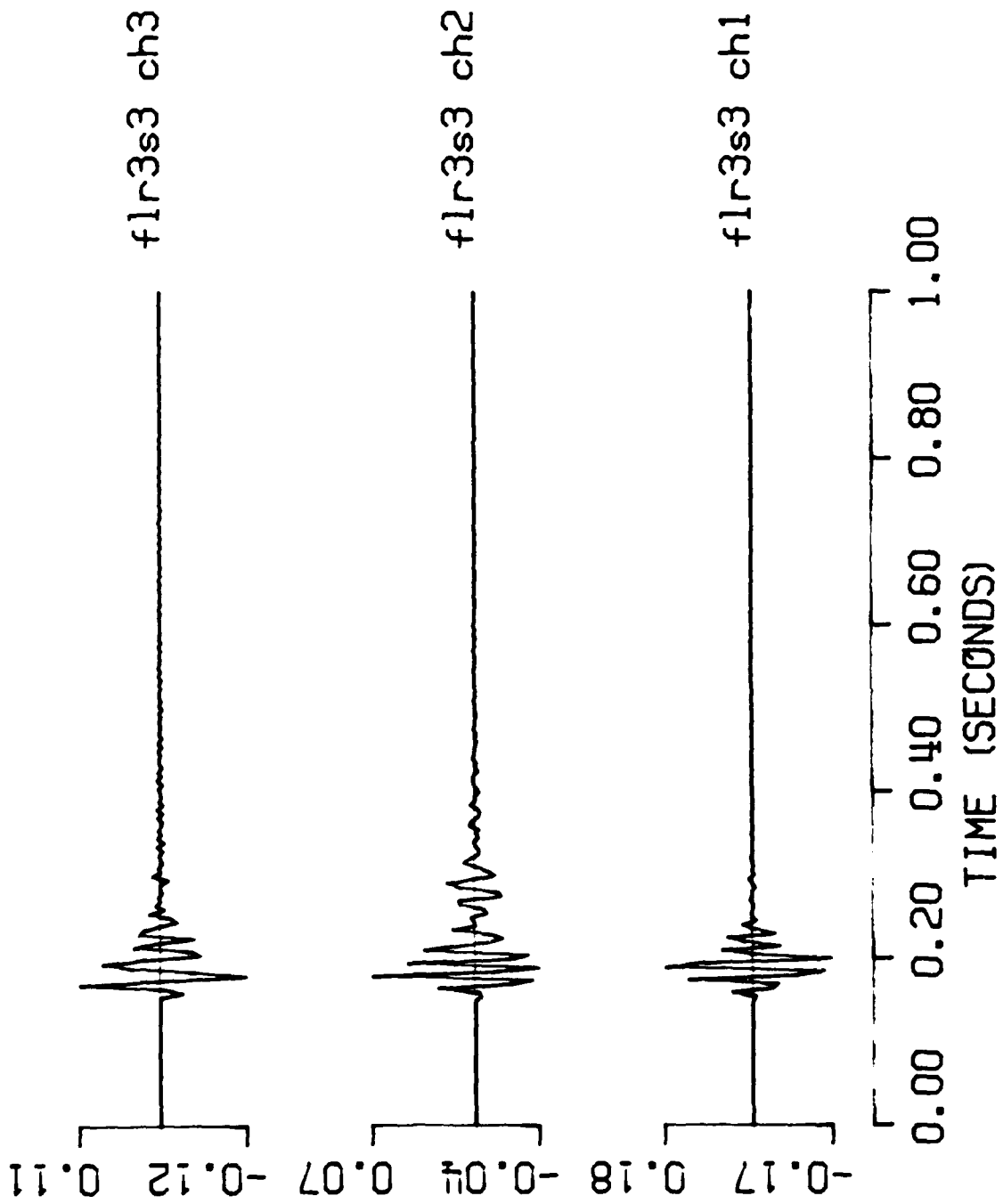


Figure 9. Floor Shot SP3 station 4  
Acceleration (gals)

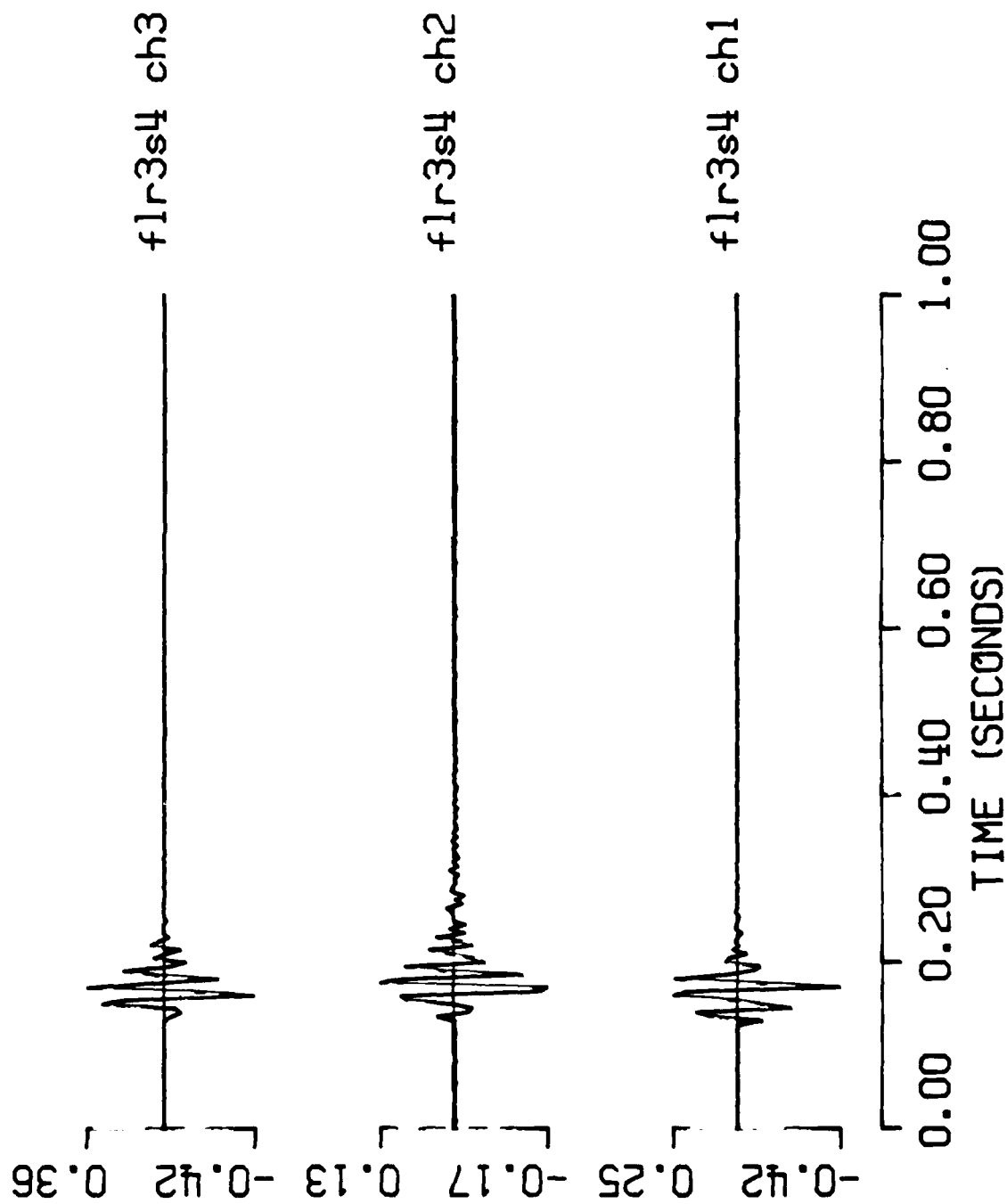


Figure 10. Floor Shot SP9 station 1 (600 sample/sec)  
Acceleration (gals)

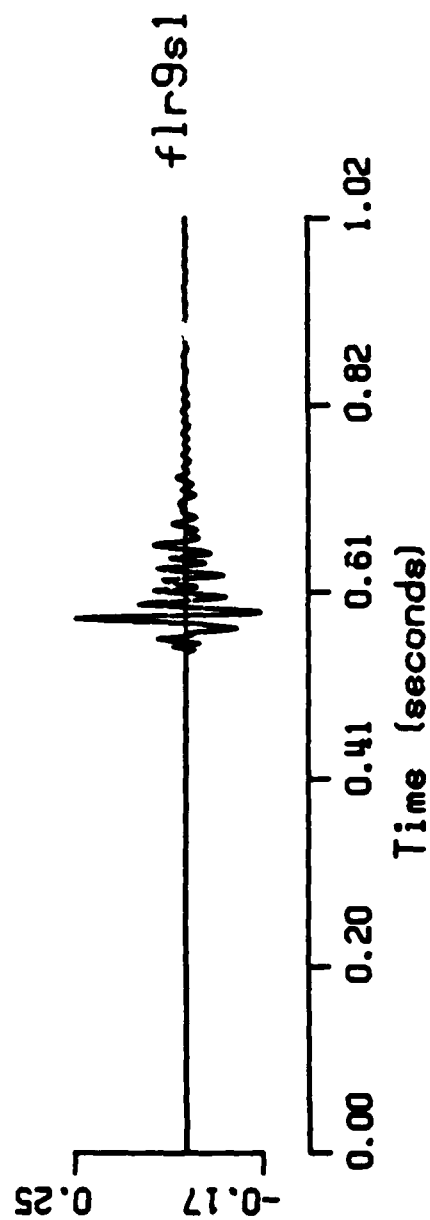




Figure 11. Floor Shot SP9 station 2  
Acceleration (gals)

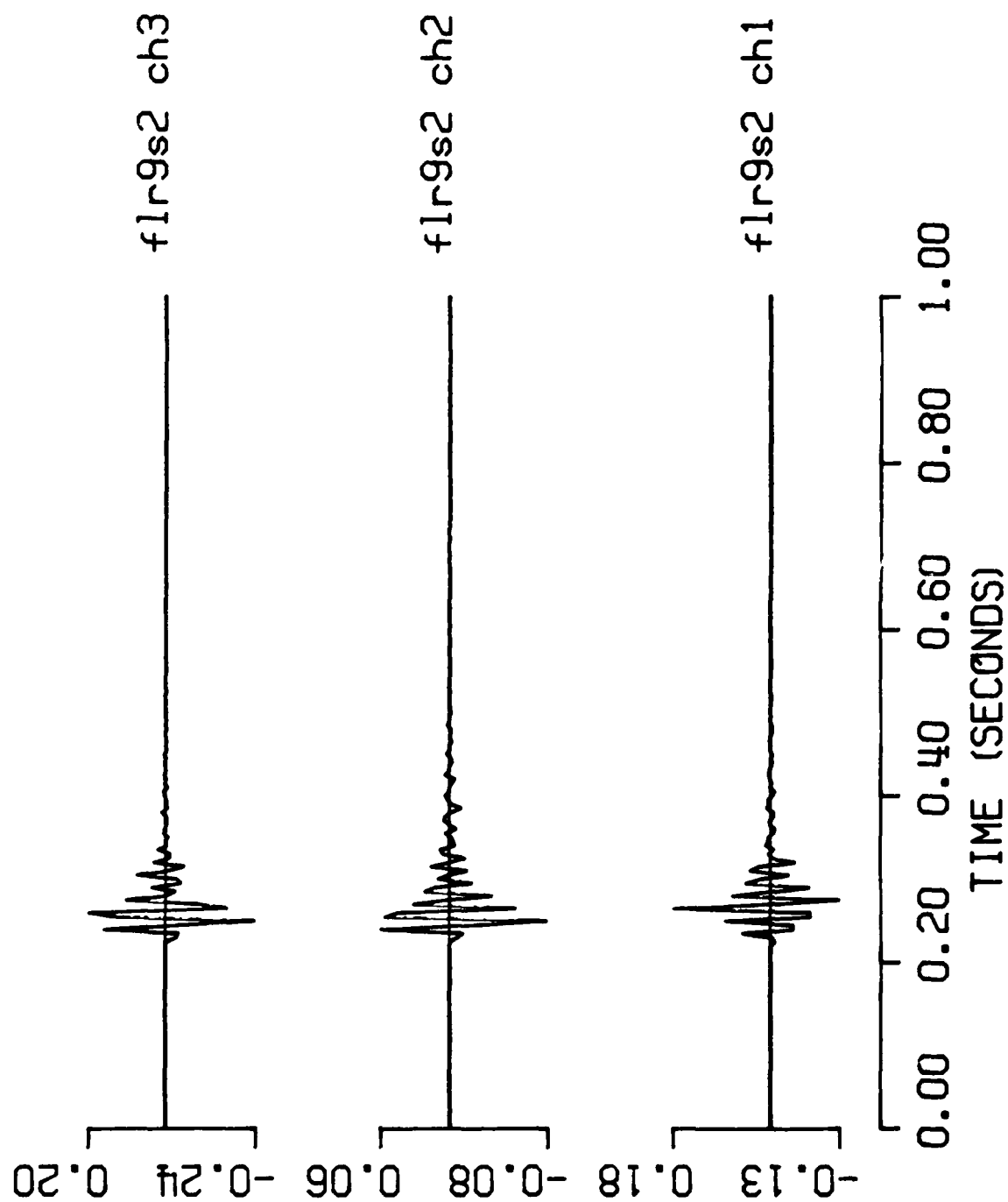


Figure 12. Floor Shot SP9 station 3  
Acceleration (gals)

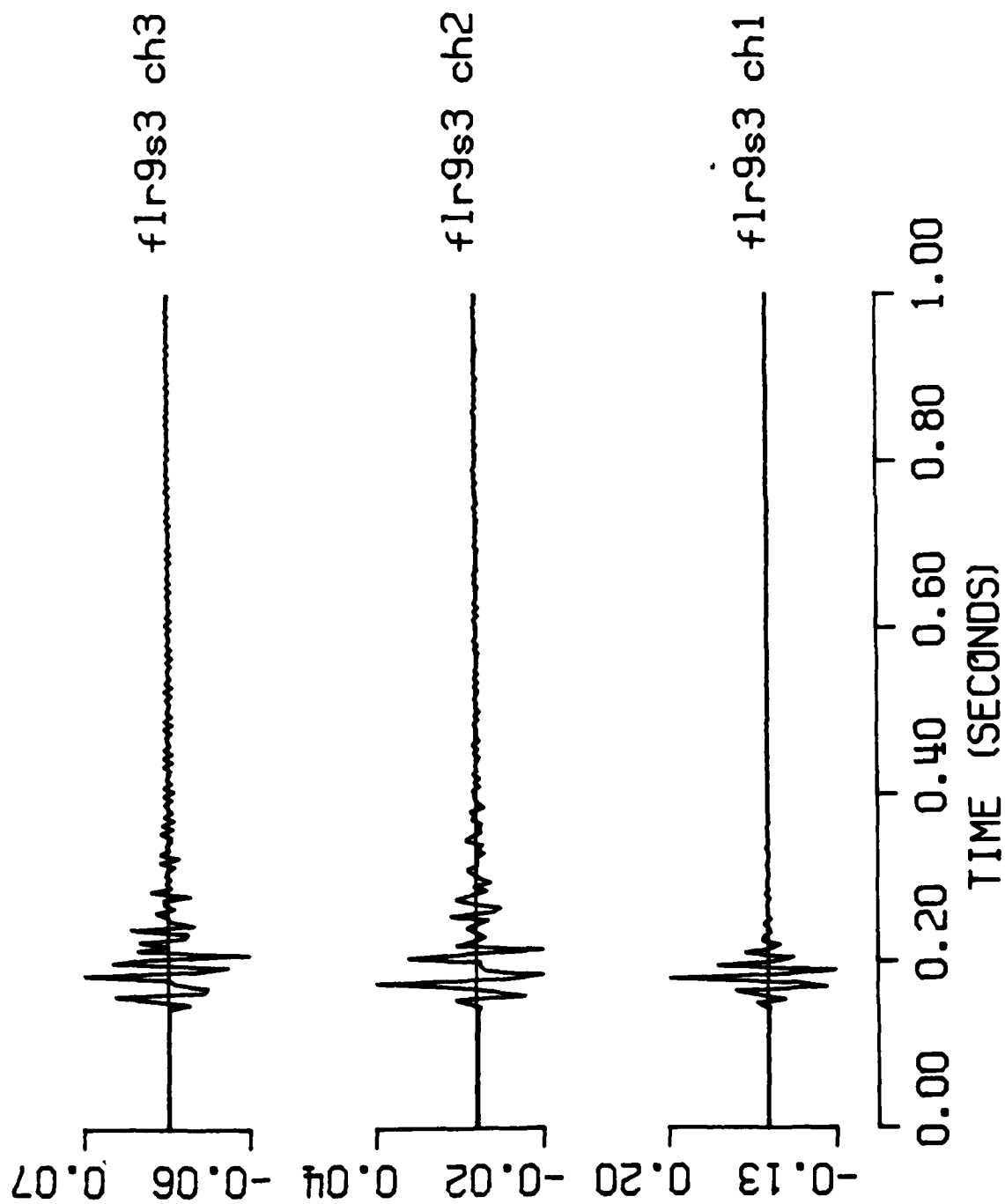


Figure 13. Floor Shot SP9 station 4 (600 sample/sec)  
Acceleration (gals)

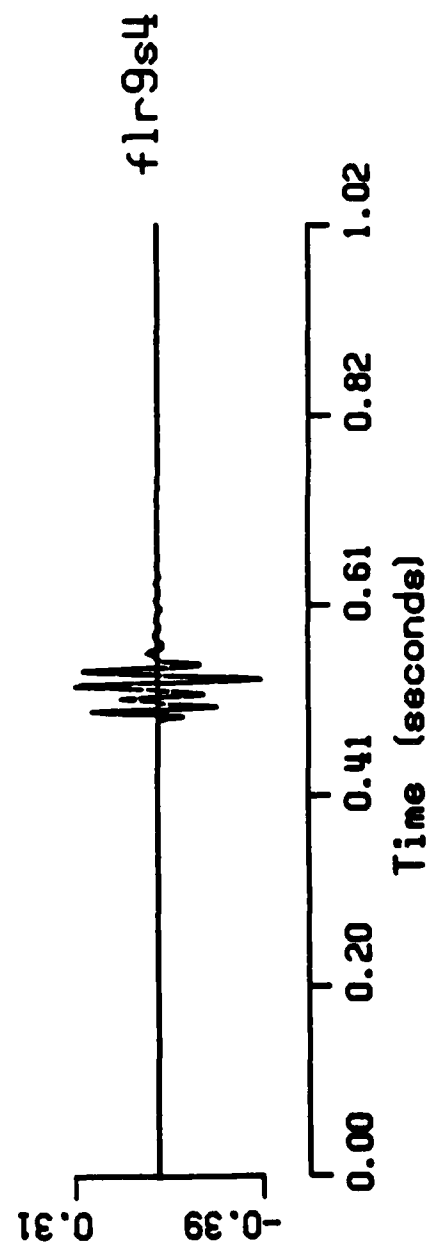


Figure 14. Floor Shot SPA4 station 1  
Acceleration (gals)

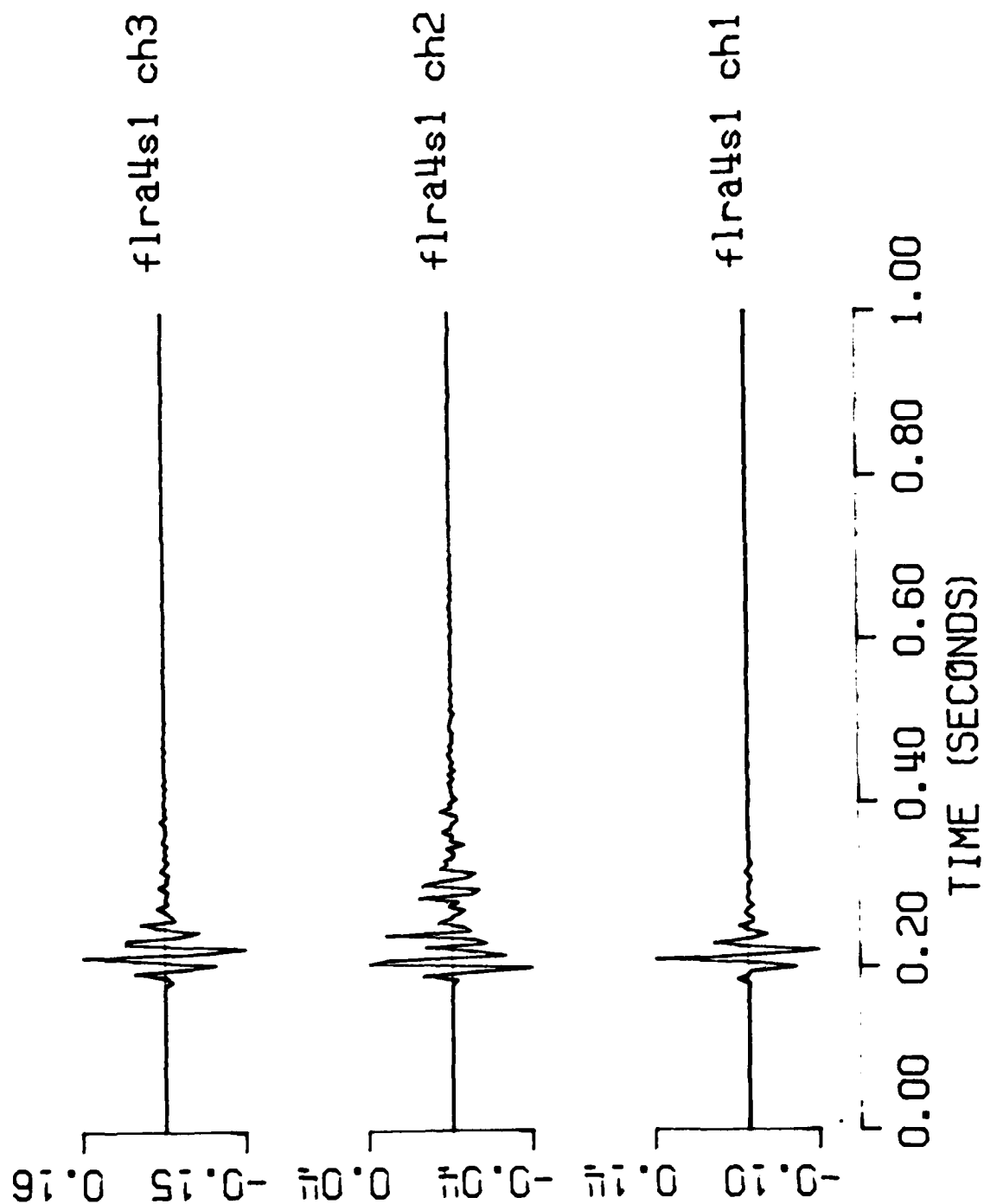


Figure 15. Floor Shot SPA4 station 2  
Acceleration (gals)

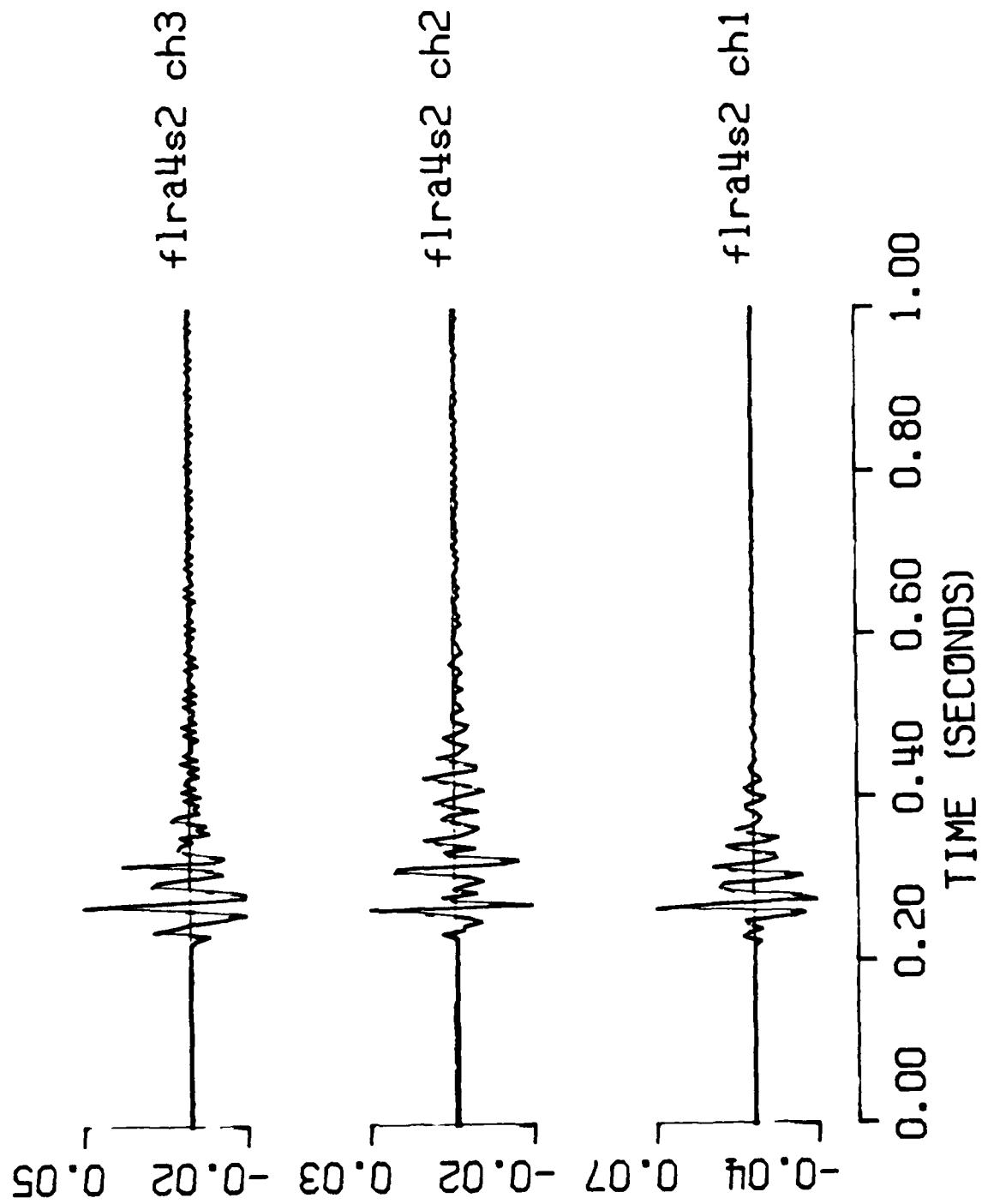


Figure 16. Floor Shot SPA4 station 3  
Acceleration (gals)

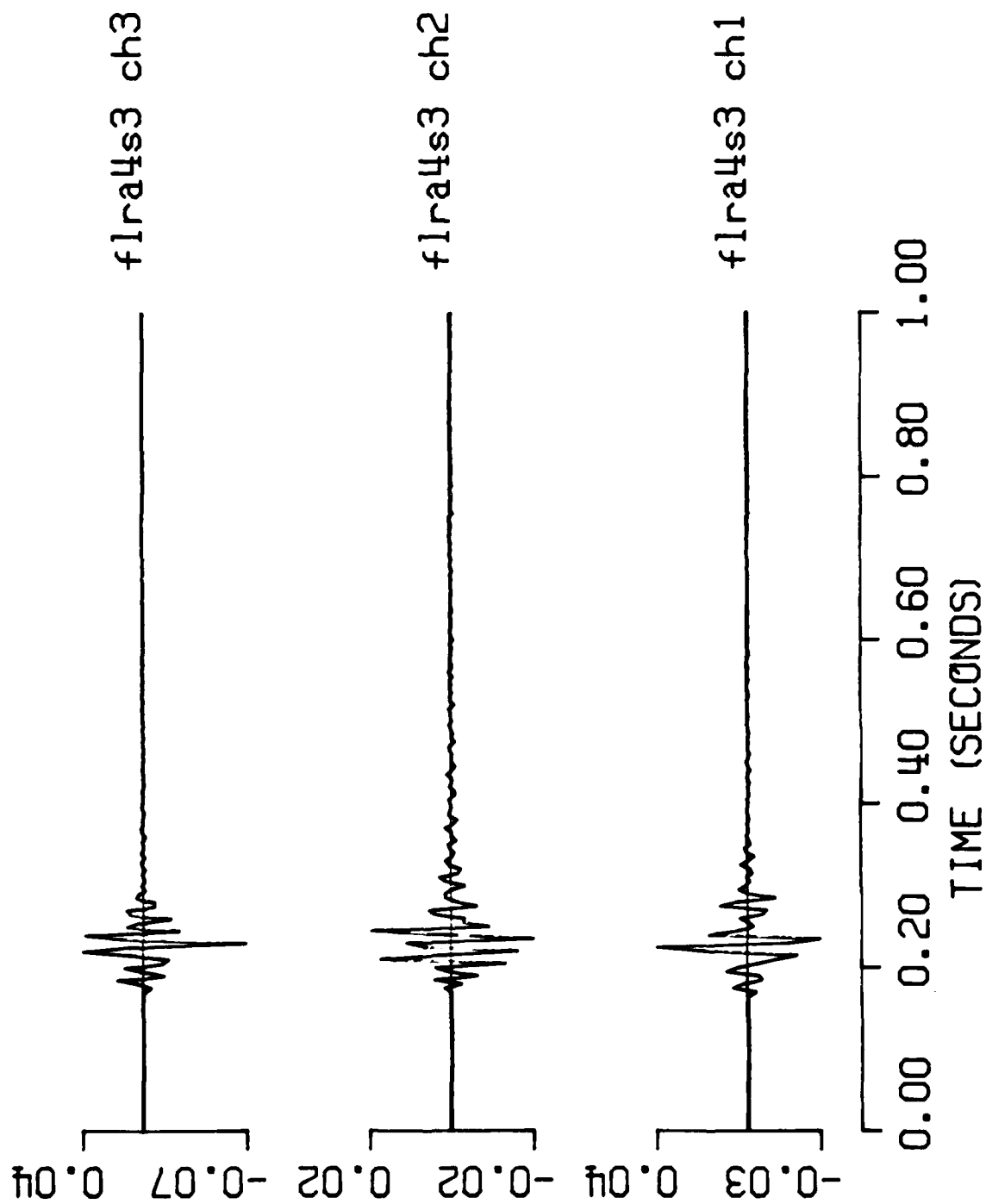


Figure 17. Floor Shot SPE4 station 1  
Acceleration (gals)

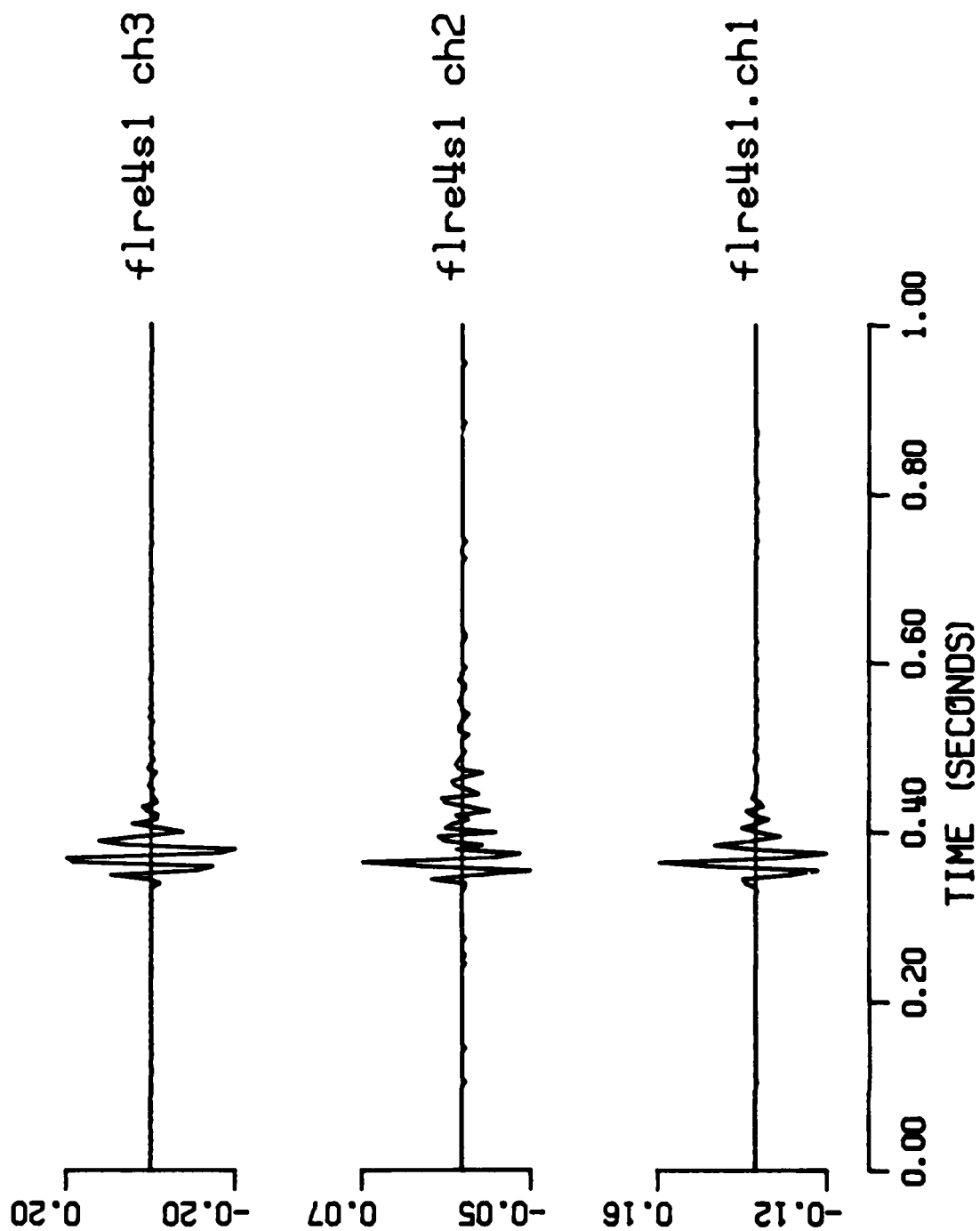


Figure 18. Floor Shot SPE4 station 2  
Acceleration (gals)

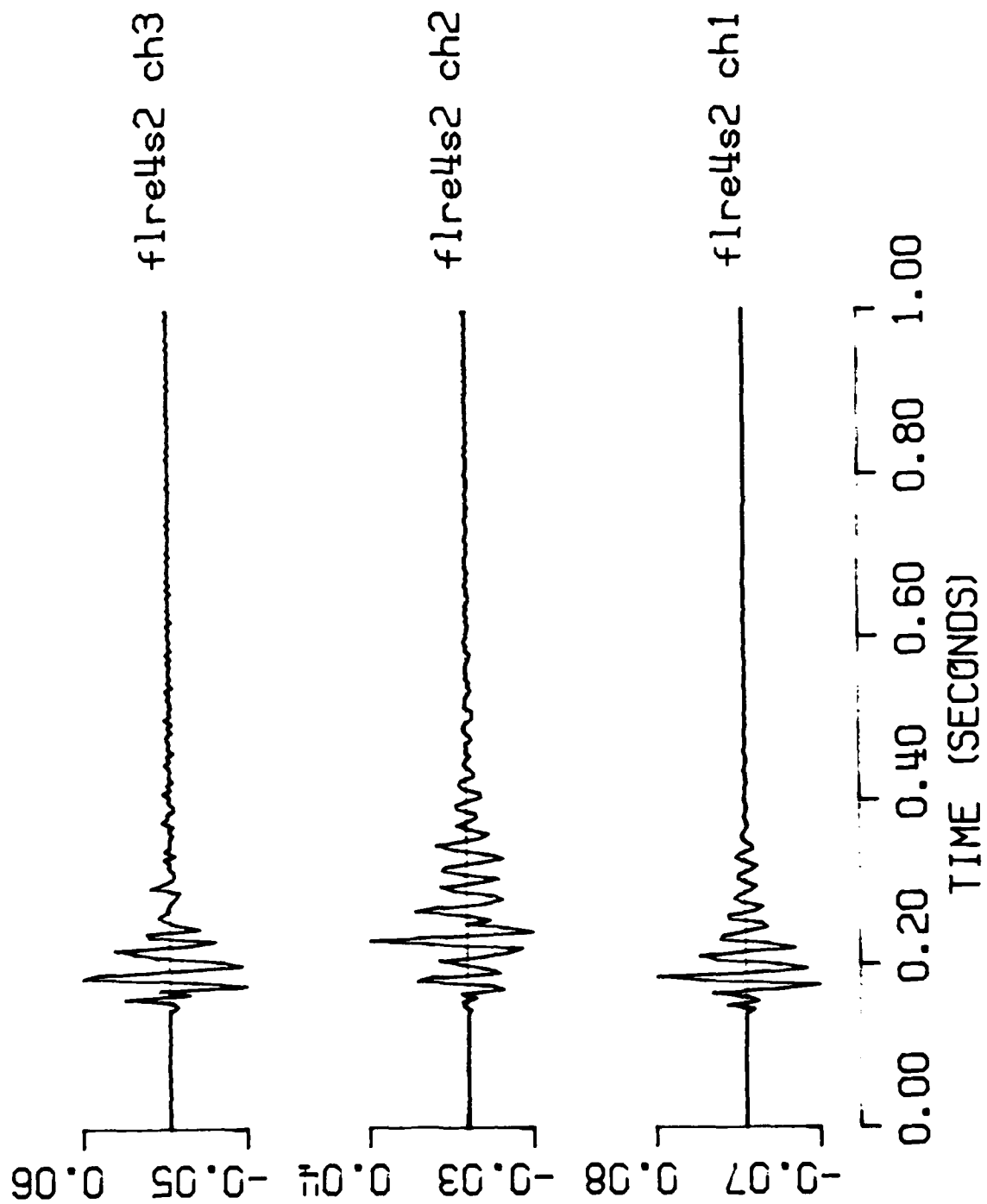




Figure 19. Floor Shot SPE4 station 3  
Acceleration (gals)

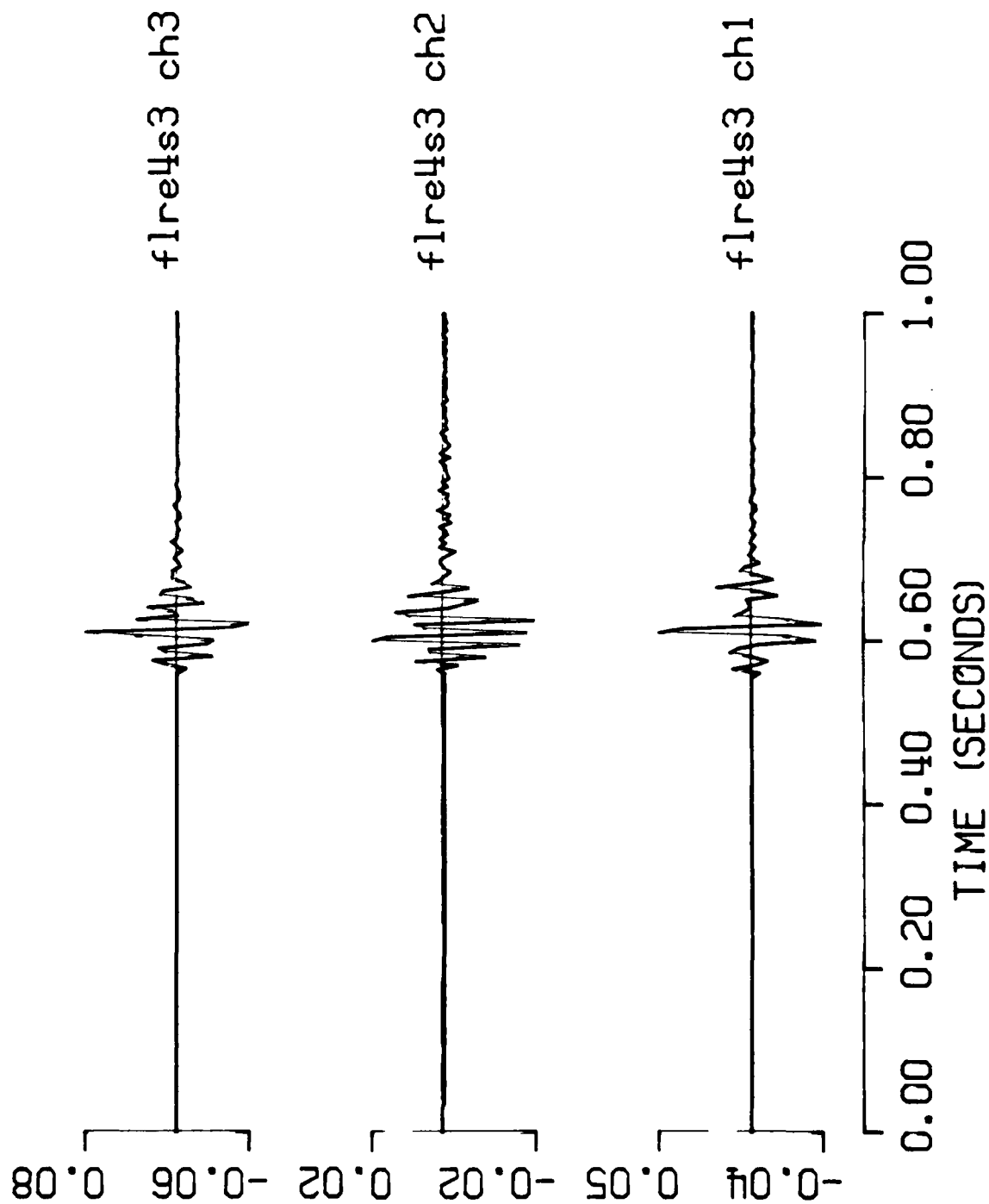


Figure 20. Bench Shot station 1  
Velocity (cm/s)

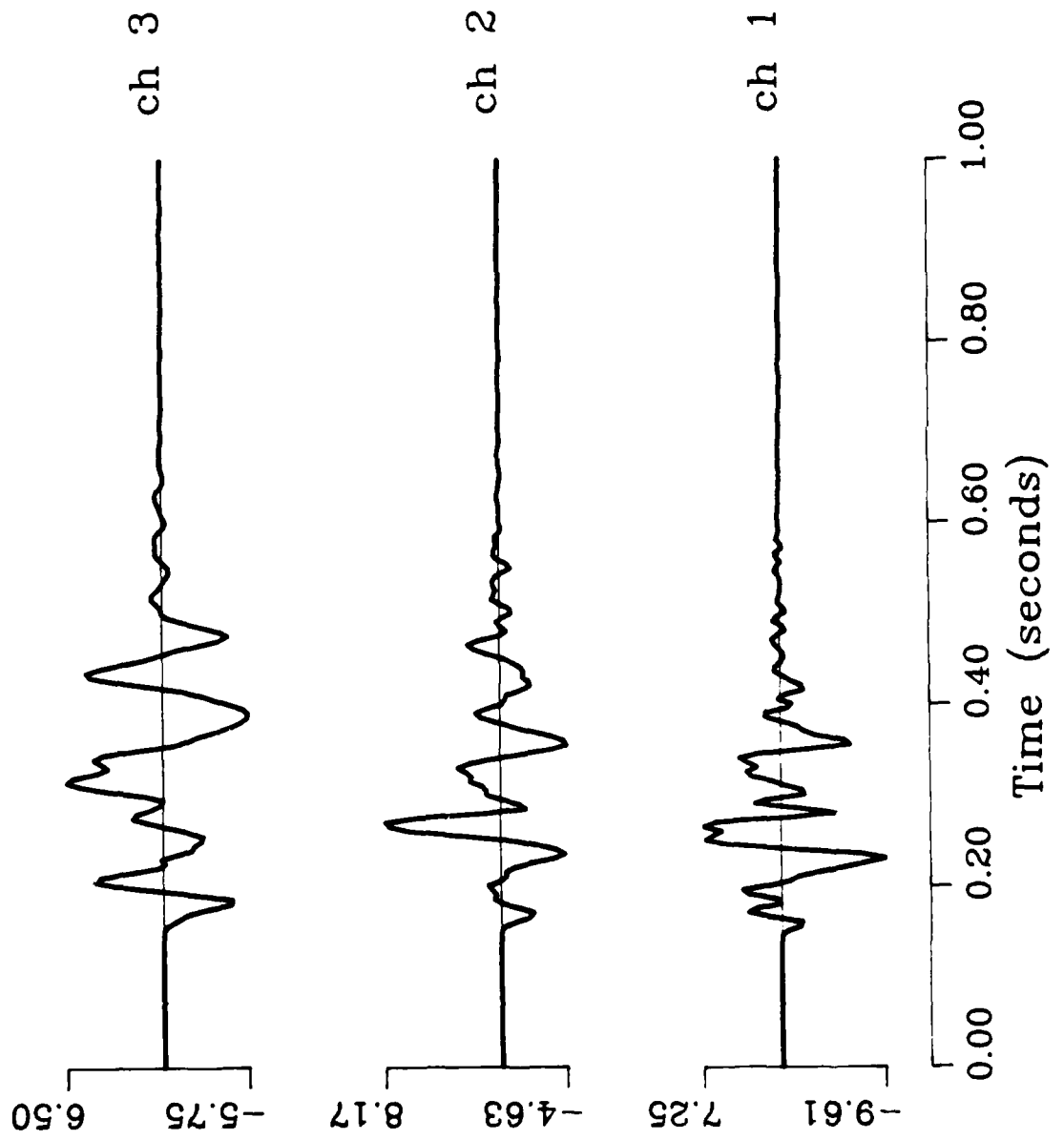


Figure 21. Bench Shot station 3  
Velocity (cm/s)

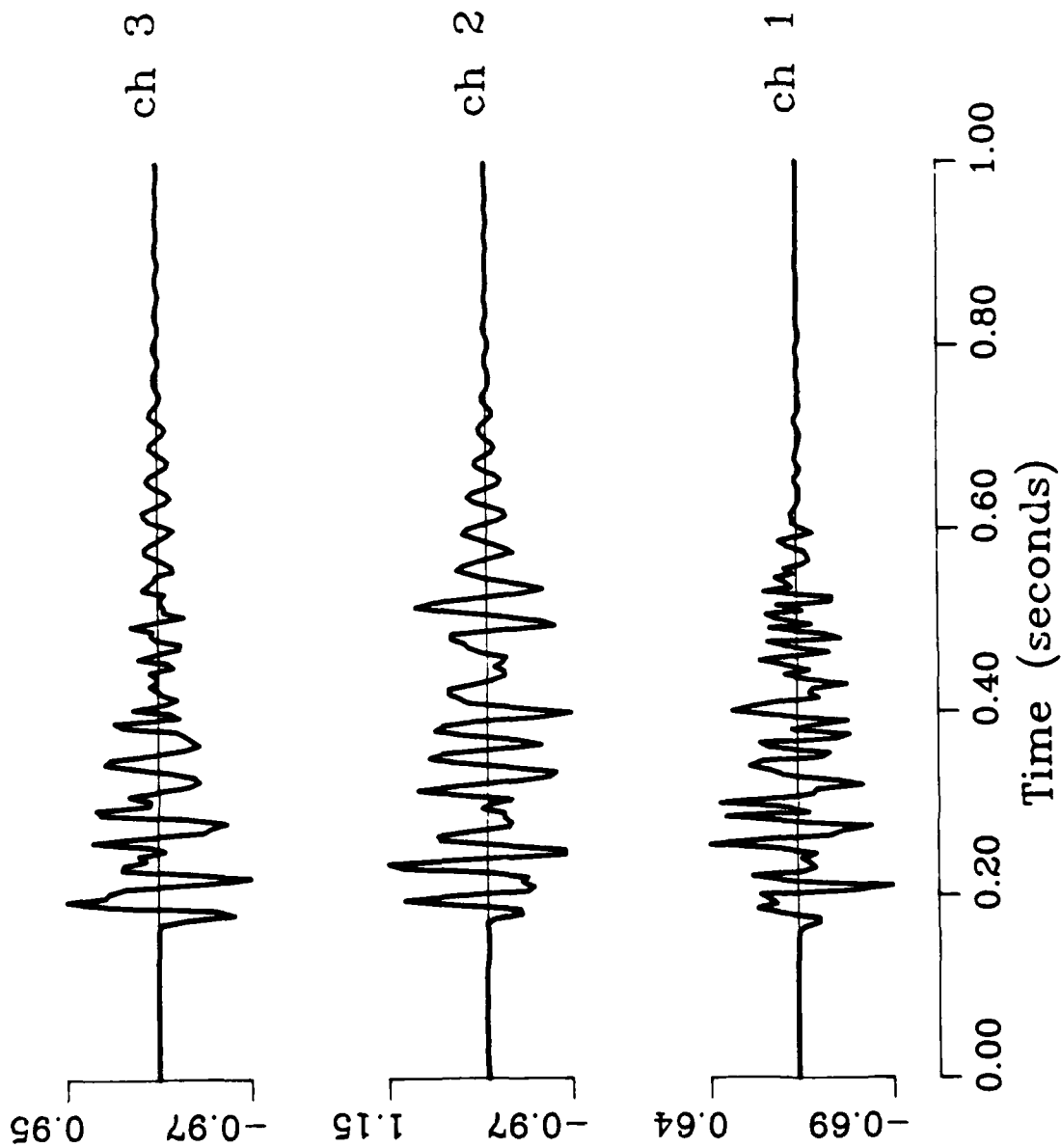


Figure 22. Bench Shot station 4  
Velocity (cm/s)

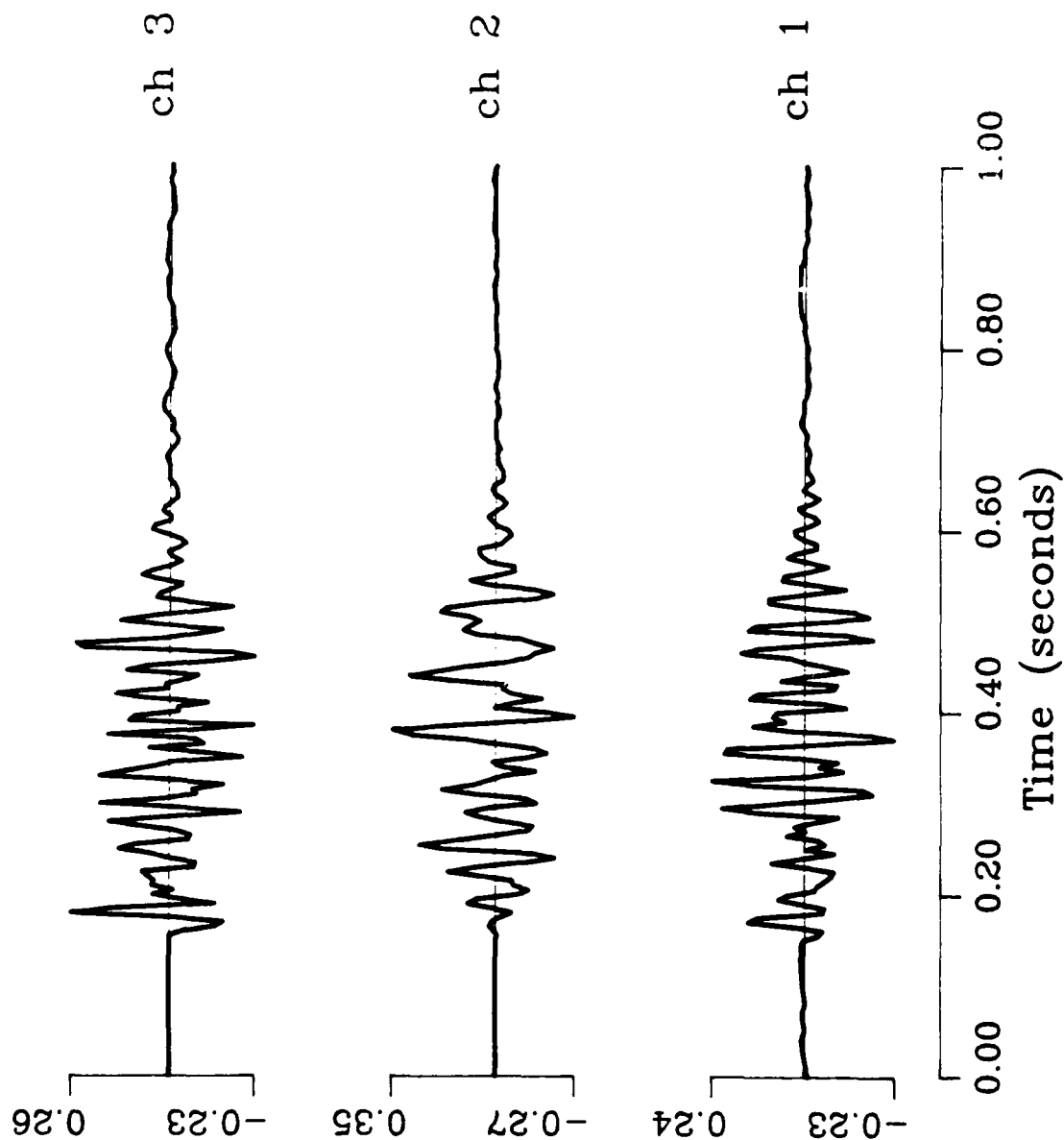


Figure 23. Floor Shot SP3 station 1  
Velocity (cm/s)

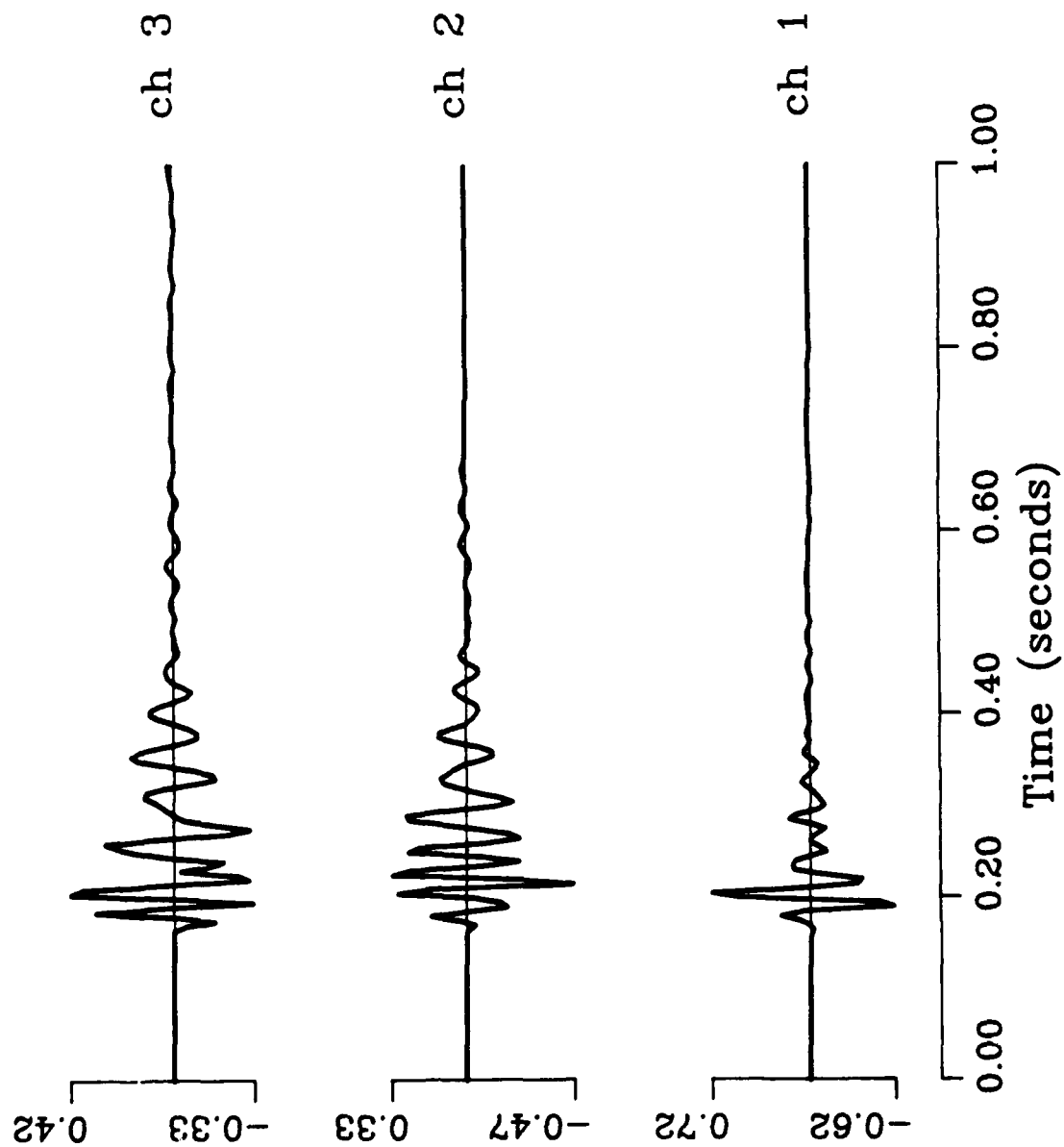


Figure 24. Floor Shot SP3 station 3  
Velocity (cm/s)

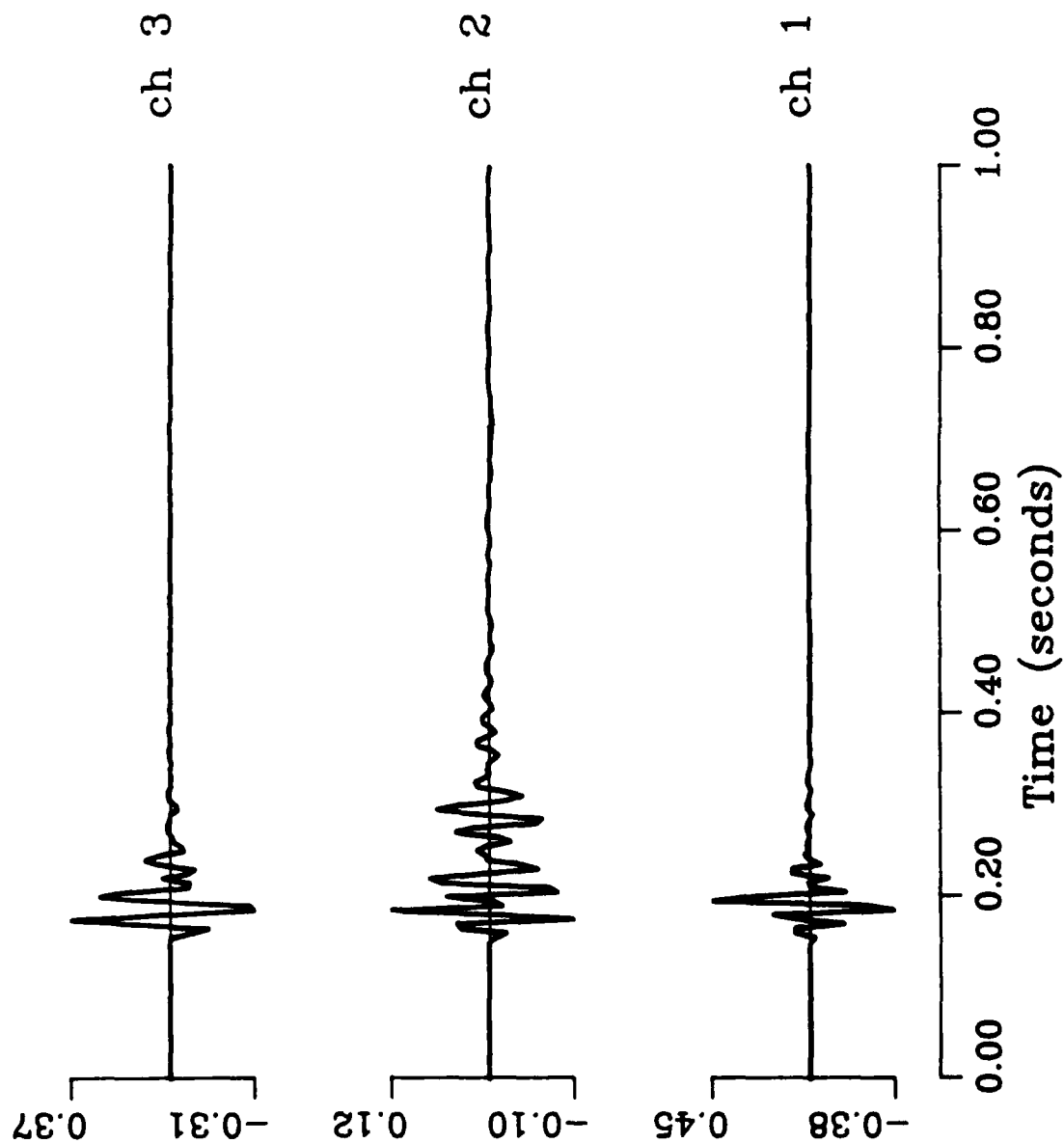


Figure 25. Floor Shot SP3 station 4  
Velocity (cm/s)

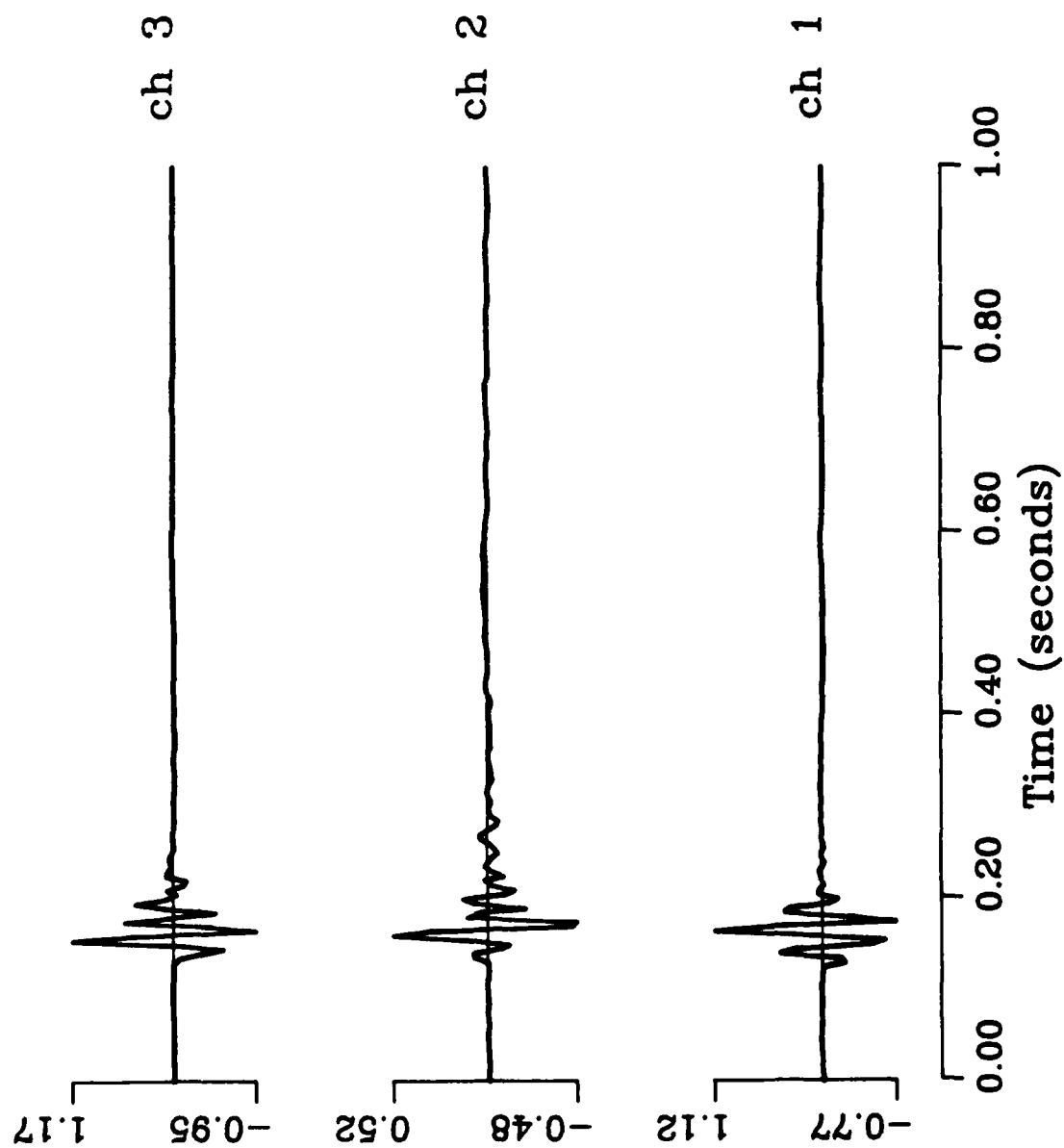


Figure 26. Floor Shot SP9 station 1 and station 4 (600 samples/sec)  
Velocity (cm/s)

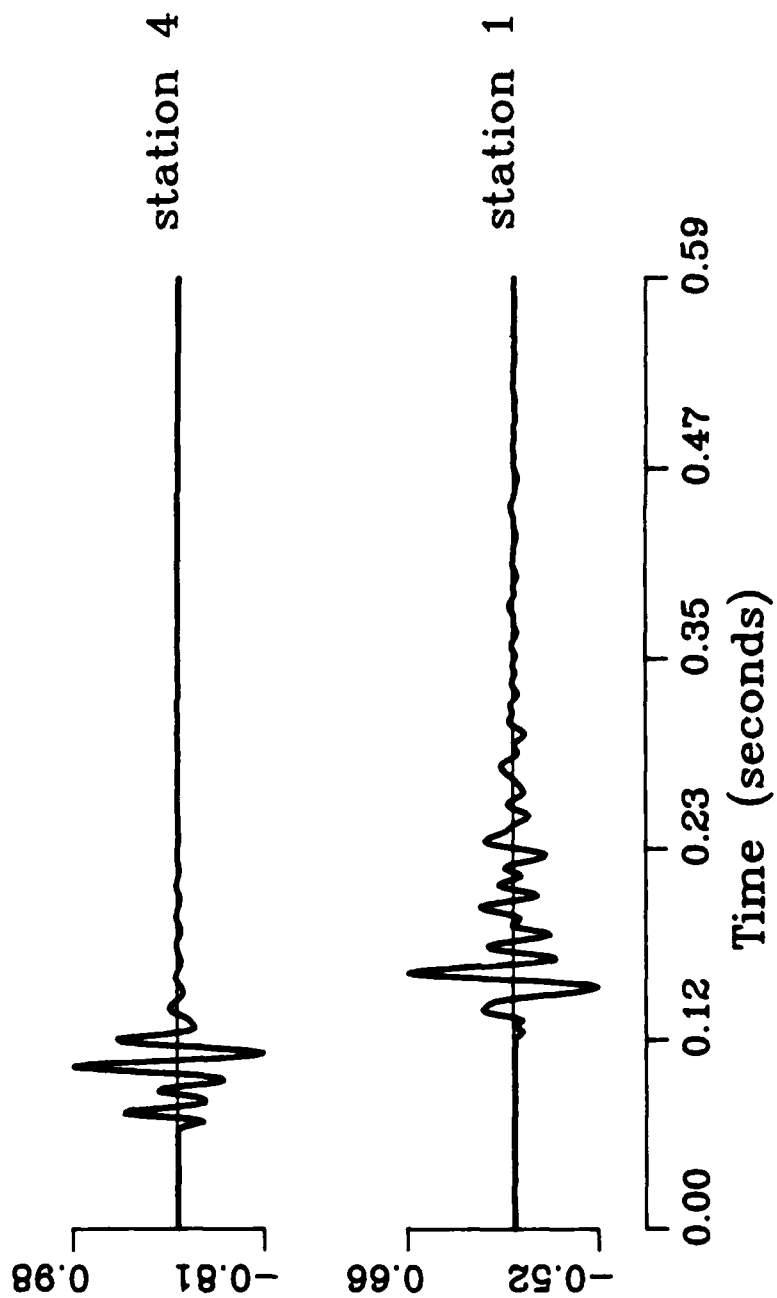
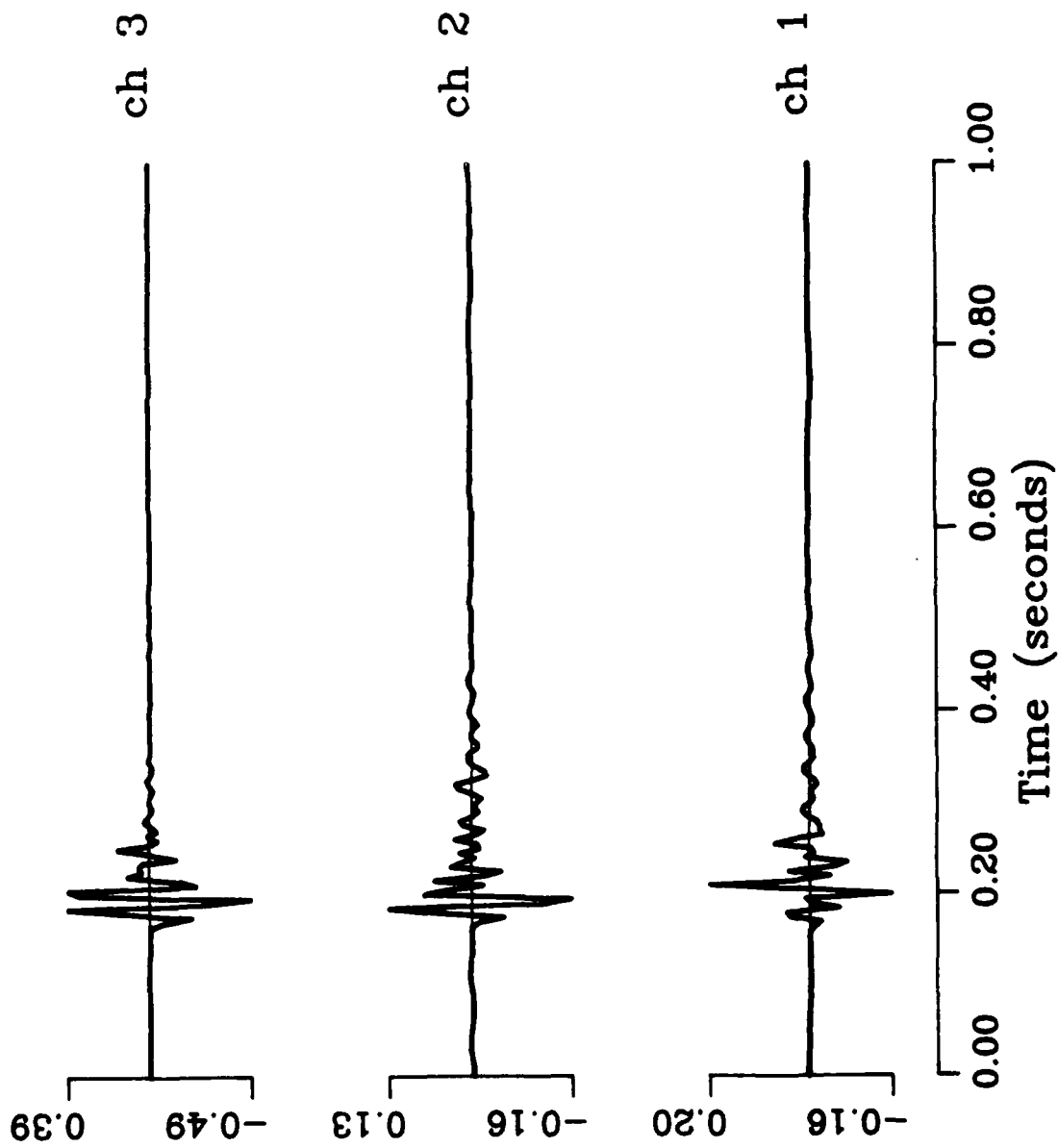




Figure 27. Floor Shot SP9 station 2  
Velocity (cm/s)



**Figure 28.** Floor Shot SP9 station 3  
Velocity (cm/s)

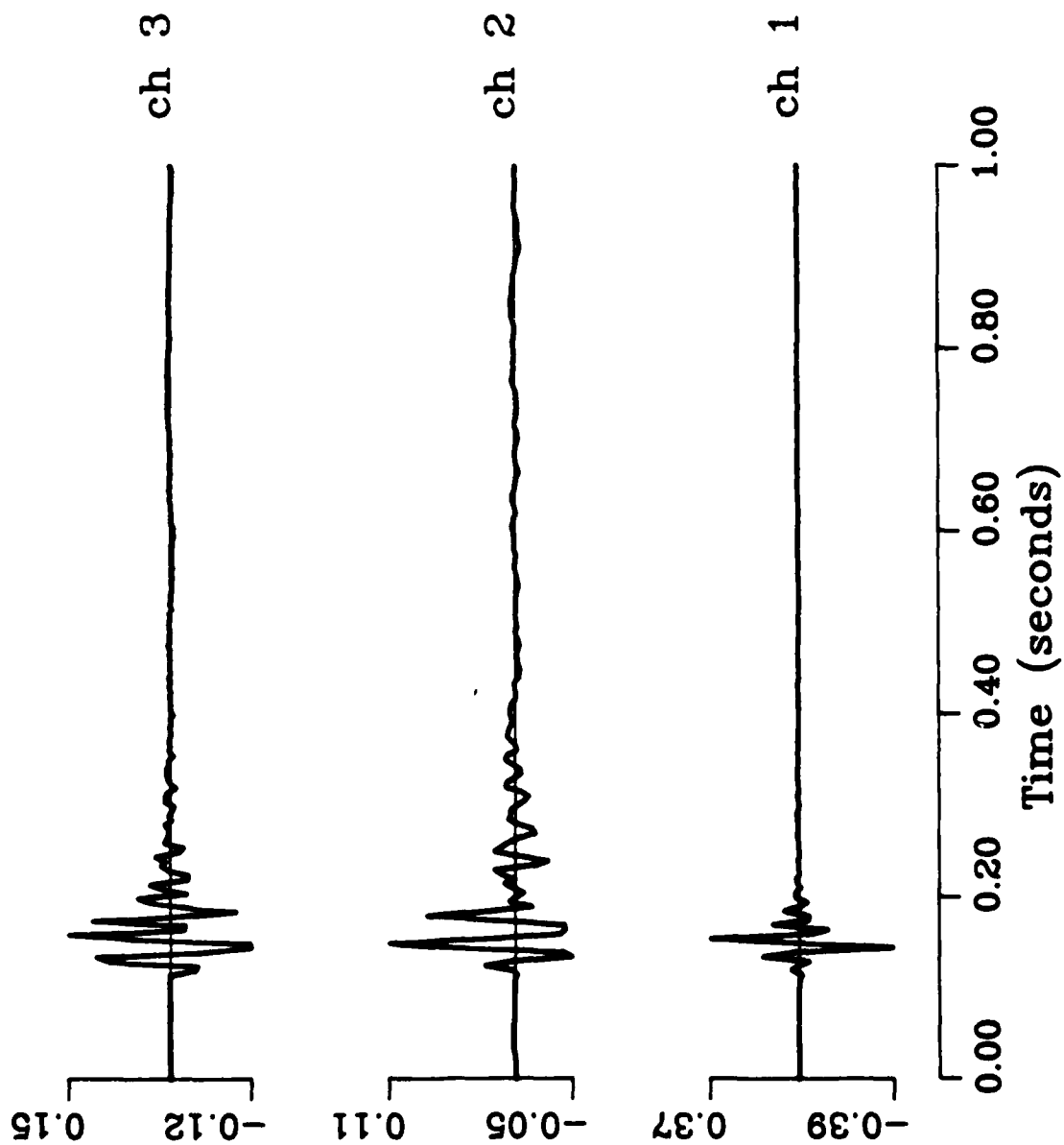


Figure 29. Floor Shot SPA4 station 1  
Velocity (cm/s)

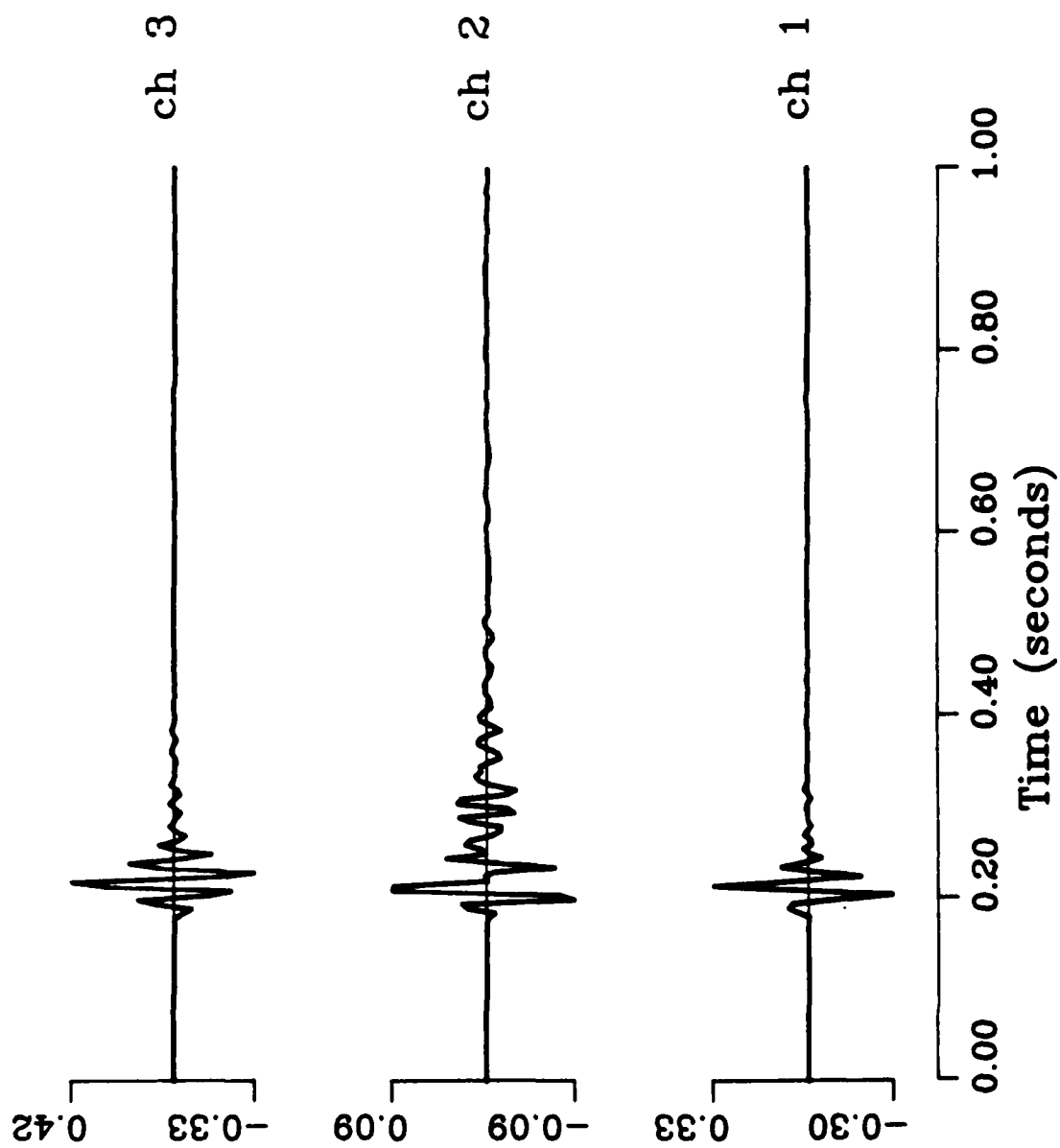


Figure 30. Floor Shot SPA4 station 2  
Velocity (cm/s)

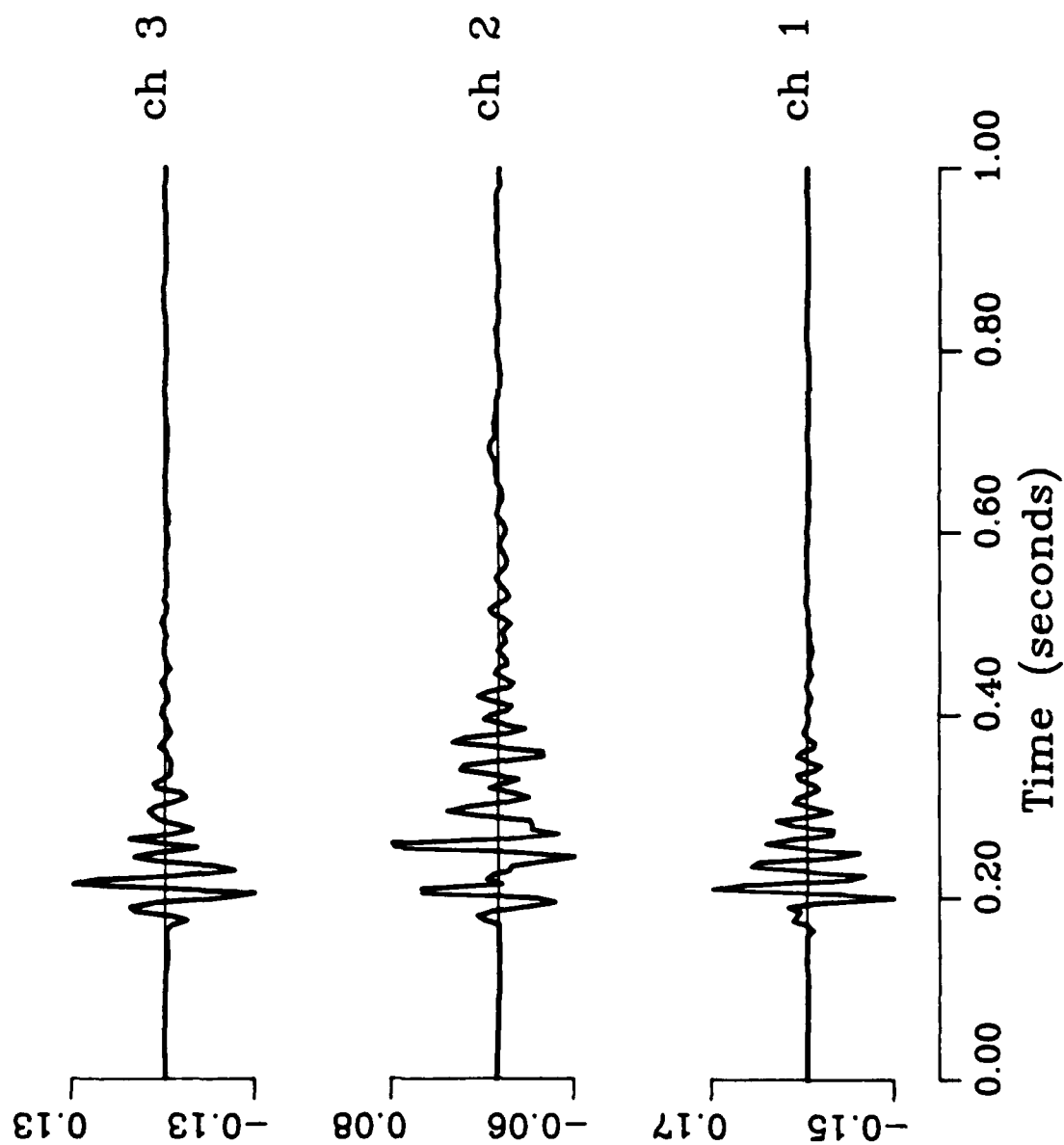


Figure 31. Floor Shot SPA4 station 3  
Velocity (cm/s)

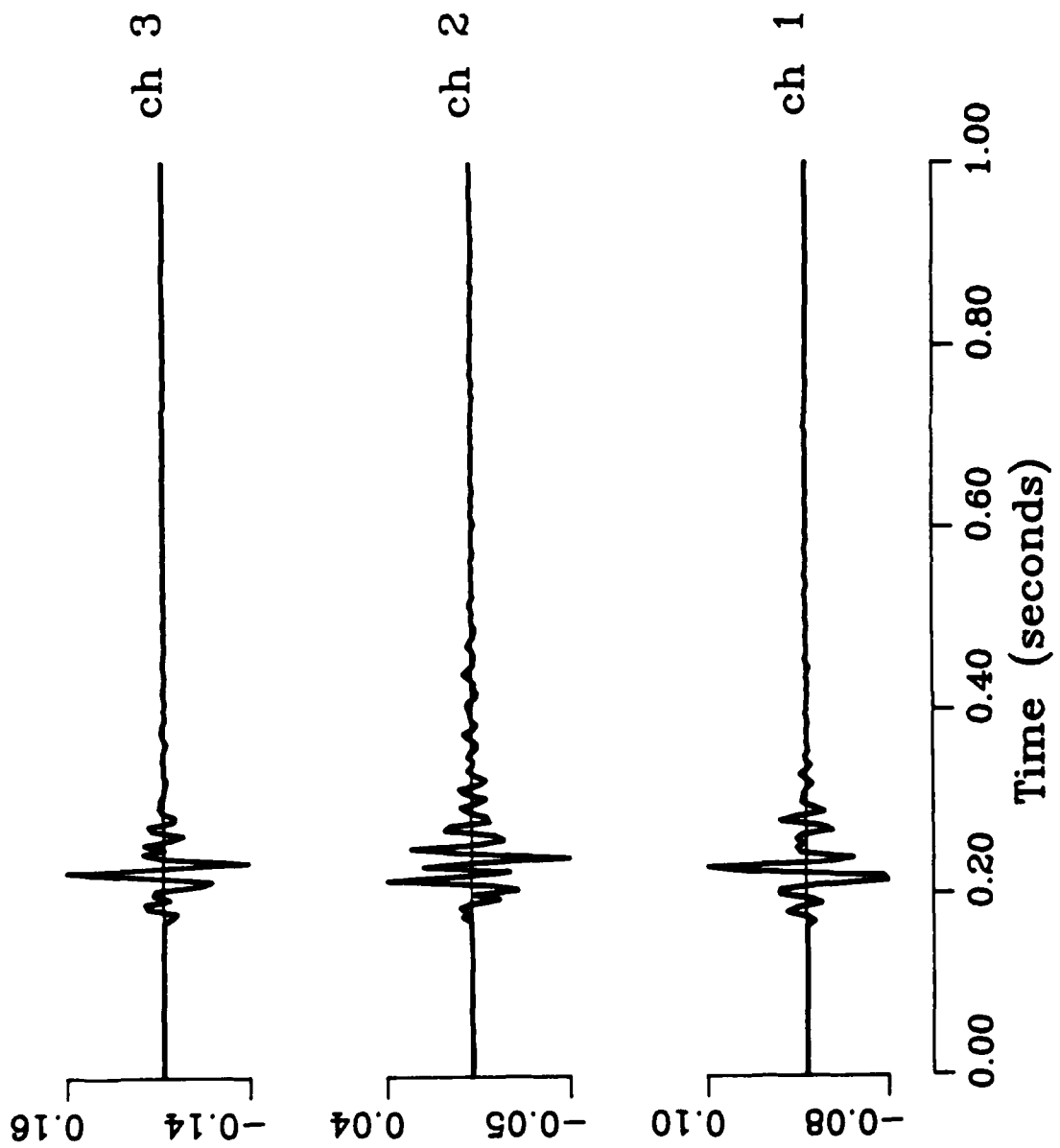


Figure 32. Floor Shot SPE4 station 1  
Velocity (cm/s)

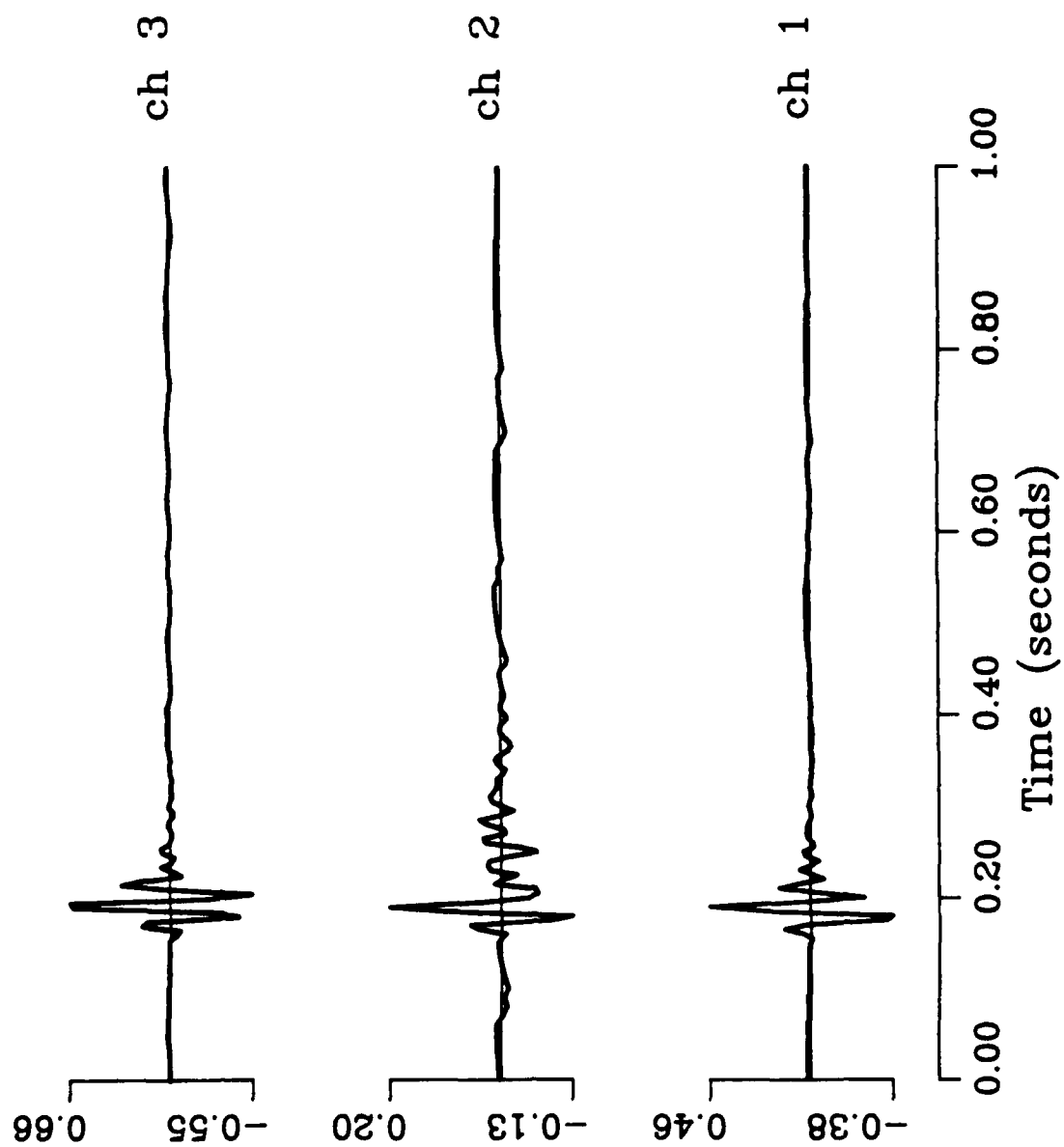


Figure 33. Floor Shot SPE4 station 2  
Velocity (cm/s)

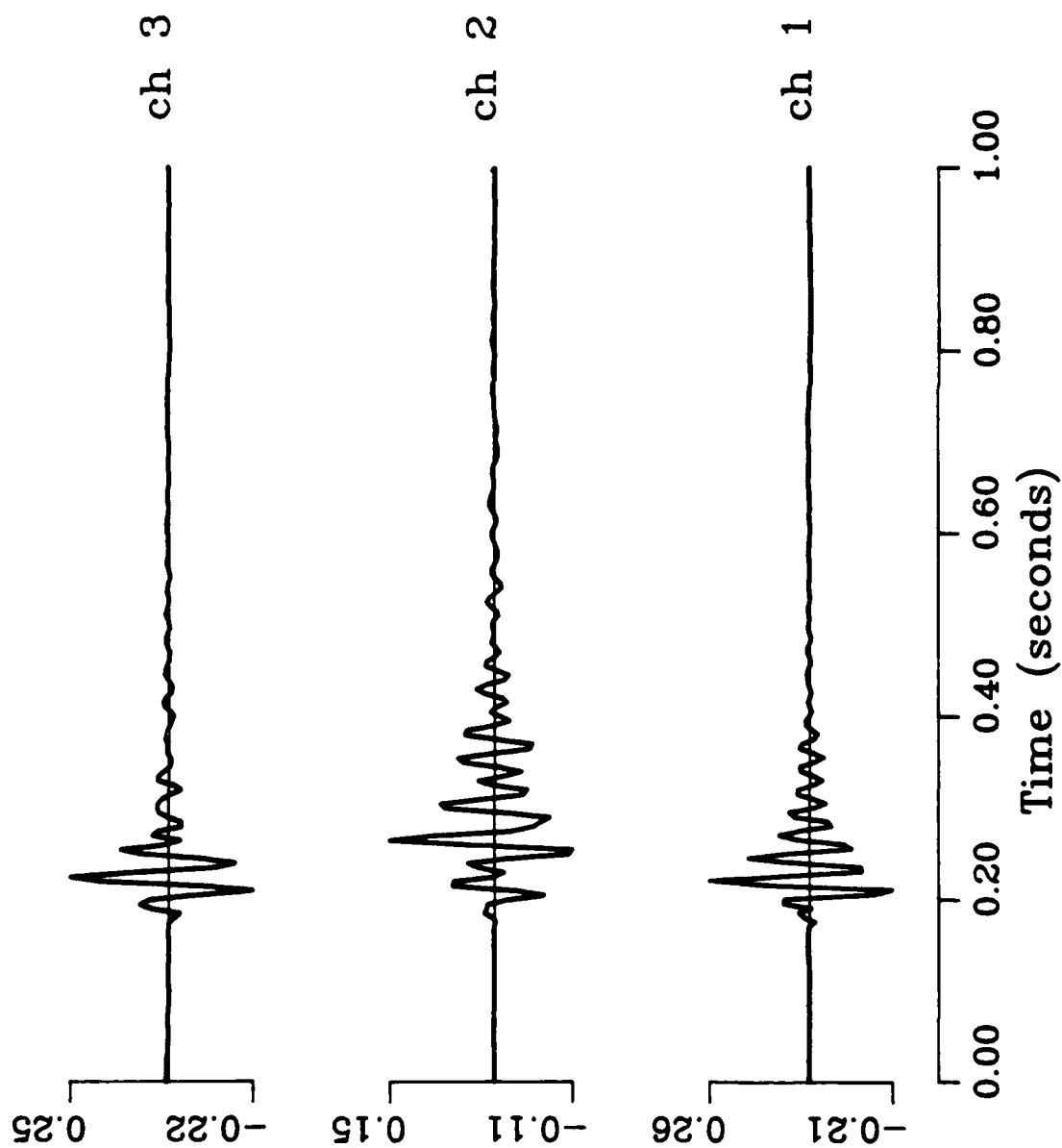
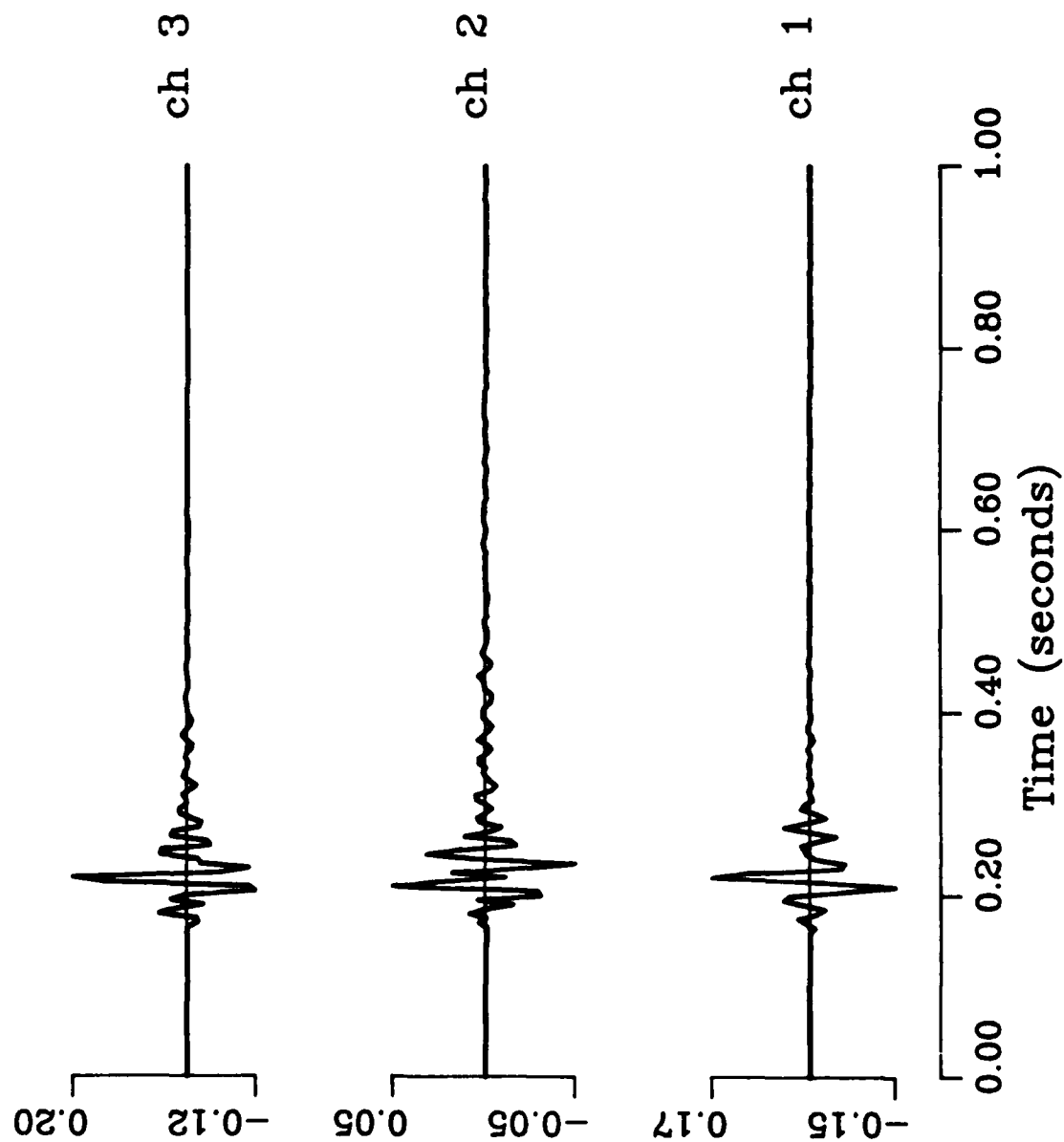


Figure 34. Floor Shot SPE4 station 3  
Velocity (cm/s)





## PRELIMINARY DATA ANALYSIS

### Noise Estimates

Pre-explosion noise samples are taken from the raw acceleration time series, Fourier transformed, and compared to acceleration spectra to provide estimates of data bandwidth. For the single shot data, the noise estimates place a lower frequency band ranging from 3-10 Hz. For the production shot, the signal-to-noise ratio remains high to below 1 Hz. Upper frequency limitations occur for the 200 sample per second data due to the antialias filter at 70 Hz. Some samples of noise and signal spectral estimates are shown in Figures 35-38.

### Time Series Comparisons

Shot-receiver distances between stations 2 and 3 of the two single shots (SPE4 and SPA4) and stations 3 and 4 of the multiple shot are similar (Table 1) and allow a comparison among the velocity time series as presented in Figures 39-44. Velocity waveforms are remarkably similar for the two single shots in both wave shape and total duration. Zero to peak amplitudes for shot E4 exceed shot A4 but by a factor of two or less for all components (Figures 39-41) except for the transverse component at station 3, where the amplitudes are nearly equal (Figure 43). Production shot time series duration exceeds the single shots by factors of two to three. Peak vertical velocity amplitudes of the production shot exceed the single shot amplitudes by factors of 1.4 to 3.7 (Figures 39 and 42). This is contrasted by over two orders of magnitude difference in total explosive charge between the production and single shots. Amplitude comparisons among the other components of the multiple and single shots, however, are not very meaningful since orientation of the multiple

Floor Shot SP3  
Acceleration Spectra

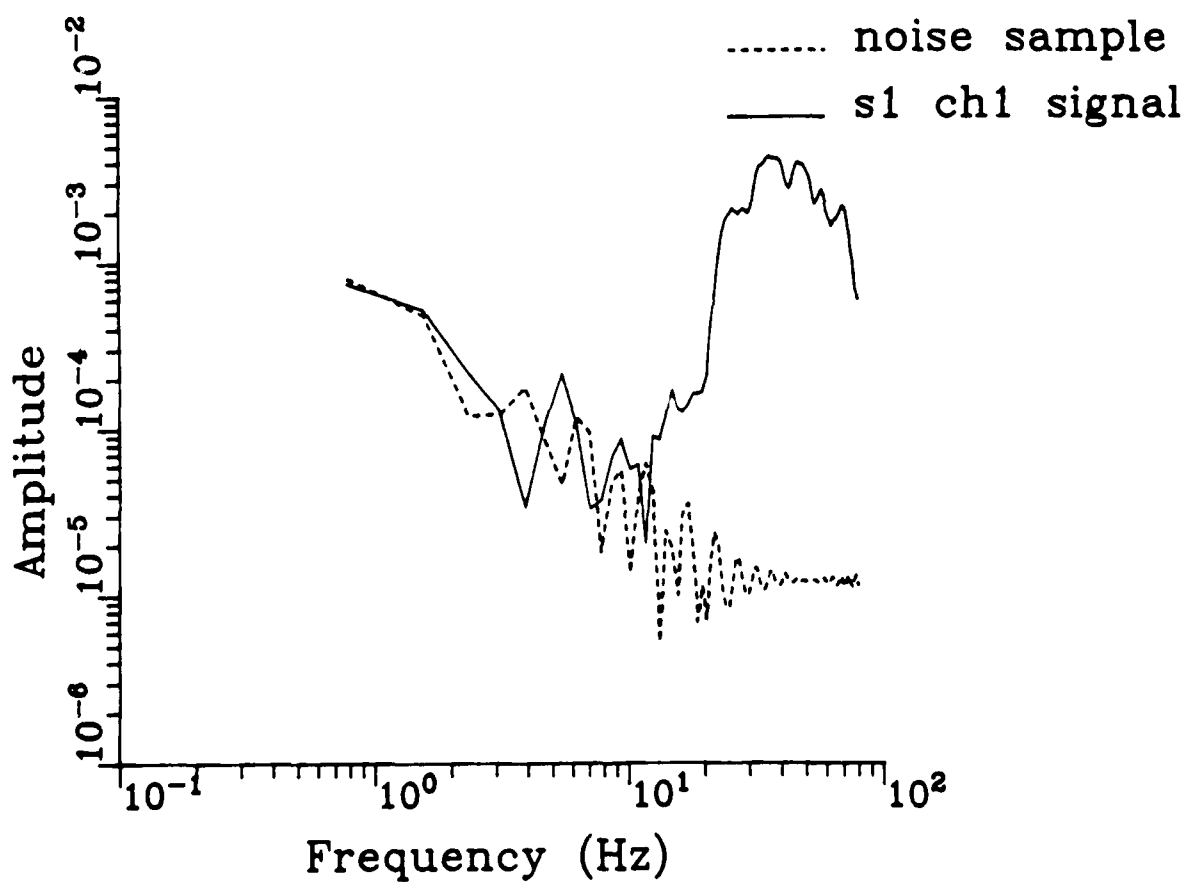
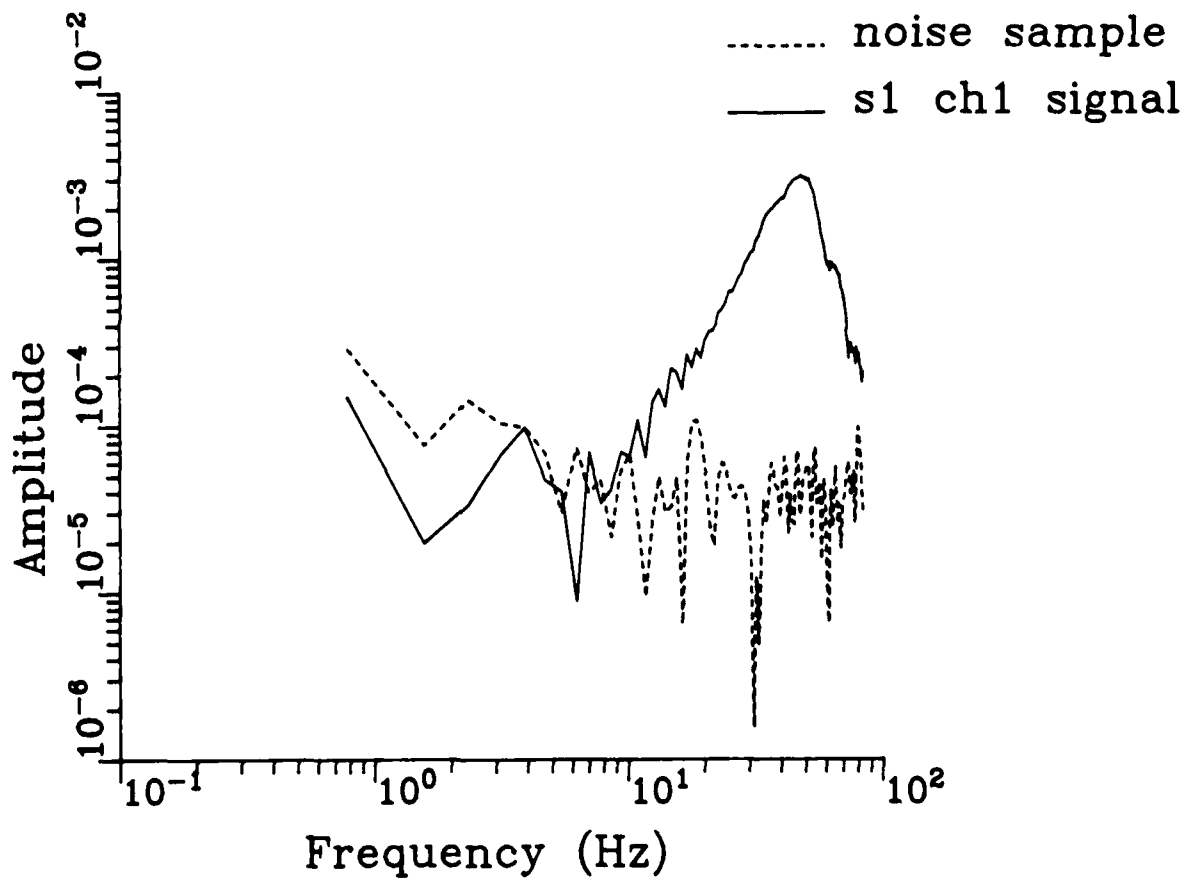


Figure 35. Noise estimate for floor shot SP3, station 1, vertical channel. Noise estimates are padded out to the same length (512 time samples) as the whole waveform spectral estimates. Vertical scale is gal-seconds (g-s).

Floor Shot E4  
Acceleration Spectra



**Figure 36.** Noise estimate for floor shot SPE4, station 1, vertical channel. Noise estimates are padded out to the same length (512 time samples) as the whole waveform spectral estimates. Vertical scale is gal-seconds (g-s).

Floor Shot A4  
Acceleration Spectra

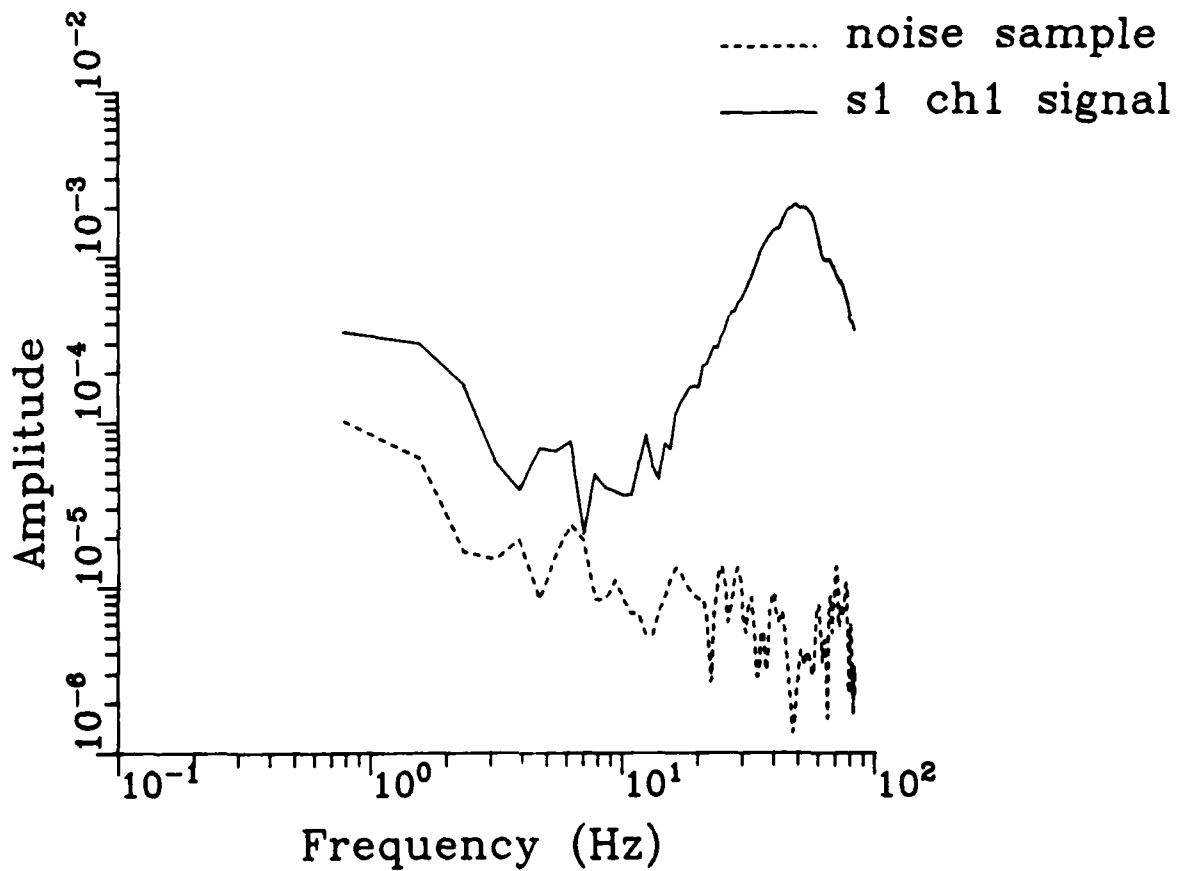
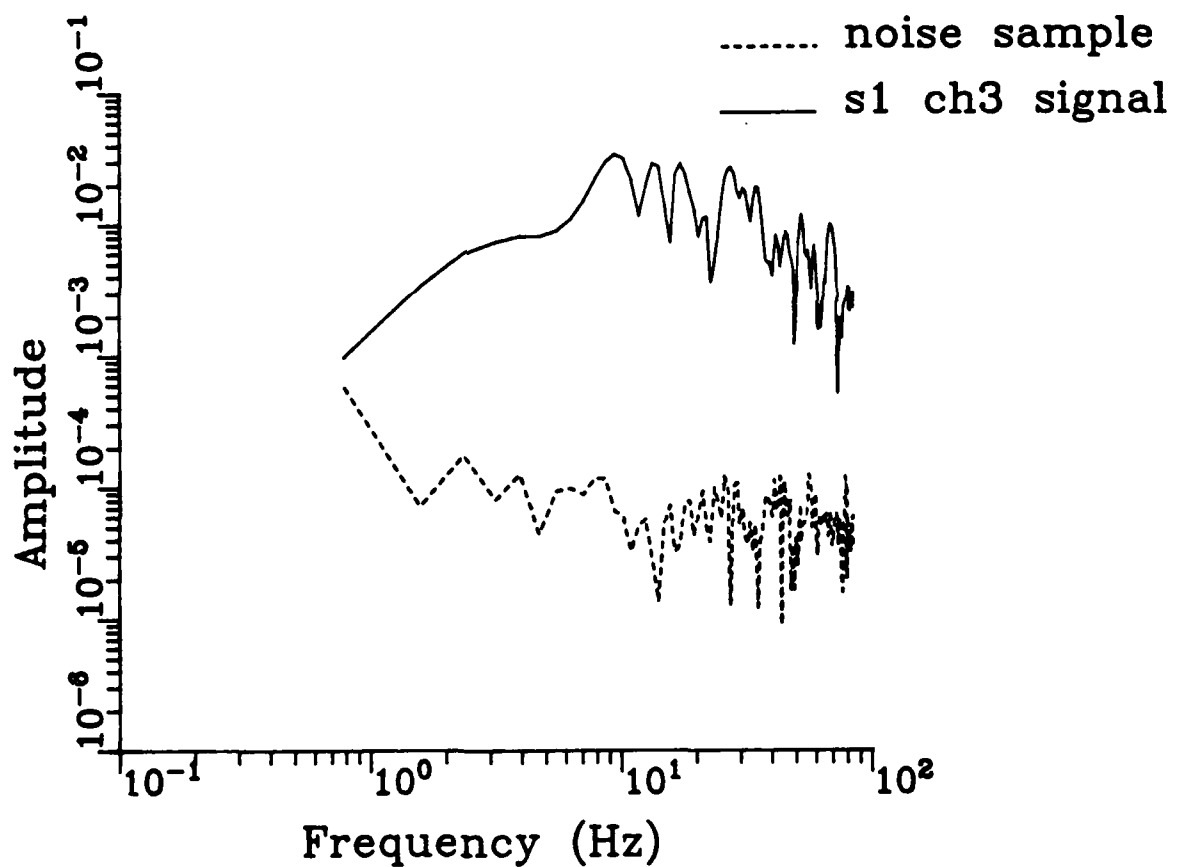


Figure 37. Noise estimate for floor shot SPA4, station 1, vertical channel. Noise estimates are padded out to the same length (512 time samples) as the whole waveform spectral estimates. Vertical scale is gal-seconds (g-s).

# Bench Shot Acceleration Spectra



**Figure 38.** Noise estimate for bench shot, station 1, channel 3. Noise estimates are padded out to the same length (512 time samples) as the whole waveform spectral estimates. Vertical scale is gal-seconds (g-s).

shots relative to receiver locations cannot be converted to a true radial or transverse motion due to the finite spatial effects of the multiple shot array.

Time series comparisons are supplemented by a comparison of velocity spectra (Figures 45-50) with a vertical scale in  $\text{cm-s}^2$ . Single shot spectra are relatively simple at stations 2 and 3, exhibiting little spectral scalloping and in the 3-70 Hz bandwidth for all but the transverse and radial components of station 2 (Figures 46 and 47). Corner frequencies for the velocity spectra are picked at the point where the velocity amplitudes peak. This parameter is inversely proportional to the "characteristic time" which is a measure of the cavity radius (Mueller and Murphy, 1971). The two single-shot explosive types exhibit nearly identical corner frequencies, differing by 2 Hz or less at all comparable distances. At station 2, the vertical channel (Figure 45) exhibits higher corner frequency (42 Hz) than the transverse (25 Hz) (Figure 46) or radial (28 Hz) (Figure 47) components. This trend is repeated at station 3 (Figures 48-50) with the corner frequencies shifted slightly to lower frequencies: vertical component at 40 Hz, transverse at 23 Hz and radial at 27 Hz. Single shot spectra compare favorably with each other in spectral shape and amplitude with emulsion signals exhibiting slightly higher spectral amplitudes than ANFO signals, correlating with the slightly higher explosive yield of the emulsion events.

Multiple shot velocity spectra exhibit the characteristic spectral scalloping effects due to multiple between-hole and between-row delays among individual shots. Corner frequencies of this multiple shot spectra are much harder to pick accurately due to the multiple shot interference phenomena. However, the corners are significantly lower, in the range of 15-18 Hz, than the single shot spectral corners. Production shot spectra are also flatter out to higher frequencies than the single shot spectra. For example, the high frequency decay of the radial component of the multiple shot spectrum at station 3 begins to decay at 60 Hz, while the radial

Figure 39

Single and Multiple Shot Comparison

Channel 1 Velocity (cm/s)

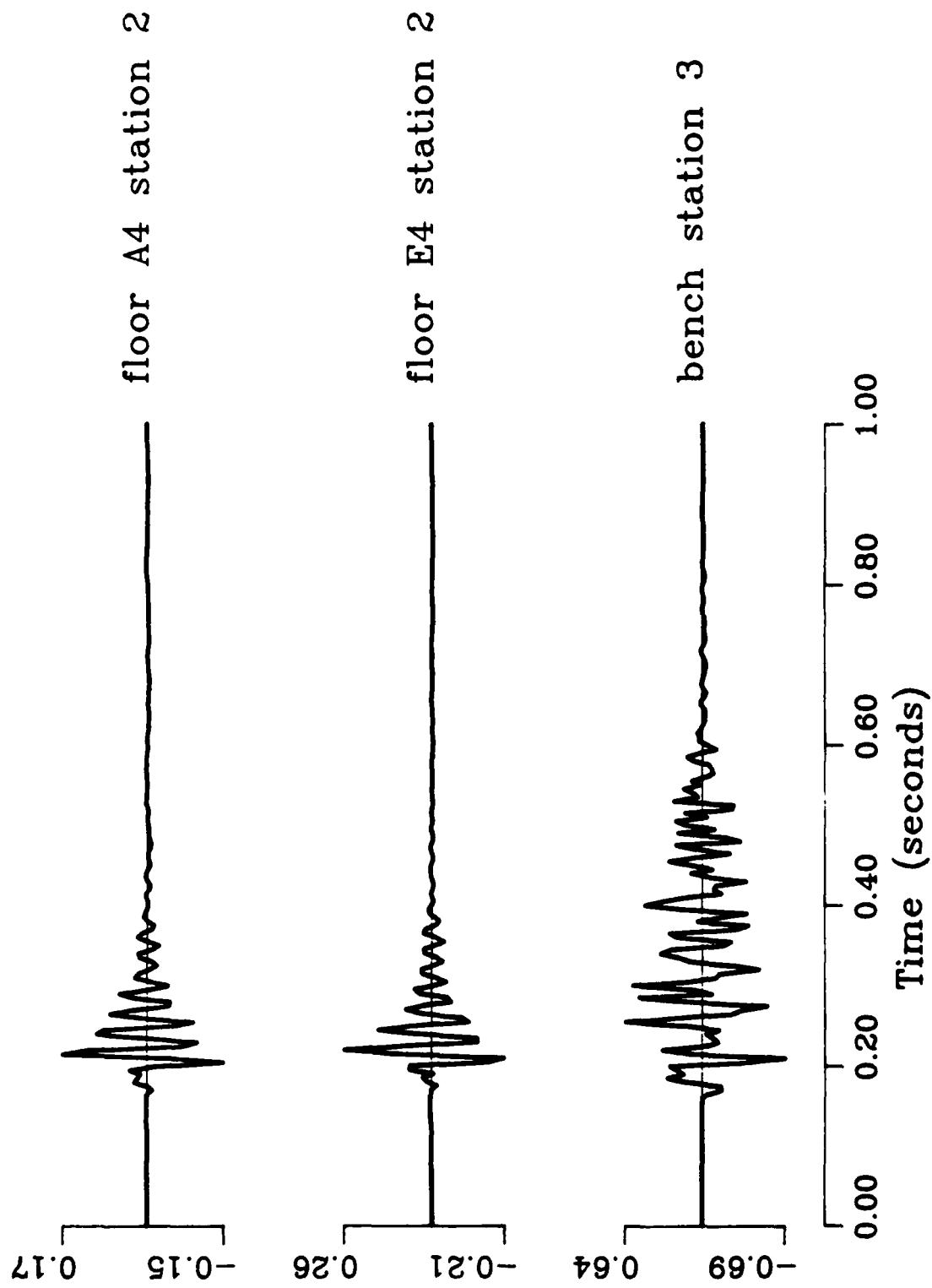


Figure 40

Single and Multiple Shot Comparison  
Channel 2 Velocity (cm/s)

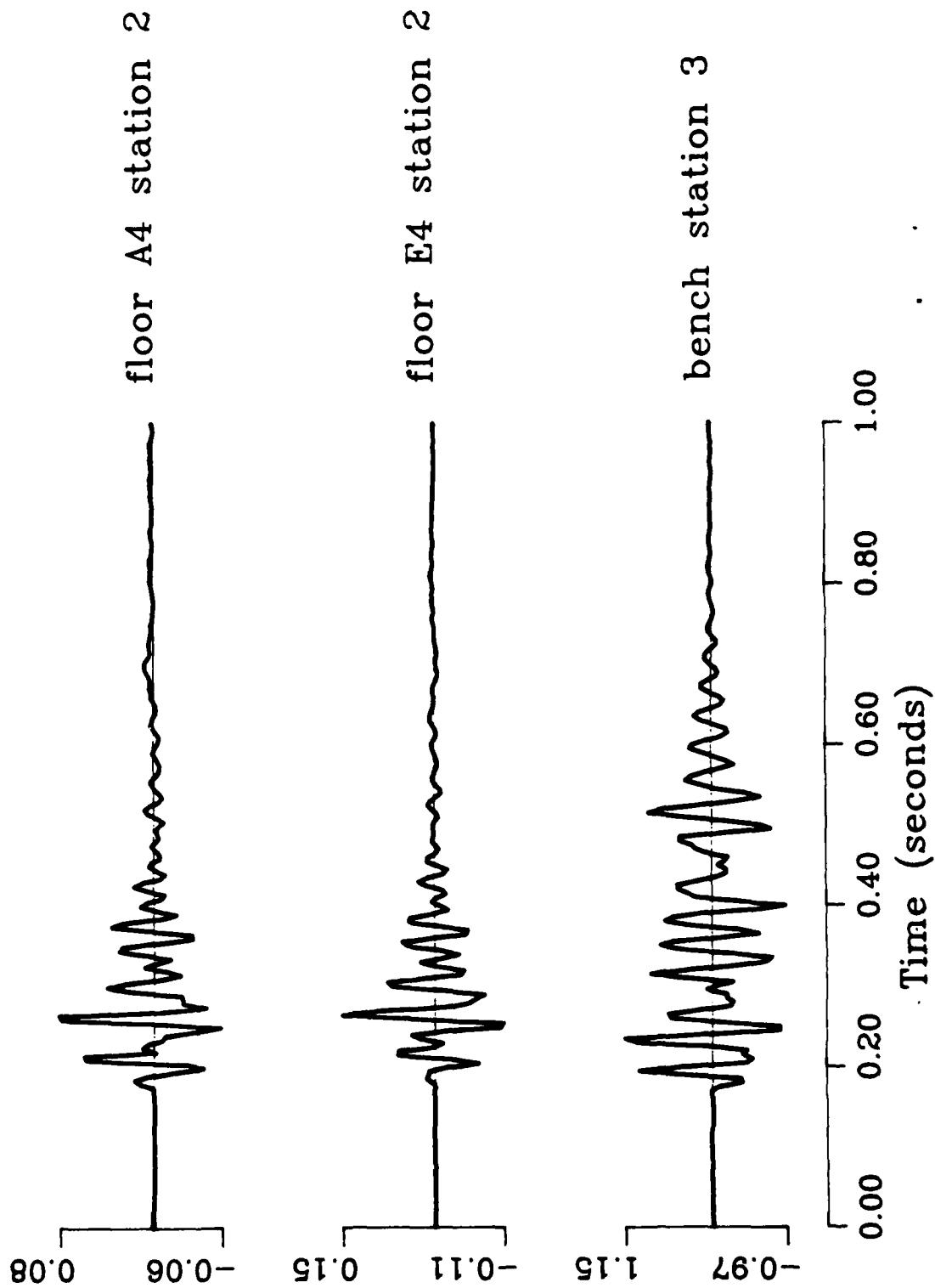




Figure 41

Single and Multiple Shot Comparison  
Channel 3 Velocity (cm/s)

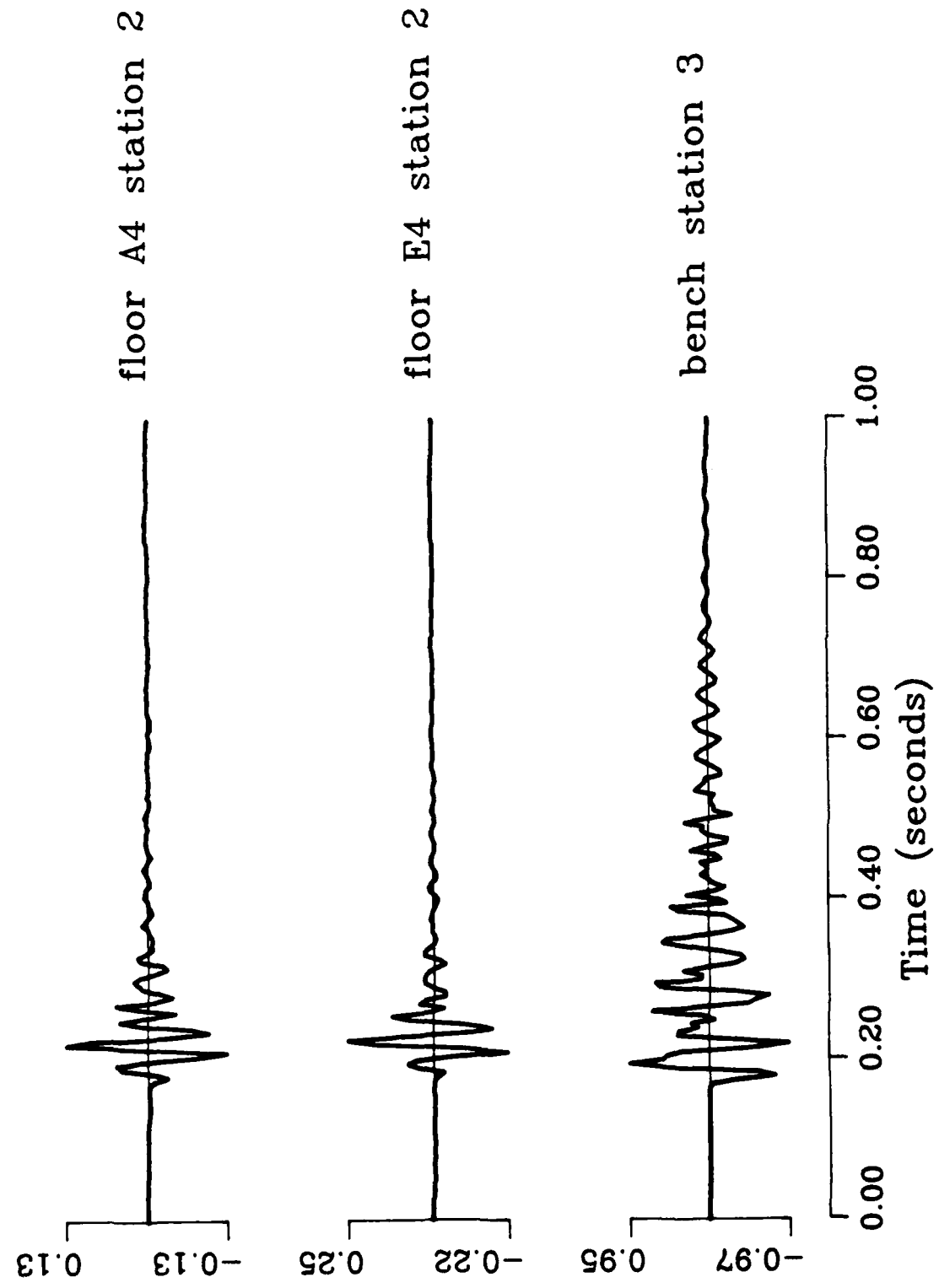


Figure 42

Single and Multiple Shot Comparison  
Channel 1 Velocity (cm/s)

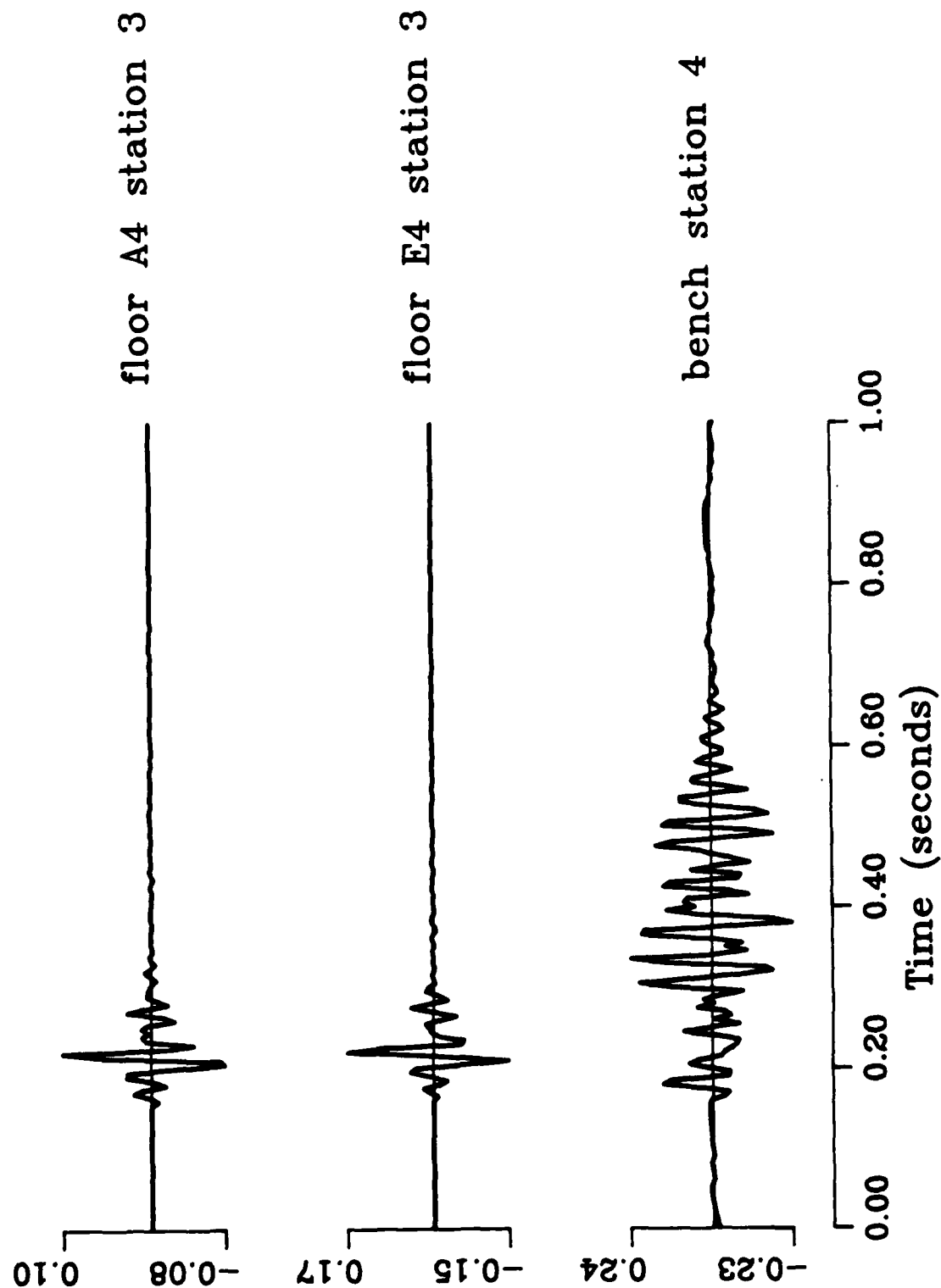


Figure 43

Single and Multiple Shot Comparison  
Channel 2 Velocity (cm/s)

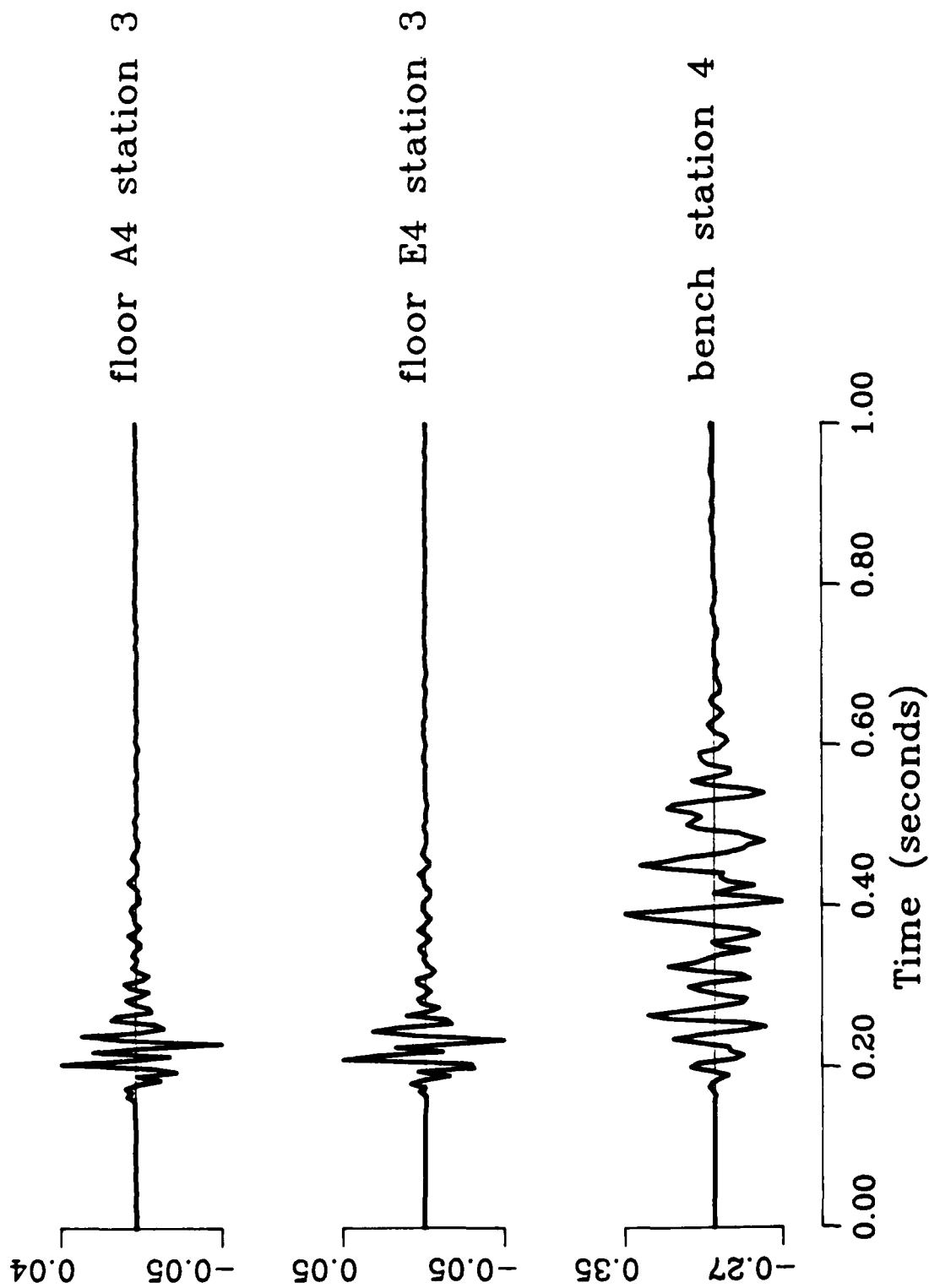


Figure 44

Single and Multiple Shot Comparison

Channel 3 Velocity (cm/s)

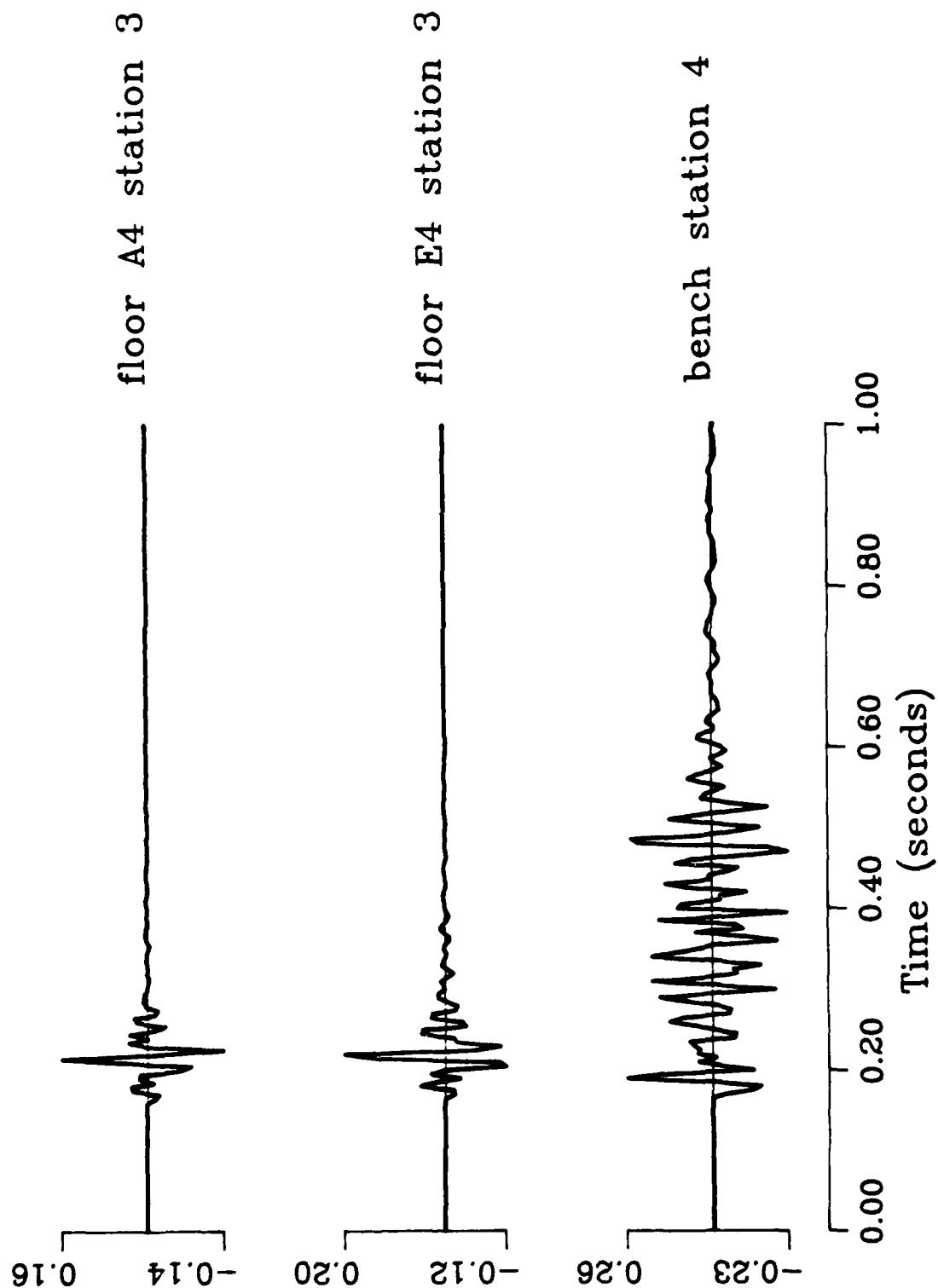


Figure 45

Single and Multiple Shot Comparison

Velocity Spectra (channel 1)

- floor A4 station 2
- floor E4 station 2
- bench station 3

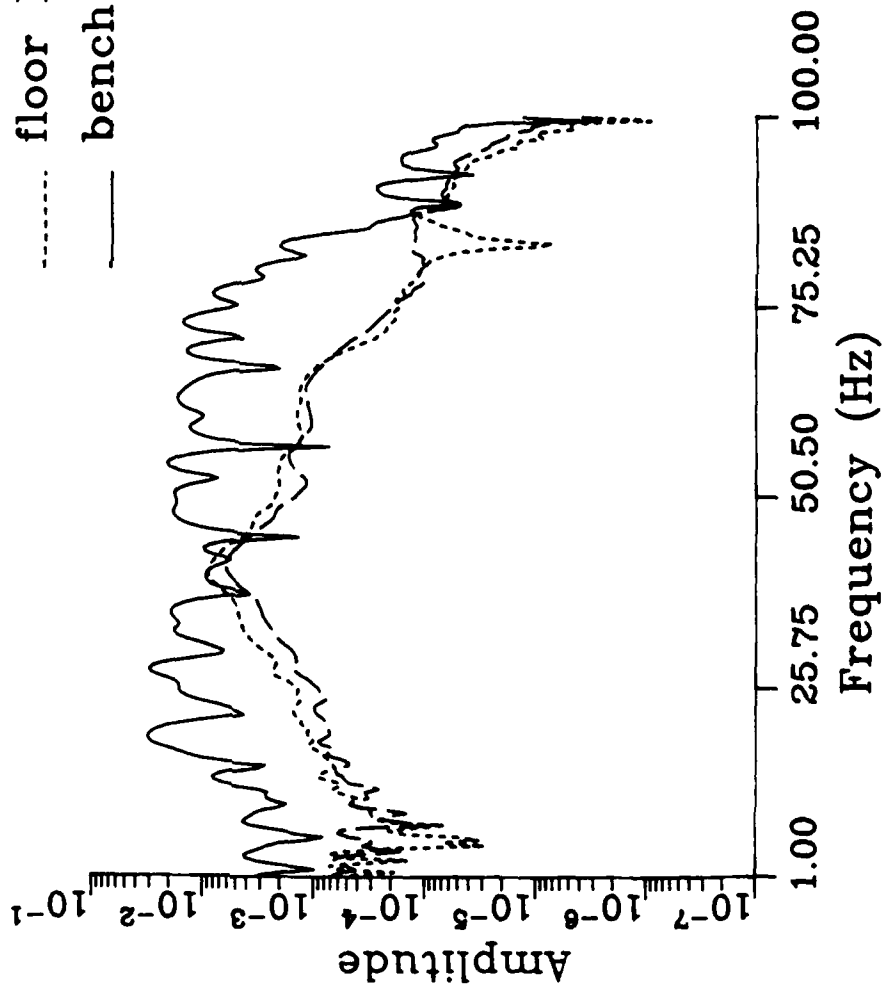


Figure 46

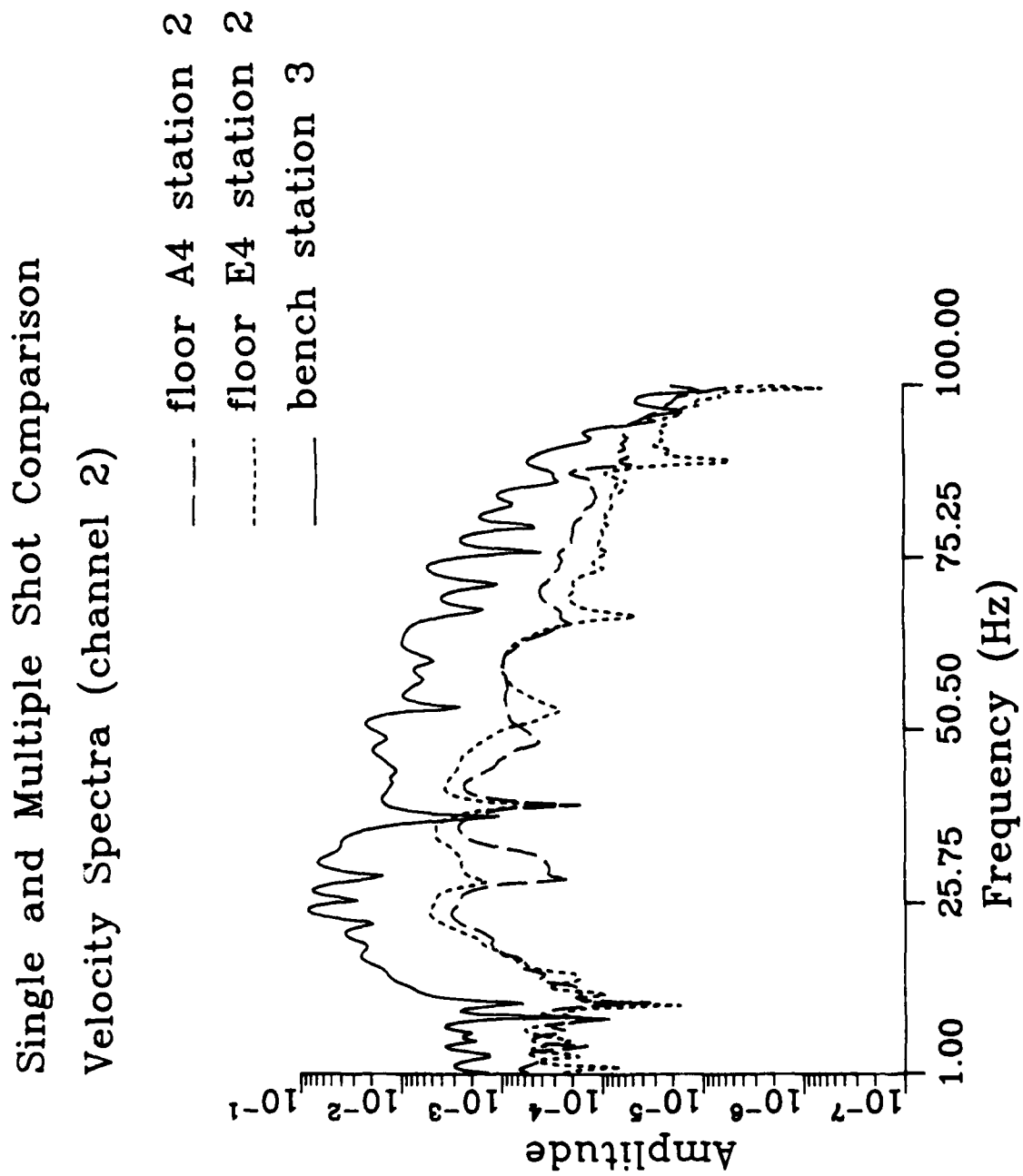


Figure 47

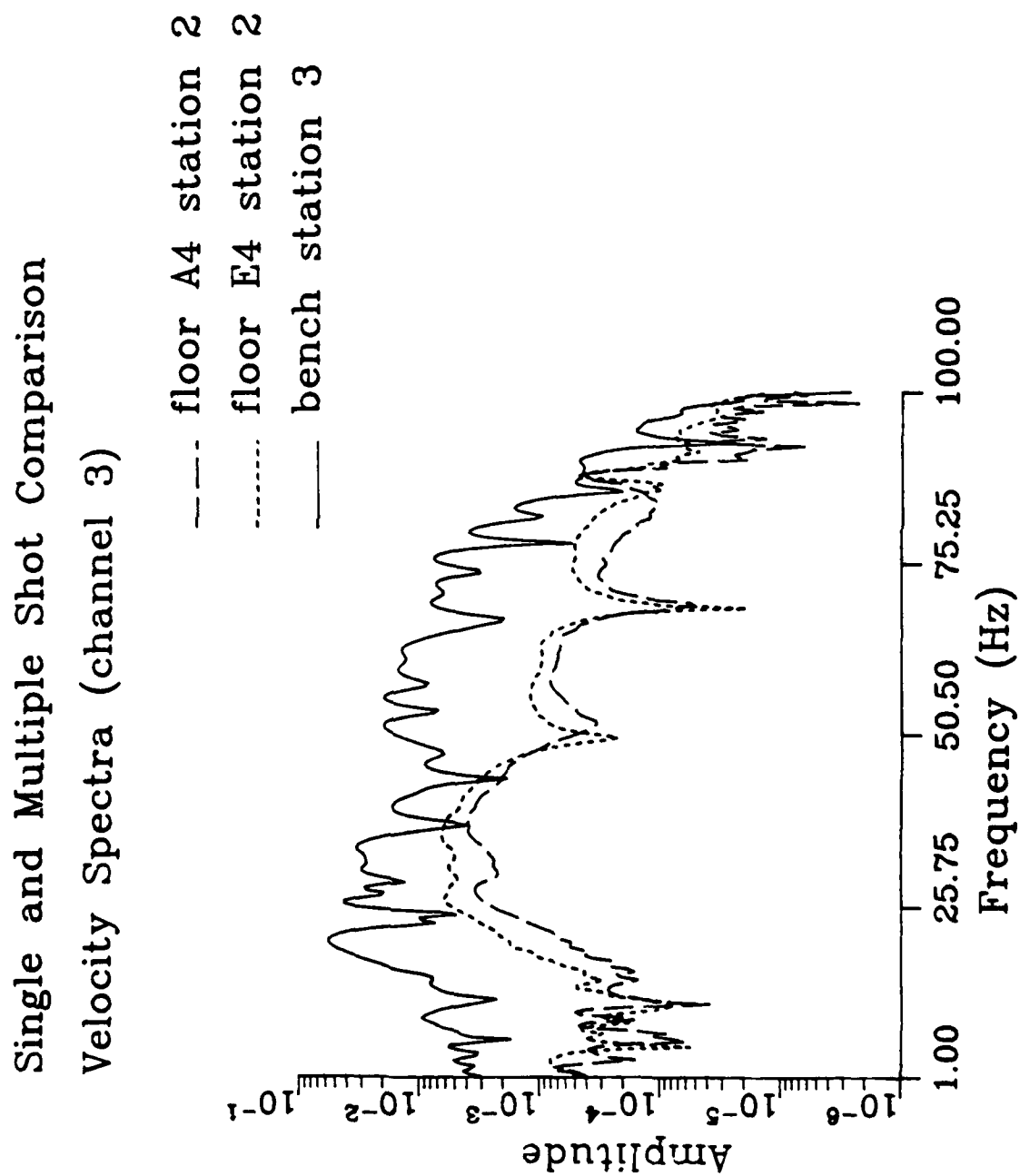


Figure 48

Single and Multiple Shot Comparison

Velocity Spectra (channel 1)

- floor A4 station 3
- floor E4 station 3
- bench station 4

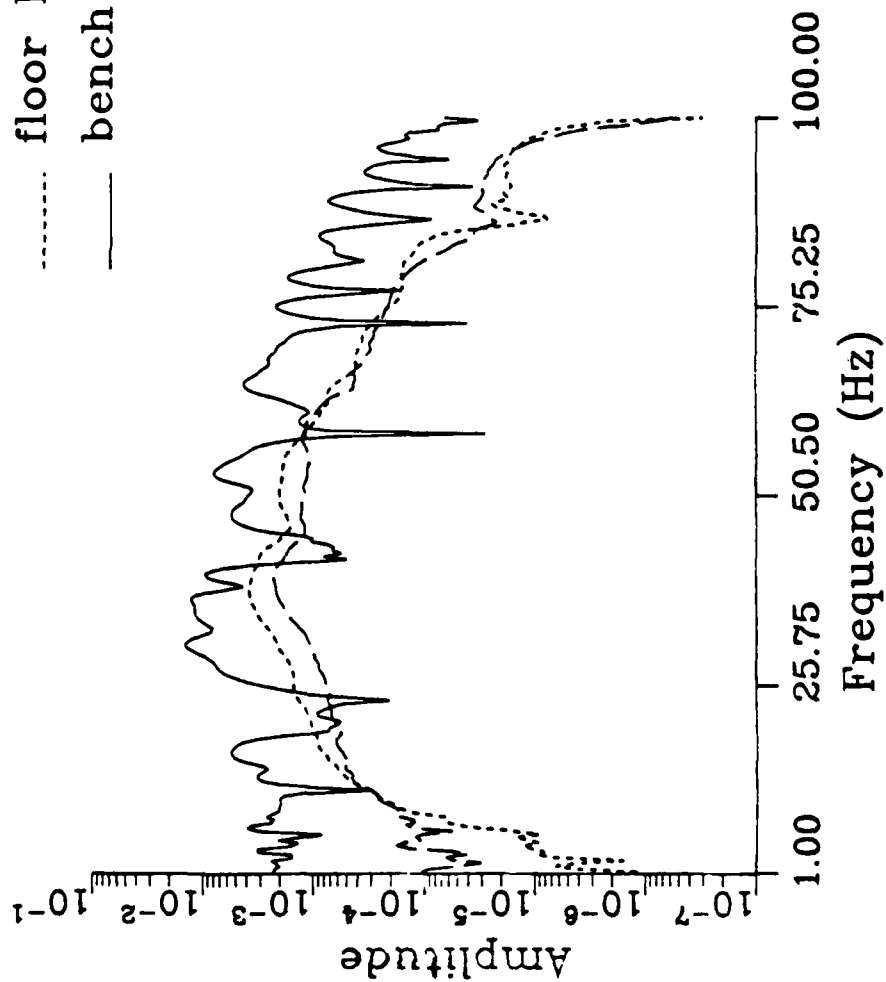




Figure 49

Single and Multiple Shot Comparison

Velocity Spectra (channel 2)

- floor A4 station 3
- floor E4 station 3
- bench station 4

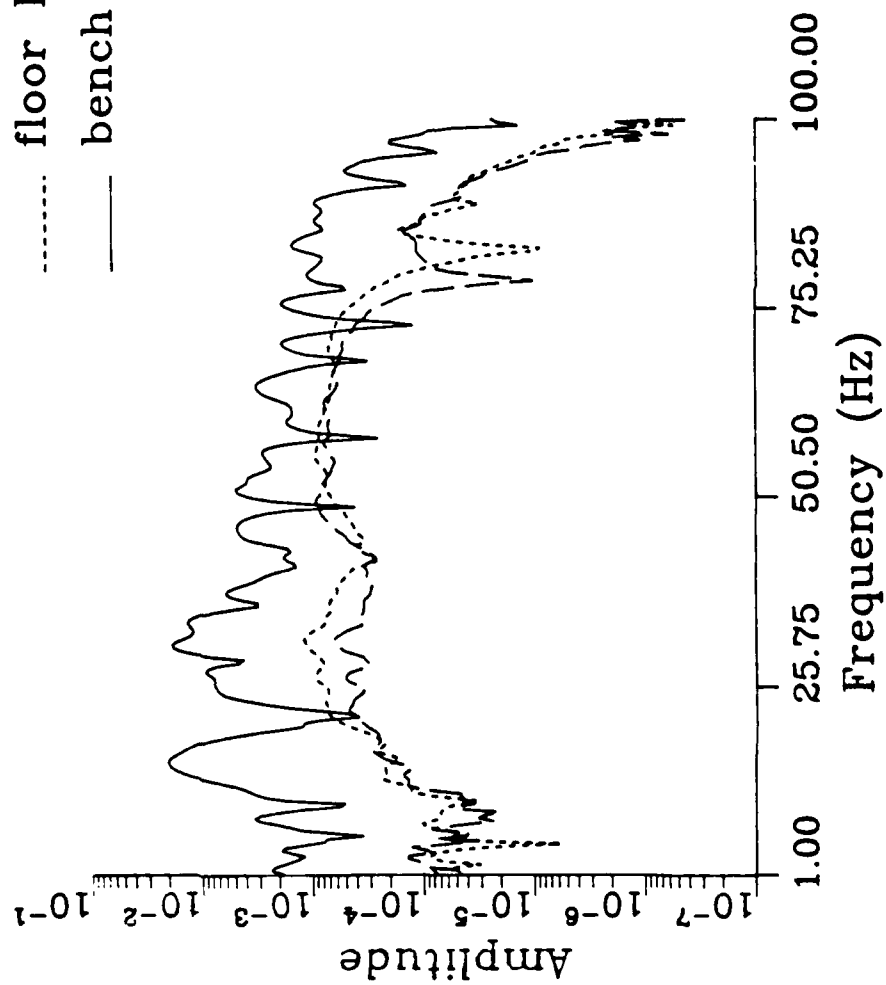
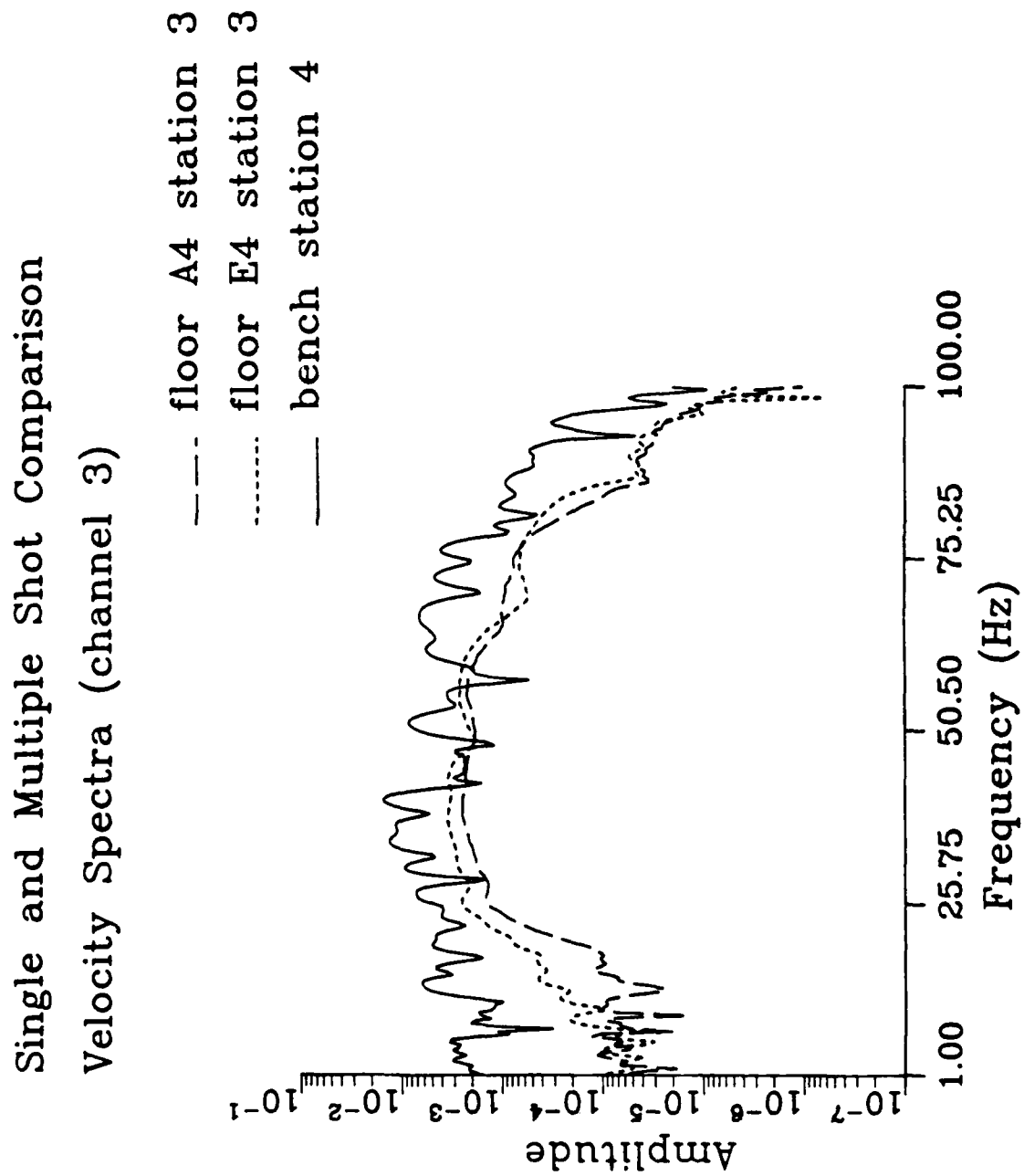


Figure 50



components of the single shot spectra at station 2 begin to roll off at about 40 Hz (Figure 47). Average spectral amplitudes of the production shot represent close to an order of magnitude increase over single shot peak amplitudes as seen in the station2/station 3 transverse component (Figure 46) and decreasing to a factor of three difference for station 3/station 4 vertical and radial components (Figures 48 and 50). Single shot peak spectral amplitudes approach multiple shot spectral amplitudes at some frequencies as shown in the station 2/ station 3 vertical channel spectral comparison (Figure 45).

### Range Effects

Zero to peak amplitudes versus scaled range ( $m/kt^{1/3}$ ) for the single shots for all three channels (Figure 51) exhibit amplitude decay rates varying from -1.3 for the vertical records to -0.7 for the radial records. Considerable scatter in the peak amplitude plots is noted with correlation values for the linear fits ranging from 0.2 (radial) to 0.7 (transverse and vertical). An order of magnitude maximum scatter for the vertical and radial components and slightly less than an order of magnitude for the transverse component suggests that radial peak amplitudes are the least consistent with regards to a linear decay with range. The vertical and transverse peak amplitudes show more consistency with range except for a noticeable outlier in vertical amplitudes at a scaled range close to 200  $m/kt^{1/3}$ . Amplitude decay with range values agree closely between vertical and transverse components and are twice as high as the decay value for the radial component.

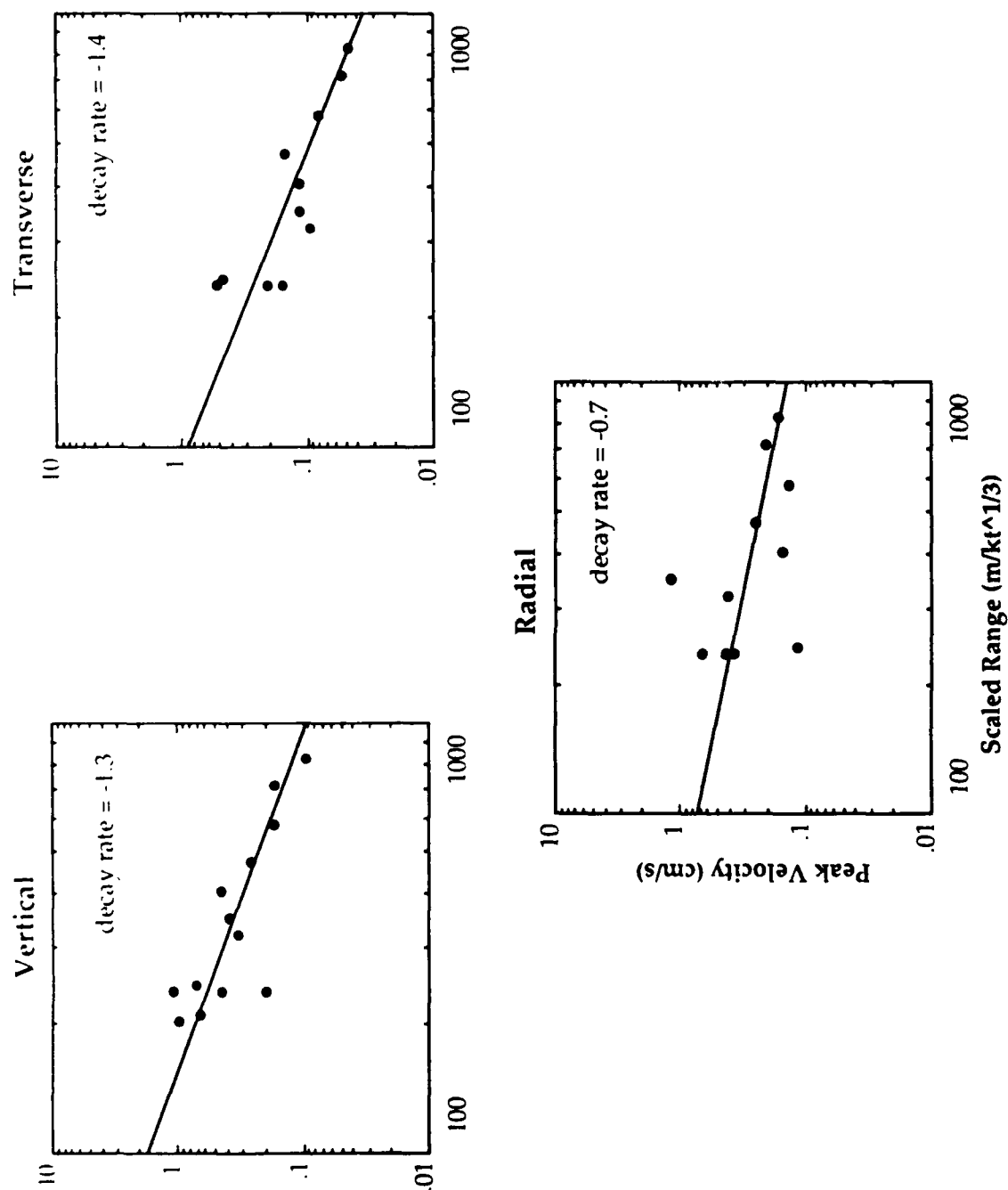


**Figure 51.** Zero to peak velocity amplitudes for all single shot time series plotted as a function of scaled range. Velocity amplitudes are in cm/s.

## CONCLUSIONS

Preliminary analysis of the Pomona quarry seismic data characterizes both the single and multiple shot sources. The main results are summarized below:

- (1) Data bandwidth for the single for the single shot data sampled at 200 samples per second indicate reasonable signal to noise ratios between 3-70 Hz. Production shot bandwidths extend to lower frequencies ( $< 1$  Hz).
- (2) The two different explosive types, ANFO and emulsion, represented in the single shot sources exhibit very similar velocity waveforms and spectral shapes. The higher peak velocity and spectral amplitudes from the emulsion sources may reflect the slightly higher explosive charge rather than any difference in coupling between the two source types.
- (3) Temporal finiteness effects are manifested by the over two orders of magnitude increase in explosive charge between the multiple and single shots which contrasts with only a factor of five maximum peak amplitude increase observed when comparing the single and multiple shot seismograms. The constructive and destructive interference of the multiple shot array may account for this discrepancy. Additionally, total shot duration of the multiple shot array is represented by a threefold increase in the time series length over the single shots.
- (4) Multiple shot delay times show up to a 20% variance from the planned delay times. The modulated Fourier amplitude spectrum with a

regular interference pattern characteristic of multiple delay seismic data is consequently disrupted. Instead, irregular spectral scalloping is observed due to the constructive and destructive interference of the multiple delay shots which is randomized by the delay time variance.

- (5) Spectral scalloping corresponding to the time delays of the multiple shot arrays obscures the low frequency spectral corner; however, it is clear that the corner frequency is shifted to much lower frequencies than the single shot corners. This corner frequency shift may reflect the larger single shot explosive charge of the multiple shot array. However, this shifting may also include spatial finiteness effects due to the extended geometry of the multiple shot array.
- (6) Single shot corner frequencies compare within 2 Hz for the two different explosive types. Corner frequencies with range are shifted to slightly lower frequencies for the single shot data, with vertical component corners approximately 1.5 times larger than radial or transverse component corners regardless of range.
- (7) Single shot peak velocity amplitudes decay with rates much larger than can be accounted for by simple geometrical spreading rates. The large amount of scatter in the cube-root-yield, scaled range decay indicates that anelastic scattering or complex geologic structures may be responsible for the higher decay rates.

## ACKNOWLEDGEMENTS

The authors gratefully acknowledge the cooperation and support of Frank Chiappeta for his help with the data acquisition on this project.

# **MISTY ECHO**

## **THE SEISMIC SOURCE PHYSICS EXPERIMENT**

**Kenneth H. Olsen**  
ESS-3, Geophysics, MS-C335  
&  
**Connon R. Odom**  
J-8, Command, Control, & Communications, MS-P947  
Los Alamos National Laboratory  
Los Alamos, NM 87545

**Brian W. Stump**  
Department of Geological Sciences  
Southern Methodist University  
Dallas, TX 75275-0395

**Robert E. Reinke**  
AFWL/NTE  
Kirtland AFB, NM 87117-6008



## INTRODUCTION

Although it would seem to be a relatively straightforward problem, there is still much that is poorly understood about the generation of elastic waves by large underground explosions. In general, seismic signals produced by such explosions are considerably more complicated than what would be expected from a simple model, such as a pressure pulse applied to the interior of a spherical cavity in a homogeneous half space. Part of the complexity is related to the fact that large explosions are detonated in media which are heterogeneous in terms of both physical properties and pre-existing stress and there is dynamic interaction between the explosion and these heterogeneities, including the free surface of the earth. Also contributing to the complexity is that the source is not a simple pulse applied at an idealized (spherical) boundary at a distance where all motions are in the linear or 'true' elastic realm, but rather consists of a small volume where temperatures and forces are very great and initial mechanical response is governed by non-linear hydrodynamic and strong shock wave phenomena. The shocks propagate outward, evolving through a non-linear plastic regime where the physical and mechanical properties of the medium are poorly known and are difficult to study by both theoretical and laboratory techniques.

The MISTY ECHO experiment is the latest in a long-term program by the authors designed to obtain a better basic understanding of the explosion source process. Several previous nuclear shots at Pahute Mesa and Yucca Flats, kiloton-size high-explosive surface and suspended bursts at White Sands Missile Range (WSMR), and small underground scaled HE array experiments are components of our long-range seismic source physics program; in MISTY ECHO the emphasis is on the study of the plastic-to-elastic transition in the free-field regime within Rainier Mesa.

## OBJECTIVES

The seismic source physics experiment (sometimes also known as the "ground motion" or "high-frequency seismic" experiment) on MISTY ECHO was designed to provide high-quality data on the fundamental physical processes which govern the evolution of a strong shock wave from close to the explosion into elastodynamic (seismic) waves which propagate out to regional and teleseismic (worldwide) ranges. The unique aspect of the MISTY ECHO experiment is the emphasis on triaxial measurements in the *free-field* away from the complicating effects of tunnel openings and walls, the mesa surface, and other major inhomogeneities due to engineering construction, etc., within the mesa. Free-field measurements over a wide azimuthal interval in these distance/acceleration/overpressure ranges have seldom been done on US nuclear events. In order to better understand the plastic-to-elastic transition we closely coordinate and compare our measurements with CORRTX and other very strong shock pressure, acceleration, and stress measurements (typically made by SLA experimenters) at ranges inside stemming. Simplistically, one might describe the tunnel part of the experiment as a study of the internal details of the Plastic-to-Elastic (nonlinear-to-linear) transfer function "box": CORRTX/SLA-shock data are the inputs and the ground surface seismic measurements are the outputs.

## JUSTIFICATION

Although our prime goal is improved understanding of basic physics, our results have obvious applications to nuclear test verification problems, to phenomenology and containment of underground explosions, and to DNA tunnel engineering and experiment planning technology.

## EXPERIMENT DESCRIPTION

The measurement array for MISTY ECHO consisted of two main components: (1) the free-field triaxial accelerometer array within the tunnel complex, with digital and analog recording in the DNA experimenter's recording alcove; and (2) an array of 13 portable, self-triggering digital data logging systems recording force-balance accelerometers or seismometers on the mesa surface above the shot.

### *In-tunnel instrumentation*

The location of free-field accelerometers at tunnel level (gauge numbers T1 - T8) are shown on the tunnel plan of Fig. 1 and as-built parameters are summarized in Table 1. The 4th column of Table 1 gives the nominal expected acceleration levels in g units which were used for estimating clipping levels, etc.. The strategy for siting the free-field gauges was to sample the wave field as uniformly as possible throughout the undisturbed geological material of Rainier Mesa. Therefore, relatively unobstructed paths were chosen so as to distribute sensors over as wide an interval of ranges and azimuths as was practical. The azimuthal interval covered by free-field observations is 70°.

Each ground motion station consisted of three Endevco 2262 accelerometers mounted in a tri-axial configuration on a phenolic block. The phenolic block was attached to an end cap glued to one end of a 20-inch-length of PVC pipe (3.5" ID). Gas-block potting compound was poured into the pipe to seal the accelerometers against moisture.

The key to successful free-field measurements in tunnel experiments is to grout-in the oriented accelerometer array in fresh boreholes at least 2-tunnel radii away from the walls. For MISTY ECHO, oriented gauges (X-axis positive toward the working point [WP], Z-axis up, and Y-axis pointing horizontally to the right looking toward the WP) were emplaced in vertical holes at least 20 feet (6 m) below the tunnel floor (= invert in the jargon) and these gave excellent data at all ranges. Gauges were secured with a rock-matching grout ("recipe HPNS2[cc]") appropriate to the density-acoustic velocity properties of the bedded tuff formation in this particular region of N-tunnel. Cables were run from gauge sites to the recording alcove; all except one of the eight signal cables were completely inside the gas seals defining "Containment Vessel - 2". The cable from gauge T7 passed through a gas seal plug at a Drift Protection Plug (DPP), and therefore was gas-blocked in the standard manner.

Excitation and signal conditioning for the accelerometers was provided by Ectron 776BA amplifiers located in the Instrumentation Alcove. The output of the Ectron amplifiers was digitized at 2681 frames per second by DES-0 12-bit digitizers. Battery-backed CMOS memory in the DES-0 units stored 2730 frames of data beginning at Zero Time. The DES-0's also transmitted the digitized data in a Bi-Phase L format via a fiber optic link to the Area 12 Recording Station (12-RS) outside the tunnel complex.

At 12-RS, the Bi-Phase L data stream was recorded on magnetic tape for backup purposes. Data decoding equipment in 12-RS stored 6370 samples from each channel (about 2.38 s after Zero Time). Hard-copy plots from the stored data were available on shot day.

### *Mesa-top surface array*

Thirteen three-channel digital event recorders with three-component accelerometers were deployed at the mesa surface as shown in Figure 2 and summarized in Table 2. The accelerometers were placed in 9" holes and then backfilled with native materials. The entire array was deployed 48 hours prior to the MISTY ECHO explosion.

Since each instrument is self-contained with signal conditioning, amplification, and triggering algorithms, they can operate unattended with no external power. This design also makes deployment a quick and simple task. Two types of data-logging devices were used: (1) Terra Technology (TT) digital event recorders with 12-bit analog-to-digital convertor (A-to-D) and 200 samples per second, and (2) the Refraction Technology (RT) Digital Acquisition Systems with 16 bit A-to-D and up to 4000 samples per second.

The accelerometers were all force-balance units manufactured by Terra Technology with instrument corner frequencies between 50 and 100 Hz. Each accelerometer package was oriented so that the three accelerometers output vertical (CH1), transverse (CH2), and radial (CH3) components directly.

The free surface array was designed to give good azimuthal coverage of the explosive ground motion. In addition, the closest free surface gages coincided with the slant distances of the farthest free-field gages.

## RESULTS

The combined free-field and free surface instrument array is summarized in Figure 2. Data were recovered from seven of the eight free-field instrumentation sites. The vertical acceleration (Z) channel was lost at T2 while the radial acceleration (X) was lost at T4. In the free-field, 19 out of 24 gauges returned satisfactory data.

At the free surface, 13 three-component self-contained recorders were deployed. Two of the stations, S11 and S10, pretriggered and filled their memory prior to the explosion. The radial acceleration at station S12 was also lost because of a bad connection. A total of 32 acceleration records out of 39 possible were recovered from the free-surface installation.

Slant ranges and all peak accelerations are summarized in the following table:

Station	Slant Range (m)	R Acc (g's)	T Acc (g's)	Z Acc (g's)
T1	193	154.		30.0
T2	342	38.0	28.0	
T3	492	28.0	13.0	11.5
T4	585		1.40	4.70
T5	620	10.4	2.50	4.30
T7	887	4.00	0.80	2.20
T8	596	6.50	2.70	3.20
S1	1240	0.44	0.32	1.50
S2	1220	2.50	5.00	5.00
S4	1150	0.33	0.26	0.67
S5	940	2.45	3.50	4.90
S6(TT)	1220	0.91	0.46	1.13
S6(RT)	1220	1.05	0.54	1.27
S7	910	1.85	1.20	3.15
S8	1260	0.83	0.71	0.94
S9	1600	1.00	0.61	0.83
S12	1990		0.59	1.44
S13	680	1.30	1.80	1.45

### *Free-Field Data:*

The free-field waveforms for all components are reproduced in Figures 3a, 4a, and 5a. Each waveform is scaled to its peak amplitude so that wave shapes can be directly compared. The peak amplitudes are given in the above table and summarized in graphical form in Figures 3b-5b.

The radial accelerograms (Figure 3a) are relatively simple pulses (Station 1 ceased operating 70 ms after the P arrival). Stations 3 and 5 clipped slightly (less than 15%); the peak amplitude estimates at these stations take this clipping into account. There is a general increase in pulse duration with range in these figures which may be indicative of attenuation in the wet tuff medium. Stations 8 and 7 exhibit acceleration pulse widths which are nearly twice that of the other stations. These two sites are among the most distant free-field observations, although Station 5, which is between these two, is much shorter in duration. The locations of Stations 7 and 8 are both to the NE of the shot while all other gages are to the N or NW. Thus, it is possible that the apparent increase in pulse width for Stations 7 and 8 may be an azimuthal rather than a range effect. The radial accelerations follow a power law decay with range,  $R^{-2.43}$ . Individual accelerations depart little from this trend. Nearly two orders in magnitude of acceleration are spanned while less than one order of magnitude in range is covered by the data.

The vertical accelerograms are given in Figure 4a. As found for the radial data, Stations 7 and 8 exhibit broader pulses than the other sites. This observation may be caused by propagation path differences to the NE of the WP or possibly by an azimuthally dependent radiation pattern from the source. The ratio of the peak radial-to-vertical acceleration amplitudes begins at 5.1 (193 m) and decreases to 1.8 at 887m. This decreasing ratio at shot level may be a result of increased multipathing as source to receiver range increases. The vertical acceleration decay with range is given in Figure 4b.

The transverse free-field acceleration waveforms are reproduced in Figure 5a. The most notable observation in this data is the increasing complexity in the transverse motions as source to receiver distance increases. At the 887 m range, the transverse accelerogram is over 500 ms in duration with a great deal of complexity. Again, this is a reflection of complex propagation path effects and can be explained in terms of scattering theory. At some ranges in the free-field data, the transverse motion is as great as 73% of the radial motion. Even though the transverse motions most likely can be explained in terms of multipathing, these data also follow a simple power law,  $R^{-4.0}$ .

A spectral comparison of the radial free-field data at Stations 2 (342 m) and 7 (887 m) is given (Figure 6) to document the bandwidth of the data and its variation with range. Both acceleration spectra are flat near 1 Hz. The closest station begins to decay to the high frequencies near 50 Hz. The data from Station 7 decay at a lower frequency, 20 Hz, reflective of its increased propagation distance. The long period levels decrease by a factor of 10-15 between the two observations. The peak time domain accelerations decay by a factor of 9.5. The equivalent seismic-source corner frequency can not be estimated from these free-field data until longer time windows are available for its estimation. This will require future playback and redigitization of the analog Bi-Phase L backup tape.

### *Free Surface Data:*

A number of the free surface gages deployed on MISTY ECHO show evidence of spall, the tensile failure of near surface materials caused by near-total reflection of the primary shock wave. Spall was identified by 1 g dwells on the vertical acceleration (ch1) followed by an impulsive rejoin. The accelerograms from Station 2 are reproduced in Figure 7. As indicated in

Figure 2, Stations 1, 2, 5, and 7 spalled. The observed asymmetry in the spall pattern may be a reflection of the geological structure of Rainier Mesa.

A characteristic set of accelerations from outside the spall zone is given in Figure 8a where Station 8 is reproduced. In this case, the peak vertical acceleration is just under 1 g and the duration of strong ground motion is less than 3 seconds. The corresponding acceleration spectra are given in Figure 8b. Spectra are characterized by rising energy density levels from the low frequencies up to 0.7-2 Hz, followed by a region of relatively flat spectral levels, and a decay in spectral amplitude at the very high frequencies (10-20 Hz).

The complete free surface data set can be compared to the free-field peak amplitudes (Figures 9-11). The farthest range in the free-field data set just overlaps with the slant range to the closest free surface data. In general, the power-law decay trend of the free-field acceleration amplitudes with range extends into the free surface data. The free surface peak amplitudes have not been scaled for a free surface amplification factor. It is interesting to note that the free surface data do not seem to exhibit a consistent factor of two bias over free-field data at comparable ranges as might at first be expected.

Whereas the free-field data show little scatter about the mean curve as a function of range, the free surface data show marked variations in amplitude at a constant range. There is approximately a factor of ten scatter in the free surface peak acceleration amplitudes. This large variation, which is not observed in the free-field data, is most likely a result of variations in the near surface geology of the weathered zone at the mesa surface.

Although the peak accelerations show significant differences at the free surface, the displacement wave shapes determined by double integration of the accelerograms do not. Figure 12a and 12b display all the relative radial and vertical free surface displacements. The initial P-wave followed by a developing Sv/Rayleigh pulse is easy to identify, especially on the vertical displacement (Figure 12a). Finally, a vertical displacement spectra comparison is made between Station 6 and 1 in Figure 13. Both spectra track one another with a common corner frequency at 0.9 Hz, followed by spectral scalloping indicative of interference phenomena. Station 1 is between 3 and 6 dB higher in amplitude than Station 6.

## CONCLUSIONS:

Simultaneous free-field and ground surface data have been recovered from the same nuclear explosion and investigated in terms of their consistency. The free-field data show remarkably small scatter, while the free surface accelerations show as much as a factor of ten variation in amplitudes at nearly identical distances. Comparison of free-field and free surface data at the same slant range appears to show *no* consistent factor of two increase in free surface amplitudes due to reflection. The free-field accelerograms show evidence for azimuthal variations in wave shapes, although a more substantial data set is needed to constrain such effects. Free surface displacements indicate azimuthal symmetry in both time-domain wave shapes and frequency-domain spectral shapes. Further work is needed in modeling these free-field and free surface data in order to constrain the physical parameters leading to the differences and similarities in the observed wavefields.

Table 1.

### Summary of Tunnel Accelerometer Array for MISTY ECHO

(WP coordinates: N891,751.22; E633,168.39; elev. 6104.56)

MISTY ECHO Gauge #	Nevada Coords. (bottom of emplacement hole)	RANGE		Design radial accel. level (g)	Comments
		ft.	meters		
T1	N892,225.83 E632,750.22 6053.98	633.3	193.0	100-300	
T2	N892,787.24 E632,743.92 6053.81	1120.4	341.5	30-90	Z-axis failed*
T3	N893,359.97 E633,043.80 6046.96	1615.0	492.3	10-30	
T4	N893,337.24 E632,088.20 6049.35	1919.2	585.0	7-20	R-axis failed*
T5	N893,493.00 E632,117.67 6054.38	2034.5	620.1	5-20	
T6	N893,762.30 E632,601.20 6046.45	2059.1	627.6	5-20	all axes (Z,R,T) failed*
T7	N894,122.02 E634,848.06 6038.25	2908.4	886.5	1-5	
T8	N893,389.50 E634,231.53 6040.50	1955.8	596.1	5-20	

\* failed during grout pour and curing.

Table 2.

**MISTY ECHO**  
**Summary of Surface Accelerometer Array**  
**on Top of Rainier Mesa**

MISTY ECHO Surface Gauge #	Portable Recorder Type	SLANT RANGE (km)	Comments
S1	TT	1.24	Co-located for intercomparison of digital recorder systems
S2	TT	1.22	
S4	TT	1.15	
S5	TT	0.94	
S6	TT & RT	1.22 "	
S7	TT	0.91	
S8	TT	1.26	
S9	TT	1.60	
S12	RT	1.99	
S13	TT	0.68	
S11	RT	--	Failed*
S10	RT	--	Failed*

TT = Terra Technology digital event cassette recorder - 200 samples/s (AFWL)

RT = Refraction Technology data acquisition system - 1000 samples/s (SMU)

\* failed due to many false pre-shot triggers.

## FIGURE CAPTIONS

- Figure 1: Plan of a section of N-Tunnel at Area 12-NTS showing locations of the free-field accelerometer array in relation to the MISTY ECHO working point.
- Figure 2: Plan-view of the combined free surface and free-field arrays for the MISTY ECHO experiment.
- Figure 3a: Relative radial accelerograms (X) from the free-field of MISTY ECHO.
- Figure 3b: Peak radial accelerations from the free-field of MISTY ECHO.
- Figure 4a: Relative vertical accelerations (Z) from the free-field of MISTY ECHO.
- Figure 4b: Peak vertical accelerations from the free-field of MISTY ECHO.
- Figure 5a: Relative transverse accelerations (Y) from the free-field of MISTY ECHO.
- Figure 5b: Peak transverse accelerations from the free-field of MISTY ECHO.
- Figure 6: Acceleration spectra from the radial free-field data at T7 and T2. Vertical scale is g-sec.
- Figure 7: Radial (ch3), transverse (ch2), and vertical (ch1) accelerations from the free surface station S2. Vertical scales are g's.
- Figure 8a: Radial (ch3), transverse (ch2), and vertical (ch1) accelerations from the free surface station S8. Vertical scales are g's.
- Figure 8b: Acceleration spectra that accompany the accelerograms in Figure 8a. Vertical scales are g-sec.
- Figure 9: Free-field (open squares) and free surface (closed squares) peak radial accelerations from MISTY ECHO.
- Figure 10: Free-field (open triangles) and free surface (closed triangles) peak vertical accelerations from MISTY ECHO.



Figure 11: Free-field (open circles) and free surface (closed circles) peak transverse accelerations from MISTY ECHO.

Figure 12a: Relative free surface vertical displacements from MISTY ECHO.

Figure 12b: Relative free surface radial displacements from MISTY ECHO.

Figure 13: Vertical displacement spectra from free surface data at S1 and S6.



# MISTY ECHO SEISMIC

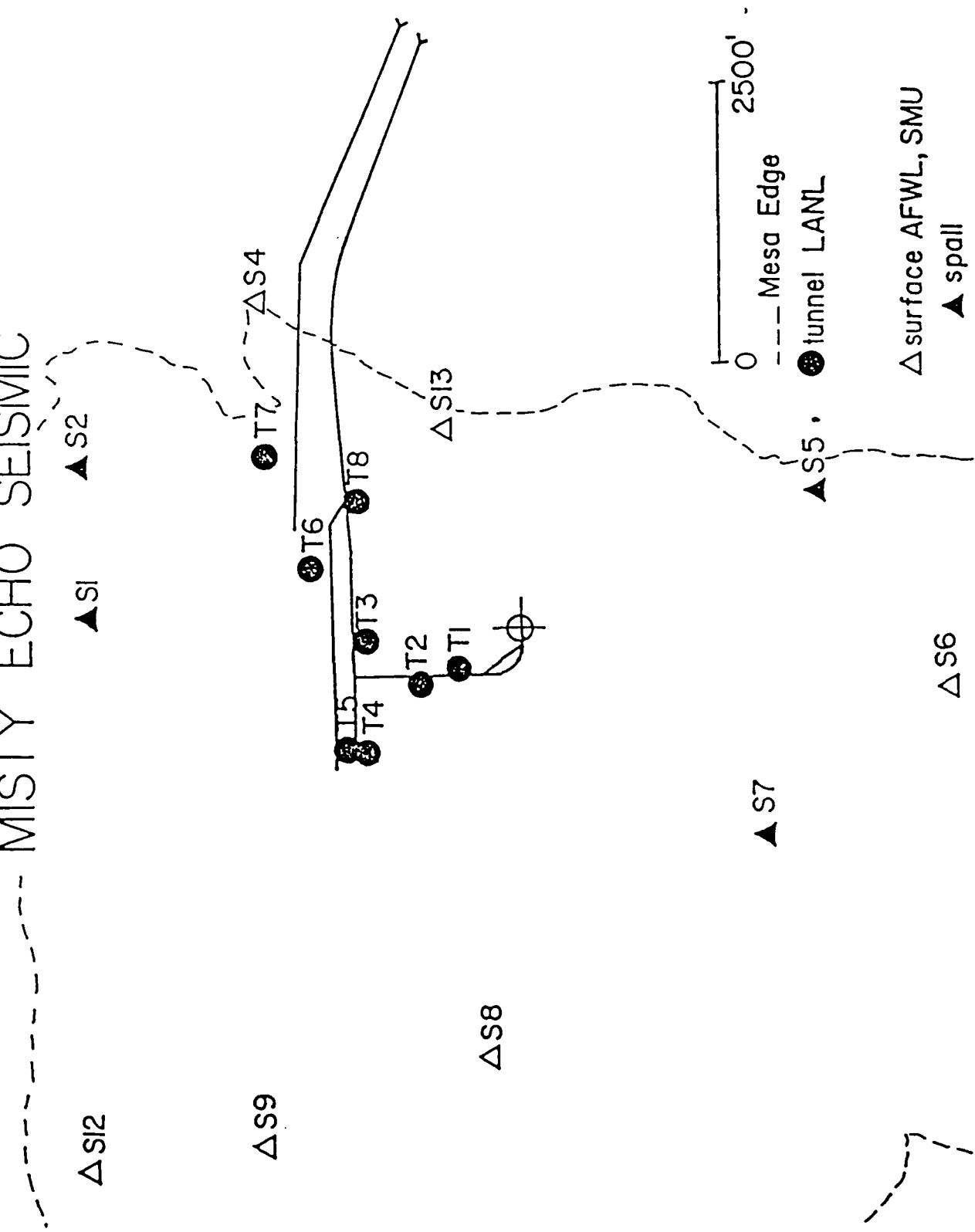


Figure 2: Plan-view of the combined free surface and free-field arrays for the MISTY ECHO experiment.

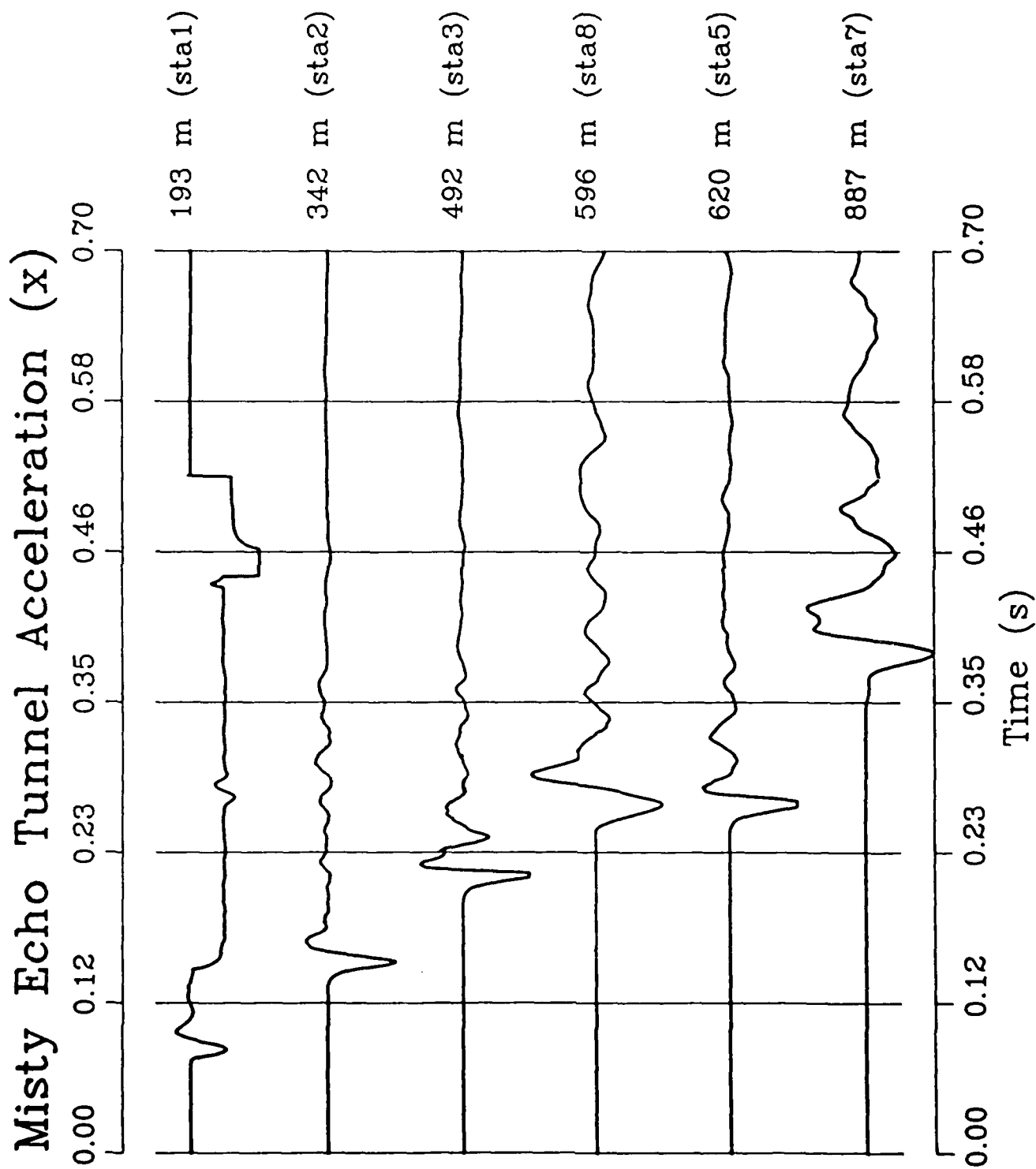


Figure 3a: Relative radial accelerograms (X) from the free-field of MISTY ECHO.

# MISTY ECHO FREE-FIELD ACCELERATION

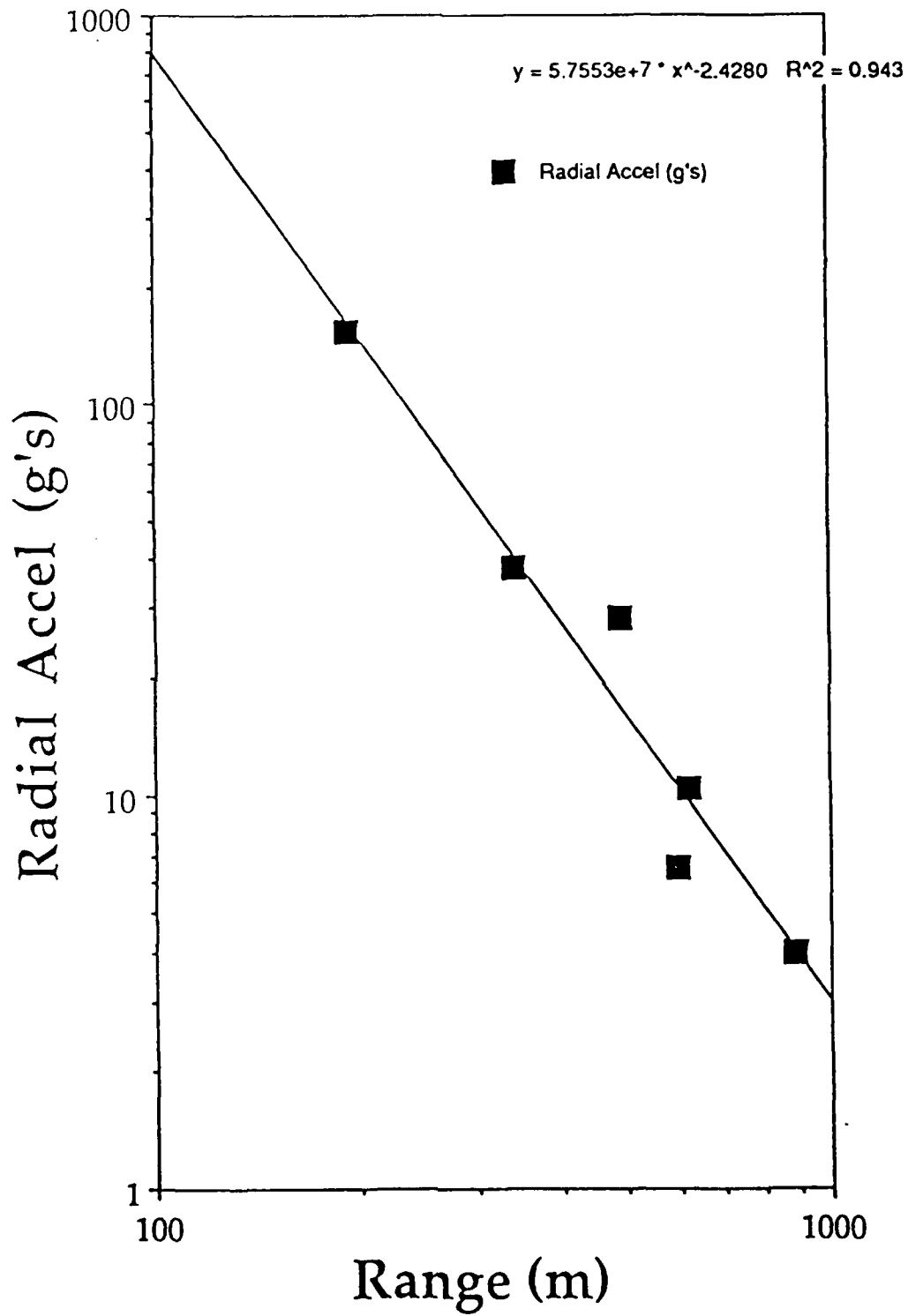


Figure 3b: Peak radial accelerations from the free-field of MISTY ECHO.

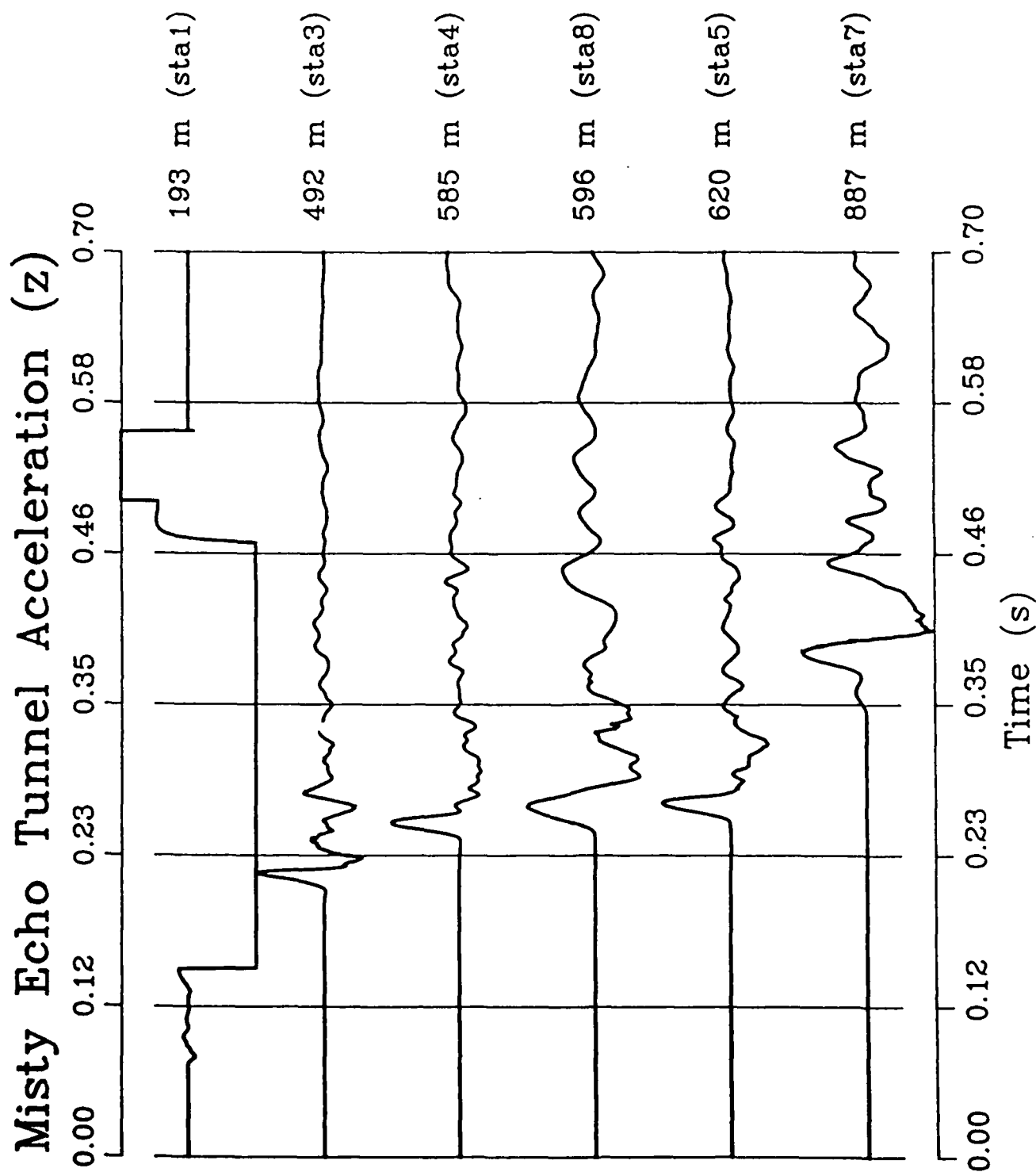


Figure 4a: Relative vertical accelerations (Z) from the free-field of MISTY ECHO.

# MISTY ECHO FREE-FIELD ACCELERATION

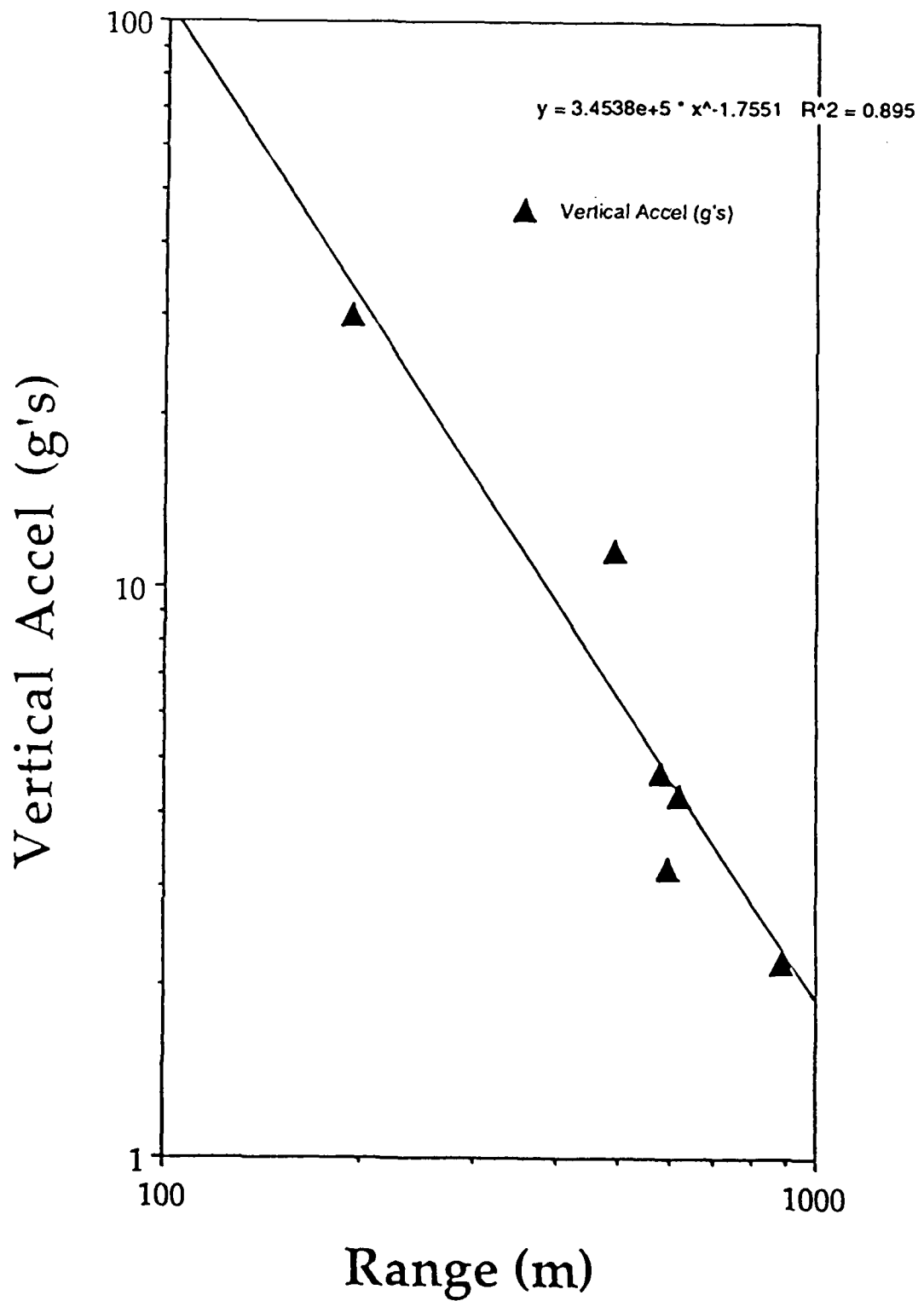


Figure 4b: Peak vertical accelerations from the free-field of MISTY ECHO.

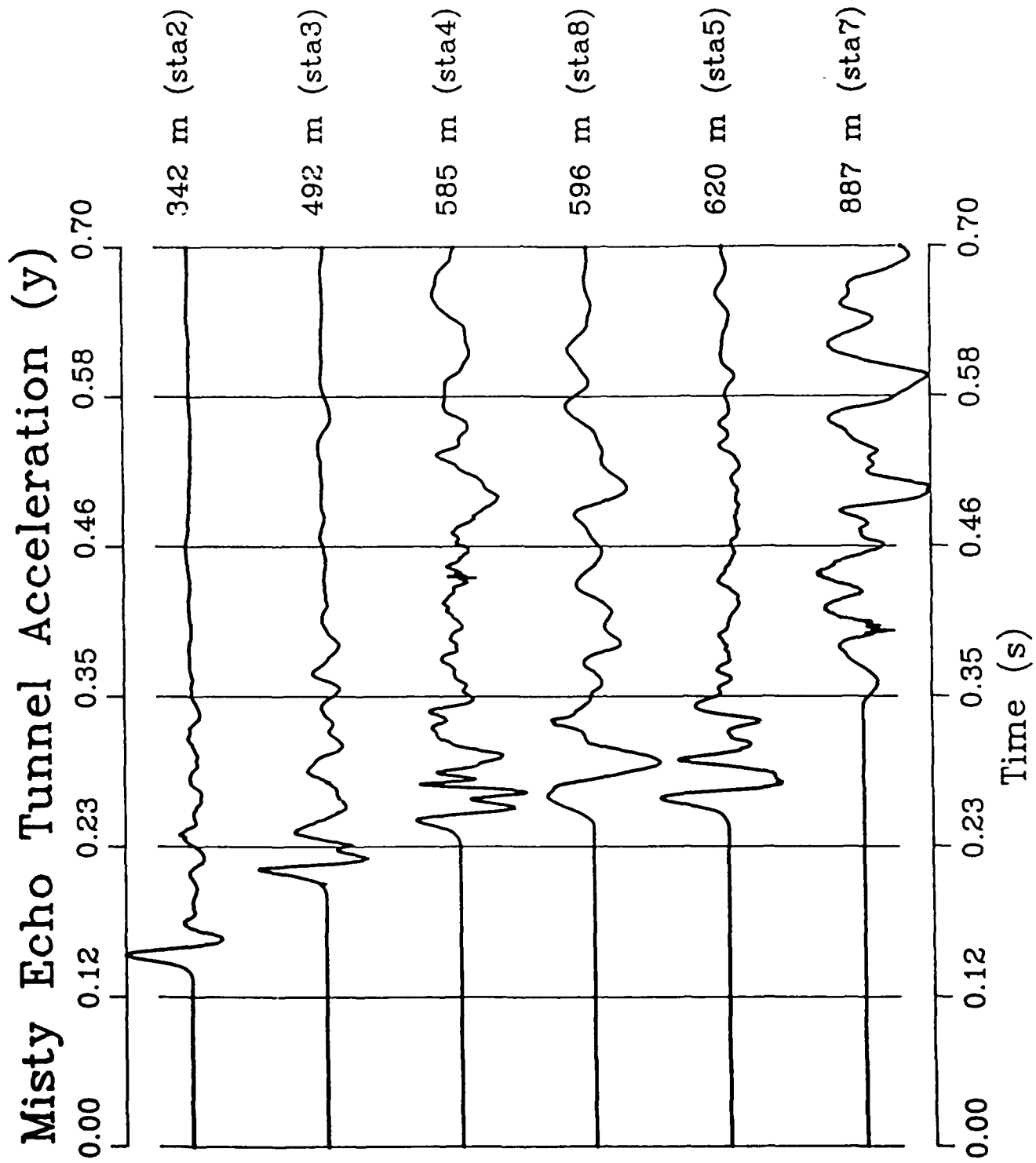


Figure 5a: Relative transverse accelerations (Y) from the free-field of MISTY ECHO.



# MISTY ECHO FREE-FIELD ACCELERATION

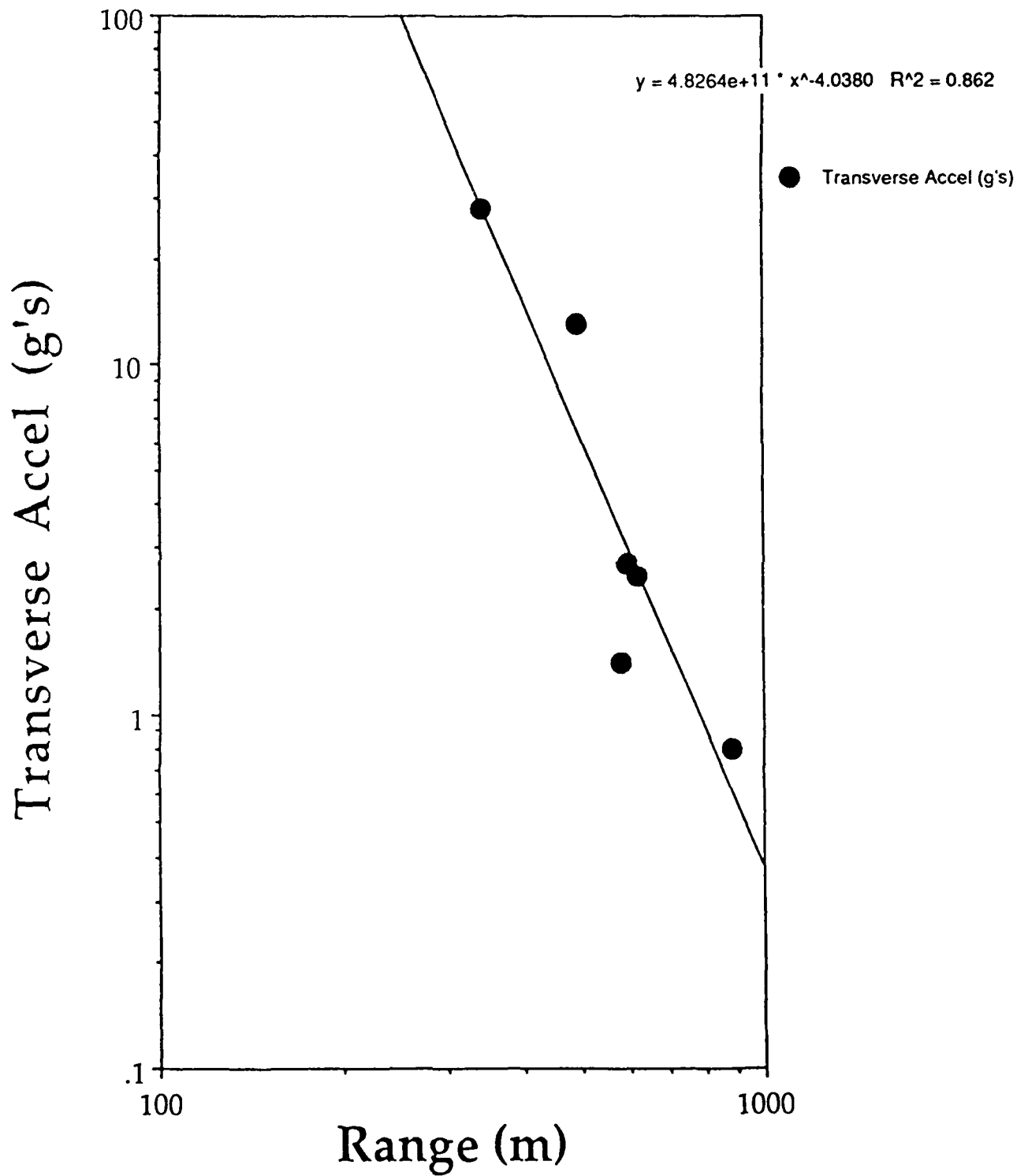


Figure 5b: Peak transverse accelerations from the free-field of MISTY ECHO.

# Misty Echo Tunnel Acceleration

Radial

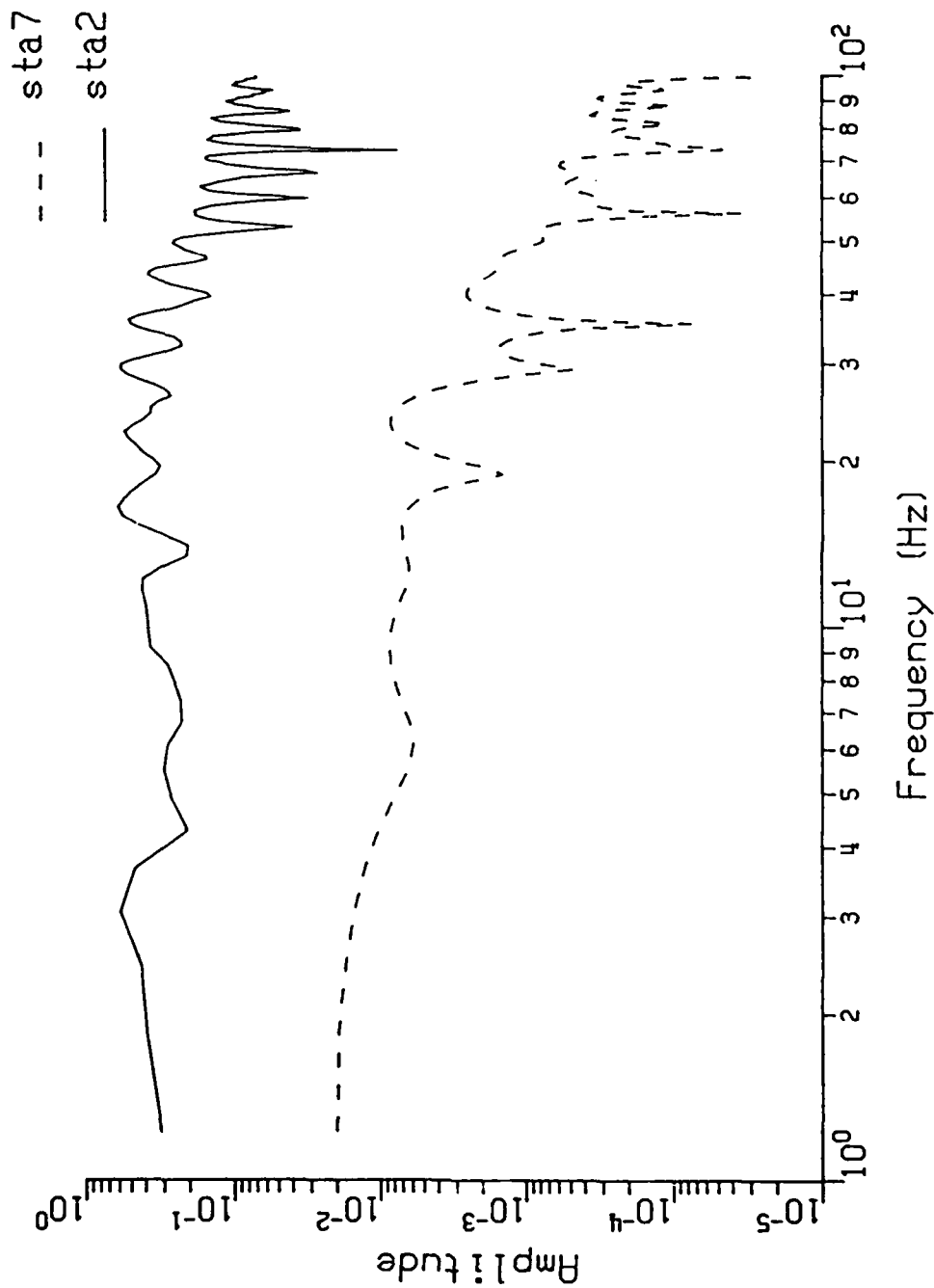


Figure 6: Acceleration spectra from the radial free-field data at T7 and T2. Vertical scale is g-sec.

# Misty Echo

## Surface Acceleration

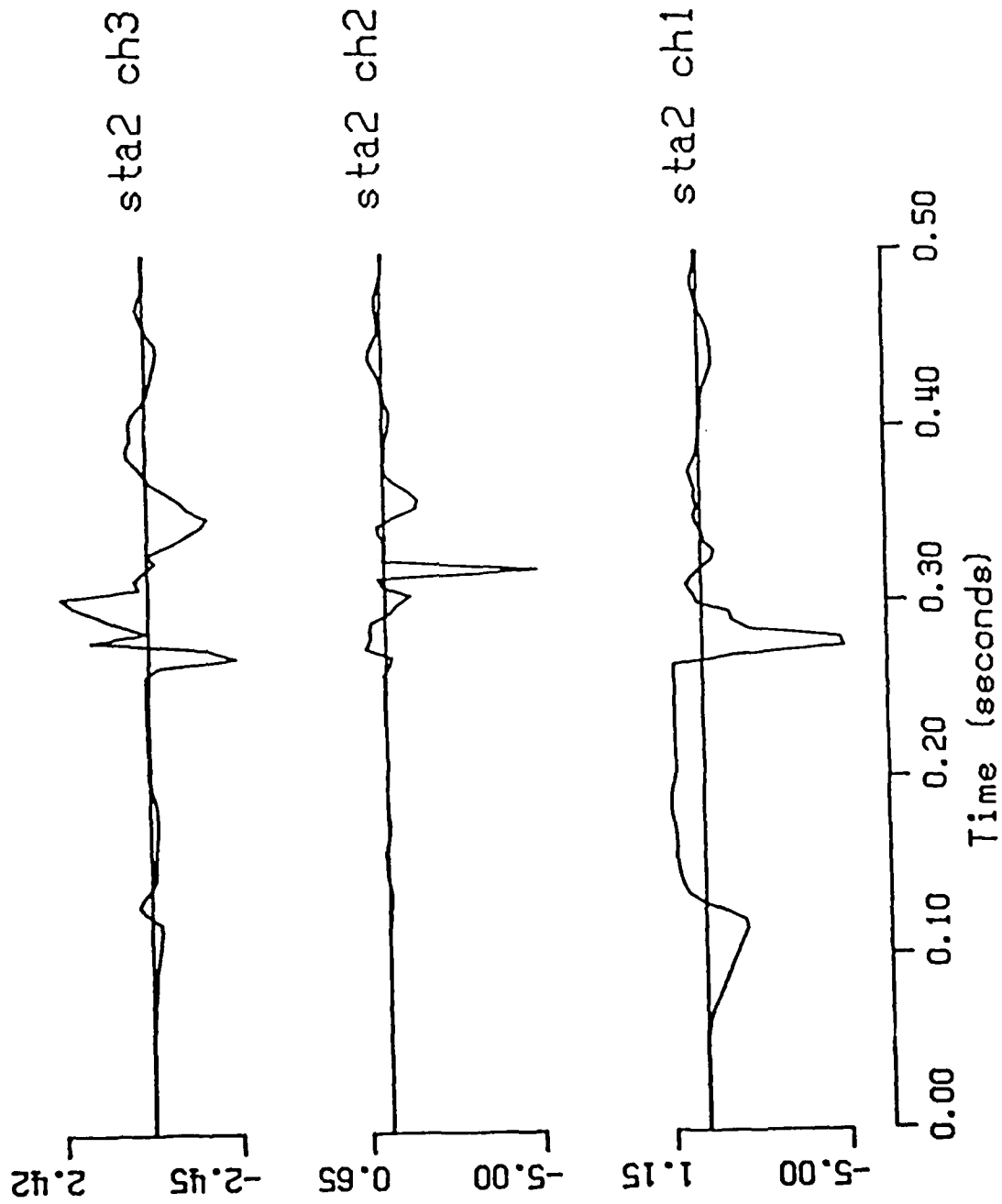


Figure 7: Radial (ch3), transverse (ch2), and vertical (ch1) accelerations from the free surface station S2. Vertical scales are g's.

# Misty Echo

## Surface Acceleration

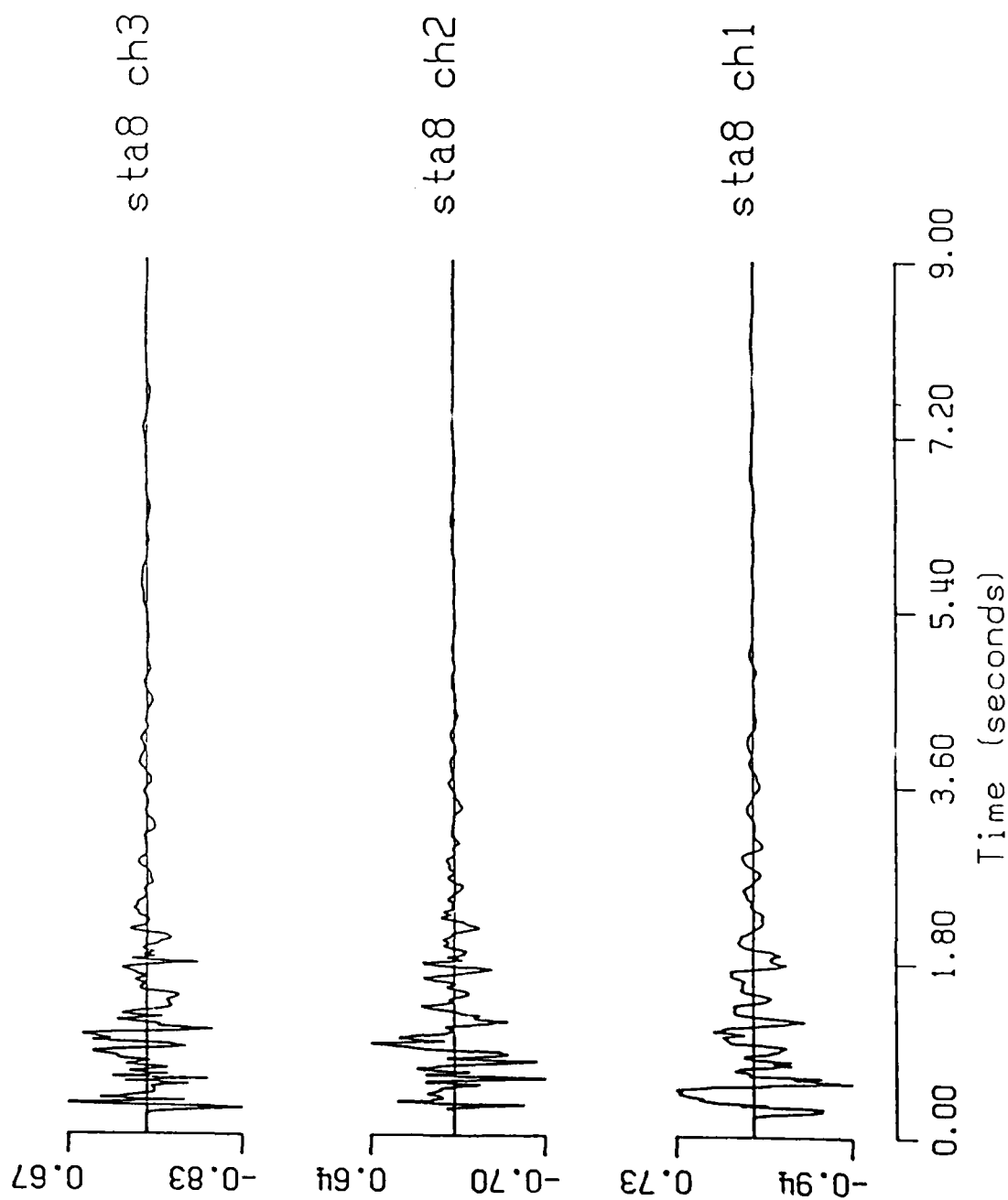


Figure 8a: Radial (ch3), transverse (ch2), and vertical (ch1) accelerations from the free surface station S8. Vertical scales are g's.

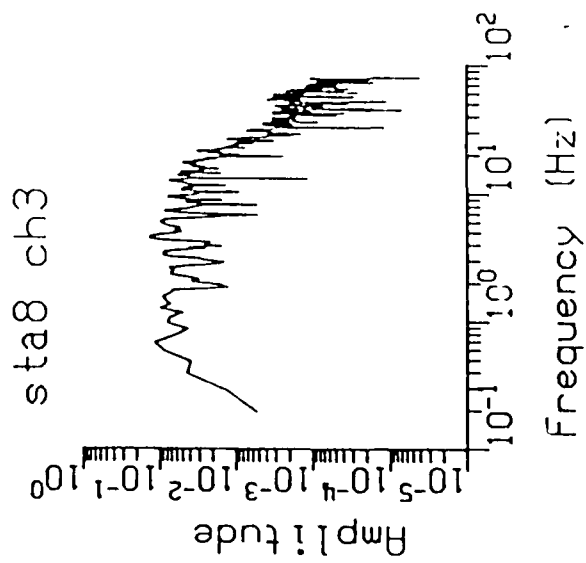
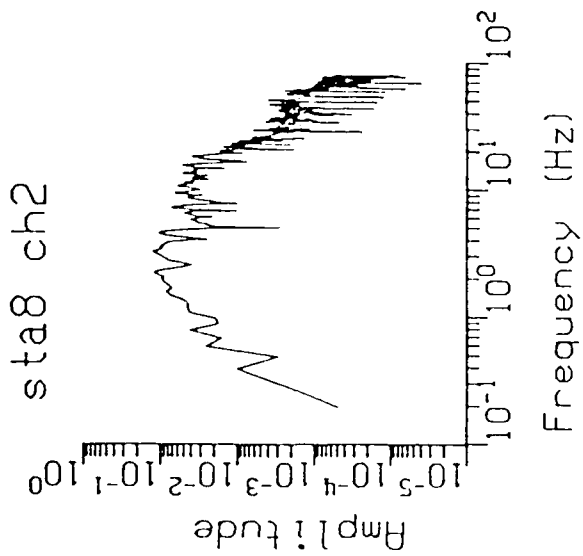
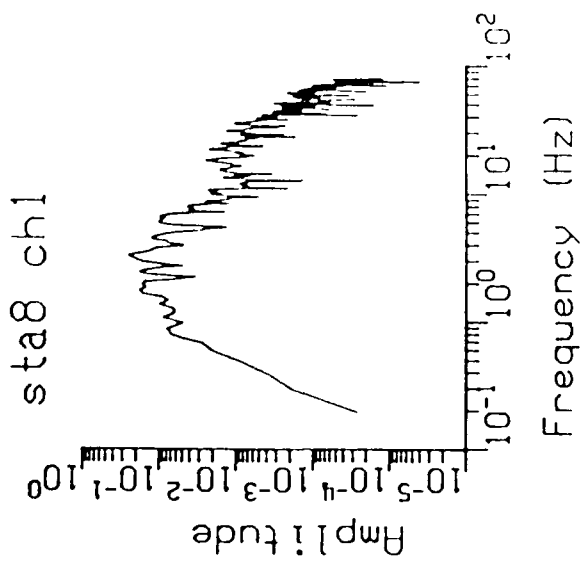


Figure 8b: Acceleration spectra that accompany the accelerograms in Figure 8a. Vertical scales are g-sec.

# MISTY ECHO FF AND FS DATA

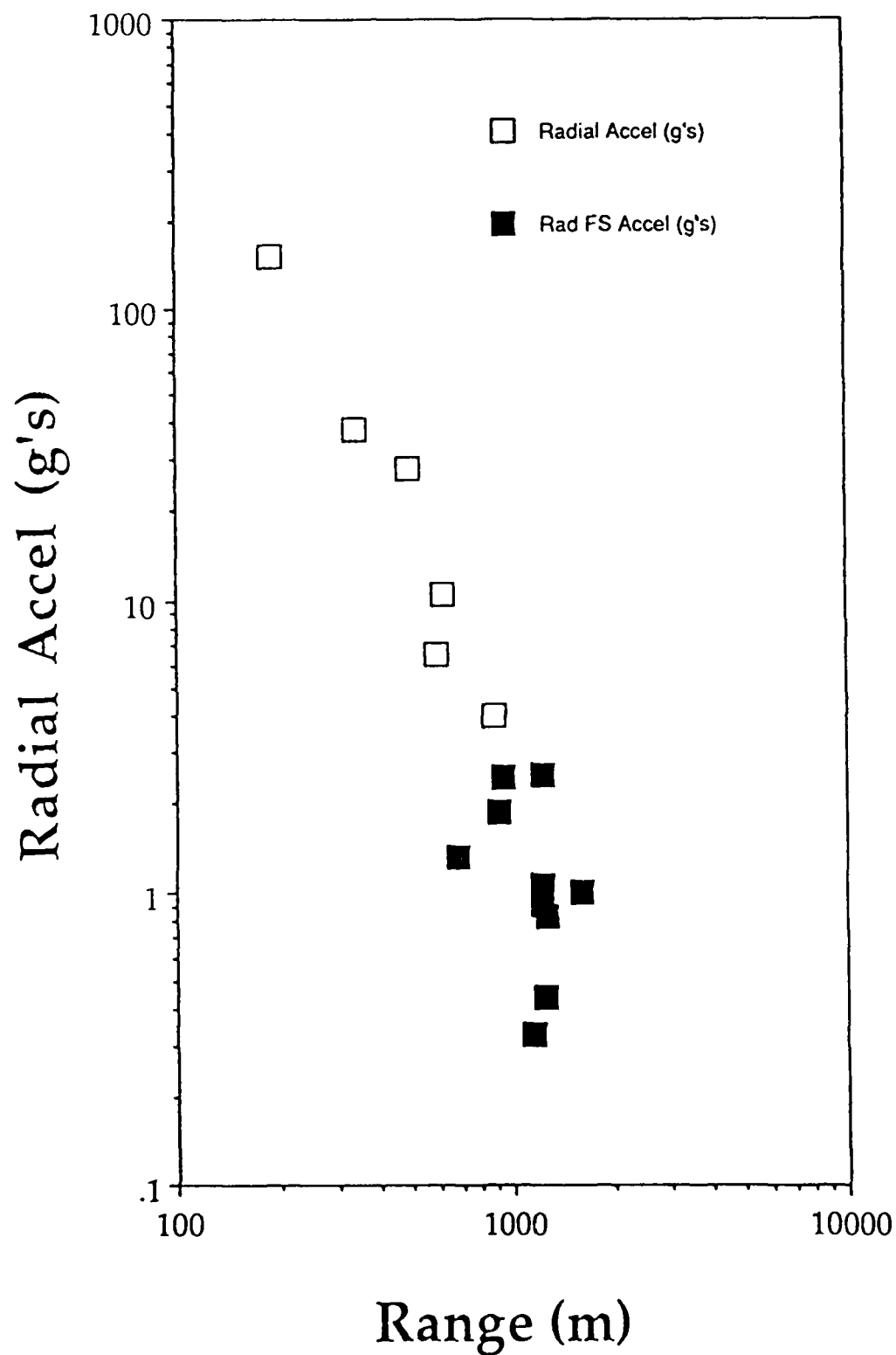


Figure 9: Free-field (open squares) and free surface (closed squares) peak radial accelerations from MISTY ECHO.

# MISTY ECHO FF AND FS DATA

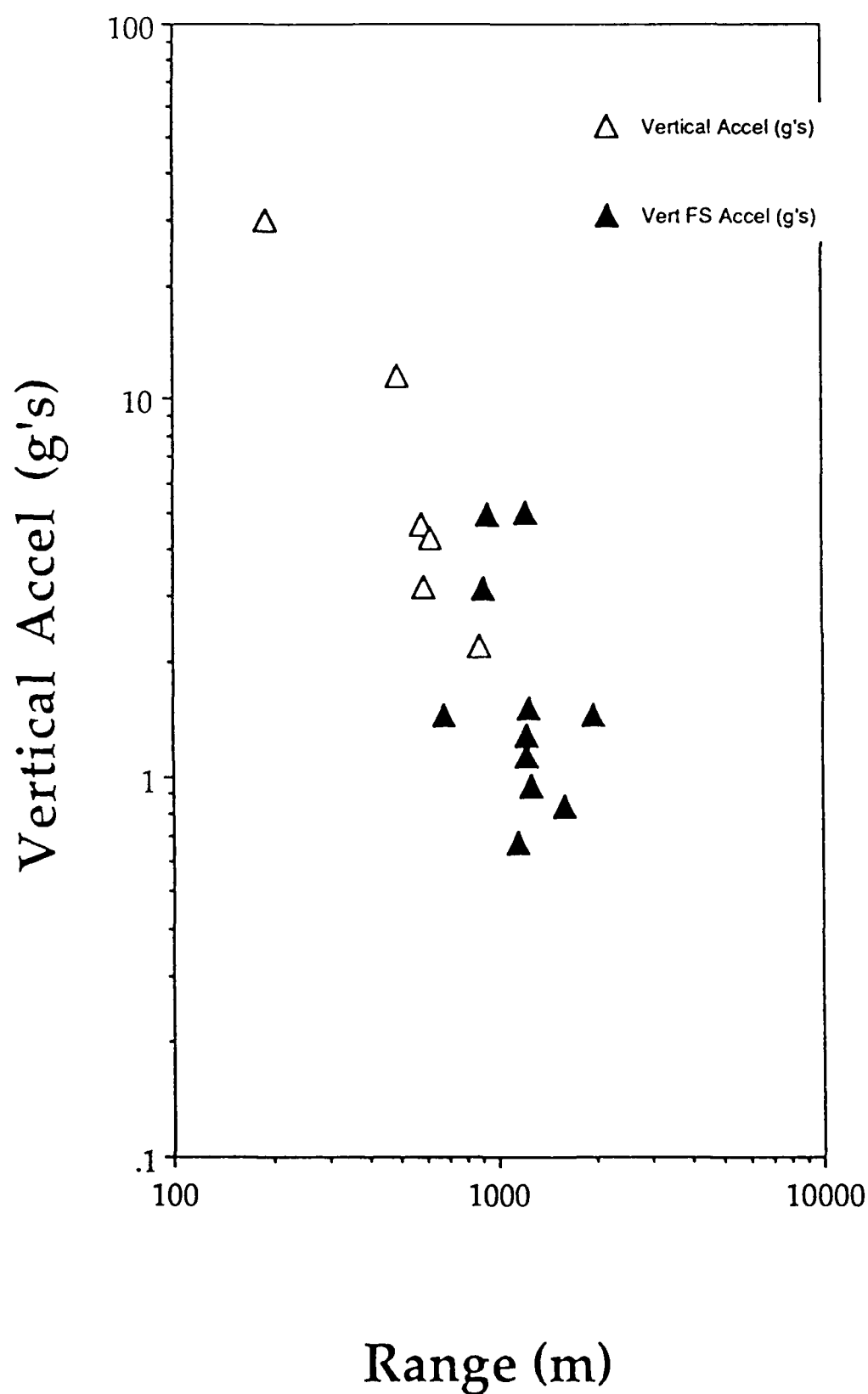


Figure 10: Free-field (open triangles) and free surface (closed triangles) peak vertical accelerations from MISTY ECHO.

# MISTY ECHO FF AND FS DATA

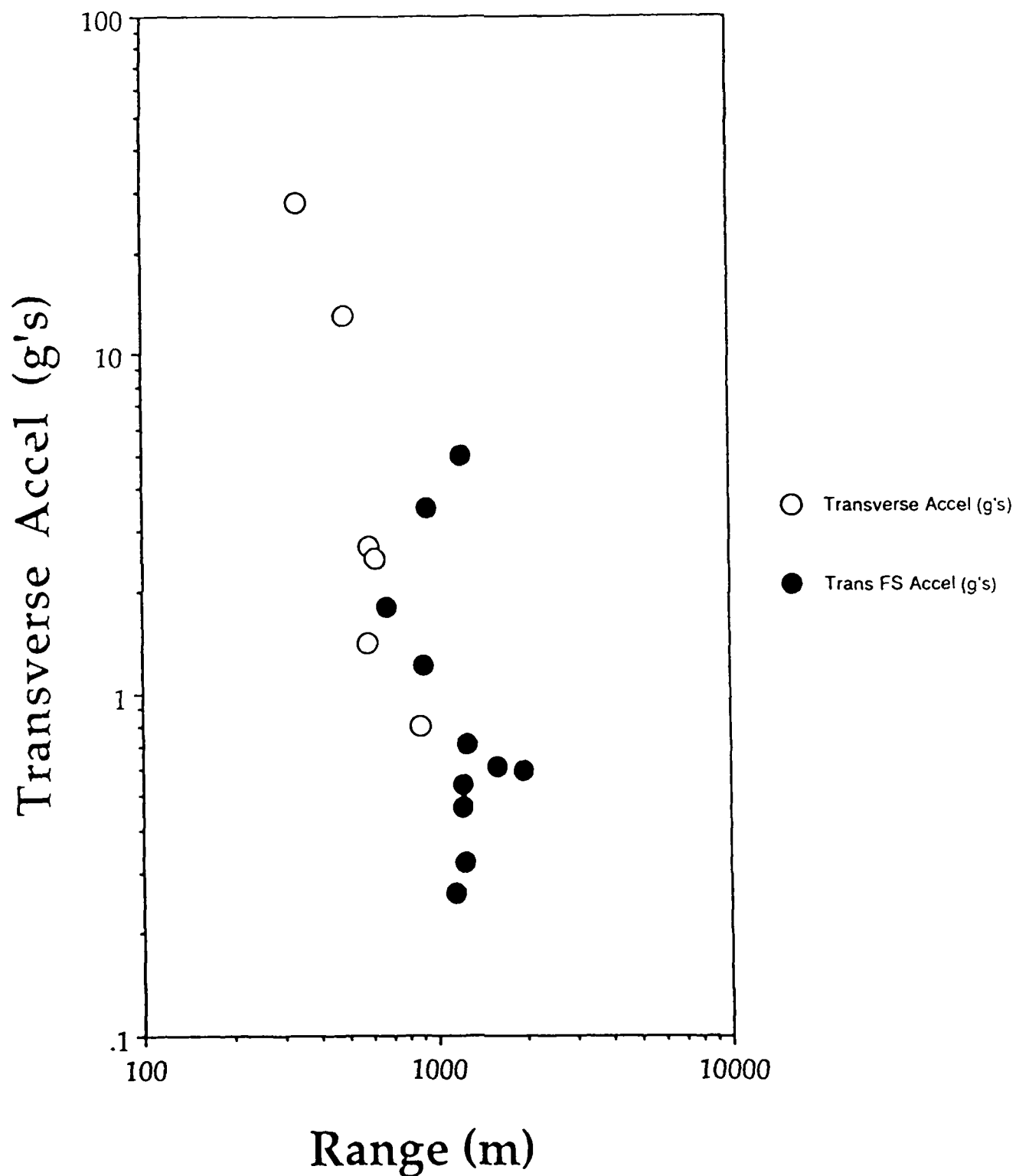


Figure 11: Free-field (open circles) and free surface (closed circles) peak transverse accelerations from MISTY ECHO.



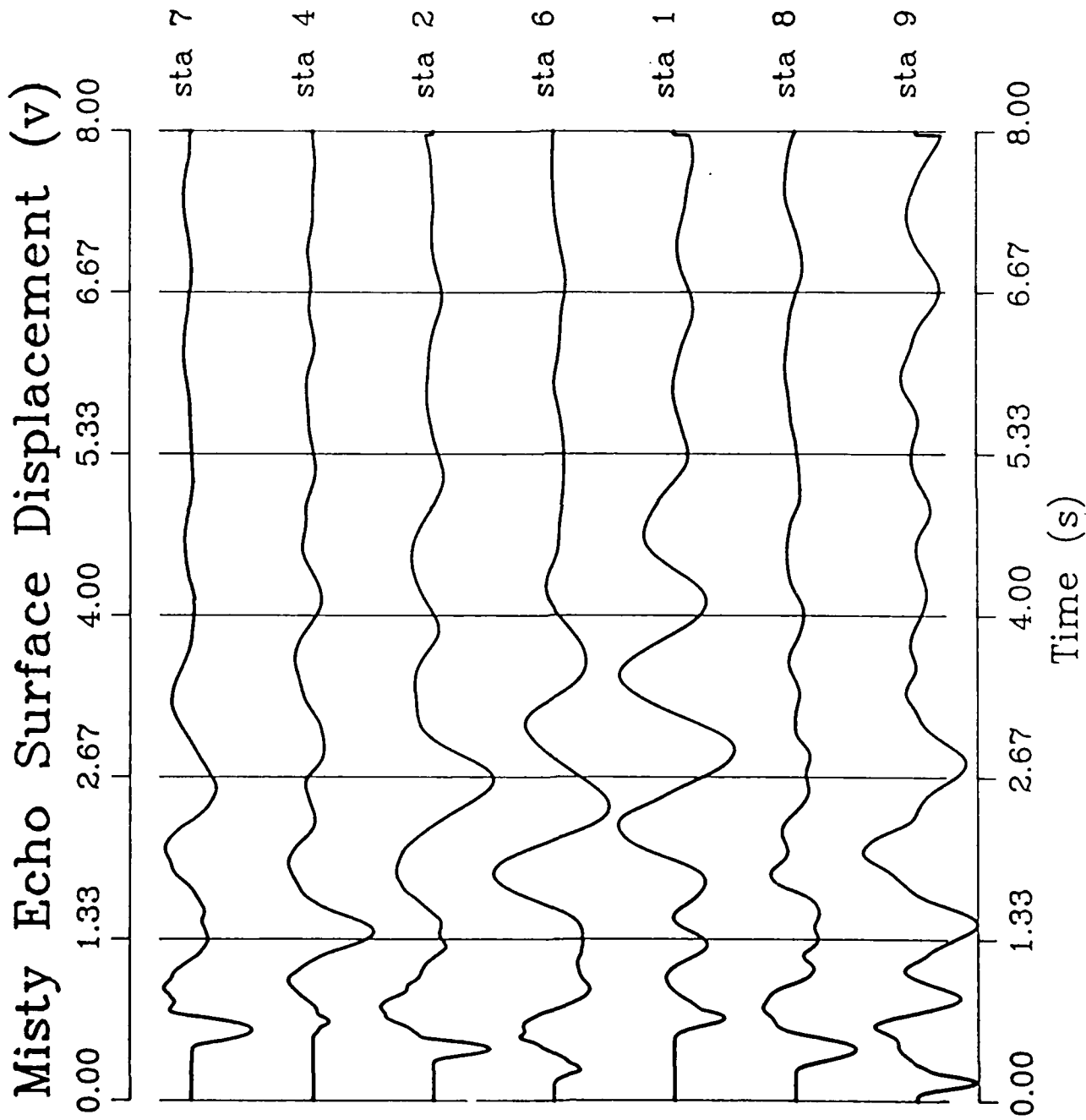


Figure 12a: Relative free surface vertical displacements from MISTY ECHO.

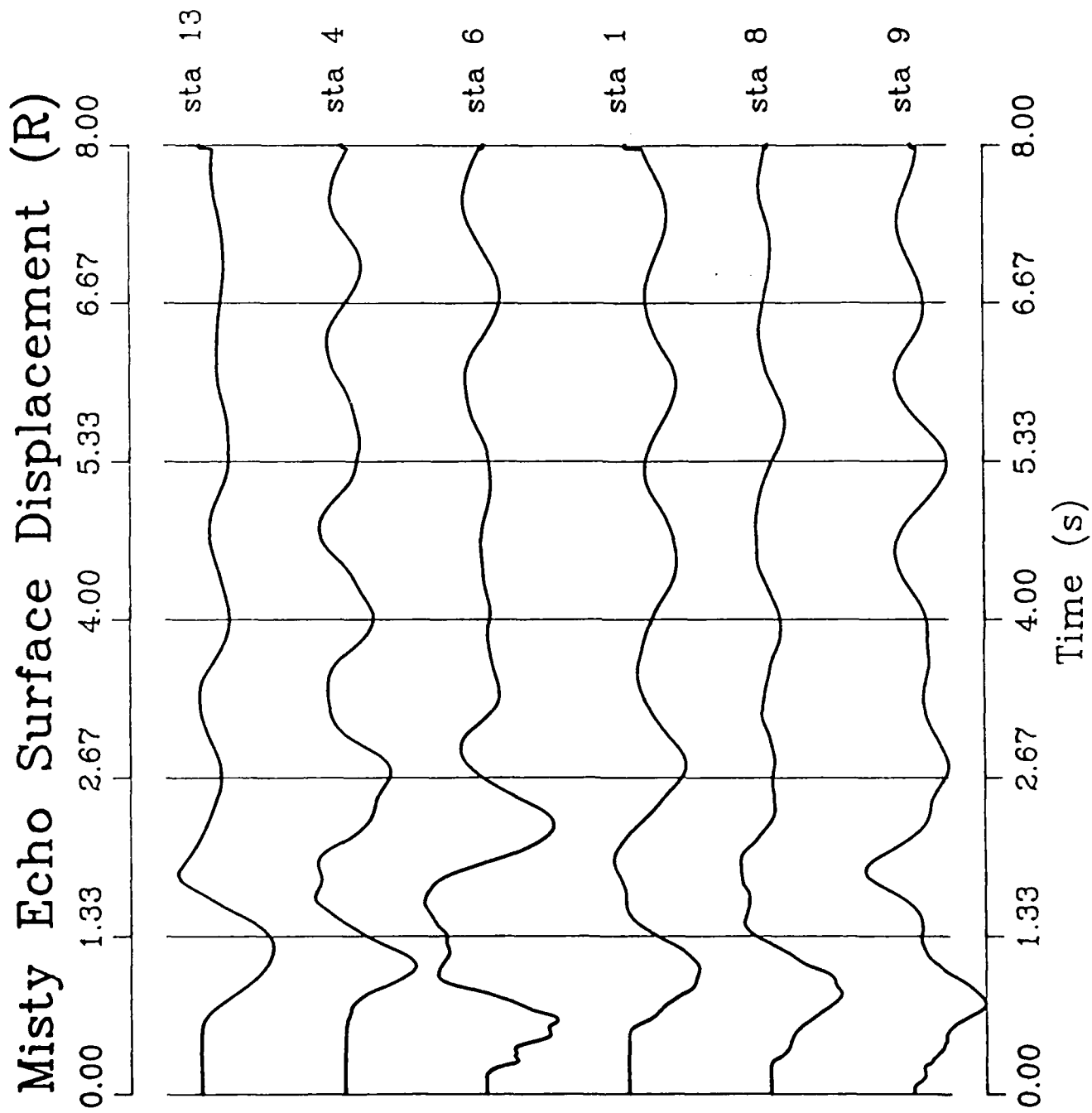


Figure 12b: Relative free surface radial displacements from MISTY ECHO.

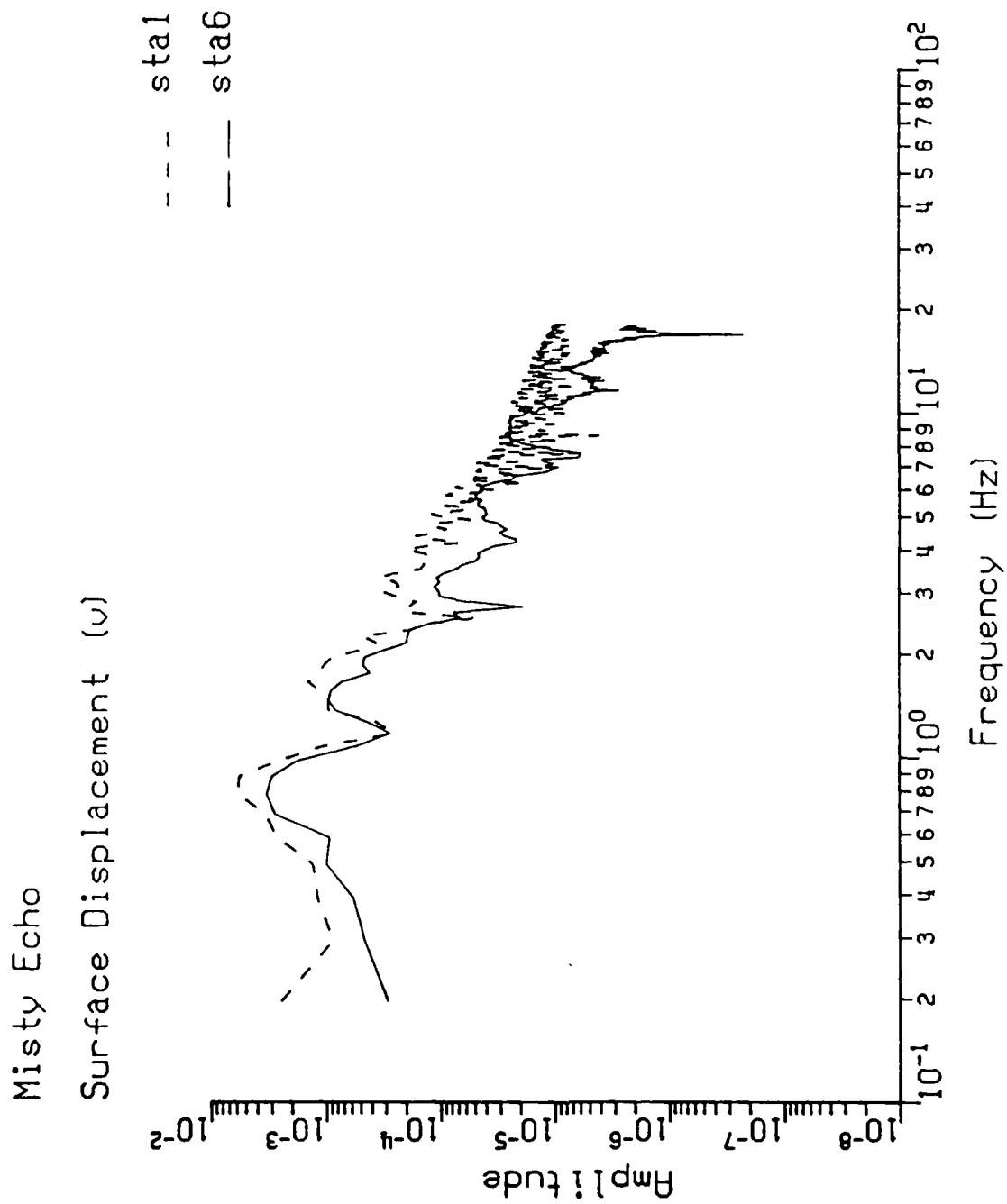


Figure 13: Vertical displacement spectra from free surface data at S1 and S6.

CONTRACTORS (United States)

Professor Keiiti Aki  
Center for Earth Sciences  
University of Southern California  
University Park  
Los Angeles, CA 90089-0741

Professor Thomas Ahrens  
Seismological Lab, 252-21  
Div. of Geological & Planetary Sci.  
California Institute of Technology  
Pasadena, CA 91125

Professor Charles B. Archambeau  
Cooperative Institute for Resch  
in Environmental Sciences  
University of Colorado  
Boulder, CO 80309

Dr. Thomas C. Bache Jr.  
Science Applications Int'l Corp.  
10210 Campus Point Drive  
San Diego, CA 92121 (2 copies)

Dr. Muawia Barazangi  
Institute for the Study of  
of the Continent  
Cornell University  
Ithaca, NY 14853

Dr. Douglas R. Baumgardt  
Signal Analysis & Systems Div.  
ENSCO, Inc.  
5400 Port Royal Road  
Springfield, VA 22151-2388

Dr. Jonathan Berger  
IGPP, A-205  
Scripps Institution of Oceanography  
University of California, San Diego  
La Jolla, CA 92093

Dr. S. Bratt  
Science Applications Int'l Corp.  
10210 Campus Point Drive  
San Diego, CA 92121

Dr. Lawrence J. Burdick  
Woodward-Clyde Consultants  
P.O. Box 93245  
Pasadena, CA 91109-3245 (2 copies)

Professor Robert W. Clayton  
Seismological Laboratory/Div. of  
Geological & Planetary Sciences  
California Institute of Technology  
Pasadena, CA 91125

Dr Karl Coyner  
New England Research, Inc.  
76 Olcott Drive  
White River Junction, VT 05001

Dr. Vernon F. Cormier  
Department of Geology & Geophysics  
U-45, Room 207  
The University of Connecticut  
Storrs, Connecticut 06268

Dr. Steven Day  
Dept. of Geological Sciences  
San Diego State U.  
San Diego, CA 92182

Dr. Zoltan A. Der  
ENSCO, Inc.  
5400 Port Royal Road  
Springfield, VA 22151-2388

Professor John Ferguson  
Center for Lithospheric Studies  
The University of Texas at Dallas  
P.O. Box 830688  
Richardson, TX 75083-0688

Professor Stanley Flatte'  
Applied Sciences Building  
University of California,  
Santa Cruz, CA 95064

Dr. Alexander Florence  
SRI International  
333 Ravenswood Avenue  
Menlo Park, CA 94025-3493

Professor Steven Grand  
University of Texas at Austin  
Dept of Geological Sciences  
Austin, TX 78713-7909

Dr. Henry L. Gray  
Associate Dean of Dedman College  
Department of Statistical Sciences  
Southern Methodist University  
Dallas, TX 75275

Professor Roy Greenfield  
Geosciences Department  
403 Deike Building  
The Pennsylvania State University  
University Park, PA 16802

Dr. Indra N. Gupta  
Teledyne Geotech  
314 Montgomery St.  
Alexandria, VA 22314

Professor David G. Harkrider  
Seismological Laboratory  
Div of Geological & Planetary Sciences  
California Institute of Technology  
Pasadena, CA 91125

Professor Donald V. Helmberger  
Seismological Laboratory  
Div of Geological & Planetary Sciences  
California Institute of Technology  
Pasadena, CA 91125

Professor Eugene Herrin  
Institute for the Study of Earth  
and Man/Geophysical Laboratory  
Southern Methodist University  
Dallas, TX 75275

Professor Robert B. Herrmann  
Department of Earth & Atmospheric  
Sciences  
Saint Louis University  
Saint Louis, MO 63156

Professor Bryan Isacks  
Cornell University  
Dept of Geological Sciences  
SNEE Hall  
Ithaca, NY 14850

Professor Lane R. Johnson  
Seismographic Station  
University of California  
Berkeley, CA 94720

Professor Thomas H. Jordan  
Department of Earth, Atmospheric  
and Planetary Sciences  
Mass Institute of Technology  
Cambridge, MA 02139

Dr. Alan Kafka  
Department of Geology &  
Geophysics  
Boston College  
Chestnut Hill, MA 02167

Professor Leon Knopoff  
University of California  
Institute of Geophysics  
& Planetary Physics  
Los Angeles, CA 90024

Professor Charles A. Langston  
Geosciences Department  
403 Deike Building  
The Pennsylvania State University  
University Park, PA 16802

Professor Thorne Lay  
Department of Geological Sciences  
1006 C.C. Little Building  
University of Michigan  
Ann Arbor, MI 48109-1063

Dr. Randolph Martin III  
New England Research, Inc.  
76 Olcott Drive  
White River Junction, VT 05001

Dr. Gary McCartor  
Mission Research Corp.  
735 State Street  
P.O. Drawer 719  
Santa Barbara, CA 93102 (2 copies)

Professor Thomas V. McEvilly  
Seismographic Station  
University of California  
Berkeley, CA 94720

Dr. Keith L. McLaughlin  
S-CUBED,  
A Division of Maxwell Laboratory  
P.O. Box 1620  
La Jolla, CA 92038-1620

Professor William Menke  
Lamont-Doherty Geological Observatory  
of Columbia University  
Palisades, NY 10964

Professor Brian J. Mitchell  
Department of Earth & Atmospheric  
Sciences  
Saint Louis University  
Saint Louis, MO 63156

Mr. Jack Murphy  
S-CUBED, A Division of Maxwell Lab  
11800 Sunrise Valley Drive  
Suite 1212  
Reston, VA 22091 (2 copies)

Professor J. A. Orcutt  
IGPP, A-205  
Scripps Institute of Oceanography  
Univ. of California, San Diego  
La Jolla, CA 92093 La Jolla, CA 92093

Professor Keith Priestley  
University of Nevada  
Mackay School of Mines  
Reno, NV 89557

Professor Paul G. Richards  
Lamont-Doherty Geological  
Observatory of Columbia Univ.  
Palisades, NY 10964

Wilmer Rivers  
Teledyne Geotech  
314 Montgomery Street  
Alexandria, VA 22314

Dr. Alan S. Ryall, Jr.  
Center of Seismic Studies  
1300 North 17th Street  
Suite 1450  
Arlington, VA 22209-2308 (4 copies)

Professor Charles G. Sammis  
Center for Earth Sciences  
University of Southern California  
University Park  
Los Angeles, CA 90089-0741

Professor Christopher H. Scholz  
Geological Sciences  
Lamont-Doherty Geological Observatory  
Palisades, NY 10964

Dr. Jeffrey L. Stevens  
S-CUBED,  
A Division of Maxwell Laboratory  
P.O. Box 1620  
La Jolla, CA 92038-1620

Professor Brian Stump  
Institute for the Study of Earth & Man  
Geophysical Laboratory  
Southern Methodist University  
Dallas, TX 75275

Professor Ta-liang Teng  
Center for Earth Sciences  
University of Southern California  
University Park  
Los Angeles, CA 90089-0741

Dr. Clifford Thurber  
University of Wisconsin - Madison  
Dept. of Geology & Geophysics  
1215 West Dayton St.  
Madison, WI 53706

Professor M. Nafi Toksoz  
Earth Resources Lab  
Massachusetts Institute of Technology  
42 Carleton Street  
Cambridge, MA 02142

Professor Terry C. Wallace  
Department of Geosciences  
Building #77  
University of Arizona  
Tucson, AZ 85721

Weidlinger Associates  
ATTN: Dr. Gregory Wojcik  
4410 El Camino Real, Suite 110  
Los Altos, CA 94022

Professor Francis T. Wu  
Department of Geological Sciences  
State University of New York  
at Binghamton  
Vestal, NY 13901

OTHERS (United States)

Dr. Monem Abdel-Gawad  
Rockwell Internat'l Science Center  
1049 Camino Dos Rios  
Thousand Oaks, CA 91360

Professor Shelton S. Alexander  
Geosciences Department  
403 Deike Building  
The Pennsylvania State University  
University Park, PA 16802

Dr. Ralph Archuleta  
Department of Geological Sciences  
Univ. of California at  
Santa Barbara  
Santa Barbara, CA

J. Barker  
Department of Geological Sciences  
State University of New York  
at Binghamton  
Vestal, NY 13901

Mr. William J. Best  
907 Westwood Drive  
Vienna, VA 22180

Dr. N. Biswas  
Geophysical Institute  
University of Alaska  
Fairbanks, AK 99701

Dr. G. A. Bollinger  
Department of Geological Sciences  
Virginia Polytechnical Institute  
21044 Derring Hall  
Blacksburg, VA 24061

Mr. Roy Burger  
1221 Serry Rd.  
Schenectady, NY 12309

Dr. Robert Burrige  
Schlumberger-Doll Resch Ctr.  
Old Quarry Road  
Ridgefield, CT 06877

Science Horizons, Inc.  
ATTN: Dr. Theodore Cherry  
710 Encinitas Blvd., Suite 200  
Encinitas, CA 92024 (2 copies)

Professor Jon F. Claerbout  
Professor Amos Nur  
Dept. of Geophysics  
Stanford University  
Stanford, CA 94305 (2 copies)

Dr. Anton W. Dainty  
Earth Resources Lab  
Massachusetts Institute of Technology  
42 Carleton Street  
Cambridge, MA 02142

Professor Adam Dziewonski  
Hoffman Laboratory  
Harvard University  
20 Oxford St.  
Cambridge, MA 02138

Professor John Ebel  
Dept of Geology and Geophysics  
Boston College  
Chestnut Hill, MA 02167

Dr. Donald Forsyth  
Dept of Geological Sciences  
Brown University  
Providence, RI 02912

Dr. Anthony Gangi  
Texas A&M University  
Department of Geophysics  
College Station, TX 77843

Dr. Freeman Gilbert  
Inst. of Geophysics & Planetary Physics  
University of California, San Diego  
P.O. Box 109  
La Jolla, CA 92037

Mr. Edward Giller  
Pacific Seirra Research Corp.  
1401 Wilson Boulevard  
Arlington, VA 22209

Dr. Jeffrey W. Given  
Sierra Geophysics  
11255 Kirkland Way  
Kirkland, WA 98033

Rong Song Jih  
Teledyne Geotech  
314 Montgomery Street  
Alexandria, VA 22314

Professor F.K. Lamb  
Univ. of Illinois at Urbana-Champaign  
Department of Physics  
1110 West Green Street  
Urbana, IL 61801

Dr. Arthur Lerner-Lam  
Lamont-Doherty Geological Observatory  
of Columbia University  
Palisades, NY 10964

Dr. L. Timothy Long  
School of Geophysical Sciences  
Georgia Institute of Technology  
Atlanta, GA 30332

Dr. Peter Malin  
University of California at  
Santa Barbara  
Institute for Central Studies  
Santa Barbara, CA 93106

Dr. George R. Mellman  
Sierra Geophysics  
11255 Kirkland Way  
Kirkland, WA 98033

Dr. Bernard Minster  
IGPP, A-205  
Scripps Institute of Oceanography  
Univ. of California, San Diego  
La Jolla, CA 92093

Professor John Nabelek  
College of Oceanography  
Oregon State University  
Corvallis, OR 97331

Dr. Geza Nagy  
U. California, San Diego  
Dept of Ames, M.S. B-010  
La Jolla, CA 92093

Dr. Jack Oliver  
Department of Geology  
Cornell University  
Ithaca, NY 14850

Dr. Robert Phinney/Dr. F. A. Dahlen  
Dept of Geological  
Geological Science University  
Princeton University  
Princeton, NJ 08540

RADIX System, Inc.  
Attn: Dr. Jay Pulli  
2 Taft Court, Suite 203  
Rockville, Maryland 20850

Dr. Norton Rimer  
S-CUBED  
A Division of Maxwell Laboratory  
P.O. 1620  
La Jolla, CA 92038-1620

Professor Larry J. Ruff  
Department of Geological Sciences  
1006 C.C. Little Building  
University of Michigan  
Ann Arbor, MI 48109-1063

Dr. Richard Sailor  
TASC Inc.  
55 Walkers Brook Drive  
Reading, MA 01867

Thomas J. Sereno, Jr.  
Science Application Int'l Corp.  
10210 Campus Point Drive  
San Diego, CA 92121

Dr. David G. Simpson  
Lamont-Doherty Geological Observ.  
of Columbia University  
Palisades, NY 10964



Dr. Bob Smith  
Department of Geophysics  
University of Utah  
1400 East 2nd South  
Salt Lake City, UT 84112

Dr. S. W. Smith  
Geophysics Program  
University of Washington  
Seattle, WA 98195

Dr. Stewart Smith  
IRIS Inc.  
1616 N. Fort Myer Drive  
Suite 1440  
Arlington, VA 22209

Rondout Associates  
ATTN: Dr. George Sutton,  
Dr. Jerry Carter, Dr. Paul Pomeroy  
P.O. Box 224  
Stone Ridge, NY 12484 (4 copies)

Dr. L. Sykes  
Lamont Doherty Geological Observ.  
Columbia University  
Palisades, NY 10964

Dr. Pradeep Talwani  
Department of Geological Sciences  
University of South Carolina  
Columbia, SC 29208

Dr. R. B. Tittmann  
Rockwell International Science Center  
1049 Camino Dos Rios  
P.O. Box 1085  
Thousand Oaks, CA 91360

Dr. Gregory van der Vink  
IRIS, Inc.  
1616 No. Fort Myer Drive  
Suite 1440  
Arlington, VA 22209

Professor John H. Woodhouse  
Hoffman Laboratory  
Harvard University  
20 Oxford St.  
Cambridge, MA 02138

Dr. Gregory B. Young  
ENSCO, Inc.  
5400 Port Royal Road  
Springfield, VA 22151-2388

FOREIGN (OTHERS)

Dr. Peter Basham  
Earth Physics Branch  
Geological Survey of Canada  
1 Observatory Crescent  
Ottawa, Ontario, CANADA K1A 0Y3

Professor Ari Ben-Menahem  
Dept of Applied Mathematics  
Weizman Institute of Science  
Rehovot  
ISRAEL 951729

Dr. Eduard Berg  
Institute of Geophysics  
University of Hawaii  
Honolulu, HI 96822

Dr. Michel Bouchon  
I.R.I.G.M.-B.P.  
38402 St. Martin D'Herès  
Cedex FRANCE

Dr. Hilmar Bungum/NTNF/NORSAR  
P.O. Box 51  
Norwegian Council of Science,  
Industry and Research, NORSAR  
N-2007 Kjeller, NORWAY

Dr. Michel Campillo  
I.R.I.G.M.-B.P. 68  
38402 St. Martin D'Herès  
Cedex, FRANCE

Dr. Kin-Yip Chun  
Geophysics Division  
Physics Department  
University of Toronto  
Ontario, CANADA M5S 1A7

Dr. Alan Douglas  
Ministry of Defense  
Blacknest, Brimpton,  
Reading RG7-4RS  
UNITED KINGDOM

Dr. Manfred Henger  
Fed. Inst. For Geosciences & Nat'l Res.  
Postfach 510153  
D-3000 Hannover 51  
FEDERAL REPUBLIC OF GERMANY

Ms. Eva Johannisson  
Senior Research Officer  
National Defense Research Inst.  
P.O. Box 27322  
S-102 54 Stockholm, SWEDEN

Tormod Kvaerna  
NTNF/NORSAR  
P.O. Box 51  
N-2007 Kjeller, NORWAY

Mr. Peter Marshall, Procurement  
Executive, Ministry of Defense  
Blacknest, Brimpton,  
Reading RG7-4RS  
UNITED KINGDOM (3 copies)

Dr. Robert North  
Geophysics Division  
Geological Survey of Canada  
1 Observatory crescent  
Ottawa, Ontario, CANADA K1A 0Y3

Dr. Frode Ringdal  
NTNF/NORSAR  
P.O. Box 51  
N-2007 Kjeller, NORWAY

Dr. Jorg Schlittenhardt  
Fed. Inst. for Geosciences & Nat'l Res.  
Postfach 510153  
D-3000 Hannover 51  
FEDERAL REPUBLIC OF GERMANY

University of Hawaii  
Institute of Geophysics  
ATTN: Dr. Daniel Walker  
Honolulu, HI 96822

FOREIGN CONTRACTORS

Dr. Ramon Cabre, S.J.  
Observatorio San Calixto  
Casilla 5939  
La Paz Bolivia

Professor Peter Harjes  
Institute for Geophysik  
Rhur University/Bochum  
P.O. Box 102148, 4630 Bochum 1  
FEDERAL REPUBLIC OF GERMANY

Dr. E. Husebye  
NTNF/NORSAR  
P.O. Box 51  
N-2007 Kjeller, NORWAY

Professor Brian L.N. Kennett  
Research School of Earth Sciences  
Institute of Advanced Studies  
G.P.O. Box 4  
Canberra 2601, AUSTRALIA

Dr. B. Massinon  
Societe Radiomana  
27 Rue Claude Bernard  
75005, Paris, FRANCE (2 copies)

Dr. Pierre Mechler  
Societe Radiomana  
27, Rue Claude Bernard  
75005, Paris, FRANCE

Dr. Svein Mykkeltveit  
NTNF/NORSAR  
P.O. Box 51  
N-2007 Kjeller, NORWAY (3 copies)

GOVERNMENT

Dr. Ralph Alewine III  
DARPA/NMRO  
1400 Wilson Boulevard  
Arlington, VA 22209-2308

Dr. Robert Blandford  
DARPA/NMRO  
1400 Wilson Boulevard  
Arlington, VA 22209-2308

Sandia National Laboratory  
ATTN: Dr. H. B. Durham  
Albuquerque, NM 87185

Dr. Jack Evernden  
USGS-Earthquake Studies  
345 Middlefield Road  
Menlo Park, CA 94025

U.S. Geological Survey  
ATTN: Dr. T. Hanks  
Nat'l Earthquake Resch Center  
345 Middlefield Road  
Menlo Park, CA 94025

Dr. James Hannon  
Lawrence Livermore Nat'l Lab.  
P.O. Box 808  
Livermore, CA 94550

Paul Johnson  
ESS-4, Mail Stop J979  
Los Alamos National Laboratory  
Los Alamos, NM 87545

Ms. Ann Kerr  
DARPA/NMRO  
1400 Wilson Boulevard  
Arlington, VA 22209-2308

Dr. Max Koontz  
US Dept of Energy/DP 5  
Forrestal Building  
1000 Independence Ave.  
Washington, D.C. 20585

Dr. W. H. K. Lee  
Office of Earthquakes, Volcanoes,  
& Engineering  
345 Middlefield Rd  
Menlo Park, CA 94025

Dr. William Leith  
U.S. Geological Survey  
Mail Stop 928  
Reston, VA 22092

Dr. Richard Lewis  
Dir. Earthquake Engrg & Geophysics  
U.S. Army Corps of Engineers  
Box 631  
Vicksburg, MS 39180

Dr. Robert Masse'  
Box 25046, Mail Stop 967  
Denver Federal Center  
Denver, CO 80225

Richard Morrow  
ACDA/VI  
Room 5741  
320 21st Street N.W.  
Washington, D.C. 20451

Dr. Keith K. Nakanishi  
Lawrence Livermore National Laboratory  
P.O. Box 808, L-205  
Livermore, CA 94550 (2 copies)

Dr. Carl Newton  
Los Alamos National Lab.  
P.O. Box 1663  
Mail Stop C335, Group ESS-3  
Los Alamos, NM 87545

Dr. Kenneth H. Olsen  
Los Alamos Scientific Lab.  
P.O. Box 1663  
Mail Stop C335, Group ESS-3  
Los Alamos, NM 87545

Howard J. Patton  
Lawrence Livermore National Laboratory  
P.O. Box 808, L-205  
Livermore, CA 94550

Mr. Chris Paine  
Office of Senator Kennedy  
SR 315  
United States Senate  
Washington, D.C. 20510

AFOSR/NP  
ATTN: Colonel Jerry J. Perrizo  
Bldg 410  
Bolling AFB, Wash D.C. 20332-6448

HQ AFTAC/TT  
Attn: Dr. Frank F. Pilotte  
Patrick AFB, Florida 32925-6001

Mr. Jack Rachlin  
USGS - Geology, Rm 3 C136  
Mail Stop 928 National Center  
Reston, VA 22092

Robert Reinke  
AFWL/NTESG  
Kirtland AFB, NM 87117-5008

Dr. Byron Ristvet  
HQ DNA, Nevada Operations Office  
Attn: NVCG  
P.O. Box 98539  
Las Vegas, NV 89193

HQ AFTAC/TGR  
Attn: Dr. George H. Rothe  
Patrick AFB, Florida 32925-6001

Donald L. Springer  
Lawrence Livermore National Laboratory  
P.O. Box 808, L-205  
Livermore, CA 94550

Dr. Lawrence Turnbull  
OSWR/NED  
Central Intelligence Agency  
CIA, Room 5G48  
Washington, D.C. 20505

Dr. Thomas Weaver  
Los Alamos National Laboratory  
P.O. Box 1663  
MS C 335  
Los Alamos, NM 87545

GL/SULL  
Research Library  
Hanscom AFB, MA 01731-5000 (2 copies)

Secretary of the Air Force (SAFRD)  
Washington, DC 20330  
Office of the Secretary Defense  
DDR & E  
Washington, DC 20330

HQ DNA  
ATTN: Technical Library  
Washington, DC 20305

DARPA/RMO/RETRIEVAL  
1400 Wilson Blvd.  
Arlington, VA 22209

DARPA/RMO/Security Office  
1400 Wilson Blvd.  
Arlington, VA 22209

GL/XO  
Hanscom AFB, MA 01731-5000

GL/LW  
Hanscom AFB, MA 01731-5000

DARPA/PM  
1400 Wilson Boulevard  
Arlington, VA 22209

Defense Technical  
Information Center  
Cameron Station  
Alexandria, VA 22314  
(5 copies)

Defense Intelligence Agency  
Directorate for Scientific &  
Technical Intelligence  
Washington, D.C. 20301

Defense Nuclear Agency/SPSS  
ATTN: Dr. Michael Shore  
6801 Telegraph Road  
Alexandria, VA 22310

AFTAC/CA (STINFO)  
Patrick AFB, FL 32925-6001

Mr. Alfred Lieberman  
ACDA/VI-OA'State Department Building  
Room 5726  
320 - 21st Street, NW  
Washington, D.C. 20451

TACTEC  
Battelle Memorial Institute  
505 King Avenue  
Columbus, OH 43201 (Final report only)